Solution Synthesis and Actuation of Magnetic Nanostructures

Dissertation

zur Erlangung des akademischen Grades

doctor rerum naturalium

(Dr. rer. nat.)

im Fach Physik

eingereicht an der

Mathematisch-Naturwissenschaftlichen Fakultät

der Humboldt-Universität zu Berlin

von

Diplom Physiker Peter Johannes Vach

Präsident der Humboldt-Universität zu Berlin:

Prof. Dr. Jan-Hendrik Olbertz

Dekan der Mathematisch-Naturwissenschaftlichen Fakultät:

Prof. Dr. Elmar Kulke

Gutachter/innen: 1. Prof. Dr. Dr. h.c. Peter Fratzl

2. Prof. Dr. Holger Stark

3. Prof. Dr. Jürgen P. Rabe

Tag der mündlichen Prüfung: 15.12.2014

Kurzfassung

Viele neue Technologien basieren auf Materialien die im Nanometerbereich strukturiert sind. Damit diese im großen Maßstab zur Anwendung gebracht werden können, werden Methoden benötigt solche nanostrukturierten Materialien kostengünstig zu produzieren. Magnetische Felder sind eine vielversprechende Möglichkeit die Anordnung von Mikro- und Nanostrukturen zu beeinflussen. In dieser Doktorarbeit wird eine Methode für die Herstellung magnetischer Nanostrukturen in Lösung präsentiert. Die Herstellungsmethode ist skalierbar, kostengünstig und kann große Mengen produzieren. Die synthetisierten Strukturen haben zufällige Formen und bewegen sich unter dem Einfluss eines externen rotierenden Magnetfelds im rechten Winkel zu der Ebene in der das Magnetfeld rotiert. Die dimensionslosen Geschwindigkeiten dieser zufällig geformten Propeller sind vergleichbar mit jenen früher publizierter Mikropropeller mit genau definierten helikalen Formen. Das beobachtete Verhältnis zwischen Anregungsfrequenz und Propellergeschwindigkeit konnte mittels eines einfachen Drehmomentgleichgewichts verstanden werden. Dieses vertiefte Verständnis der Propellerbewegung ermöglichte eine theoretische Studie zur Kontrolle von Propellerschwärmen. Die Aufgabe besteht darin mehrere Propeller entlang unterschiedlicher, frei wählbarer Bahnen zu steuern, was schwierig ist da alle Propeller identischen externen Magnetfeldern ausgesetzt sind. Eine bestimmte Kontrollstrategie wurde gefunden, welche die magnetische Feldstärke minimiert, die zum Erreichen einer vorgegebenen Genauigkeit nötig ist. Die Entdeckung dieser Kontrollstrategie ist ein wichtiger Schritt auf dem Weg zu einer experimentellen Realisierung von kontrollierbaren Propellerschwärmen, welche neue Möglichkeiten zur Herstellung von Mikrostrukturen und Anwendungsfelder in der Mikrorobotik eröffnen würden. Schließlich wurde auch das kollektive Verhalten von großen Mengen von magnetischen Propellern untersucht. Sowohl zufällig geformte als auch helikale Propeller bilden Zusammenballungen, die im dynamischen Gleichgewicht kreisförmig sind und langsam rotieren. Gleichförmig helikale Propeller ordnen sich in diesen Zusammenballungen hexagonal an. Der Vergleich zwischen Beobachtungen und Simulationen zeigte, dass hydrodynamische Interaktionen für die Bildung der Zusammenballungen nicht notwendig sind, aber dazu führen dass sich eine Randregion bildet, in welcher die Winkelgeschwindigkeit der Propeller stark erhöht ist. Die beobachtete Bildung von Zusammenballungen legt eine einfache Methode nahe, mit der Nanostäbchen ausgerichtet und angeordnet werden könnten.

Abstract

New ways to cheaply produce and assemble useful micro- and nanostructures are needed to facilitate their deployment in novel technologies. Magnetic fields are a promising possibility to guide the assembly of micro- and nanostructures. This thesis presents a method to synthesize magnetic nanostructures in solution which can be actuated by external rotating magnetic fields. The synthesis method is scalable and can cheaply produce randomly shaped magnetic nanostructures in large quantities. The synthesized structures have random shapes and were observed to propel under the influence of an external magnetic field, perpendicular to the plane in which the external field is rotating. The random shapes move with dimensionless speeds that are comparable to those of previously published, nanofabricated propellers with controlled helical geometries. The observed relationship between actuating frequency and propulsion speed could be understood with a simple torque balance model. This improved understanding opened the door for a theoretical study on swarm control, i.e. the steering of several magnetic propellers along independent trajectories. This is a challenging task since all propellers are subject to the same actuating field. A particular control strategy (critical control) was found, that minimizes the required magnetic field strength needed to achieve a certain control precision. The discovery of critical control is an important step towards the practical realization of swarm control, possibly enabling new approaches to microassembly and other microrobotics tasks. Finally, the collective behavior of large numbers of propellers, moving upwards against gravity and towards a glass surface, was investigated. Both randomly shaped, as well as nanofabricated propellers were observed to form clusters which are circular and rotate slowly in dynamic equilibrium. The nanofabricated propellers displayed hexagonal ordering inside the clusters. Comparing the observed cluster dynamics to simulations revealed that hydrodynamic interactions between the propellers are not necessary for cluster formation, but lead to the formation of a boundary layer at the cluster edge, in which the angular velocity of the propellers is significantly higher than in the rest of the rotating cluster. The observed cluster formation suggests a simple method for the efficient alignment and organization of nanorods.

Table of Contents

1.   Introduction

Techniques to manipulate and organize matter on small scales hold enormous potential for science and technology [1]. Despite significant advances in this area, human ingenuity can still not artificially reproduce what even the most prosaic bacteria create without any apparent effort. Inventing new ways to exert control over matter on small scales thus remains a fascinating and highly promising endeavor.

Clean-room (top-down) techniques provide a high degree of precision, but are generally expensive and have several limitations. For example, they tend to be limited to 2D, often cannot manipulate matter dispersed in solution and are unable to operate at a distance, e.g. act on matter inside a container or living tissue. Conversely, the self-assembly of molecular or nanoscopic components (bottom-up techniques) proceeds in general without much external control. This limits the complexity of structures that can be produced by self-assembly.

Magnetic fields are an attractive way to influence the assembly of micro- and nanoscopic structures. In the end of 2011, when the research reported in this thesis was begun, the organizing effects that magnetic fields can exert on magnetic materials had already been demonstrated in some fascinating studies [2-9] and have since then been used in further intriguing investigations by several groups [10-15].

The topic of this thesis is the actuation of magnetic micro- and nanostructures by external magnetic fields and the use of magnetic actuation for the organization of matter on small scales. One possibility to achieve this are magnetic propellers, actuated by rotating external magnetic fields, which had been initially produced using expensive clean room equipment [5, 6]. The goal of the research reported here was to use self-assembly to produce similar actuators cheaply and in large quantities. At first, several attempts were made to reproduce the helical or chain-like arrangement of previous actuators. However, it was then discovered that randomly shaped magnetic nanostructures can be effectively actuated and sorted (e.g. by size or propulsion speed), simply using rotating external magnetic fields. Based on this discovery, the propulsion of individual propellers was studied both experimentally as well as theoretically. Furthermore, a method to control several propellers simultaneously was discovered and investigated theoretically. Finally, it was observed that the synthesized propellers display interesting collective behavior and simulations were performed to gain an improved understanding of the relevant physics.

1.1 Motivation

The main motivation behind the research reported here was the ambition to help finding solutions to pressing, global problems. Contributions to such solutions are made in both fundamental as well as applied sciences. However, in fundamental sciences, the scientific quality of a question is often judged exclusively by its interestingness, i.e. the extent by which it appeals to the curiosities of the scientific community. Consequently, the desire to help solving practical problems is not always seen as becoming to a scientist. While curiosity is an important motivation for scientific research, it is not the only possible one. Trying to solve important, real-world problems is a good motivation for research as well and can be "a stimulus to curiosity" [16]. In fact, it might improve the scientific enterprise itself, if this motivation would be more commonly adopted and appreciated [16].

Luckily for scientists, there is no shortage of problems [17, 18]. Climate change [19-23], extreme poverty [24], biodiversity collapse [25-33], or the depletion of fresh water resources [34, 35] and fertile soil [36] are among the most urgent. Cheap and abundant renewable energy together with cheap energy storage would be a big step towards solving several of these problems [37-40]. Many recent advances towards this goal were based on the (limited) ability to organize matter on the micro- and nanoscale [41-55], which is the promise of nanotechnology [1]. For example, specifically shaped surfaces can greatly increase the efficiency of solar cells [47], particular iron oxide nanostructures are highly efficient for solar water splitting [51] and a nanowire architecture allowed the use of silicon as a lithium ion battery anode material [55]. New ways to cheaply produce such useful micro- and nanostructures are needed to allow the deployment of the corresponding technologies on a large scale. The work presented here aims to contribute to this overarching goal, by expanding the range of techniques available for the organization of matter on small scales.

1.2 Scope of the Work

This thesis deals in particular with magnetic micro- or nanoscopic structures that can be actuated by external magnetic fields and the physical mechanisms behind such actuation. Carbon coated aggregates of iron oxide nanoparticles, synthesized using hydrothermal carbonization, were used in most of the described experiments. Other randomly shaped magnetic nanostructures were synthesized as well, but their magnetic actuation was not characterized in detail. All known types of magnetic actuation are considered in this thesis,

although propellers are a focus of the presented work. The relationship between propeller geometry and propulsion speed was studied using a tomographic 3D reconstruction technique. Furthermore, this thesis deals with the task of controlling several such propellers in parallel, a challenging task with relations to microrobotics and control theory. The collective behavior of magnetic propellers was investigated, but no attempts were made to relate these findings to the rich literature on emergent, or collective (swarm) behavior.

Several related research topics are not discussed in this thesis, but nevertheless guided the research reported here. These topics include actuation of structures above 100 μm [56], biological swimming [57-62], artificial, microscopic actuators not driven by magnetic fields [63-71] and magnetic steering thereof [69, 70, 72], approaches to the synthesis of magnetic nanostructures not used in the work reported here [73-77], applications of magnetic nanoparticles [78] (catalyst retrieval [79-81], MRI contrast agents [82], storage media [83]), swarm behavior different from that of magnetic nanopropellers [84-86], robotics [87-89] and pattern formation [90-97].

2.   Background

This chapter briefly introduces the theoretical concepts necessary for the understanding of the reported experiments, theoretical analyses and simulations, and concisely reviews previous work.

2.1   Basic Theoretical Concepts

2.1.1   Actuation of Magnetic Iron Oxide Nanostructures

The magnetic iron oxides magnetite (Fe_3O_4) and maghemite (γ-Fe_2O_3) were used for the experiments described in this thesis. The crystal structure of both is the inverse spinel [98]. The unit cell contains 8 tetrahedral sites and 16 octahedral sites that can be occupied by iron atoms. The tetrahedral sites are occupied by Fe(III), for both magnetite and maghemite. The octahedral sites are occupied in a 1:1 ratio with Fe(II) and Fe(III) in magnetite. In maghemite, 5 of 6 octahedral sites are occupied by Fe(III) the rest is vacant (Figure 2-1). The 5d orbitals of Fe(II) and Fe(III) are not completely filled, thus (according to Hund's rules) the unpaired electron spins bestow a magnetic dipole moment on the iron atoms (approximately 5 μ_B for Fe(III) and 4 μ_B for Fe(II)) [98].

Classical electrodynamics predicts that close-by magnetic dipoles would tend to align anti-parallel to each other. In certain materials, however, the quantum mechanical exchange interaction (arising from the Pauli exclusion principle and tending to align close-by spins parallel to each other) is stronger than the magnetic dipole interaction. At sufficiently low temperatures, this leads to ferromagnetism, i.e. the spins of unpaired electrons align and endow the material with a macroscopic magnetic moment, even in the absence of an external magnetic field [99]. In magnetite and maghemite the situation is, however, more complex. Here the exchange interaction leads spins on each sublattice to align parallel to each other, but the spins on the tetrahedral sublattice are anti-parallel to those on the octahedral sublattice. Due to the fact that the effective magnetic moments of the sublattices are not equal, this leads nonetheless to a macroscopic magnetic moment, even in the absence of an external magnetic field. This type of magnetic behavior is called ferrimagnetic [99]. In the case of magnetite this results in 32 μ_B per unit cell, leading to a saturation magnetization of 480 kAm^{-1} [100]. The saturation magnetization for maghemite is 380 kAm^{-1} [100].

4
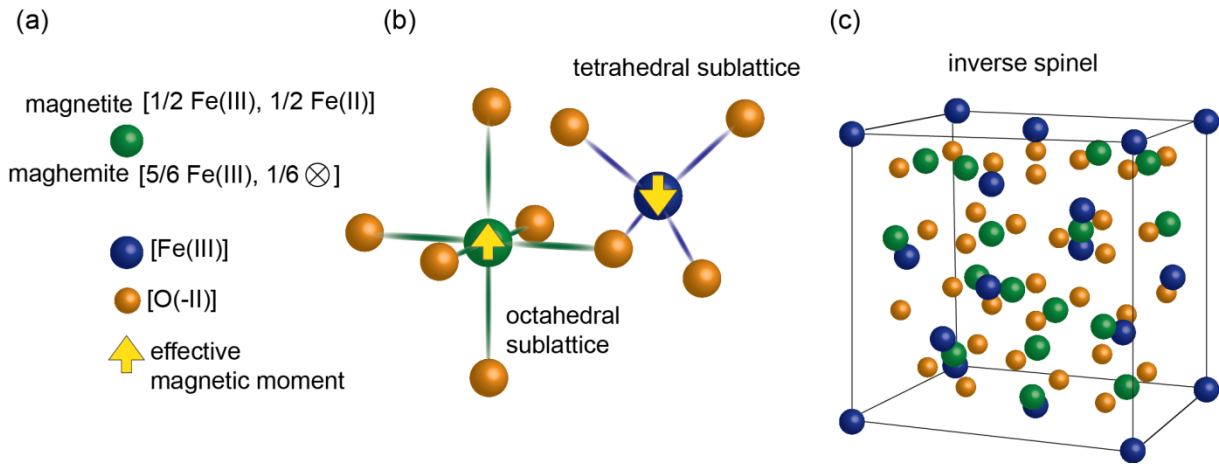
Figure 2-1: Schematic representation of the inverse spinel structure leading to ferrimagnetism. (a) Explanation of symbols used. Green spheres denote octahedral sites. In the case of magnetite these are occupied by either Fe(II) or Fe(III) atoms in a 1:1 ratio. For maghemite the octahedral sites are occupied by either Fe(III) or vacancies ($\otimes$) in a 5:1 ratio. Blue spheres denote tetrahedral sites which are invariably occupied by Fe(III) in both magnetite and maghemite. Orange spheres denote oxygen atoms. Yellow arrows denote the effective magnetic moment (averaged over the sublattice). (b) In the inverse spinel structure of magnetite and maghemite, the sublattices have effective magnetic moments that are opposed to each other, but of unequal magnitude (ferrimagnetism). (c) Schematic representation of the unit cell of maghemite and magnetite (inverse spinel). Adapted from [101] by permission of The Royal Society of Chemistry. (http://www.rsc.org/shop/books/2013/9781849735537.asp).

An external magnetic field can exert a torque on a magnetic nanostructure made from magnetite or maghemite, due to the fact that the orientation of its magnetic dipole moment is physically linked to the orientation of the nanostructure (which would not be the case for a paramagnetic bead). This linkage is due to two effects. Firstly, it is energetically favorable for the magnetic moment of magnetite or maghemite to be aligned with the [111] crystal direction, due to magnetocrystalline anisotropy [98, 102]. Secondly, shape anisotropy makes it energetically favorable for the magnetic moment to point in a certain direction, which could for example be a direction of elongation. This is due to the fact that the energy contained in the total magnetic field produced by a structure that is not point-symmetric (demagnetizing field), depends on the direction of magnetization [99].

Thermal noise affects the magnetic properties of ferrimagnetic materials by reducing the spin alignment. For ferromagnetic materials the Curie-Weiss law is valid. At high temperatures ($T > T_C$) the magnetization at a finite applied field B begins to decrease to zero as $\frac{M}{B} \propto \frac{1}{(T-T_C)^\beta}$, where M is the magnetization, T the temperature, β an exponent and T_C is called the Curie temperature (which is about 645 °C for maghemite [100]). For ferrimagnetic materials

this dependence is somewhat more complicated: $\frac{M}{B} \propto \frac{T-c}{T^2-T_C^2}$, where c is a constant [103].

Nanostructures are affected by thermal noise in a more complicated way, as the amount of thermal noise that destabilizes alignment depends on the number of interacting spins. This dependence is shown schematically in Figure 2-2. A ferrimagnetic structure can be in one of four magnetic states. In the superparamagnetic state (SP), the spins are aligned, but the direction of magnetization constantly flips due to thermal noise [104]. The average time between two magnetization reversals is called the Néel relaxation time τ_N. It grows sharply when the structure size passes a certain value [105, 106]. Setting a threshold value for τ_N defines the transition to the stable single domain state (SSD) [107, 108]. In the SSD state all spins are aligned and the volume magnetization of the nanostructure is approximately equal to the saturation magnetization even in the absence of a magnetic field. The alignment of all spins becomes energetically unfavorable with increasing structure size, since the energy contained in the magnetic field produced by the structure can be reduced by the formation of domains with opposing magnetizations. This multi-domain state (MD) is characteristic for all macroscopic ferrimagnetic materials in the absence of external magnetic fields of saturating strength. The volume magnetization therefore decreases again after peaking in the SSD state. The SP state similarly transitions into the conventional paramagnetic (P) state for sufficiently large structures above the Curie temperature.
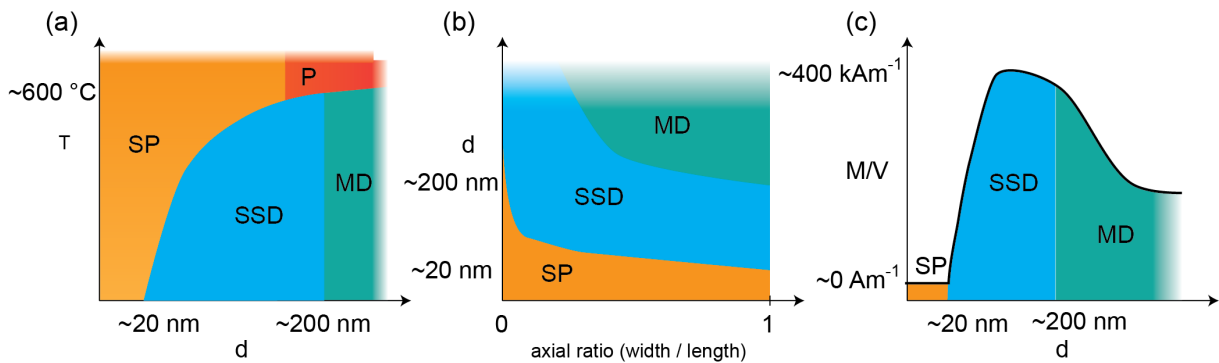
Figure 2-2: (a) Magnetic state diagram for a magnetic nanostructure of size d and temperature T. SP denotes the superparamagnetic state, SSD the stable single domain state, P the paramagnetic state and MD the multi-domain state. (b) The magnetic state of a nanostructure depends also on its geometry. The state diagram plots here the axial ratio against the structure size. (c) The volume magnetization of a ferrimagnetic nanostructure, which can be retained in the absence of an external field, grows at first quickly with size as the SSD state is reached. This volume magnetization decreases again and reaches a constant (bulk) value when the MD state is reached.

The nanostructures used in this thesis can be described as being in a multi-domain state, due to the fact that they consist of several particles which, in addition, might be in the SP, the SSD or the MD state themselves. Nonetheless, it is usually sufficient to describe the magnetization state of a nanostructure with a dipolar net magnetization. For a uniformly magnetized sphere, this description is indeed exact. For more complex shapes the description is an approximation. If the applicability of this approximation is doubtful it is possible to use a multipole expansion, a numerical model of rigidly linked magnetic dipoles, or micromagnetic calculations [99, 109].

2.1.2 Hydrodynamics of Actuated Nanostructures

The Navier-Stokes equations, which describe the motion of fluids, can be made dimensionless by introducing the Reynolds number:

$$Re = \frac{\rho L V}{\eta} \tag{1}$$

Here ρ and η are the density and viscosity of the fluid, and L and V are a typical length scale and a typical velocity of a structure moving in the fluid. The Reynolds number can be thought of as the ratio between inertial and viscous forces [110]. For $Re \ll 1$, the inertial term in the Navier-Stokes equations can thus be dropped, leading to the Stokes equations [111]:

$$\eta \nabla^2 \boldsymbol{u} - \nabla p = 0 \tag{2}$$

$$\nabla \boldsymbol{u} = 0 \tag{3}$$

where $\boldsymbol{u}$ is the fluid velocity and p the pressure. This continuum description seems to remain valid down to a few nanometers [112]. Two important theorems by Helmholtz are worth mentioning. Firstly, the solution to the Stokes equations is unique. Secondly, the energy dissipated by the flow field which is a solution to the Stokes equations, is lower than for any other solenoidal field ($\boldsymbol{u}^*$ with $\nabla \boldsymbol{u}^* = 0$) which satisfies the same boundary conditions [113].

The Reynolds number of an actuated nanostructure can be estimated as follows. Assuming $L < 2 \times 10^{-5}$ m, a rotation frequency $\omega < 200$ Hz and a liquid medium of water at room temperature (20 °C), the Reynolds number can be calculated:

$$Re < \frac{2 \times 10^{-5} \text{ m}}{10^{-3} \text{ N m}^{-2} \text{ s}} \times 10^3 \text{ kg m}^{-3} \times 200 \text{ s}^{-1} \times 10^{-5} \text{m} = 4 \times 10^{-2} \ll 1 \tag{4}$$

The Stokes equations (equations 2 and 3) are thus indeed suited for the hydrodynamic description of actuated magnetic nanostructures. Analytical solutions of these equations can

only be obtained for simple situations, like the flow past a translating sphere of radius R [113]. From this solution the translational friction coefficient can be determined to be $6\pi\eta R$ (Stokes law).

The flow around a rotating sphere can be solved as well [113]. In spherical coordinates the solution is given by:

$$v(r) = \frac{R^3\omega}{r^2}\sin(\theta)\,\hat{e}_\phi \tag{5}$$

For a sphere of radius R rotating with frequency ω and $r = |r|$ (r being the coordinate vector). θ and ϕ denote the polar and azimuthal angle respectively. This solution satisfies $\nabla^2 v = 0$, which means that the pressure p is constant in the entire volume (which is not the case for a translating sphere). Since the flow field has no radial component, mixing does not occur, i.e. the distances of test-particles in the solution to the rotating sphere stay constant. From this flow-field the rotational friction coefficient of a sphere can be determined to be $8\pi\eta R^3$.

Another useful analytical result is the frequency Ω with which two identical spheres (radius R) will rotate around each other, when fixed in a 2D plane and rotating (in identical directions) in this plane with frequency ω [114].

$$\Omega = 2\omega\left(\frac{R}{r}\right)^3 \tag{6}$$

Here $r > 2R$ is the separation of the two propellers, which remains equal to its initial value. Two rotating spheres thus do neither attract nor repel each other, when rotating in the described way.

It is interesting to note that the produced flow fields are independent of the viscosity of the liquid. A screw moving through a solid material obviously does not produce such a flow field. The motion of a screw in a solid is thus different from the movement of a propeller in a liquid of very high viscosity. This is due to the fact that the boundary conditions in low Reynolds number hydrodynamics are generally assumed to be no-slip, i.e. the fluid velocity in the immediate vicinity of a solid interface is equal to the velocity of the solid interface. This is clearly not true for the movement of a screw in a solid.

Thermal noise cannot be neglected for structures smaller than about 10 µm. This can be seen by considering that a sphere of 5 µm radius in water at room temperature will diffuse about 0.5 µm during one second and knowing that the square root of the mean square displacement

due to diffusion grows with the square root in time. Diffusion affects the position as well as the orientation of the structure. Diffusion coefficients for rotation and translation can be obtained by dividing the thermal energy ($k_B T$) by the respective friction coefficients, according to the Einstein relation. Increasing the magnetic field strength cannot prevent rotational diffusion, since the magnetic field can only fix one of the two rotational degrees of freedom. To counter rotational diffusion the actuating field frequency needs to grow with the inverse cube of the nanopropeller scale, an effect which can prohibit effective magnetic actuation [115].

2.2   Survey of Actuation Strategies

This section was partially adapted from [116] as well as another submitted manuscript. Several mechanisms for magnetic actuation have been proposed [117-120]. Gradient fields can exert forces on magnetic materials and have been used successfully to move microscopic objects [121-126]. Magnetic field gradients, however, decay like $1/r^4$, where r is the distance from a dipolar source of magnetic fields. Therefore, when the source of the magnetic field is far away from the devices to be actuated, it becomes favorable to use the torques exerted by homogenous magnetic fields, since these only decay like $1/r^3$ [118].

Exerting torques does, however, not immediately lead to translatory movement. It is thus necessary to find a way to convert torques into effective forces. The published methods to achieve such conversion can be grouped into three categories: propellers, rollers and swimmers. Magnetic propellers are magnetic structures, which are actuated by rotating magnetic fields. The hydrodynamic coupling between rotation and translation leads to the propeller moving through the liquid, parallel to the vector of rotation of the magnetic field [5, 6, 11, 116, 127, 128]. Rollers are objects that move along a surface when actuated by rotating or precessing magnetic fields [8, 129-132]. Swimmers are objects that change shape during one period of the actuating field, in a way that leads to a net displacement of the structure [9, 133-138]. These three categories are not mutually exclusive, since structures can share attributes of more than one category. For example, most propellers are also rollers if they are close to a surface.

How the application of torques can lead to translatory movement can be understood in the framework of low Reynolds number hydrodynamics (see section 2.1.2). According to the scallop theorem, it is not possible to achieve translatory motion by reciprocal movement in a

Newtonian fluid at low Reynolds number [139]. One way around this limitation is to actuate a structure in a non-reciprocal way, for example by applying a rotating magnetic field (Figure 2-3 b). If the actuated structure is flexible, actuation can also be achieved with a field that would only induce reciprocal motion in a rigid structure (Figure 2-3 a). Interestingly translatory movement is also possible if a rigid structure is actuated in a reciprocal manner close to an elastic interface [140]. In viscoelastic media (e.g. many biological fluids) also reciprocal deformation cycles can lead to swimming.

Symmetry breaking is also required. For rollers, this is typically achieved by being close to an interface. Propellers have to exhibit sufficiently asymmetric shapes in order to achieve translatory movement. Symmetry breaking for swimmers has generally been achieved using a head-tail design, where either a magnetic head is used to actuate a flexible tail, or the tail itself is magnetic [9, 133-138]. These requirements for torque based translatory motion are summarized in Figure 2-3.
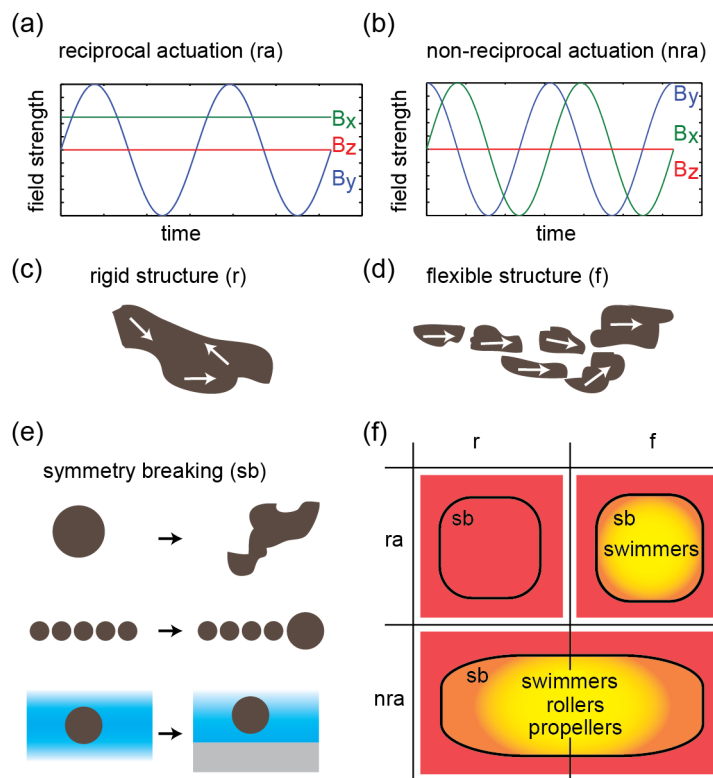
Figure 2-3: Summary of requirements for torque based translatory motion. (a) This is an example of a magnetic field that will typically induce reciprocal motion in a rigid magnetic structure. The field strengths of the three components of the magnetic field vector are plotted against time. (b) The same plot as (a) for a rotating magnetic field, which induces non-reciprocal motion also in a rigid structure. (c) Schematic of a rigid magnetic structure. White arrows indicate the magnetization state. (d) Schematic of a flexible magnetic structure. The structure can incorporate physical linkers (e.g. DNA) or might be held together by magnetic interactions alone. (e) Symmetry breaking is necessary for translatory motion. This can be achieved by asymmetries in the structure itself, mixtures of different symmetric particles, or the presence of an interface. (f) The requirements can be summarized in this table. Red areas mark regions where translatory motion is impossible. Yellow areas mark regions where translatory motion is possible. A gradient in the yellow areas was used to indicate that the conditions presented here are necessary, but not sufficient. This figure is part of a submitted manuscript.

2.2.1 Rolling Along a Surface

The first detailed study on the rolling mechanism was published in 2008 by Tierno et al. [8]. They used DNA to construct pairs of one bigger and one smaller paramagnetic bead. The resulting magnetic shape anisotropy of the construct enabled the application of torques, which is not possible for single paramagnetic beads. Symmetry breaking was immediately achieved, since the doublets were floating slightly above a solid glass surface (x,y plane), due to electrostatic repulsion.

By applying precessing magnetic fields ($\boldsymbol{B}(t) = (B_1 \sin(\omega t), B_2, B_1 \cos(\omega t))$), these particles could be moved in the x direction (perpendicular to the vector of rotation of the actuating field) and steered around microfluidic channels [141]. It was shown later, that pairs of equally sized paramagnetic beads behave similarly [130]. However, this time it was also observed that depending on the opening angle ($\tan^{-1}(B_1/B_2)$) of the precessing field, the doublets did not necessarily move along the x direction. The y-component parallel to the vector of rotation could be interpreted as propulsion, which means that this two bead system could potentially act as an extremely simple propeller. It was not tested whether this propulsion effect would also work in bulk liquid. This type of surface roller has also been subjected to rotating magnetic fields on top of a surface with patterned magnetization [142].

Rolling has also been realized with chain-like assemblies of superparamagnetic beads [129] or Nickel coated gold nanorods [131]. Nickel nanowires could also be used for rolling actuation. These were able to roll upwards a nearly vertical surface and transport polystyrene beads [132, 143, 144]. NdFeB microparticles could serve as rollers as well [145].

2.2.2 Propulsion of Chiral Objects

Many different approaches have been used to fabricate helical magnetic micro- and nanopropellers. Here, the term micropropeller is used for objects below 100 μm in size and the term nanopropeller for objects smaller than 5 μm. One of the first micropropellers was created by Zhang et al. using self-scrolling thin films [146, 147]. These bio-inspired "artificial bacterial flagella" are between 30 and 50 μm in size and have been studied in great detail [6, 148-152]. Smaller propellers (about 0.25 × 1.5 μm) were fabricated by Ghosh and Fischer using glancing angle vapor deposition (GLAD) [5] and recently by Schamel et al. (about 0.1 × 0.4 μm) [153]. These have been used to demonstrate the separation of chiral species by magnetic fields [154] and, after applying a cytocompatible coating, were able to move through human blood [155]. Due to their small size, special attention has been paid to the effect of thermal noise on these propellers [115, 156, 157]. Using direct laser writing (DLW), helical micropropellers with precisely controlled geometric parameters were fabricated and, after coating them with a magnetic material, have been used in numerous studies [11, 158-165]. It has also been shown, that the magnetic material can be internalized, by applying DLW to photoresist mixed with superparamagnetic nanoparticles, which were aligned by an external magnetic field during the writing process [166].

The propellers discussed so far required expensive equipment for their production. Different attempts have been made to reduce the production costs of propellers, by using self-assembly or templates. Curved nickel nanowires have been assembled into helix-like structures and could be used as propellers when actuated by a rotating magnetic field [152]. The metallization of helical liposome scaffolds could also be used to create structures that were able to propel when actuated by rotating magnetic fields [167]. Plant based magnetic helical propellers have been created, by coating the spiral xylem vessels of vascular plants with titanium and nickel layers [127]. Nickel coated helical palladium nanosprings were created by a template electrosynthesis method and could be used as propellers [128].

The propulsion of the presented chiral structures is due to a hydrodynamic coupling between rotation and translation. It follows from the Stokes equations (equations 2 and 3) that the speed v and the rotation frequency ω_p of the propeller must be linearly related to the applied external force F and torque τ [168]:

$$\begin{pmatrix} F \\ \tau \end{pmatrix} = \mathbf{P} \begin{pmatrix} v \\ \omega_p \end{pmatrix} = \eta \begin{pmatrix} LA & L^2C \\ L^2C & L^3D \end{pmatrix} \begin{pmatrix} v \\ \omega_p \end{pmatrix} \qquad (7)$$

Here η is the fluid viscosity, L is a size parameter for the propeller and A, C, and D, are parameters that depend only on the shape of the propeller. The symmetric and positive definite matrix **P** is called the resistance matrix [111]. In general it is a 6×6 matrix, but here it is only 2×2. This is because here F, τ, v and ω_p are scalar quantities, since the propeller must move on average parallel to the rotation axis for symmetry reasons. Equation 7 is thus a simplification that ignores movement on timescales $t < 1/\omega_p$. A and D are related to translational and rotational friction respectively. C describes the coupling between rotation and translation. **P** being positive definite implies:

$$LAa^2 + L^3Db^2 > -2L^2Cab \tag{8}$$

for arbitrary real numbers a and b. It follows that $A > 0$ and $D > 0$. Assuming $Cab < 0$ equation 8 can be rewritten as:

$$\frac{Aa^2}{L^2 4b^2} + \frac{D}{2} + \frac{L^2 D^2 b^2}{4Aa^2} > \frac{C^2}{A} \tag{9}$$

Since particular a and b that simultaneously satisfy $\frac{Aa^2}{L^2 4b^2} + \frac{L^2 D^2 b^2}{4Aa^2} = \frac{D}{2}$ and $Cab < 0$ can always be found $\left(\frac{a^2}{b^2} = \frac{DL^2}{A}\right)$, equation 9 implies:

$$D > \frac{C^2}{A} \tag{10}$$

In the case of magnetic propellers, the external force is zero ($F = 0$). Therefore, the speed of the propeller is related to the frequency of rotation as:

$$v = -\frac{LC}{A}\omega_p \tag{11}$$

In order to compare the propulsion properties of propellers of different shapes it is therefore useful to introduce a dimensionless speed [138], that depends only on the shape of the propeller:

$$U = \frac{v}{\omega_p L} \times 10^3 = -\frac{C}{A} \times 10^3 \tag{12}$$

The maximum reported dimensionless speeds of different propeller designs, measured parallel to the vector of rotation of the actuating field, are compared in Figure 2-4. The accumulated research on magnetically actuated micro- and nanopropellers has been reviewed several times [118-120, 169-171].
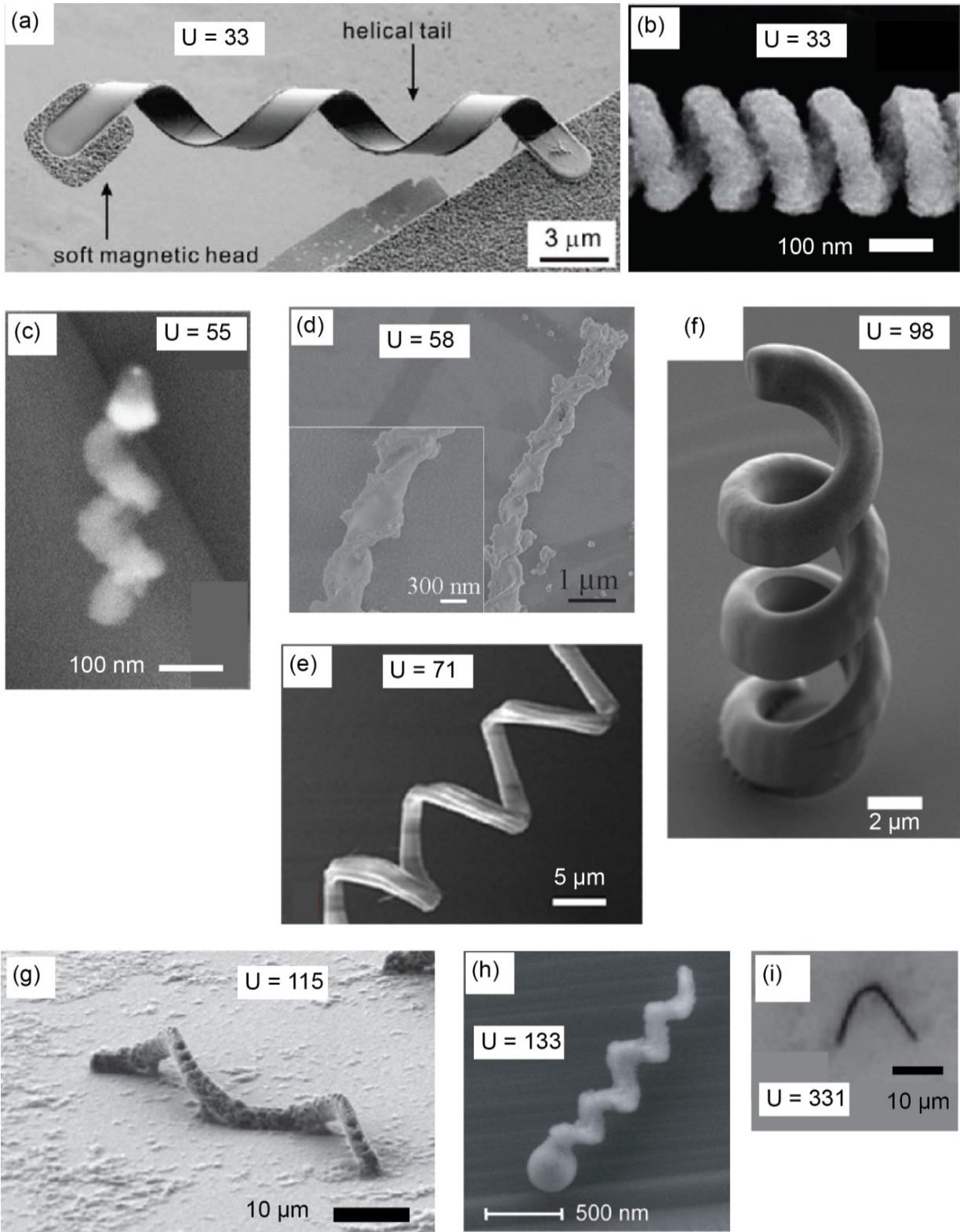
Figure 2-4: Comparison of dimensionless speed values for different propeller designs. The speed measurements reported here were all done in water close to a solid interface, except for (c) which was measured in 3 mg/ml viscoelastic hyaluronan solution and (i) which was measured in a high density 0.5 µm-diameter microbead solution. (a) Micropropeller made from self-scrolling thin films [6]. Scale bar: 3 µm. $U \approx 10^3 \frac{8 \, \mu ms^{-1}}{38 \, \mu m \, 10 \, Hz} = 33$. Adapted with permission from [6]. Copyright 2009 ACS. (b) Nanopropeller from template electrosynthesis [128]. Scale bar: 100 nm. $U \approx 10^3 \frac{15 \mu ms^{-1}}{3 \mu m \, 150 \, Hz} = 33$. Adapted from [128] with permission from The Royal Society of Chemistry. (c) Extremely small nanopropeller made using glancing angle vapor deposition (GLAD) [153]. Scale bar: 100 nm. $U \approx 10^3 \frac{1.1 \, \mu ms^{-1}}{0.4 \, \mu m \, 50 \, Hz} = 55$. Adapted with permission from [153]. Copyright 2014 ACS. (d) Micropropeller produced using helical lipid microstructures [167]. Scale bars are 300 nm (inset) and 1 µm. $U \approx 10^3 \frac{0.41 \, \mu ms^{-1}}{11.8 \, \mu m \, 0.6 \, Hz} = 58$. Adapted with permission from [167]. Copyright 2012 Wiley-VCH. (e) Micropropeller based on spiral xylem vessels [127]. Scale bar: 5 µm. $U \approx 10^3 \frac{250 \, \mu ms^{-1}}{50 \, \mu m \, 70 \, Hz} = 71$. Adapted with permission from [127]. Copyright 2013 ACS. (f) Micropropeller fabricated using direct laser writing (DLW) [11]. Scale bar: 2 µm. $U \approx 10^3 \frac{86 \, \mu ms^{-1}}{35 \, \mu m \, 25 \, Hz} = 98$. Adapted with permission from [11]. Copyright 2012 Wiley-VCH. (g) Micropropeller fabricated by direct laser (DLW) writing of photoresist containing superparamagnetic nanoparticles aligned by an external magnetic field [166]. Scale bar: 10 µm. $U \approx 10^3 \frac{28.2 \, \mu ms^{-1}}{60 \, \mu m \, 4.1 \, Hz} = 115$. Adapted with permission from [166]. Copyright 2014 Wiley-VCH. (h) Nanopropeller made using GLAD [5]. Scale bar: 500 nm. $U \approx 10^3 \frac{40 \mu ms^{-1}}{2 \mu m \, 150 \, Hz} = 133$. Adapted with permission from [5]. Copyright 2009 ACS. (i) Micropropeller based on magnetically assembled curved nickel nanowires [152]. Scale bar: 10 µm. $U \approx 10^3 \frac{10.6 \, \mu ms^{-1}}{16 \, \mu m \, 2 \, Hz} = 331$. Adapted with permission from [152]. Copyright 2010 IEEE.

In general, the parameters C and A in equation 11 can depend on the frequency of the external actuating field (ω). This can happen if the axis of rotation changes with the actuation frequency, or if the structure is not completely rigid [156]. Assuming that C and A are independent of ω and the magnetization is constant and remains unchanged by the external field, a simple relationship between ω and the propeller speed v can be derived. Since the axis of rotation does not change, the orientation of the propeller can be described by a single angle φ. The projection of the magnetization vector onto the plane perpendicular to the axis of rotation defines φ.

By replacing ω_p by $\dot{\varphi}$ and $-\frac{LC}{A}$ by c_v , equation 11 can be rewritten as:

$$v = c_v \dot{\varphi}, \tag{13}$$

Two torques act on the propeller, fluid friction τ_F and magnetic torque τ_M:

$$\tau_F = c_F \dot{\varphi} \tag{14}$$

15

$$\tau_M = BM\sin(\omega t - \varphi) \tag{15}$$

where $c_F = \eta L^3(D - C^2/A)$ is the rotational friction constant, M the magnetization of the propeller and B the field strength of the rotating actuating field. ω is the frequency of the rotating magnetic actuating field and t is time. According to equation 10, c_F is always positive. Interestingly the rotational friction constant c_F is reduced when the coupling between rotation and translation is strong (large C). This suggests that arbitrarily shaped structures will have a tendency to rotate around an axis with strong rotation translation coupling.

In the strongly over-damped case of low Reynolds numbers, the torques τ_F and τ_M must be equal at all times. This torque balance results in the following differential equation.

$$\dot{\varphi} = \frac{BM}{c_F}\sin(\omega t - \varphi) \tag{16}$$

This differential equation has been solved several times [154, 172, 173] and the solution was brought into a simple form [116, 174-179]. The discussion presented here is based on [116].

The analytical solution of equation 16 is:

$$\varphi(t) = \omega t + \varphi_0(t) \tag{17}$$

with

$$\varphi_0(t) = 2\arctan\left[\frac{-\omega_C + \sqrt{\omega^2 - \omega_C^2}\tan\left[-\frac{1}{2}\sqrt{\omega^2 - \omega_C^2}\,(t + \Phi)\right]}{\omega}\right] \tag{18}$$

where Φ is a parameter that depends on the initial conditions and $\omega_C = \frac{BM}{c_F}$ is the critical frequency of the propeller.

In the case of $\omega < \omega_C$ this can be rewritten as follows.

$$\varphi_0(t) = 2\arctan\left[\frac{-\omega_C + i\sqrt{\omega_C^2 - \omega^2}\tan\left[-\frac{1}{2}i\sqrt{\omega_C^2 - \omega^2}\,(t + \Phi)\right]}{\omega}\right] \tag{19}$$

$$= 2\arctan\left[\frac{-\omega_C - \sqrt{\omega_C^2 - \omega^2}\tanh\left[-\frac{1}{2}\sqrt{\omega_C^2 - \omega^2}\,(t + \Phi)\right]}{\omega}\right] \tag{20}$$

The steady state solution, in the limit $t \to \infty$ is:

$$\varphi_0(t) = 2\arctan\left[\frac{-\omega_C - \sqrt{\omega_C{}^2 - \omega^2}}{\omega}\right] = -\pi + 2\arctan\left[\frac{\frac{\omega}{\omega_c}}{1 + \sqrt{1 - \left(\frac{\omega}{\omega_c}\right)^2}}\right] \tag{21}$$

i.e. at large times, $\varphi_0(t)$ becomes constant. Thus the magnetic moment follows the magnetic field with the same frequency, but with a constant phase shift φ_0. This phase shift can be calculated using $\arcsin[x] = 2\arctan\left[\frac{x}{1+\sqrt{1-x^2}}\right]$:

$$\varphi_0 = -\pi + \arcsin\left[\frac{\omega}{\omega_c}\right] = -\arcsin\left[\frac{\omega}{\omega_c}\right] \tag{22}$$

since $\sin(y) = x \Leftrightarrow y = (-1)^k \arcsin[x] + k\pi$, with $k \in \mathbb{Z}$. By defining $\sin(\tilde{\varphi}_0) = \frac{\omega}{\omega_c}$, the final steady state solution becomes:

$$\varphi(t) = \omega t - \tilde{\varphi}_0 \tag{23}$$

This solution is obtained from the general solution for $\Phi \to \infty$.

In the case $\omega > \omega_C$ the magnetic moment still follows the magnetic field, but the magnetic moment is repeatedly overtaken by the magnetic field, thereby rotating effectively at a lower frequency ω_{eff}. In order to obtain an analytical expression for ω_{eff} one can observe that $\varphi_0(t)$ is a periodic function in t that decreases by 2π in a period T_0 defined by the argument of the tangent:

$$\tan\left[-\frac{1}{2}\sqrt{\omega^2 - \omega_C{}^2}\ (t + \Phi)\right] \tag{24}$$

This reveals the periodicity as $\pi = T_0 \frac{1}{2}\sqrt{\omega^2 - \omega_C{}^2}$. Thus the effective frequency is:

$$\omega_{\text{eff}}(\omega) = \omega - \frac{2\pi}{T_0} = \omega - \sqrt{\omega^2 - \omega_C{}^2} \tag{25}$$

The final relationship between the actuating frequency of the external field and the propeller speed is thus:

$$v(\omega) = \begin{cases} c_v \omega & \text{for } \omega < \omega_C \\ c_v\left(\omega - \sqrt{\omega^2 - \omega_C{}^2}\right) & \text{for } \omega > \omega_C \end{cases} \tag{26}$$

The assumption that the axis of rotation is independent of the actuating frequency is not always valid. For a rod-like structure magnetized neither parallel, nor perpendicular to its short axis, it can be intuitively understood that this structure will rotate around its short axis at

high frequencies (minimizing rotational friction), but not at low frequencies. This situation has been analyzed for ellipsoids [156] and helical shapes [180].

Which geometric shape is optimal for propulsion is an interesting question. A recent study on helical propellers by Morozov et al. suggested that from a geometric point of view, a regular helix (with circular cross-section along the helix) is optimal [180]. Yet, when taking considerations about the magnetization of the propeller into account, a normal helix (with the cross section elongated perpendicular to the long axis of the helix) seemed preferable [180]. Morozov et al. find no significant difference between a normal and a binormal helix (with the cross section elongated parallel to the long axis of the helix) (see Figure 2-5). In contrast to this, Keaveny et al. find that the normal helix is about 1.7 times faster than the binormal helix [181]. Using an optimization algorithm which considered only slender shapes with a single centerline (no branched shapes), Keaveny et al. found an optimal slender propeller shape consisting of only about one helical turn [181].
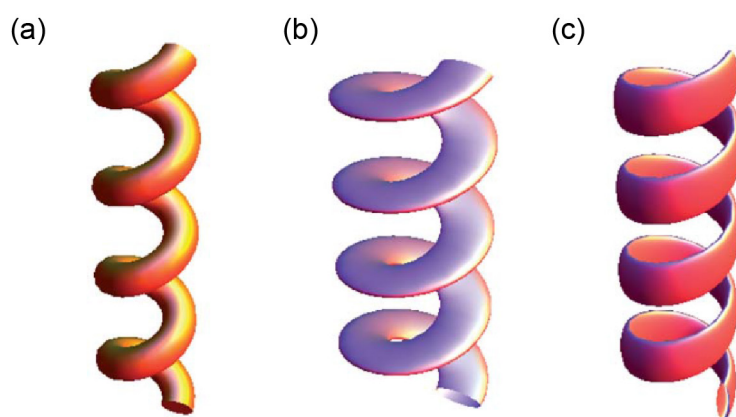
Figure 2-5: Illustration of regular (a), normal (b) and binormal (c) helical propellers. Adapted from [180] with permission from The Royal Society of Chemistry.

2.2.3 Swimming by Cyclic Shape Deformation

Although a wide range of cyclic shape deformations can lead to swimming [139, 182-184], experimental realizations of magnetically actuated swimming were predominantly based on bending waves. In 2005, Dreyfus et al. reported a swimmer, composed of a chain of superparamagnetic beads linked by DNA and attached on one end to a red blood cell [9] (24 μm in size). When actuated by a magnetic field ($B(t) = (B_1, B_2\sin(\omega t),0)$), this structure moved in the x direction, with the red blood cell being towed by the chain-like structure. Gao et al. realized a swimmer, by linking a magnetic nickel nanorod to a gold nanorod via a thin silver filament [137] (6.5 μm in size), actuated by a precessing magnetic field ($B(t) =$

$(B_1, B_2\cos(\omega t), B_2\sin(\omega t)))$. This swimmer could be modified to enable catalytic propulsion (in a solution containing hydrogen peroxide) in addition to magnetic actuation [136]. Furthermore, attaching glucose oxidase to this swimmer allowed the magnetically controllable biocatalytic patterning of helical metal microstructures [185]. A similar design, 5.8 μm in size, used only a nickel nanorod with a silver tail, achieving significantly faster movement [138]. A precessing magnetic field could also be used to induce swimming motion in self-assembled ribbons consisting of paramagnetic colloids [186]. In a different approach superparamagnetic cobalt nanoparticles self-assembled into chain-like structures and were magnetically attached to magnetic colloids. The resulting head-tail structures could be actuated by magnetic fields $(\boldsymbol{B}(t) = (B_1, B_2\sin(\omega t), 0))$, however, potential influences of gradient fields could not be excluded [133].

2.3 Magnetic Actuation for Microrobotics

This section was partially adapted from a submitted manuscript.

2.3.1 Steering Single Microrobots

Micro- and nanorobots have been the subject of numerous studies due to their high potential for applications, ranging from microassembly and sensing to minimally invasive medicine and environmental remediation [12, 64, 171, 187-189]. As described in section 2.2, magnetic fields can be used to "fuel" such devices and are particularly promising for the actuation of microscopic devices in a liquid environment. The potential of untethered magnetically steered devices has been demonstrated in several microassembly tasks. Building on earlier work [190, 191], Tasoglu et al. used a combination of magnetic gradients and alternating homogenous fields to actuate a cuboid made of NdFeB particles in polyurethane [12]. This microrobot could be used to move various millimeter sized hydrogel building blocks around in 2D and, using ramps, even to stack the building blocks in 3D. A different microrobot design relying on resonant magnetic actuation in the kHz frequency range, could be used to move silicon disks (100 μm diameter) in a controlled way [192]. Magnetically actuated propellers could also be equipped with a cage-like device that enabled the controlled placement of 6 μm microparticles [11]. Microrobotic grippers, developed by Diller et al. reversibly grip a suitable object (millimeter scale), move around with it and assemble such objects into complex 3D arrangements [193]. Rotating magnetic particles could be used to trap and transport

microorganisms [145]. The biocatalytic patterning described in section 2.2.3 can be seen as a micro-assembly task as well [185].

2.3.2   Swarm Control

By applying rotating magnetic fields with suitable frequencies and axes of rotation, the position of one magnetic propeller can thus be controlled in a straightforward manner. Similarly, identical propellers placed in a homogenous environment will all respond in identical ways to the applied magnetic fields. This might be interesting for applications like the assembly of microstructures, where a single set of instructions from the magnetic field could be executed by a large number of propellers in parallel.

Swarm control, i.e. the ability to steer individual members of a group of propellers independently along predefined trajectories, is more difficult, but also possible. Different actuating strategies have been used to realize swarm control, all based on the idea that differences in magnetic or geometric properties can be exploited to actuate microscopic objects individually. In 2D, this has been done using electrostatically actuated microrobots [194] or resonant crawling robots with distinct resonant frequencies [192]. These approaches required specialized 2D surfaces. Magnetic objects performing a stick-slip motion could be independently positioned on non-specialized surfaces [195]. In 3D, the positions of different magnetic objects could be independently controlled using magnetic gradient fields [196]. However, all of these previous approaches to swarm control used magnetic objects hundreds of micrometers in size. At smaller scales, it becomes increasingly difficult to produce sufficiently strong magnetic gradient fields. Magnetic propellers can therefore be much smaller than larger objects moved with similar speeds by gradient fields. Magnetic propellers close to [5] or below (see section 4.3 and [153]) one micrometer in size have been produced and effectively actuated. So far magnetic propellers have not been used for swarm control, potentially due to the fact that a simple relationship between actuating frequency and propeller speed has only recently been described [116, 154].

When magnetic propellers differ in their properties (i.e. shape or magnetization), swarm control becomes possible due to the nonlinear relationship between the frequency of the actuating magnetic field and the propulsion speed of the propellers [120, 164]. Although this shows that swarm control for propellers should be feasible in principle, it is difficult to determine how propellers should be actuated to achieve swarm control in practice.

2.4 Collective Behavior of Magnetic Micro- and Nanostructures

2.4.1 Self-assembly Induced by Static Magnetic Fields

The self-assembly of paramagnetic or superparamagnetic particles has been investigated in many studies [197-225]. Applying a constant magnetic field to a suspension of micrometer sized paramagnetic particles typically results in the formation of chain-like structures that look like a string of beads [202, 218, 220, 226]. Smaller superparamagnetic nanoparticles under the influence of a constant magnetic field tend to form multiple chain superstructures as well [201, 209, 210, 212, 217, 222, 224] (zipped-chain superstructures [223, 227]). Such chain-like assemblies have been used for micromixing [200], as force sensors [208, 218], tunable photonic materials [211, 214, 216, 221, 228, 229], magnetically controllable polarizers [215], and for magnetic actuation as discussed in section 2.2. Chain formation is also the mechanism behind magnetorheological fluids [219]. Application of a magnetic field can destabilize a colloidal crystal, when the field is applied perpendicular to the 2D colloidal arrangement [225]. Altering the shape of magnetic nanostructures has been shown to have an effect on their assembly as well [230].

In the absence of external magnetic fields, superparamagnetic particles tend to form more globular arrangements [231]. Self-assembly is nonetheless possible in the absence of external magnetic fields. Ordered superlattices of magnetic nanocrystals could also be achieved using doctor blade casting without external magnetic fields [219]. Maghemite nanoparticles were observed to form structures reminiscent of coffee rings in evaporating solution [232]. Cobalt nanoparticles were observed to form complex structures in evaporating solutions, also in the absence of external magnetic fields [206, 207]. Ahniyaz et al. used the transient application of a magnetic field to assemble superparamagnetic nanocubes into highly ordered superlattices [204].

Ferrofluids (i.e. solutions containing superparamagnetic nanoparticles) self-organize into fascinating macroscopic shapes when subjected to external magnetic fields (Rosensweig instabilities). On the micro-scale, interesting colloidal self-assembly phenomena can be observed, when non-magnetic colloids are submerged in a ferrofluid. Yellen and coworkers showed that the application of an external magnetic field can result in the controlled self-assembly of complex, well-defined multi-particle assemblies [2, 3, 233]. If magnetic as well as non-magnetic colloidal particles were suspended in ferrofluid, the application of an

external field resulted like-wise in the formation of a wealth of highly ordered structures [13]. Similar systems have been used to create tunable photonic structures [234].

Chemically synthesizing magnetic nanomaterials under the influence of an external magnetic field has also resulted in chain-like and more complex arrangements [235] (see also section 3.8.3). Chain formation could also be inhibited by applying an alternating external magnetic field [236]. Ferro- or ferrimagnetic nanostructures in the SSD or MD size range tend to form chain-like aggregates [237-242] as well as chain-like assemblies that look like beads on a string (see Figure 2-6) [240-243]. Wang et al. were able to synthesize magnetic iron oxide nanorods passivated by a silica layer [244]. These structures could be used as building blocks for a liquid crystal solution with optical properties that could be controlled by an external magnetic field [244]. The magnetic field induced assembly of magnetic micro- and nanoparticles has been reviewed several times in recent years [245-248].
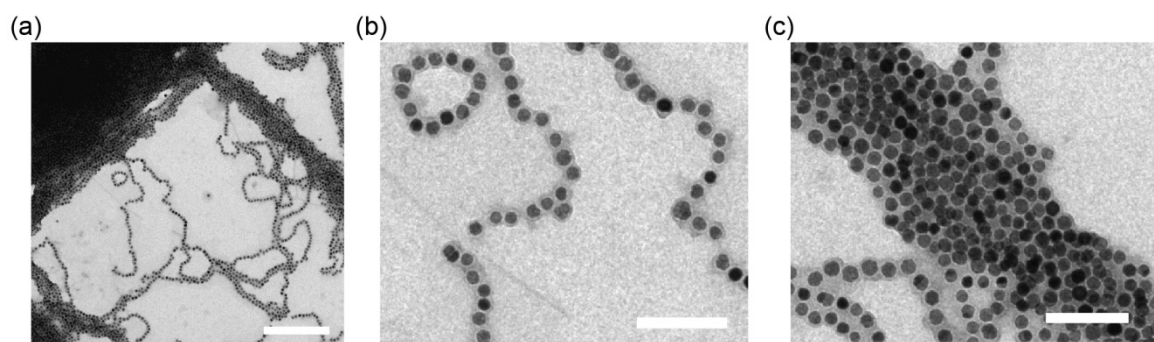
Figure 2-6: Biogenic magnetite nanoparticles in a lipid membrane (magnetosomes). (a) Overview image, different types of self-assembled structures are visible. Scale bar is 1 μm. (b) Chain-like assemblies and a flux-closure ring are visible. Scale bar is 250 nm. (c) Multiple chains form a larger aggregate (zipped-chain superstructure). Scale bar is 250 nm.

The self-assembly properties of magnetic materials can also be exploited in combination with prefabricated micro- and nanostructures (e.g. magnetic tape [249]). One such approach is known as magnetolithography, which uses the local field gradients produced by metal masks to attract magnetic nanoparticles to specific locations [7, 250, 251]. A more sophisticated approach was demonstrated by Demirörs et al. [10, 252]. By dispersing dia- and paramagnetic particles in a fluid with a specially chosen magnetic susceptibility, the forces exerted by field gradients on both types of particles and of particles of different size can be finely tuned. Using microfabricated magnetic template structures, complex microstructures could be produced in a highly reproducible and massively parallel manner.

2.4.2 Dynamic Self-assembly Using Non-constant Magnetic Fields

The first report of self-assembly induced by rotating magnetic fields was published in 2000 by Grzybowski and Whitesides, using circular millimeter sized rotors [4]. The rotors are attracted by magnetic gradient fields to a center point, repel each other through hydrodynamic interactions (finite Reynolds number) and thus arrange in interesting patterns [253-255]. It was shown later that for chiral rotors these hydrodynamic interactions depend on the rotor handedness [256]. These experiments involved up to 25 rotors.

Larger numbers of particles could be studied using microscopic paramagnetic or superparamagnetic particles. Their self-assembly, as induced by time-dependent magnetic fields, has been investigated in several studies [257-261]. The particles are typically arranged in the 2D imaging plane and the actuating field is rotating in the imaging plane with a constant component perpendicular to the imaging plane. The effective interactions between the particles can be repulsive or attractive, depending on the relative strengths of the in-plane and out of plane components of the actuating field. If the particles are not spherical, shape anisotropy can change the point at which the interaction switches from attractive to repulsive [262]. Since anisotropic particles, unlike spherical particles, rotate under the influence of a rotating magnetic field, hydrodynamic interactions might play a role as well. Applying a rotating field to paramagnetic particles on a substrate with striped magnetization, allowed the transport of particles in addition to particle assembly [263-266]. In such systems it is possible to tune the effective inter-particle forces from repulsive to attractive [267]. Recently Pietro Tierno used rotating magnetic fields to facilitate the assembly of paramagnetic colloids into different crystalline arrangements on top of a substrate with patterned magnetization [268]. It has also been possible to remotely control the 2D motion of magnetic beads along an arbitrary pathway on a microstructured chip surface [269]. Yan et al. actuated Janus colloids with a discoid magnetic symmetry using precessing magnetic fields [14]. They observed that this led individual particles to rotate with periodical tilting (like the nutation of a gyroscope), retaining phase freedom. In assemblies of such particles, the rotation synchronized and many different structures (different kinds of tubes, chains and sheets) formed in a controllable way, depending on the frequency and the precession angle of the actuating field.

For ferromagnetic microparticles, it has been observed that the aggregation kinetics could be influenced by time-varying external magnetic fields [270]. By applying an alternating magnetic field perpendicular to a liquid interface containing ferromagnetic particles, colloidal asters could be produced and manipulated [271-273]. The assembled structures could also be

used to manipulate other non-magnetic particles. Erb et al. used rotating magnetic fields, as well as constant magnetic fields to organize alumina platelets covered with magnetic nanoparticles [15, 274, 275].

Cluster formation of magnetic dipoles under the influence of a rotating magnetic field has been investigated in several theoretical studies [276-278]. When hydrodynamic interactions were not taken into account, Brownian dynamics simulations of magnetic dipoles under the influence of a rotating magnetic field resulted in the formation of particle layers perpendicular to the vector of rotation of the actuating field [278]. Using Langevin dynamics and Monte Carlo simulations of magnetic dipoles confined to 2D, cluster formation could be observed [277]. Hydrodynamic interactions were not simulated and only briefly considered. It was found that cluster formation happens only in a specific regime and proceeds through spinodal decomposition. Hydrodynamic interactions were considered explicitly in a more recent publication [276]. The dependence of the hydrodynamic coupling between spherical particles on the distance between particles (r) was considered up to order $1/r^3$ (far field approximation). Thermal noise was taken into account. The liquid medium was considered to be homogenous (no wall effects). Including hydrodynamic interactions seemed to shrink the parameter regime (field strength and frequency) in which cluster formation is possible. However, cluster formation proceeded faster in the presence of hydrodynamic interactions. Also cluster rotation was only observed when hydrodynamic interactions were included. The angular velocity increased slightly with distance from the cluster center. Particles were observed to arrange hexagonally, but hydrodynamic interactions weakened the hexagonal ordering.

Nguyen et al. simulated large systems consisting of rotating objects in 2D, which interact only through steric effects [279]. The rotors are driven by constant external torques and energy is dissipated through rotational and translational friction (given by the Einstein relation). Inertia is taken into account and the model consists of coupled Langevin equations. They consider dense mixtures of clockwise and counterclockwise rotors and observe phase separation through spinodal decomposition and the formation of rotating crystals.

3. Materials and Methods

3.1 Hydrothermal Synthesis of Magnetic Nanostructures

Hydrothermal Carbonization (HTC) is a chemical process, which offers an environmentally friendly way of converting waste biomass into interesting carbon nanostructures [280-290]. Magnetic nanostructures had been created with HTC previously by other groups. Iron oxide was either synthesized in-situ [291-294], or preformed iron oxide nanoparticles were subjected to HTC to achieve a carbon coating [236, 295-297]. It has been shown that iron oxide catalyzes the HTC process [298]. The following synthesis procedure was used for the experiments described in this thesis [116].

Two different types of magnetic nanoparticles were used as precursors: NanoArc iron(III) oxide nanoparticles purchased from Alfa Aesar, or magnetite nanoparticles produced by Marc Widdrat (Department of Biomaterials, MPIKG) [299]. Using either type of particles, the synthesis products were quite similar. Most experiments described in this thesis were using nanostructures based on NanoArc particles. In a typical synthesis 0.1 g magnetic iron oxide nanoparticles were mixed with 0.6 g Glucose dissolved in 15 ml distilled water. The solution was sonicated for about 15 minutes and filled into a stainless steel autoclave. The autoclave was sealed and heated to 180 °C for 24 h. The synthesis products were washed with ethanol and water several times using magnetic separation to recover the assembled materials between washing rounds.

3.2 Nanofabricated Propellers

Nanopropellers fabricated using glancing angle vapor deposition (GLAD) were kindly provided by Deborah Schamel (Fischer lab, MPIIS Stuttgart). An exemplary SEM image of the nanopropellers is shown in Figure 3-1. These nanostructures are produced by rotating a wafer while SiO_2 is deposited by vapor deposition on seed particles on the wafer. The helical shape results from shadowing effects (see [5] for details).
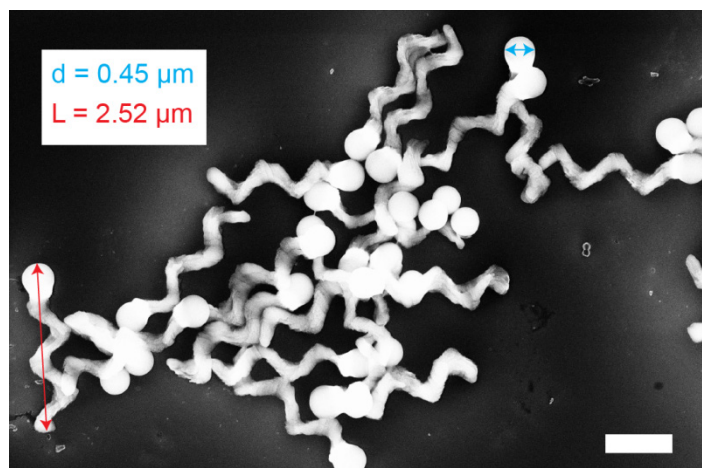
Figure 3-1: Electron microscopy image of the nanofabricated propellers. Image courtesy of Debora Schamel (group of Prof. Fischer, MPIIS Stuttgart). Scale bar is 1 μm.

3.3   Material Characterization

3.3.1   Electron Microscopy

The nanostructure of the synthesized iron-oxide carbon hybrid material was investigated using electron microscopy. Scanning electron micrographs were obtained either with a Jeol JSM7500F (occasionally using a backscattered electron (BSE) detector) in collaboration with Dr. Luca Bertinetti (Department of Biomaterials, MPIKG) or using a Zeiss Gemini Leo 1550 by Heike Runge (Department of Biomaterials, MPIKG). For transmission electron microscopy, samples were prepared by drying a certain volume of suspended nanostructures onto a carbon coated grid. Imaging was performed by Dr. Jens Baumgartner (Department of Biomaterials, MPIKG), Marc Widdrat (Department of Biomaterials, MPIKG) and Dr. Nicolas Brun (Department of Colloid Chemistry, MPIKG) on a Zeiss EM 912 Omega with 120 kV acceleration voltage.

3.3.2   Energy-dispersive X-ray Spectroscopy

The elemental composition of the synthesized nanostructures was investigated using energy-dispersive x-ray spectroscopy (EDX) in collaboration with Dr. Luca Bertinetti (Department of Biomaterials, MPIKG). Measurements were performed at 8kV and the spectra were acquired using an Oxford Inca Energy Dispersive Spectroscopy System equipped with an X-Max silicon drift detector.

3.4 Microscopy Setup

A custom-made microscope based on a slotted aluminum baseplate [300] was designed by Dr. Mathieu Bennet (Department of Biomaterials, MPIKG) to provide a platform that can accommodate the magnetic setup and to have the potential to implement multiple light sources and cameras [61, 116].

3.4.1 Magnetic Field Generation

The microscope is equipped with custom made triaxial Helmholtz coils with controller (C-SpinCoil-XYZ, Micro Magnetics Inc.) arranged around the sample holder. The sample is held in the center of the magnetic setup by a custom-made aluminum sample holder secured on a xyz motorized translation stage (PT3/M-Z8, Thorlabs), which is controlled by supplier software (apt user application, Thorlabs). The 3D-axis Helmholtz coils are used to generate DC magnetic fields with a precision of 5% of the Earth's magnetic field ($\pm$ 2.5 µT). Using this setup, AC and DC magnetic fields (0.1 - 2 mT, 1 - 100 Hz) can be applied using a Labview based program. The Earth magnetic field can be cancelled in both the AC and the DC mode.

3.4.2 High Speed Imaging

Brightfield images are recorded using a high speed camera (CR3000x2, Optronis). The illumination for transmission imaging (pE-100, 635 nm, CoolLED Ltd.) is attached on top of the magnetic setup using a custom-made holder for the LED head and aluminum rods. An image of the illumination source is created at the entrance aperture of the condenser lens (Thorlabs). The light is collected by the objective and imaged using an achromatic doublet lens. The high-speed camera is controlled with software developed by the camera manufacturer (Timebench, Optronis). The optical components and cameras are secured on the microscope baseplate using a combination of custom-made and commercially available pieces (Thorlabs, SM-1 and SM-2 series).

3.4.3 Fluorescence Imaging

The microscope setup also allows fluorescence imaging. Fluorescence imaging is implemented in an epifluorescence inverted mode. The two excitation sources (pE-100, 400 nm and 470 nm, CoolLED Ltd.) are combined using a dichroic mirror mount that accommodates the LED heads (pE-Combiner, CoolLED). A beamsplitter (Thorlabs) is placed

after the imaging lens to split the signals. 50 % of the signal is reflected to the fluorescence camera (NeosCMOS, Andor Technology plc.) and 50 % is transmitted to the high-speed camera. The light is spatially and spectrally filtered using apertures and an excitation filter (HC Tripleband Exciter 482/587, AHF Analysentechnik AG) respectively. The light is reflected off a dichroic mirror (HC Triple Line Beamsplitter R405/488/594, AHF Analysentechnik AG) and an image of the source is created at the back focal plane of the objective (60X, NA1.2, WI, Planapochromat, Nikon Gmbh). The fluorescence is collected using the same objective and imaged onto the fluorescence camera using an achromatic doublet lens (Thorlabs). The fluorescence camera is controlled using the Andor iQ software (Andor technology).

Magnetic carbon nanostructures were labeled with a fluorescent dye by incubating them for three hours with 1-Pyrenyldiazomethane (PDAM, Invitrogen) in Dimethyl sulfoxide (DMSO, Merck). Presumably, the dye attaches to the carboxylic groups present on the HTC carbon [280]. As a control, it was unsuccessfully attempted to label nanostructures with fluorescein maleimide (Sigma). This suggests that the PDAM indeed reacts with the carboxylic acid present on the hydrothermal carbon coating. After washing with DMSO, ethanol and water, the structures were observed in water inside a glass capillary (0.2x2x50 mm, Vitrotubes, Vitrocom) using fluorescent imaging.

3.5   Specific Experimental Procedures

This section was partially adapted from [116].

3.5.1   Propeller Selection Procedure

Propellers able to move against gravity could be selected for subsequent electron microscopy in the following way: The washed synthesis products were sonicated and redispersed in water. About 10 µl of this solution were carefully deposited at the bottom of a glass vial (shell vials with plugs, 8 x 35mm, Supelco) containing by volume 20 % ethanol in water. Since ethanol has a lower density than water and a similar viscosity, this was an appropriate way to ensure that the nanostructure solution sinks to the bottom of the vial during deposition. The vial was then placed in a turning magnetic field for a certain amount of time, during which the nanopropellers moved to the top of the vial, where they could be easily collected (see Figure 3-2). The duration of the experiment together with the length of the water column sets a lower

limit for the speed of the propellers. Magnetic fields were generated using the Helmholtz coils of the custom built microscope.

Control experiments were performed to check whether the nanopropellers moved to the top of the vial due to propulsion, rather than some other mechanism. The phase between the x and y sinusoidal field was set to either 0° (time-reversible actuation) or 90° (non-time-reversible actuation) keeping everything else the same. Nanostructures could be collected at the top of the vial only when the phase was 90°.

Typically 5 µl of the liquid collected at the top of the vial would then be dried onto a carbon coated grid for electron microscopy. For the observation of particularly small propellers, extremely dilute samples had to be used in order to limit aggregation of nanopropellers during drying.
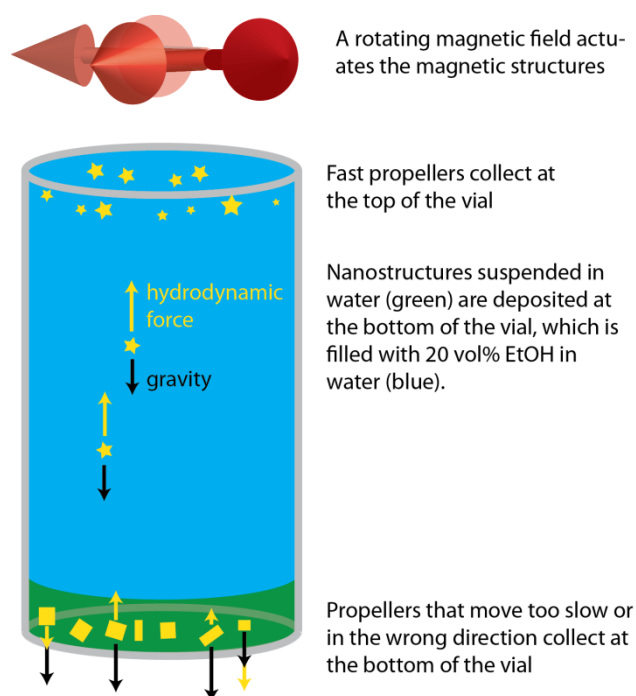
Figure 3-2: This schematic illustrates the selection process described above. Whether a structure moves to the top or stays at the bottom depends on the force balance between gravity and the hydrodynamic forces that arise from the coupling between rotational and translatory movement. The selection process is discussed in more detail in section 4.3.1.

3.5.2   Consecutive Optical and SEM Imaging of Propellers

Optical images of nanoscopic propellers cannot convey information about the shape of the propellers, which determines their propulsion properties. Conversely, electron microscopy can resolve the nanostructure of the propeller, but operates in vacuum were propulsion is not

possible. To work around these limitations, a method was developed that allows the characterization of propellers by electron microscopy after their propulsion properties have been investigated using the optical microscope.

Propellers were first observed in the optical microscope inside a droplet deposited on top of a glass coverslip, which had previously been marked with a laser cutter (PALM MicroBeam, Zeiss) and additionally sputtered with Gold/Palladium to avoid charge buildup during the electron microscopy measurements. Individual propellers for which the propulsion speed had been measured, were then continuously monitored during the drying of the droplet. Subsequently the laser cutter markings were used to identify the correct particle in scanning electron microscopy.

Optical images are compared with corresponding electron microscopy images in Figure 3-3. Optical size estimation was performed based on the assumption that the true outline of a shape is found at approximately 60 % in a normalized intensity image. This measurement strategy is based on initial imaging experiments with microbeads of known size. Estimating the size of a propeller based on optical images seems to be possible with a precision of about 300 nm. Therefore it is possible to identify nanopropellers which are smaller than 1 µm in every dimension, using optical microscopy (see Figure 3-3 i).
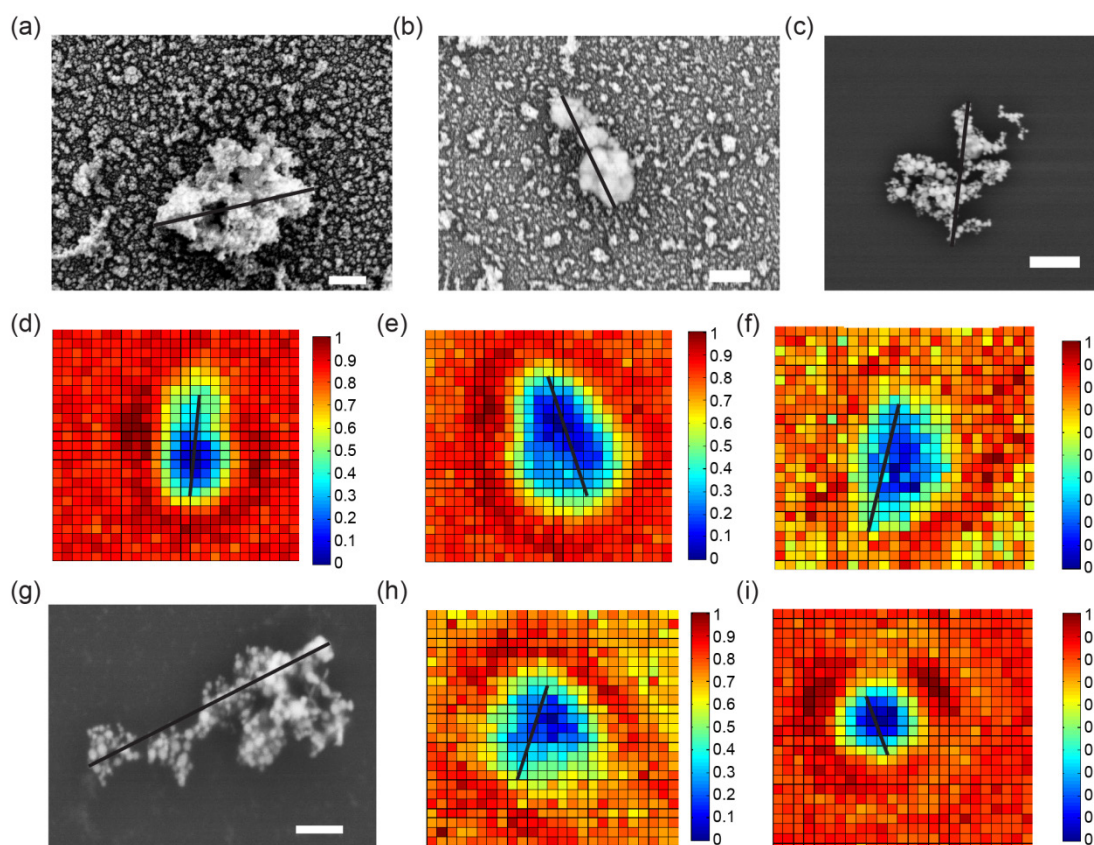
Figure 3-3: The simplest method of nanopropeller size estimation is based on optical images. To estimate the accuracy of this method, optical size estimates were cross checked with electron microscopy images of nanopropellers. To this end the largest diffraction pattern of a nanopropeller in focus was selected in a video recording its movement. After contrast normalization the nanopropeller sizes were measured as indicated by the black lines in panels (d), (e), (f), (h) and (i). The results are sorted by matching electron images and optical images: (a) = 0.88 μm and (d) = 0.97 μm; (b) = 1.22 μm and (e) = 1.19 μm; (c) = 1.15 μm and (f) = 1.16 μm; (g) = 1.16 μm and (h) = 0.91 μm. The last optical image (i) is measured at 0.55 μm and corresponds to the nanopropeller used for the speed versus frequency measurements displayed in Figure 4-10. The size estimate of 0.55 μm is close to the diffraction limit and thus not very accurate, but it can be concluded from the pictures presented here that it is smaller than 1 μm. The dimensionless speed values for the presented nanopropellers were estimated as 69 for (a), 32 for (b), 41 for (c) and 27 for (g). Scale bars are 200 nm in (a), 400 nm in (b), 400 nm in (c) and 200 nm in (g). The pixel size in the optical images is 0.0875 μm per pixel. Adapted from [116]. This is an unofficial adaptation of an article that appeared in an ACS publication. ACS has not endorsed the content of this adaptation or the context of its use.

3.5.3   High-precision Speed Measurements for Single Propellers

Despite their small size, magnetic nanopropellers sediment due to gravity and will move towards the lower surface of the capillary over time. Measuring the propulsion speed close to this solid interface is convenient, but the obtained result might be different from the propulsion speed in bulk liquid. In addition, a propeller close to a solid interface will in general not move parallel to the vector of rotation of the magnetic field, but will perform a rolling motion along the surface in addition to propulsion. Finally, electrostatic or steric interactions with the surface might hinder the rotational or translatory movement of the propeller, limiting the precision of the speed measurement. In order to overcome these limitations, a measurement strategy was developed, which allows the determination of the propulsion speed in bulk liquid.

Measurements were performed in sealed glass capillaries (0.2 × 2 × 50 mm, Vitrotubes, Vitrocom). The propeller was firstly driven to the upper surface of the capillary. Secondly, the actuating field was changed, so that the propeller now moved approximately parallel to, and slightly away from the upper capillary surface. Then a video of the falling propeller was recorded. Sometimes the focus of the microscope needed to be adjusted during the recording to follow the falling motion of the propeller. Speeds were then measured in the imaging plane, neglecting the change of focus. The downward component of the movement was thus intentionally neglected for speed measurements, since this component is due to gravity and not to propulsion. The error of the measurement was dominated by diffusion of the

nanopropeller. The mean square displacement due to diffusion $\left(\sqrt{\langle x^2\rangle} \propto \sqrt{T}\right)$, expected to occur during the measurement time T, limited the precision with which the hypothetical end position could be determined, which the propeller would have reached in the absence of diffusion. The measurement error was thus proportional to $1/\sqrt{T}$ and was therefore minimized when choosing the longest possible measuring time. For this reason, videos of propellers crossing the complete field of view were typically recorded. The remaining measurement error due to diffusion could be estimated by measuring the diffusion constant of the propeller. This was done by recording a high-speed video of the freely diffusing propeller, with the magnetic field turned off. The particle positions were tracked as described in section 3.6.1 and the diffusion coefficient was then determined as shown in Figure 3-4, analogous to a method described by Crocker and Grier [301].
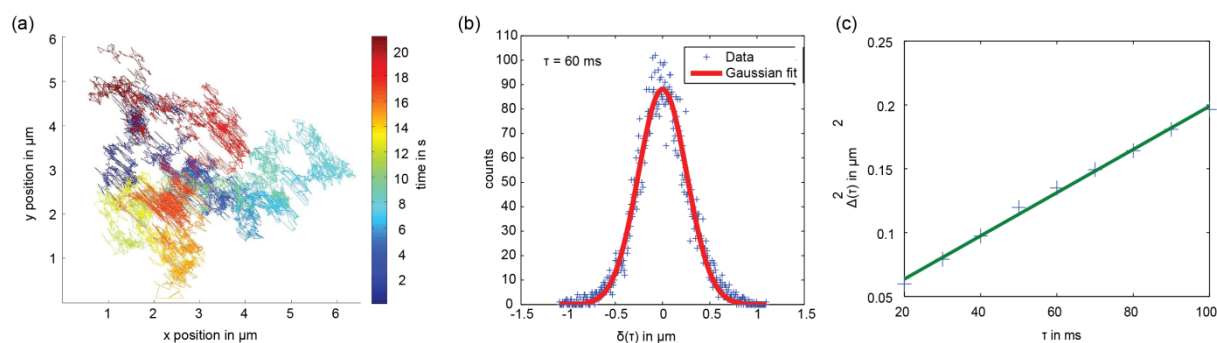
Figure 3-4: Explanation of the measurement of the diffusion coefficient of the propeller displayed in Figure 3-3 (i). A video of the freely diffusing propeller (field off) was recorded for 10527 frames at 500 frames per second. (a) Propeller positions were extracted from the video as described in section 3.6.1. (b) Then histograms of the position differences $\delta(\tau)$, between two frames at time t and $t + \tau$ were prepared. These distributions were fitted with a 1D Gaussian (using the Matlab function *nlinfit*) to determine the width $\Delta(\tau)$ of the distribution. Intermediate values of τ were chosen in order to avoid errors from position measurement errors at short timescales and insufficient statistics at long time scales. (c) The diffusion coefficient D can be extracted by a linear fit, since $\Delta(\tau)^2 = 2D\tau + \Delta_0^2$, where Δ_0^2 is an additive constant that arises from short time diffusion and measurement errors [301]. This analysis was done separately for x and y coordinates and the values $D_x = 0.94\ \mu m^2 s^{-1}$ and $D_y = 0.85\ \mu m^2 s^{-1}$ were obtained. For the error bars in Figure 4-10 the mean value $D = 0.9\ \mu m^2 s^{-1}$ was chosen. Adapted from [116]. This is an unofficial adaptation of an article that appeared in an ACS publication. ACS has not endorsed the content of this adaptation or the context of its use.

The diffusion coefficients measured in this way are an overestimate for the true diffusion coefficient of the nanopropeller, since the liquid medium in which the nanopropeller is moving is not completely at rest. Small vibrations of the sample stage increase the apparent

diffusion coefficient. Vestergaard et al. recently presented a detailed method for the optimal estimation of diffusion coefficients from single particle trajectories in the presence (or absence) of substrate or medium movement [302]. However, the method by Vestergaard et al. had not been published when the results of section 4.3.4 and section 4.3.5 were originally presented [116]. A slight overestimate of the speed measurement error is of no concern for the results of section 4.3.4 and section 4.3.5.

3.5.4 Speed Measurement for Randomly Shaped Aggregates

The average speed of as-synthesized, unselected magnetic nanostructures cannot be measured by the method described in section 3.5.3, since that method excludes all structures that propel too slowly to reach the upper capillary surface when swimming against gravity. Therefore, speeds were measured at the lower capillary surface. As-synthesized magnetic nanostructures were filled into the capillary, which was subsequently placed in the microscope sample holder with the actuating magnetic field off. After all structures had settled to the lower capillary surface, the actuating field was switched on and a video of the lower capillary surface was recorded immediately afterwards in the center of the capillary. After one such measurement the capillary was discarded, since the application of an actuating magnetic field destroys the random initial distribution of structures in the capillary. The concentration of the structures was adjusted to an intermediate range, high enough so that many propellers (on average around 17) could be characterized in one measurement, but low enough to avoid frequent hydrodynamic or magnetic interactions between the structures. The recorded videos were analyzed by manually searching for start and end positions, in between which a structure moved undisturbed by any other structure. The movement parallel to the vector of rotation of the actuating field was interpreted as propulsion, whereas the movement perpendicular to the propeller was interpreted as rolling movement (see Figure 3-5). Although it is not self-evident that this measure of propulsion speed is equivalent to the propulsion speed in bulk liquid, far away from a surface, it is a standard technique to measure propulsion speeds [5, 6, 11]. The size of the structure was determined by searching for a frame in which the propeller appeared in focus, as well as in the orientation that leads to the biggest 2D projection. The distance was then determined manually by measuring the distance between the most distant pixels in the 2D projection (see inset in Figure 3-5 a).
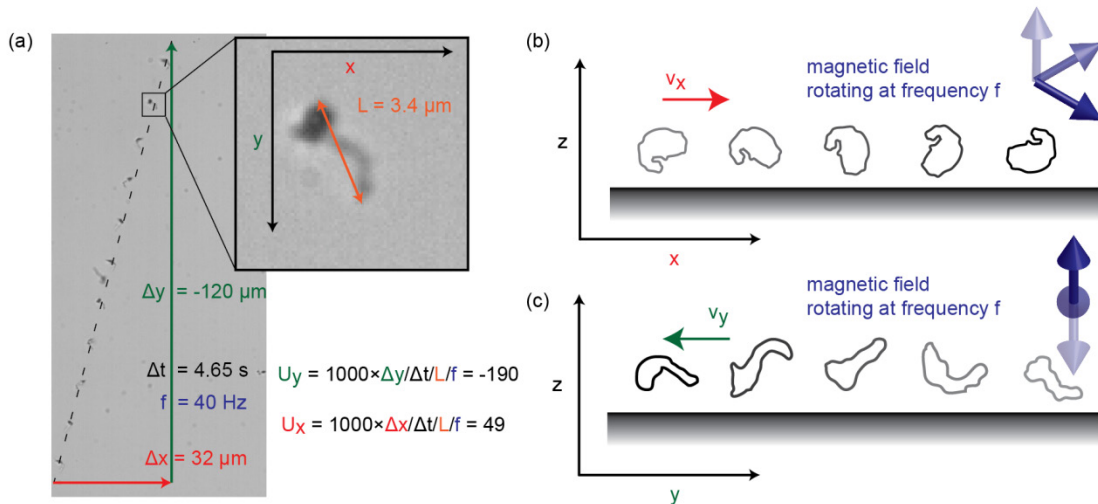
Figure 3-5: Schematic explanation of measurements of dimensionless speeds. (a) The dashed black line indicates the trajectory of a propeller. Images of the propeller after time steps of 0.42 s are superimposed on the initial frame to create a time-lapse image. In total the propeller traverses a distance of 120 μm in negative y direction and 32 μm in positive x direction during a time $\Delta t = 4.65\ s$. Speeds were measured by noting start and end positions and the time difference. The view in which the propeller appears biggest is magnified in an inset. The propeller size was always measured for the view (angle) in which the propeller appeared biggest when in focus. Based on these measurements the dimensionless propulsion speeds (U_y) and dimensionless rolling speeds (U_x) were calculated for all propellers in the dataset. (b) The rolling motion is due to the fact that the propellers are imaged close to a glass surface, towards which they are pulled by gravity. The shearing of water close to the glass and propeller surfaces mediates a friction that results in a rolling motion [8, 129]. The arrow of time is indicated in this schematic by a darkening of shape outlines and magnetic field vectors. (c) Since the propellers are in general sufficiently asymmetric they propel parallel or anti-parallel to the vector of rotation of the actuating magnetic field. The arrow of time is again indicated by a darkening of shape outlines and magnetic field vectors.

Videos were recorded for a duration of 59.22 s. This finite measurement time could lead to a bias, since faster propellers might have a higher chance of reaching the field of view during that time (and thus being measured) than slow propellers. In order to check if this bias is significant, a self-consistency check was performed by simulating the experimental procedure. The measured distributions of dimensionless speeds were assumed as true values in the simulation and the simulated measurement results were compared to the assumed true speed distributions (Figure 3-6). The simulations show that the choice of a measurement time of 59.22 s does not lead to large changes in the measured distributions. When the actuating field is switched on, the control electronics take about 10-20 s to establish a stable field. The total measurement time could thus be higher, but even measurement times of about 90 s, do

not significantly change the distribution of propulsion speed. No attempt was made to numerically remove the small but existing bias effect, since it is not clear if the finite measurement leads to an over- or underestimation of the propulsion speed standard deviation. This is due to the fact that, for long measurement times, the initial effect of faster propellers being more likely to reach the field of view, is counteracted by the depletion of fast propellers above and below the field of view (see Figure 3-6 d).
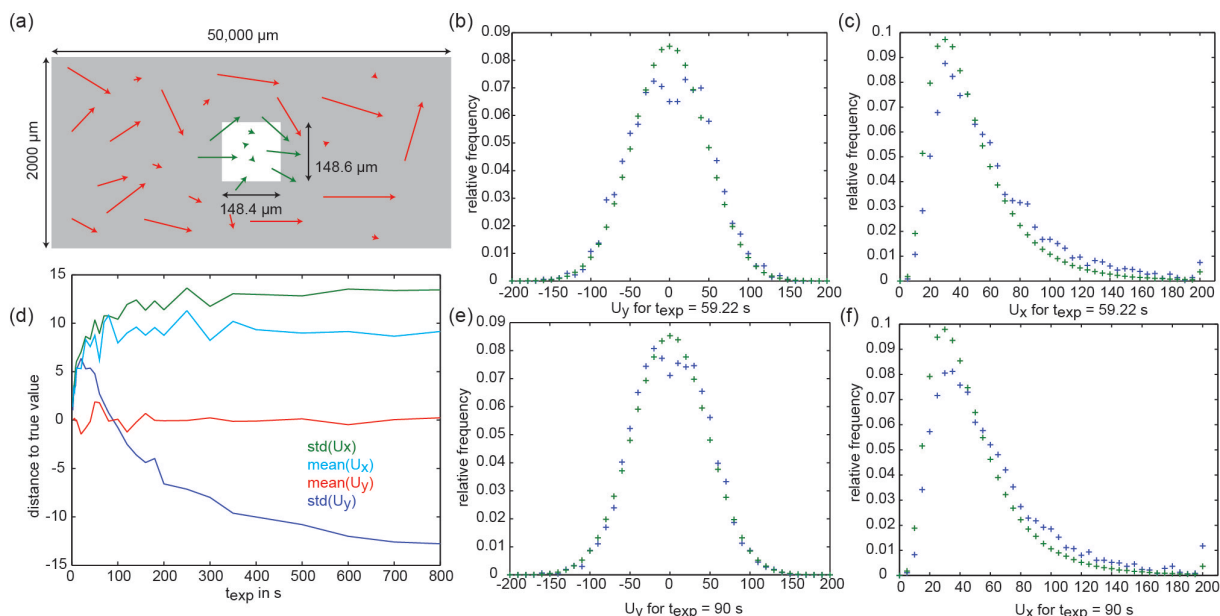
Figure 3-6: Simulation of speed measurement, to check for consistency. (a) Schematic of the experimental setup (sizes not to scale). The capillary (grey) is much bigger than the field of view (white square). Arrows indicate possible propeller movements during the simulated measurement time t_{exp}. Some propellers cross the field of view and their speed is measured (green arrows) others not (red arrows). The fact that faster propellers can reach the field of view more quickly leads to a bias. To investigate this bias the measurement was simulated, by drawing propeller properties from random distributions (Gaussian for U_y, log-normal for U_x) modeled on the measured distributions. (b) Histograms of U_y in a simulated measurement with measurement time $t_{exp} = 59.22$ s. The green crosses mark the assumed true distribution for U_x, whereas the blue crosses mark the distribution that would be measured on average (based on 1 million sample propellers). (c) Same as (b) but for dimensionless rolling speed U_x instead of U_y. (e)/(f) are the same as (b)/(c), but for $t_{exp} = 90$ s instead of $t_{exp} = 59.22$ s. (d) The difference between standard deviation and mean of U_x and U_y is plotted against t_{exp}. The mean and the standard deviation of U_x simply increase with increasing measurement time. This is due to the fact that propellers to the left of the field of view can reach the field of view more easily if they are rolling faster. The mean of U_y stays constant at zero, due to symmetry reasons (the field of view is in the middle of the capillary). The standard deviation of U_y first increases with t_{exp} since faster propellers below and above the field of view can reach the field of view during the measurement time more easily if they are faster. For large t_{exp} this effect is countered by the depletion of propellers above and below the field of view and the additional effect that propellers to the left of the field of view can reach the field of view more easily if they have low U_y.

3.5.5   Self-assembly of Flexible Swimmers

Chain-like assemblies of synthesized magnetic nanostructures were created by applying a constant homogenous field of 1 or 2 mT. This aligned the individual structures and over the course of seconds to minutes the structures assembled into chain-like super-structures. Then a sinusoidal field of field strength 1 or 2 mT was applied in the imaging plane, perpendicular

and in addition to the constant field that aligned the particles. This led to cyclic shape deformations and resulted in swimming motion (see section 4.2.2).

3.5.6   Flow Visualization

Flow patterns produced by magnetically actuated microscopic structures, propelling towards the upper surface of a glass capillary (0.2 × 2 × 50 mm, Vitrotubes, Vitrocom), were visualized using polystyrene tracer particles provided by Dr. Klaus Tauer (Department of Colloid Chemistry, MPIKG). Flow visualization at the upper capillary surface is challenging, since this region is normally quickly depleted of tracer particles due to sedimentation. Therefore the density of the liquid medium had to be higher than the density of the tracer particles. Glucose and Tris solutions can easily have a higher density than polystyrene (about 1.05 g×cm^{-3}), but the concomitant increase in solution viscosity prevented the formation of propeller clusters. Salt solutions can increase the solution density as well, but the increase in ionic strength leads to aggregation of propellers. Semi-heavy water (Deuterium Oxide, Sigma, diluted by equal amount of deionized water) was successfully used for flow visualization. The tracer particles were slowly driven towards the upper surface of the capillary by buoyancy and cluster formation by propellers was still possible.

3.5.7   Cluster Formation Experiments

In cluster formation experiments (see section 4.6) either propellers from solution synthesis (see section 3.1) or nanofabricated propellers (see section 3.2) were used. Both samples were filled into capillaries (0.2 × 2 × 50 mm, Vitrotubes, Vitrocom) at high concentrations without selection (see section 3.5.1). Rotating magnetic fields were applied with the vector of rotation perpendicular to the upper capillary surface. This led to the movement of a subset of synthesized nanostructures towards the upper capillary surface. Basically all nanofabricated propellers moved towards the upper capillary surface (Figure 3-7). Under the right conditions, both types of propellers could be observed to form clusters.
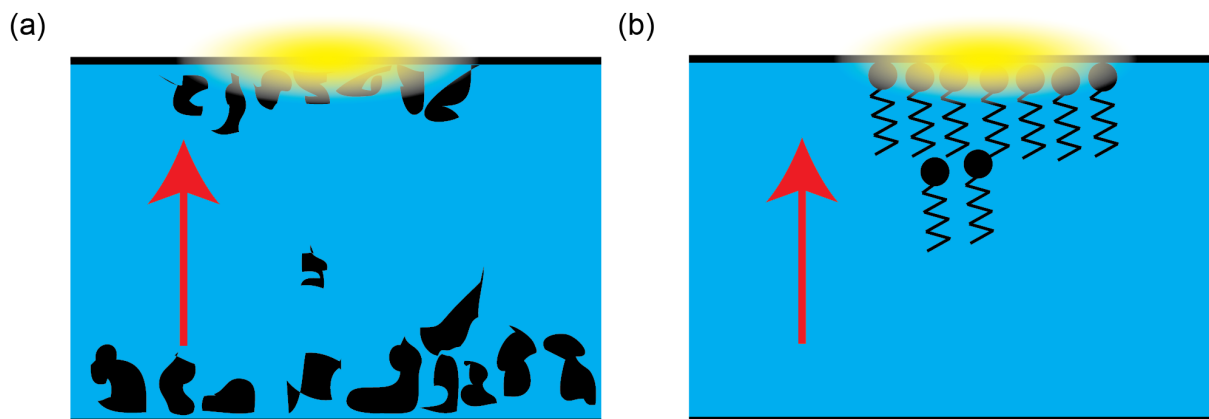
Figure 3-7: Schematic illustration of cluster formation experiments. (a) In experiments with propellers from solution synthesis, the as-synthesized structures were filled into a capillary at high concentrations. Upon application of a rotating magnetic field, a subset of the nanostructures moved upwards (red arrow) against gravity and formed clusters on the upper capillary surface. The yellow area indicates the imaging plane. Structures that were not able to swim upwards against gravity settled (or propelled) to the lower surface of the capillary. (b) In experiments with identical nanofabricated propellers almost all propellers moved towards the upper capillary surface upon application of a rotating magnetic field.

Further experiments were conducted using Carboxyl Ferromagnetic particles (CFM-80-5, Spherotech) with a diameter of about 8.5 µm. These particles were filled into a capillary at high concentration and subjected to rotating magnetic fields (vector of rotation perpendicular to the lower capillary surface). This led to some rotation of the ferromagnetic particles, which stayed sedimented to the lower capillary surface (see section 4.6.4).

3.6   Image Processing

3.6.1   Particle Tracking

Positions of individual nanopropellers were extracted automatically using custom written Matlab code, roughly based on the particle tracking method described by Crocker and Grier [301]. The algorithm first finds the minimum pixel value in the image and then fits a 2D Gaussian function to a square of 20 by 20 pixels (1.75 µm) around the minimum pixel (using the Matlab function *nlinfit*) [116]. An extended version of this code has been used for the tracking of magnetotactic bacteria [61, 62].

3.6.2 Cluster Analysis

Clusters of self-assembled propellers were analyzed by identifying the positions of individual propellers in the cluster. This was quite challenging, since the propellers are only about 0.5 μm in diameter when viewed from the top (see section 3.2), close to the resolution limit of the microscope. Custom written Matlab software was used to analyze the clusters. The images are first filtered with a Gaussian 2D filter (5 by 5 pixels, standard deviation 0.5). Then the algorithm checks for every pixel if it is smaller than all pixels in an approximately spherical region (radius 4 pixel) surrounding it. This identifies local minima. Clusters are identified by thresholding (darker). Using the Matlab function *bwareaopen* bright spots within the clusters smaller than 100 pixels are removed. Different connected areas are identified as individual clusters and analyzed separately.

(a) (b)
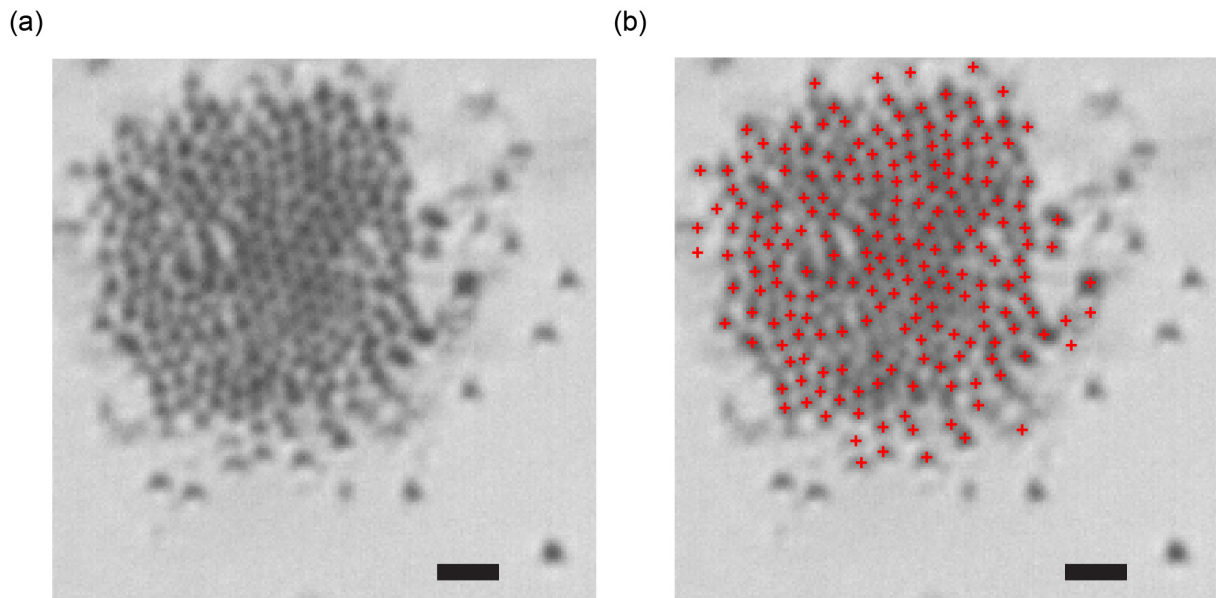
Figure 3-8: (a) A close view of a cluster cut from an optical microscopy image. (b) The cluster analysis code identifies the region where the cluster is situated and finds local minima in this region. The detected local minima are marked with red crosses. Scale bars are 2 μm.

The local minima identified as a cluster are now interpreted as propeller positions. A 2D Fourier transform is then applied to an image, in which every propeller position is marked by a white pixel on a dark background. The absolute value of the Fourier transform ($|\mathcal{F}|$) is then rescaled as $a = \log(|\mathcal{F}| + 0.1)$ and $b = \frac{a - \min(a)}{\max(a) - \min(a)}$. The resulting 2D Fourier transform image is resized to have dimensions m by m pixels ($m = 800$). The pixel with the highest value of all pixels further than $0.05m$ from the center is used as a peak-marker (x_p, y_p). The

crystal orientation, which differs from cluster to cluster, is reoriented by turning the 2D Fourier transform image counterclockwise around its center by the angle $\alpha = \tan^{-1}\left(\frac{x_p - m/2}{y_p - m/2}\right)$. Tangens is periodic in π, but this is not a problem since the 2D Fourier transform is point-symmetric around the center.

The images shown in Figure 4-27 are weighted sums of several 2D Fourier transform images, rescaled and rotated as described above, of clusters under the influence of actuating fields of the same frequency. Weighting was necessary to account for the different cluster sizes and was done in the following way: Each 2D Fourier transform image is multiplied with the number of local minima on which it is based and the resulting image is divided by the total number of local minima in all used clusters. Distances from the center (q) in the 2D Fourier transform image can be converted to distances in real space, by noting that the highest frequency at $q = m/2$, is equal to half the inverse pixel size ($1/(2 \times 0.0881 \ \mu m/pixel)$).

3.6.3 Cluster Flow Visualization

Propellers can self-assemble into quasi 2D clusters (see section 4.6). Propellers at the cluster edge move with higher velocity around the cluster than would be expected from the angular velocity of the cluster rotation. This effect is very apparent in video recordings of cluster dynamics. In order to visualize this behavior in an image, the absolute values of intensity changes ($|I_{i,j}(n) - I_{i,j}(n-1)|$) from one frame to the next were summed pixelwise (Figure 3-9). This technique apparently highlights the cluster edge. Due to the fact that the absolute velocity would be also maximal at the cluster edge if the angular velocity was constant throughout the cluster, the highlighting alone does not demonstrate that the propeller in the edge region move faster than the angular velocity of the cluster rotation. To show that the highlighting of the edge region is indeed due to the increased propeller angular velocity, an angular velocity proxy was calculated by normalizing the intensity changes in two ways. Firstly, absolute differences in intensity were eliminated by dividing the intensity with the intensity of the current pixel $\left(\frac{|I_{i,j}(n) - I_{i,j}(n-1)|}{I_{i,j}(n)}\right)$. Secondly and additionally, the intensity values are divided by the distance to the center of rotation $\left(\frac{|I_{i,j}(n) - I_{i,j}(n-1)|}{I_{i,j}(n)r_{i,j}}\right)$. To test this proxy for the angular velocity, an artificial video of homogenous rotation was created by turning one cluster image (Figure 3-9 a) repeatedly in 1° steps until reaching 90°. A visualization of the angular velocity proxy for this artificial video data is shown in Figure 3-9 c. As expected, the cluster

has approximately homogenous values of the angular velocity proxy, and the surrounding background shows lower values as it is largely rotationally symmetric. For actual video data of the cluster dynamics, the angular velocity proxy is shown in Figure 3-9 d. The edge region shows higher angular velocity than the rest of the cluster, except the middle. In the middle, residual propeller movements (diffusion and interactions) and resulting intensity changes are greatly amplified as the distance to the center of rotation becomes very small. The original method of summing intensity differences (Figure 3-9 b) is thus a good visualization of the cluster edge and fast propeller movements therein.
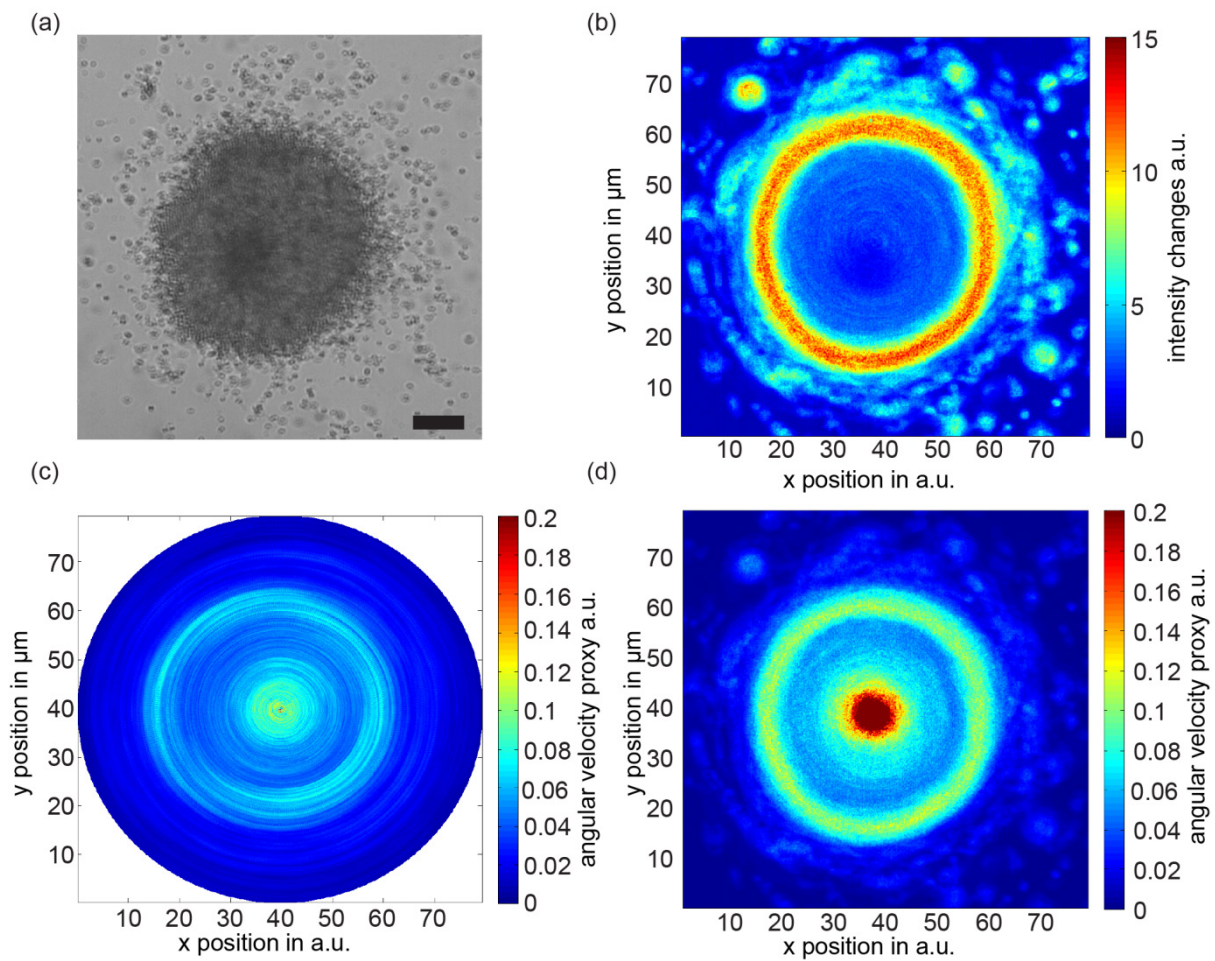
Figure 3-9: (a) Optical microscopy image of the circular cluster analyzed in the following panels. The image is taken from a video recorded at 90 frames per second. Scale bar is 10 μm. (b) Simply summing the absolute values of intensity differences between frames, results in a visualization of the boundary layer of the cluster. It can be seen in the video that propellers in this boundary layer move faster than the angular velocity of the cluster rotation. (c) To visualize this, intensity changes are normalized by dividing by the pixel intensity of the next pixel. In addition intensity changes were divided by the distance to the center of rotation to yield a proxy for the angular velocity. A homogenous rotation of the cluster is simulated by rotating the image presented in (a). The angular velocity proxy is somewhat higher in the cluster region, due to the fact that the background is rotationally symmetric. The cluster region is more or less homogenous. (d) The angular velocity proxy for the cluster shows that the angular velocity in the cluster edge is higher than it would be for a homogenous cluster rotation. The high values in the middle are due to the fact that propellers are also moving around due to thermal noise at the center of rotation and dividing by the distance of rotation leads to large values.

3.6.4   3D Shape Reconstruction

Carbon coated aggregates of magnetic nanoparticles were produced and used in the experiments described in this thesis (see sections 3.1 and 4.1). The 3D shape of these aggregates could be reconstructed by a tomographic technique based on optical images recorded for the speed measurement method described in section 3.5.4. Video images were recorded at 50 frames per second, whereas the actuating frequency was either 10, 20 or 40 Hz. Video images contain therefore five distinct projections for each measured aggregate. The actuating frequency was sufficiently low, so that the aggregates could generally follow the magnetic field. By comparing frame n with frame n+5, the assumption that the structure rotates with the actuating frequency was checked explicitly. Structures could be reconstructed if their size was big enough, so that important features are visible in the optical microscope, but small enough, so that the complete structure was approximately in focus for every orientation. Images of suitable aggregates were selected and the 2D projections of the aggregate were manually outlined. The thus defined 2D projections were projected into a voxel cube at appropriate angles. Offsets were estimated based on the movement of the structure from frame n to frame n+5. Voxels that were hit by all five projections formed the initial reconstructed 3D shape. This initial reconstruction was then refined by searching for offset values that maximized the number of voxels in the reconstructed 3D shape, using discrete optimization. This was done in a stepwise fashion. What needed to be optimized were eight translatory shift parameters (zero for the first projection, two for the four remaining projections each). The eight translatory shift parameters were first varied in steps of p_1 pixels.

42

The shift parameters that maximized the number of voxels that were passed by all five projections were subsequently varied in steps of $p_i < p_{i-1}$ pixels. This was repeated until the final step size of 1 pixel was reached. Values for p_1 were typically chosen between 3 and 5, depending on the size of the propeller to be reconstructed. The number of optimization rounds varied between three and five, also depending on the propeller size. This optimization procedure should always find the global optimum, if the objective function is convex and if the start conditions are close enough to the global optimum so that it can be reached (i.e. closer than the sum of the p_i). For a multi-peaked objective function the found optimum does not necessarily correspond to the global optimum (Figure 3-10).
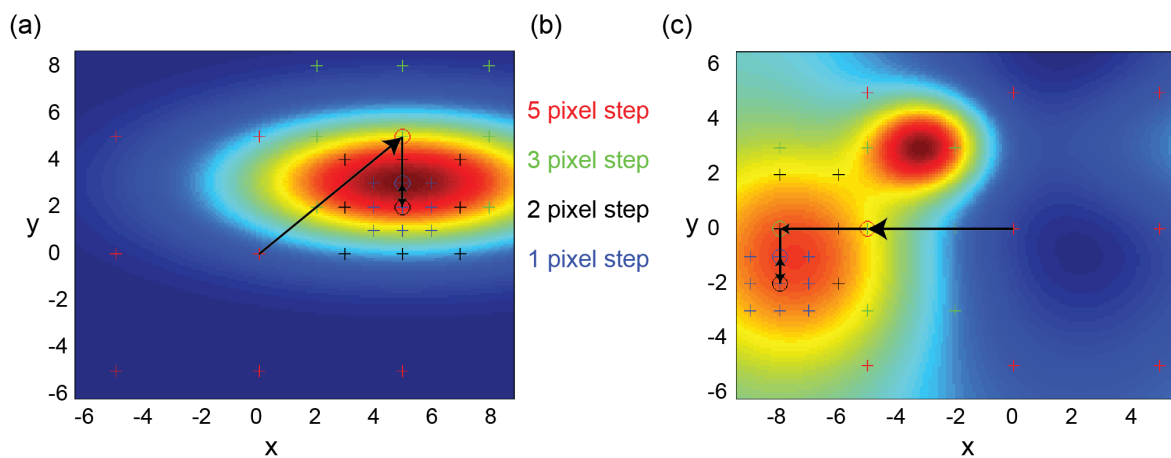
Figure 3-10: (a) The discrete optimization algorithm at work in the simple case of a convex objective function and only two variables (x and y). The color code for the four optimization steps is denoted in panel (b). Both x and y are varied by the step size. The best value (marked by circle) is the start position for the next optimization step. The progression to the found optimal value is marked by black arrows. For a convex objective function, the algorithm should always find the global optimum provided it is not too far away (i.e. smaller than the sum of the p_i) from the initial values (x=0, y=0). (c) For a multi-peaked objective function, the found optimal value may not correspond to the global optimum.

Finally, the reconstructed 3D shape was projected back to 2D for the visual verification of the reconstruction. If all prominent features of the original images were also present in the images reprojected from the reconstruction, the reconstruction was deemed successful. 47 out of 55 attempted reconstructions were successful. The reconstruction method is schematically explained in Figure 3-11. This method was inspired by a collaborative effort with Dr. Friederike Saxe, Lisa O'Conner, and Prof. Peter Fratzl, aiming at 3D motion tracking for worms.
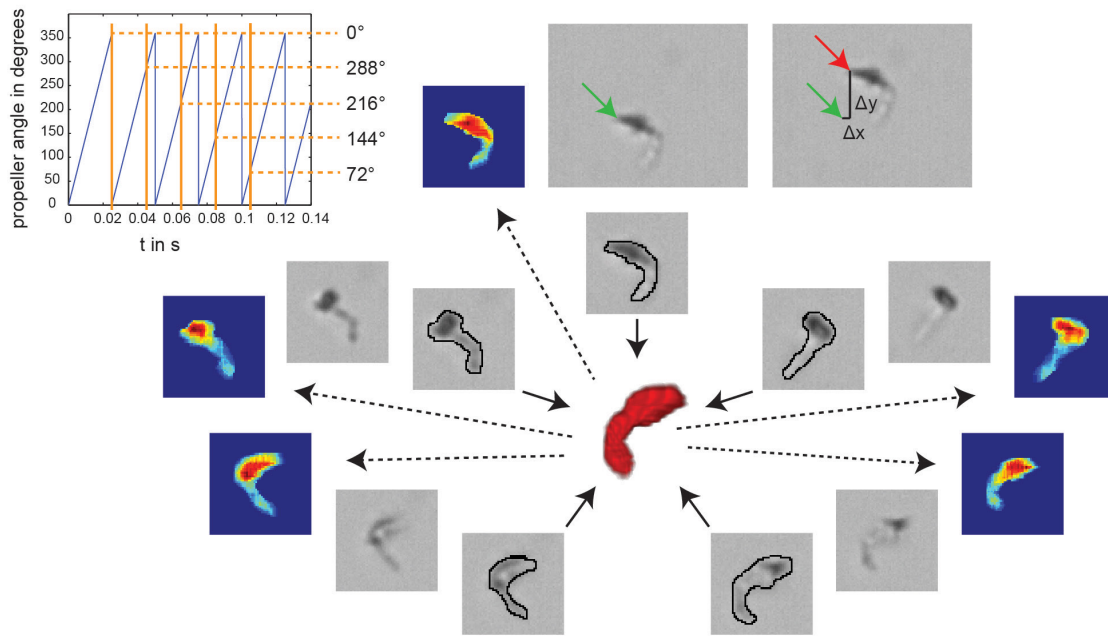
Figure 3-11: Schematic explanation of the reconstruction method. In this example the propeller rotates with 40 Hz, images were recorded with 50 frames per second. As can be seen in the plot on the top left, this results in images being taken from 5 distinct angles (0°, 72°, 144°, 216°, 288°). After 0.12 s, the angle is again the same as at t = 0 s, however the propeller has moved by $\Delta y \approx 2.5$ µm and $\Delta x \approx 0.4$ µm. The five images of the propeller are manually outlined. The area inside the outline is then projected into a voxel cube at the correct angle. The projections are offset against each other initially by $\Delta x/6$ and $\Delta y/6$. The voxels that are hit by all five projections become part of the initial reconstructed 3D shape. In the next step, discrete optimization is used to find parameters $\Delta \tilde{x}$ and $\Delta \tilde{y}$ which maximize the number of voxels in the reconstructed 3D shape. Finally, the optimized reconstructed 3D shape is projected back to 2D at the correct angles. The resulting color coded projections are displayed next to the original images. The color code implies how many voxels of the final 3D reconstructed shape were mapped to one pixel in the 2D projection (from none (blue) to many (red)). These projections are then compared to the original images. If all discernible features in the original image are also present in the reconstruction, the reconstruction is deemed successful.

3.7 Numerical Methods

3.7.1 Swarm Control Simulation

This section was partially adapted from a submitted manuscript. A control method to steer individual propellers along independent trajectories (see section 4.5) was simulated in the following way. The simulation starts by randomly drawing properties for five propellers from distributions defined by equation 47, 48, and 49. The simulation has another parameter

(*minrot* = 10), denoting the minimum number of rotations a propeller needs to perform before the vector of rotation of the actuating field can switch to an orthogonal orientation. The intended trajectory of the control task is set as a pattern of intertwined pentagons, surrounded by a decagon. The pentagons are intersecting and the speed of the propellers on intersecting pentagons is adjusted so that they alternately pass the crossing point of two pentagons first. This leads to the formation of intertwined (or braided) pentagons (see Figure 4-23). The average speed with which the propellers travel can be set and can be used to adjust the average magnetic field strength to a realistic value ($\langle B \rangle = 1$ mT). The maximum magnetic field strength is also constrained in the simulation ($B < 5$ mT).

In the simulation the propellers are moved in a step-wise fashion, alternating in x and y direction. For each step, the actuating field is calculated in the following way. At first the control problem is solved using critical control (see section 4.5.2), for a small step size. This means that the algorithm tries to reach intended future positions of the propellers starting from the current positions. The current positions are not equivalent to the intended final positions of the previous step due to diffusion and would need to be measured in an experimental realization. Thus the described control algorithm constitutes a closed loop control algorithm. If at least one propeller does not turn more than *minrot* times during this control step, the step size is increased until all propellers turn often enough. In addition, the duration of the control step must be longer than a minimum time (*mint*, used to adjust the h_2 parameter) to allow the propellers to outrun diffusion. This control step is now applied in the simulation and diffusive motion is superimposed on the propeller trajectory. The diffusion coefficient is set, assuming a medium of water at room temperature. This concludes one simulation step. The next step is taken in either x or y direction, depending on which direction is more advanced along the intended trajectory. Due to the varying step length, it can be necessary to take consecutive steps in the same direction, in order to ensure that the (x, y) positions of all propellers stay as close as possible to the intended trajectory. The outputs are the applied field frequencies and field strengths as well as the propeller positions as functions of time. These can then be analyzed, visualized and animated.

3.7.2   Simulation of Propeller Interactions

Three different types of simulations were used to investigate a situation in which magnetically actuated propellers move towards a glass surface (see section 4.6). In **Simulation 1**, only magnetic interactions were considered. **Simulation 2** simplified **Simulation 1** in order to

allow the simulation of larger numbers of propellers. **Simulation 3** included an artificial effective hydrodynamic interaction, in order to show that magnetic interactions alone cannot explain the observations. In this section, the physical situation will first be discussed and afterwards the details of the simulations are given.

The hydrodynamic interactions between propellers moving against gravity towards a glass surface are quite complex. The propellers cannot move upwards and thus pump water down, while also creating flow fields due to their spinning motion. The resulting flow fields can lead to an effective hydrodynamic attraction between propellers [58, 303]. Since the propellers attract each other already due to magnetic interactions, this complex hydrodynamic interaction was not considered when building a model for the propeller interactions. Also boundary effects due to the presence of the glass surface were neglected, except for the fact that propellers were assumed to be confined to a 2D plane.

If inertia cannot be neglected, rotors repel each other at short distances and can assemble into stable arrangements [4, 304, 305]. In this case, the resulting flow patterns are similar to those arising from several interacting point vortices, known as vortex crystals [306-308]. Vortex crystals are stable arrangements of irrotational vortices ($v_\phi \propto 1/r$), which are different from the flow field produced by a sphere at low Reynolds numbers ($v_\phi \propto 1/r^2$) (section 2.1.2). Since the Reynolds number is low in the experiments described in this thesis, such inertial effects were not incorporated into the model for propeller interactions.

In order to gain a better understanding of the hydrodynamic interactions at low Reynolds numbers, the propellers (radius R_1, rotation frequency ω_1) can be imagined to be arranged on a hexagonal lattice (see Figure 3-12 a). The hydrodynamic boundary conditions for the flow field around the central propeller can then be approximated by two concentric cylinders with radii R_1 and R_2. The rotation frequency ω_2 of the second cylinder might be positive or negative.
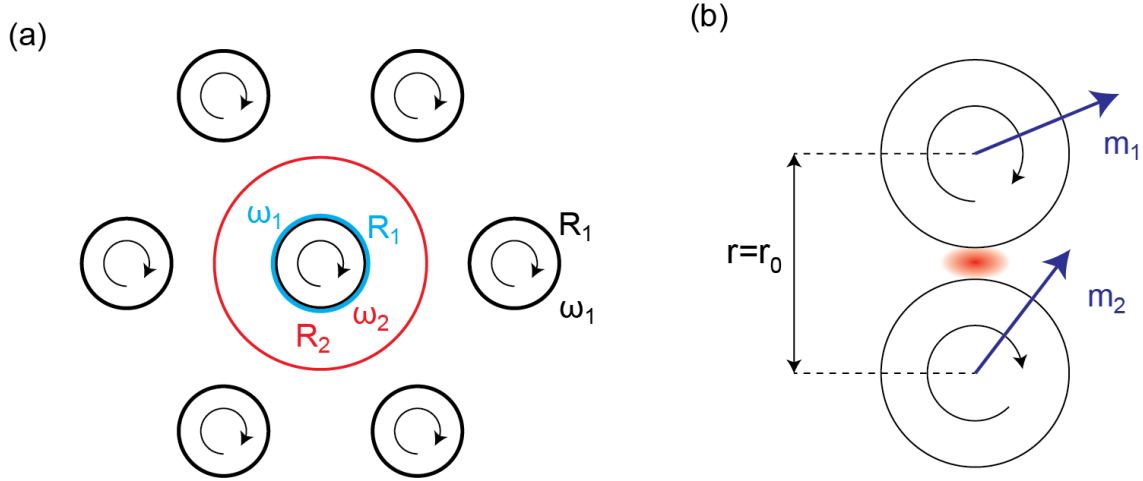
Figure 3-12: (a) Schematic of propellers in a hexagonal arrangement. The flow pattern is approximated by that of a fluid between two concentric cylinders. Analyzing this situation shows no repulsion, independently of the actuating frequency ω and the radii R_1 and R_2. (b) In **Simulation 1** interactions between propellers are modelled to include a short range repulsion. For $r > r_0$, the interaction is solely that of magnetic dipoles ($\mathbf{m_1}$ and $\mathbf{m_2}$).

For symmetry reasons, the resulting flow between the concentric cylinders has only a component along $\hat{e}_\phi$ (ϕ being the azimuth in cylindrical coordinates) and it can be verified that the solution (to the Stokes equations 2 and 3) is given by:

$$v_\phi(r, \phi, z) = \frac{1}{(R_2^2 - R_1^2)} \left[(\omega_2 R_2^2 - \omega_1 R_1^2)r + \frac{R_1^2 R_2^2 (\omega_1 - \omega_2)}{r} \right] \tag{27}$$

Since $\nabla^2 v_\phi = 0$, it follows that $\nabla p = 0$ and, for symmetry reasons, the pressure is constant everywhere, irrespective of the frequencies of rotation (ω_1 and ω_2) and the distance between the propellers. This means that the forces on the central propeller can only be due to skin friction and thus must be in the direction of $\hat{e}_\phi$. Since the flow field v_ϕ is independent of ϕ, the net effect of the forces due to skin friction is a torque on the propeller. The hydrodynamic interaction between the propellers therefore has no radial component. The same result was obtained in section 2.1.2 for pairs of rotating spheres based on equation 6. This analysis suggests that an effective hydrodynamic interaction will only have a component perpendicular to the direction connecting the propellers. It has been shown that this is also the case for pairs of identical dumbbells [309]. Non-identical dumbbells can, however, exert attractive or repulsive forces on each other [309].

Based on the discussion of the propeller system presented above, three different simulations were developed. In a first simulation (**Simulation 1**), hydrodynamic interactions were not considered at all. The interactions between propellers were modelled as dipolar magnetic

interactions together with a short range repulsion (for $r < r_0$), due to steric interactions and diffusion (Figure 3-12 b). In the absence of inertia, propellers are not expected to be significantly closer together than r_0 at any time and the exact functional form of the repulsive interaction should not matter much. The form of the short-range repulsion was therefore chosen in a way that the resulting differential equations could be efficiently numerically integrated.

$$\mathbf{F}(\mathbf{r}, \mathbf{m_1}, \mathbf{m_2}) = \begin{cases} \mathbf{F_{mag}} & \text{for } r > r_0 \\ \mathbf{F_{mag}} \exp(-c_1(r - r_0)^4) - \mathbf{r}\, c_2 \left(\dfrac{1}{r_0} - \dfrac{1}{r} \right) & \text{for } r < r_0 \end{cases} \tag{28}$$

Here $\mathbf{r}$ is the vector connecting two propellers, $\mathbf{m_1}$ and $\mathbf{m_2}$ are vectors denoting the magnetic moment of the two propellers, r is the norm of $\mathbf{r}$, r_0 is the distance at which short range repulsion sets in and c_1 and c_2 are constants. The magnetic dipole-dipole interaction $\mathbf{F_{mag}}$ is defined as:

$$\mathbf{F_{mag}} = \frac{1}{r^5} \left[(\mathbf{m_1} \cdot \mathbf{r})\mathbf{m_2} + (\mathbf{m_2} \cdot \mathbf{r})\mathbf{m_1} + (\mathbf{m_1} \cdot \mathbf{m_2})\mathbf{r} - \frac{5(\mathbf{m_1} \cdot \mathbf{r})(\mathbf{m_2} \cdot \mathbf{r})}{r^2} \mathbf{r} \right] \tag{29}$$

The interaction is therefore simply the magnetic dipole-dipole interaction for $r > r_0$. Prefactors $(\mu_0 / 4\pi)$ and units were dropped to simplify notation. The chosen form of the short-range repulsion transitions relatively slowly from attractive to repulsive (Figure 3-13). $\mathbf{F}$ is a continuous function of all its parameters (Figure 3-13 and Figure 3-14).
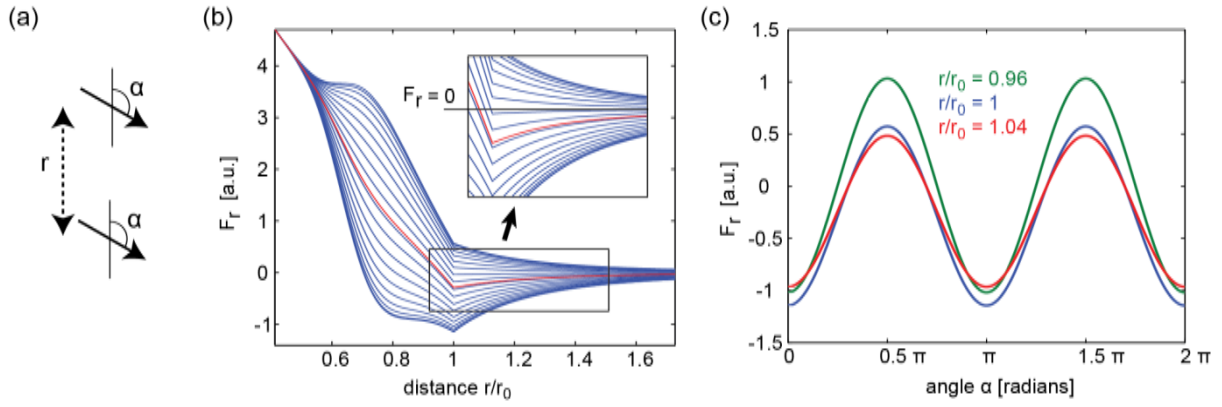
Figure 3-13: Visualization of the modeled propeller interactions. (a) Schematic illustration of the considered configuration of two magnetic dipoles. **r** is the distance between the dipoles and **α** is the rotation angle, which is the same for both dipoles. (b) The projection of the force between the dipoles on the line connecting the two dipoles is plotted against the distance, normalized by the distance at which the short range repulsion begins (r_0). Blue lines are force distance curves for different rotation angles of the dipoles. The red line is the mean force, averaged over all rotation angles. The inset shows when the force switches from attractive (negative) to repulsive (positive). (c) The dependence of the force on α is plotted for different choices of **r**. For the green line, **r** is slightly smaller than the distance r_0 at which the short range repulsion sets in. For the blue line **r** is equal to r_0 and for the red line it is slightly bigger.

Furthermore the propellers exert torques on each other, given by:

$$\tau = \mathbf{m_1} \times \left(\mathbf{r} \frac{\mathbf{m_2} \cdot \mathbf{r}}{r^5} - \frac{1}{3} \frac{\mathbf{m_2}}{r^3} \right) \tag{30}$$

In **Simulation 1**, the propeller positions as well as the magnetic moments are confined to a 2D plane. Each propeller can thus be parameterized by three parameters, two spatial coordinates (x, y) and an orientation angle (α). Since the propellers are moving in a very low Reynolds number fluid, forces are coupled linearly to changes in position:

$$\Delta x_i = \eta_t \sum_{j=1}^{n} F_x^j \, \Delta t \quad \text{for } i \neq j \tag{31}$$

$$\Delta y_i = \eta_t \sum_{j=1}^{n} F_y^j \, \Delta t \quad \text{for } i \neq j \tag{32}$$

Here n is the number of propellers in the simulation and η_t is a translational friction factor that depends on the viscosity of the fluid. Δt is a time step, so that $\frac{\Delta x}{\Delta t}$ and $\frac{\Delta y}{\Delta t}$ define velocities. Likewise torques are coupled linearly to changes in orientation.

$$\Delta\alpha_i = \left(\eta_r \sum_{j=1}^{n} \tau_z^j + \eta_r (\mathbf{m_i} \times \mathbf{B}(t))_z \right) \Delta t \quad \text{for } i \neq j \tag{33}$$

Here η_r is a rotational friction constant that depends on the viscosity of the fluid and $\frac{\Delta\alpha_i}{\Delta t}$ defines an angular velocity. $\mathbf{B}(t)$ is the time dependent external magnetic field (amplitude B_0), that is used to actuate the propellers. Together with suitable initial conditions, equations 31 to 33 define a set of coupled ordinary differential equations that can be solved by the standard Matlab solver *ode45*. Exemplary parameter settings that reproduce cluster formation are given by $c_1 = 50$, $c_2 = 8$, $|\mathbf{m}| = 1$, $r_0 = 1.2$, $\eta_t = 30$, $\eta_r = 100$ and $B_0 = 10$ (all in arbitrary units).
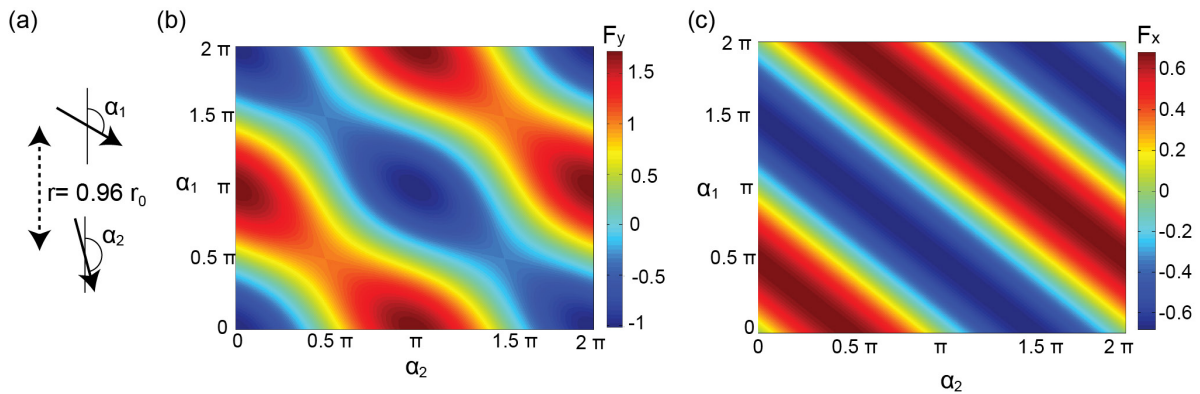
Figure 3-14: Illustration of the parameter dependence of the force model used in **Simulation 1**. (a) Schematic illustration of the considered configuration of magnetic dipoles. The distance between the propellers is slightly smaller than the distance at which the short-range repulsion sets in ($\mathbf{r} = 0.96 \, \mathbf{r_0}$). α_1 and α_2 denote the rotation angles of either dipole. (b) The dependence of the vertical (y) component of the force $\mathbf{F}$ between the dipoles as a function of the rotation angles α_1 and α_2. (c) The dependence of the horizontal (x) component of the force $\mathbf{F}$ between the dipoles as a function of the rotation angles α_1 and α_2.

In order to be able to simulate larger propeller numbers (approximately $n > 50$), the simulation described above was modified in the following ways. Torques and the actuating magnetic field were not considered explicitly anymore, since propellers rotated with the same frequency as the external field and with identical phase lags in the parameter regime that reproduced cluster formation. The variable α was thus replaced by a parameter $\alpha(t)$. In addition, a neighbor list was used to consider only the influence of propellers that were closer than a certain cutoff distance (approximately $r > 4r_0$) [310]. This second simulation (**Simulation 2**) was used to reproduce cluster formation for systems up to $n = 1600$.

A third simulation (**Simulation 3**) was implemented based on **Simulation 2** in an attempt to capture some of the hydrodynamics by introducing an effective hydrodynamic interaction. As discussed above, hydrodynamic interactions between propellers make them move as if they exerted forces on each other, perpendicular to the line connecting them (and in the 2D plane to which the propellers are confined). In **Simulation 3** the following pair-wise effective hydrodynamic interaction was chosen:

$$\mathbf{F_{hydro}} = 2\pi \frac{\omega_p}{\eta_t} \frac{(c_3 r_0)^3}{r^2} \hat{e}_\phi \tag{34}$$

Here $0 < c_3 < 0.5$, is a constant that was set equal to 0.27, which means that the no-slip boundary condition is applied for an assumed propeller radius of 0.27 r_0. ω_p is the frequency with which the propellers are rotating. This effective hydrodynamic interaction is chosen in such a way that it reproduces the expected rotational motion for pairs of rotating spheres, as described by equation 6. That this is the case can be seen by calculating the tangential velocity of the propellers $v_\perp = \eta_t \mathbf{F_{hydro}} = 2\pi\omega_p R^3/r^2$, with $R = c_3 r_0$. The tangential velocity is related to the frequency Ω with which a pair of propellers is rotating around each other as $\Omega = \frac{v_\perp}{2\pi(r/2)} = 2\omega_p \left(\frac{R}{r}\right)^3$, in accordance with equation 6. This effective hydrodynamic interaction produces movement in the simulations which is not a solution of the Stokes equations (except for two propellers), but it is a useful first approximation for the hydrodynamic interactions between many propellers.

Since an effective hydrodynamic interaction is only meaningful when averaging over several rotation cycles, the magnetic interactions were cycle averaged as well, making the magnetic interaction purely radial:

$$\mathbf{F_{mag}^{cycl}} = -\frac{m^2}{2\,r^5} \mathbf{r} \tag{35}$$

where $m = |\mathbf{m}|$. This simulation was used to reproduce cluster formation more accurately for systems with up to $n = 1600$ propellers.

3.7.3   Geometric Parameter Extraction and Random Shape Generation

Based on the reconstructed 3D shapes of propellers (see section 3.6.4) nine geometric parameters $(V, l_{max}, O, H, I, \gamma, \chi, \Psi, S)$ were extracted. (X, Y, Z) are the coordinates of voxels, where Z is the axis around which the structure rotated in experiments. The mean of the voxel coordinates (center of mass of the shape) is equal to the origin of the coordinate system. The

geometric parameters volume V, maximum voxel distance $l_{\max}$ and surface area O were calculated based on the voxels that define the shape. The surface area was defined by the number of exposed voxel faces. The surface roughness (due to cubic voxels) increased the surface area somewhat. This could be seen when calculating the sphericity of a sphere approximated with voxels, which approached a value of about 0.68 instead of 1 as expected for an actual sphere.

The handedness parameter is defined as

$$H = \sum_{i=\min Z}^{(\max Z)-1} \frac{(\vartheta_{i+1} - \vartheta_i)}{4V} \frac{(r_{i+1} + r_i)(a_{i+1} + a_i)}{n}, \tag{36}$$

where ϑ is the azimuthal angle and r the radius of the mean coordinate of an X, Y section (at $Z = i$) with area a. n is the number of X, Y sections. The handedness parameter thus measures the degree to which the angle ϑ changes between Z-sections. The change in ϑ is weighted by the mean radius, since small shape changes can lead to large changes in ϑ if r is close to zero. Furthermore, the change in ϑ is multiplied by the mean area a and divided by V in order to make H dimensionless. Figure 3-15 a provides a schematic explanation of the handedness parameter.

The inertia parameter is defined similarly as

$$I = \sum_{i=\min Z}^{\max Z} r^2 \tag{37}$$

where r is again the radius of the mean coordinate of a X, Y section (at $Z = i$).

The average width to length ratio is defined as:

$$\gamma = \sum_{i=\min Z}^{\max Z} \frac{\langle r_b \rangle}{(\max Z - \min Z)n}, \tag{38}$$

where $\langle r_b \rangle$ is the mean radius (in polar coordinates) of voxels on the boundary of a X, Y section (at $Z = i$). n is the number of X, Y sections. γ will be small for structures elongated parallel to the axis of rotation and large for structures elongated perpendicular to the axis of rotation. A schematic illustration of the parameter γ is given in Figure 3-15 b.

The chirality is defined as

$$\chi = \min \frac{V(A \cup A') - V(A \cap A')}{V(A)}, \tag{39}$$

where A defines the reconstructed shape and A' its mirror image [311]. $V(\dots)$ denotes the volume of a shape. Theoretically, χ needs to be minimized over all three rotational and all three translational degrees of freedom. This is computationally difficult for shapes with many voxels. The minimization was therefore simplified by centering both A and A' at the origin and varying only the angle around which the propeller rotated in the experiment. Due to this simplification the computed chirality measures can reach values above 1, although the chirality as defined above takes values between 0 and 1 [311]. A schematic explanation (2D case) of the chirality can be found in Figure 3-15 d.

The sphericity is defined as $\Psi = \frac{\pi^{\frac{1}{3}}(6V)^{\frac{2}{3}}}{O}$. It is one for a sphere and smaller than one for any other shape. The spikyness measure is defined as $S = V^{-\frac{1}{3}}\sqrt{\sum(X^2 + Y^2 + Z^2)}$. S is minimal for a solid sphere and maximal for a hollow sphere. S will generally be higher if the structure is elongated in one or several direction (spikes).

In total 9 geometric parameters $(V, l_{\max}, O, H, I, \gamma, \chi, \Psi, S)$ were extracted. The dimensional parameters $(V, l_{\max}, O, I)$ have dimensions of µm, µm² or µm³. Their relationship to the four measured parameters propeller length L, rotation frequency ω_p rolling speed v_x and propulsion speed v_y is analyzed in section 4.4.4.
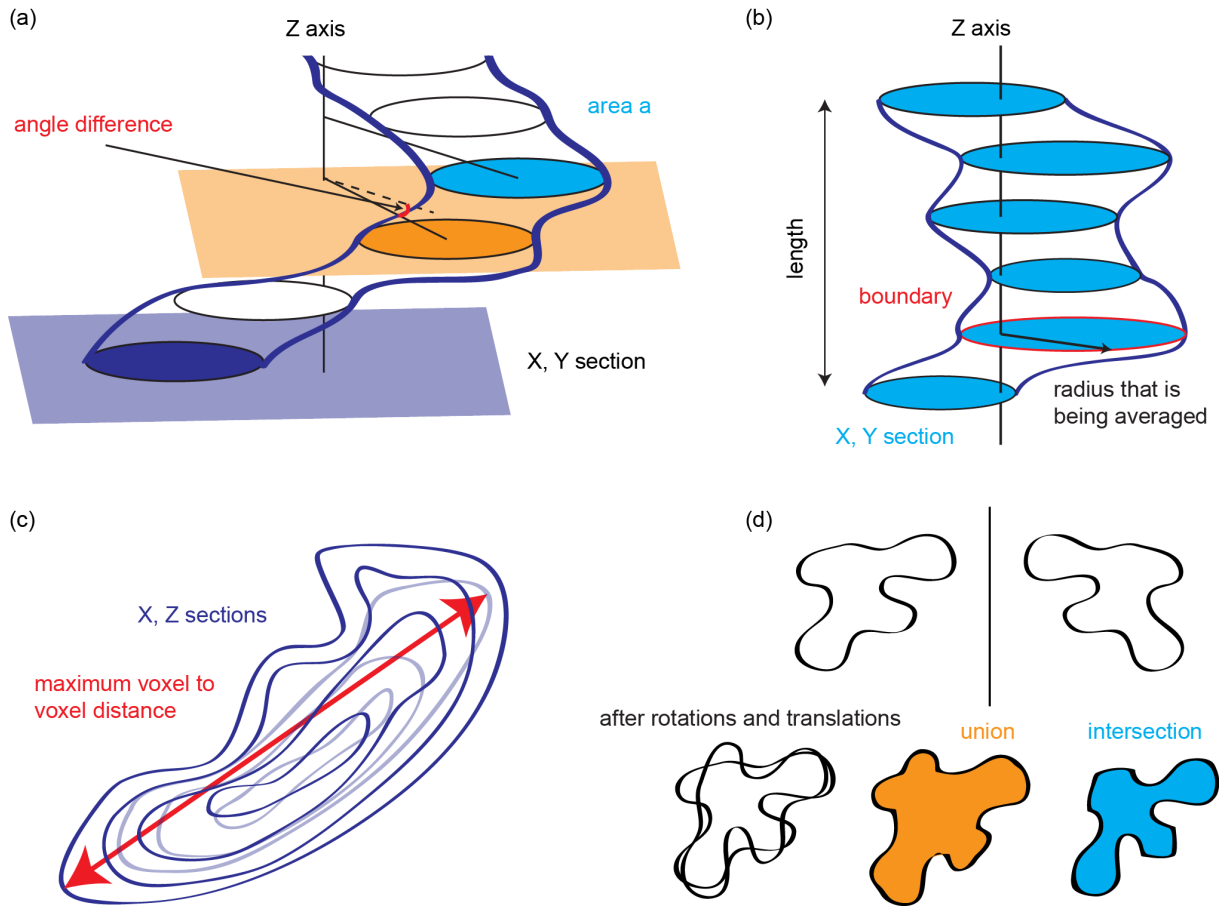
Figure 3-15: Explanatory schematics for selected geometric parameters. The axis of rotation is the Z axis. (a) The handedness parameter H is calculated based on angle differences between consecutive X, Y sections. The dashed line indicates the projection of the line connecting the Z axis and the mean voxel position in the blue X, Y section onto the previous orange X, Y section. The angle between the dashed line and the solid line in the orange X, Y section is the angle difference $(\vartheta_{i+1} - \vartheta_i)$ in equation 36. (b) The average width to length parameter γ is calculated based on the average over the mean radial values r_b of voxels at the boundary of one X, Y section. The boundary is indicated in red and the black arrow indicates r_b. (c) The maximum voxel to voxel distance l_{max} is indicated by the red arrow. The direction of l_{max} is in general not parallel to X, Y or Z. (d) The chirality parameter χ is illustrated for the 2D case. The black outlined shapes are mirror images of each other. By rotation and translation these can be made to overlap. The union is indicated in orange and the intersection in blue. Based on these, a preliminary chirality parameter $\hat{\chi}$ can be calculated. The shapes now need to be further rotated and translated in order to find the minimal value of $\hat{\chi}$, which is χ.

To test whether the synthesized shapes are random, the distributions of the geometric parameters were compared to those of random shapes (see section 4.4.1), which were generated in the following way. First, a sphere of radius $r_0 = 20 \times \xi_1 + 2$ is placed in the origin ($\mathbf{x}_0 = (0,0,0)$) of an orthogonal coordinate system (x, y, z). Here, ξ_i are random variables drawn from the uniform distribution on $[0,1]$. Then new spheres are added at

positions $\mathbf{x}_i = \mathbf{x}_{i-1} + 40\,(\xi_2, \xi_3, \xi_4) - 20\,(1,1,1)$ in a stepwise manner. The process of adding spheres is continued while $\xi_5 < t$, where t is a threshold parameter that starts at 0.001 and is increased by 0.001 in every step. The radii of new spheres are chosen so that they just touch the nearest sphere, which is not necessarily the latest created. If the new radius was larger than 5 voxels, the new sphere would be added to the shape. Otherwise the algorithm goes to the next sphere addition step without adding a sphere in this step. Exemplary shapes created by the described random process are displayed in Figure 3-16.
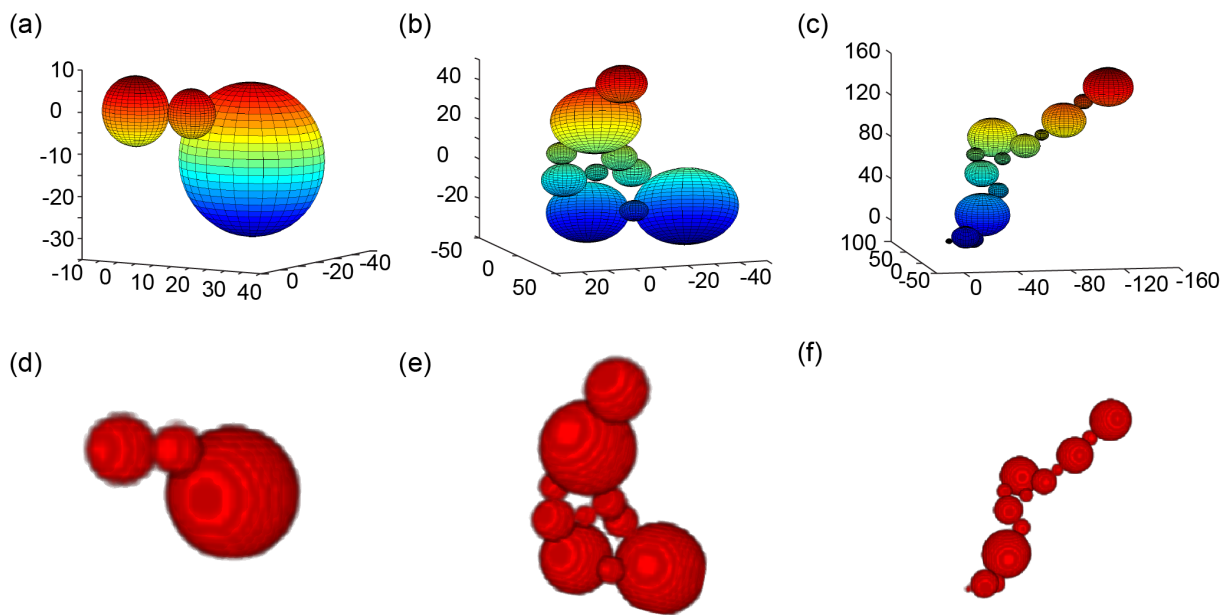
Figure 3-16: Exemplary artificial shapes from random process. (a-c) Visualization of shapes based on sphere center positions and radii. (e-f) The same shapes are visualized again after approximating the spheres by voxels and saving them in the same format as the reconstructed 3D shapes.

3.8   Inconclusive Experiments and Methods

The experiments and methods reported in this section are, as can be guessed, only a selection of failed, inconclusive or abandoned projects and procedures. The presented selection is based on its anticipated potential usefulness for future research efforts along similar lines.

3.8.1   Magnetosome Functionalization

Magnetosomes are organelles which magnetotactic bacteria use for the bio-synthesis of magnetic nanoparticles [312]. Essentially a magnetosome is a magnetic nanoparticle

surrounded by a protein-containing lipid membrane [101]. Magnetosomes can be isolated from magnetotactic bacteria [313, 314] and functionalized [315, 316]. Specifically, Ceyhan et al. were able to bind gold nanoparticles to the lipid membrane of the magnetosome, by either incorporating a biotinylated lipid, or coupling NHS-biotin to amine groups in the membrane proteins [316].

It was attempted to reproduce these results in order to subsequently study the assembly of these nanostructures under the influence of external magnetic fields. The gold nanoparticles might have allowed the imaging of single magnetosomes in dark field microscopy and, potentially, distance changes between the gold nanoparticles could have been observed by using the gold nanoparticles as plasmon rulers [317].

In a typical synthesis, 5 μl of magnetosome solution was incubated with 80 μl freshly prepared 22.5 mM NHS-biotin solution (in buffer E (10 mM HEPES, 1 mM EDTA, pH 7.4), EZ-Link Sulfo-NHS-LC-Biotin) at room temperature for 1 h with gentle agitation. The magnetosomes were then washed five times with 100 μl of buffer E, using magnetic separation, and resuspended in 20 μl of buffer E. Then 40 μl of a solution of Streptavidin coated 40 nm gold nanoparticles (BBInternational) was added yielding a final gold nanoparticle concentration of about 1 nM. This was incubated for about 3 h at room temperature. The reaction was quenched by addition of 30 μl NHS-biotin solution and the result washed five times with 100 μl buffer E using magnetic separation. TEM images of the gold nanoparticles, the magnetosomes and the reaction products can be seen in Figure 3-17. Distinguishing the gold nanoparticles from the magnetosomes proved very difficult in the absence of a clear size difference. Due to the fact that the potentially functionalized magnetosomes were still aggregating, trying to assemble them into well-defined structures using magnetic fields seemed not very promising. The project was abandoned after many protocol variations and the tentative application of magnetic fields during the synthesis did not improve the situation. Among the factors hindering these experiments were the difficulties to obtain reasonably clean (free of bacterial residues) magnetosomes and the magnetic forces between them, leading to aggregation. Since a dark-field microscope was not available at the time, it was not possible to check for the presence of gold nanoparticles using optical microscopy.
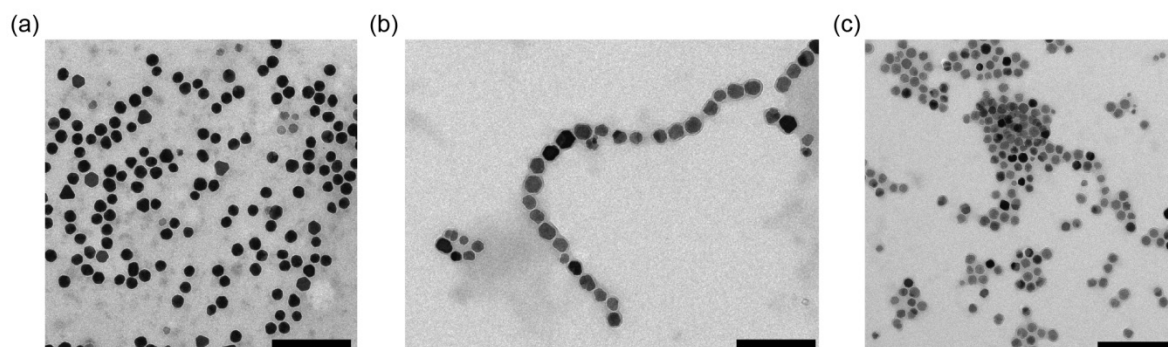
Figure 3-17: (a) Streptavidin coated gold nanoparticles. Triangular shape is common, but highly untypical for magnetosomes. This could offer a possibility for differentiation between gold nanoparticles and magnetosomes. (b) Isolated magnetosomes from *Magnetospirillum gryphiswaldense*. (c) Result of labeling experiment, after magnetic separation. Magnetosomes are most likely present due to the magnetic response. Gold nanoparticles might also be present, either due to successful functionalization or non-specific aggregation. Scale bars are 300 nm, the scale is the same in all three panels.

Magnetosome functionalization with lipids could nonetheless be successfully reproduced using the protocol reported by Ceyhan et al. [316]. In a typical synthesis 80 µl of Magnetosome solution was washed by diluting it in 400 µl of buffer H (10 mM HEPES, pH 7.5) and subsequently reducing the volume to 40 µl using magnetic separation. 200 µl of a 5.3 mM solution of biotinylated lipids (1,2-dipalmitoyl-sn-glycero-3-phosphoethanolamine-N-(biotinyl), Avanti Polar Lipids) dissolved in buffer H was added and incubated over night at room temperature. The result was washed four times with 400 µl of buffer H using magnetic separation and finally resuspended in 200 µl of buffer H. Then 20 µl of a 8.3 mM Streptavidin-FITC solution was added and incubated for one hour at room temperature. The magnetosomes were then washed as before, twice with 400 µl of buffer H. For visualization in the fluorescence microscope, the solution was diluted 10 times (Figure 3-18 a). As a control the magnetosomes were incubated with Streptavidin FITC without prior lipid functionalization, yielding a non-fluorescent product. Attempts to bind gold nanoparticles to the lipid functionalized magnetosomes remained, however, equally unsuccessful or inconclusive (Figure 3-18 b).
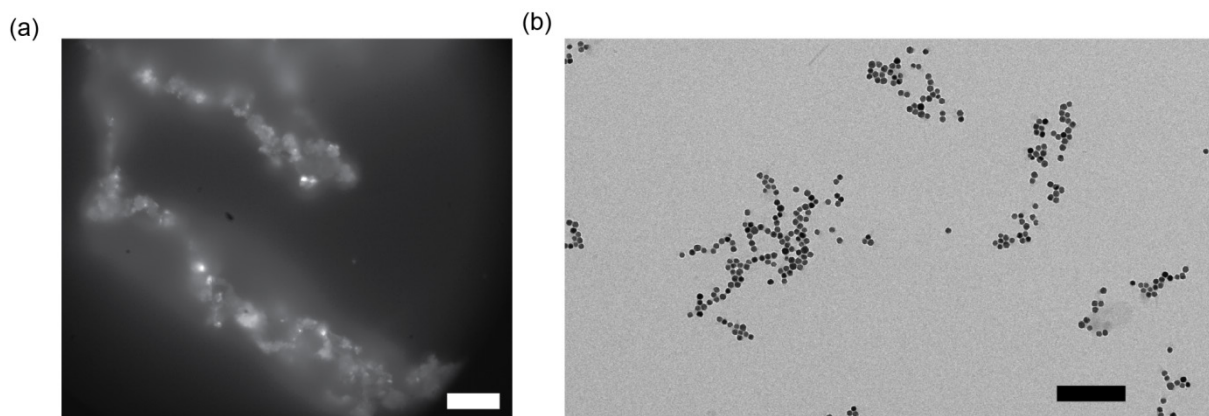
Figure 3-18: (a) Magnetosomes were successfully fluorescently labeled as described in the main text. Scale bar is 20 μm. (b) Incubating functionalized magnetosomes with gold nanoparticles, did not seem to result in efficient binding. Scale bar is 500 nm.

3.8.2 Hydrothermal Carbonization of Magnetotactic Bacteria

Magnetotactic bacteria are fascinating organisms which exert precise control over the synthesis and the arrangement of magnetic iron-oxide nanoparticles [318]. Since the magnetic nanoparticles are already organized in chain-like structures and enclosed by the bacteria, it was hypothesized that the hydrothermal carbonization of magnetotactic bacteria could lead to the formation of interesting nanostructures. Magnetotactic bacteria (*Magnetospirillum gryphiswaldense* kindly provided by Agata Olszewska, Department of Biomaterials, MPIKG) were diluted in deionized water and filled into a 20 ml autoclave without further additives. Residues of the growth medium were, however, most likely present. The autoclave was then put in an oven and heated to 180 °C for 24 h. The reaction products were washed and characterized using TEM and SEM (Figure 3-19). Rod-like structures, vaguely reminiscent of magnetotactic bacteria (though smaller) were observed. The magnetic nanoparticles seemed to have predominantly lost their chainlike arrangement. Interestingly the resulting structures looked qualitatively different from the structures obtained when performing HTC on synthetic magnetic nanoparticles in a glucose solution (Figure 4-1). Further experiments along these lines were not conducted, due to the limited availability of relatively large quantities of magnetotactic bacteria.
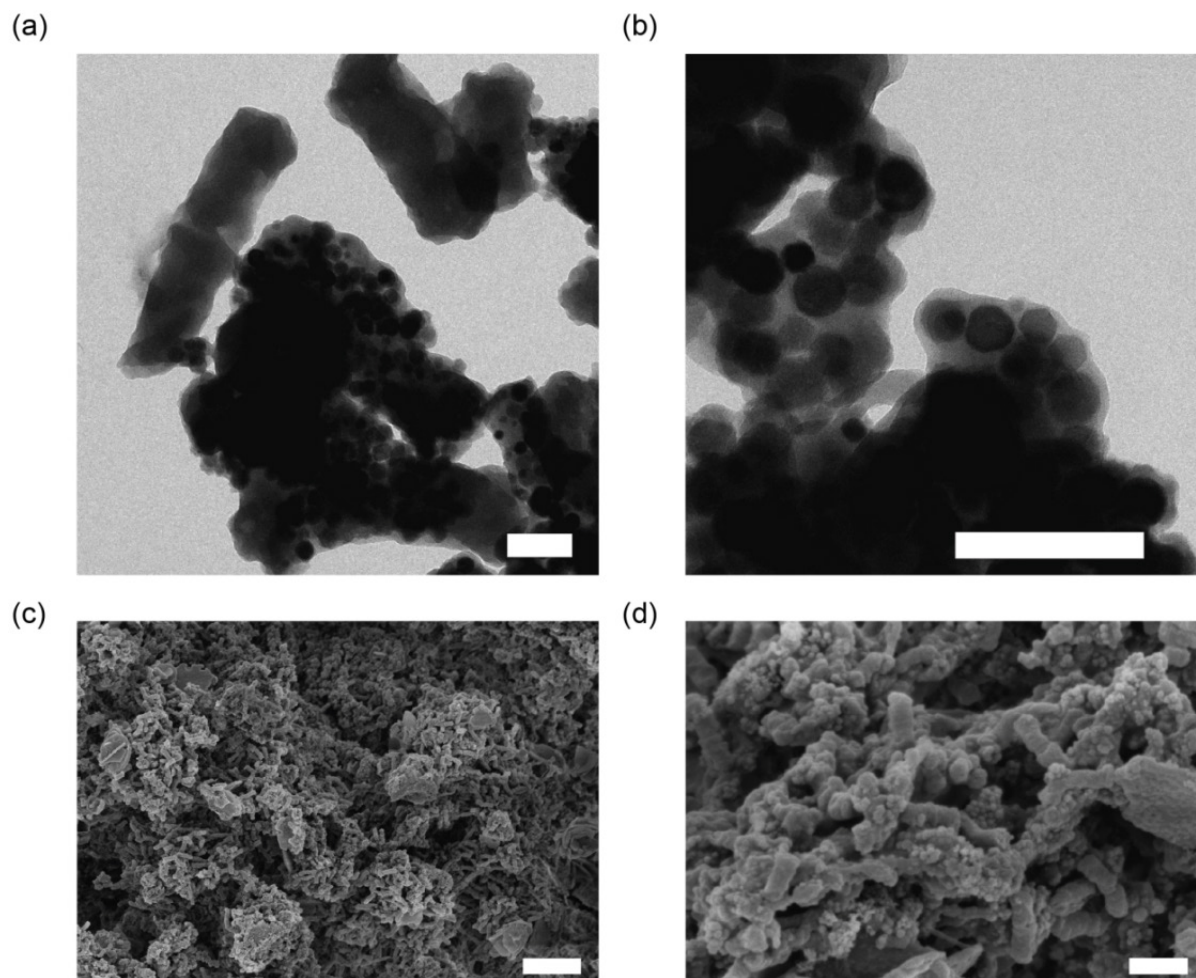
Figure 3-19: TEM images of magnetotactic bacteria after HTC. (a) Rodlike carbon structures and aggregates of carbon coated magnetosomes are reminiscent of the shape of magnetotactic bacteria. Scale bar is 200 nm. (b) At higher magnification, the carbon coating can be clearly seen. Scale bar is 200 nm. (c) The rodlike structures are also visible in SEM. Scale bar is 3 μm. (d) Scale bar is 600 nm.

3.8.3   Effect of Magnetic Fields on Synthesis or Coating

The effect of external magnetic fields on the assembly of magnetic structures has been investigated in many studies (see section 2.4.1). Influencing the organization of magnetic nanoparticles at elevated temperatures (e.g. 200 °C for HTC treatment) is more difficult, since higher magnetic fields might be needed to counteract the effects of increased thermal noise.

Even at these high temperatures, magnetic interactions between the nanoparticles seem to be the driving force behind chain-like arrangements of carbon coated magnetic nanostructures (see Figure 3-20 a and Figure 4-1). This was experimentally verified in a study by Zhang et al. by performing the HTC reaction in an alternating magnetic field (3.5 mT, 50 Hz), which reportedly prevented the formation of chain-like structures due to the disruption of dipolar

inter-particle interactions [236]. Since it was apparently possible to influence reaction outcomes using an external magnetic field, it was attempted to increase the formation of chain-like assemblies by the application of a constant, homogenous magnetic field. To this end a solenoid was built using Teflon wire, inside which the autoclave could be placed. The solenoid and the autoclave could then be placed in an oven, where the Teflon wires would lead out of the oven to a power supply. Experiments were typically conducted at field strengths of 5-6 mT. The initial field was higher though, since the voltage was adjusted so that the field fell to 5-6 mT when the temperature of the solenoid reached 200 °C. The field was also applied during the cooling of the reaction products to room temperatures and during the drying of samples onto the TEM grids, but not during the washing of the reaction products.
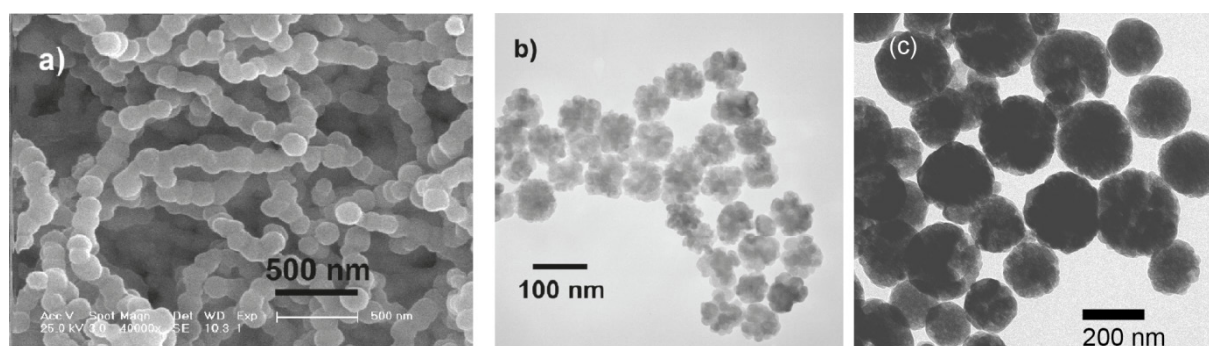
Figure 3-20: (a) Chain-like structures obtained by Zhang et al., using hydrothermal carbonization of magnetic nanoparticles synthesized by a hydrothermal method. (b) Magnetic nanoparticles synthesized by Zhang et al. prior to treatment with hydrothermal carbonization. (c) Nanoparticles obtained in collaboration with Nicolas Brun (Department of Colloid Chemistry, MPIKG). Panels (a) and (b) adapted with permission from „Assembly of Magnetic Nanospheres into One-Dimensional Nanostructured Carbon Hybrid Materials" Zhongbo Zhang, Haifeng Duan, Shenghai Li, and Yingjie Lin, Langmuir 2010 26 (9), 6676-6680. Copyright 2010 American Chemical Society.

Unfortunately, no effect of the external magnetic field on the reaction products could be observed. Nanoparticles used in these experiments were either purchased from Alfa Aesar (see section 3.1), or synthesized as described by Zhang et al. in collaboration with Nicolas Brun (see Figure 3-20 b, c).

3.8.4 Silver and Silica Coatings

Besides hydrothermal carbonization, other methods to coat magnetic nanoparticles were investigated as well. Silica had been used before to coat magnetic iron oxide nanoparticles [319-321]. In a typical synthesis NanoArc iron-oxide nanoparticles were dispersed in 30 ml

ethanol, with 9.9 ml of deionized water and 0.84 ml Ammonium hydroxide (25 % by volume). After sonication for 15 minutes, 6.9 ml of TEOS solution was added by dropwise addition. A magnetic fraction could be magnetically separated. TEM images of the magnetic, as well as the non-magnetic fraction are shown in Figure 3-21. Like HTC, the silica coating fixed the magnetic nanoparticles into aggregates of apparently random shape. Various attempts to influence the structure formation using external magnetic fields failed. However, it was possible to use these structures as propellers, similar to the structures resulting from hydrothermal carbonization. Interestingly, such actuation was not possible for silica coated magnetotactic bacteria [322]. It was not investigated, whether the silica coated structures differ in their hydrodynamic or colloidal behavior from the HTC structures.
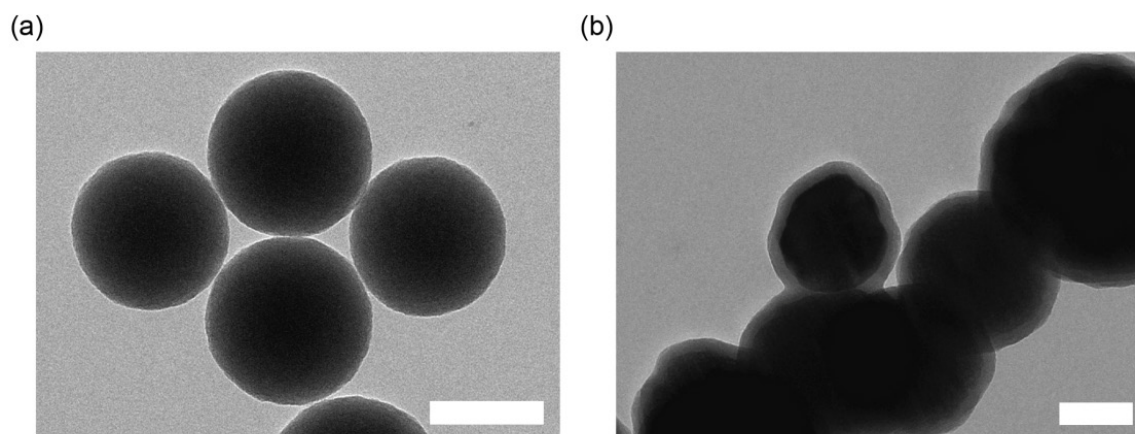
Figure 3-21: (a) TEM images of Silica beads from non-magnetic fraction of silica coating synthesis products. (b) TEM images of magnetic fraction of silica coating synthesis products. A coating around the magnetic particles is clearly visible. Scale bars are 100 nm.

Magnetic nanoparticles coated with silver [323, 324] or attached to silver nanoparticles had been produced previously [325-327]. In the experiments here larger silver nanostructures were connected to magnetic nanoparticles. In a typical experiment 1 mg of NanoArc iron-oxide nanoparticles was dispersed in 20 ml deionized water and 74 µl of 0.13 M glucose solution was added and mixed for 1 min. Then 5 ml of 1.85 mM AgNO$_3$ solution was added fast, by injecting it into the solution with a needle, to ensure immediate mixing. The solution was subsequently incubated for 45 minutes in a 5 mT magnetic field. A magnetic fraction was separated using magnetic separation and imaged in the TEM (Figure 3-22). The silver did not nicely coat the magnetic nanoparticles, but seemed to be attached to them somehow, due to the fact that silver was present in the magnetically separated phase. No effect of the application of an external magnetic field could, however, be observed.

(a)

(b)
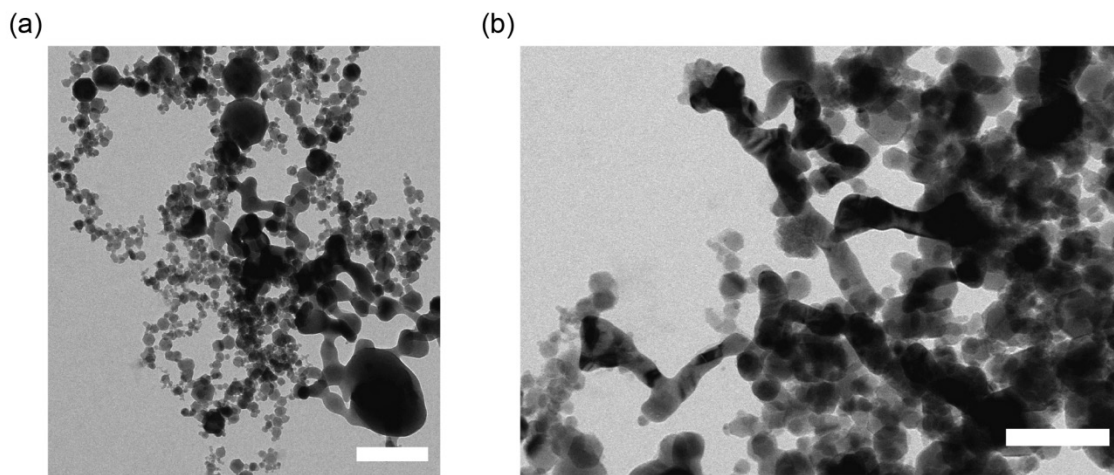
Figure 3-22: TEM images of the reaction product of silver coating experiments. (a) Iron oxide particles are visible as small greyish particles. The larger more rounded shapes are most likely silver structures. Scale bar is 200 nm. (b) The silver structures seem to be somewhat connected to the iron oxide particles, but a homogenous coating is clearly not achieved. Scale bar is 100 nm.

4.   Results and Discussion

4.1   Material Characterization of Synthesized Nanostructures

This section was partially adapted from [116] as well as a submitted manuscript. The synthesized nanostructures (see section 3.1) appear brownish to black when dispersed in solution. They can easily be dispersed by flow mixing (pipetting up and down) or using an ultrasound bath in polar liquids, like water or ethanol. For salt solutions, the ionic strength needs to be sufficiently low to avoid aggregation. The structures are magnetic and can be quickly separated from the solution by holding a permanent magnet next to a sample. No changes in material characteristics were observed even after many months of storage at room temperature.

4.1.1   Electron Microscopy

The nanostructure of the synthesized material was investigated using electron microscopy (see section 3.3.1). A carbon coating surrounding the magnetic nanoparticles is visible in TEM as well as SEM (Figure 4-1). The magnetic nanoparticles are partially organized in chain-like structures, probably due to magnetic interactions between the nanoparticles. The organization into chain-like structures happens only on the local level of a few nanoparticles, leading to complex interconnected shapes of chain-like structures pointing in different directions and more globular aggregates. To ensure that the observed carbon coating was not an imaging artefact, TEM images before and after HTC were compared (Figure 4-2). The carbon coating is only visible after treating the nanoparticles with HTC.
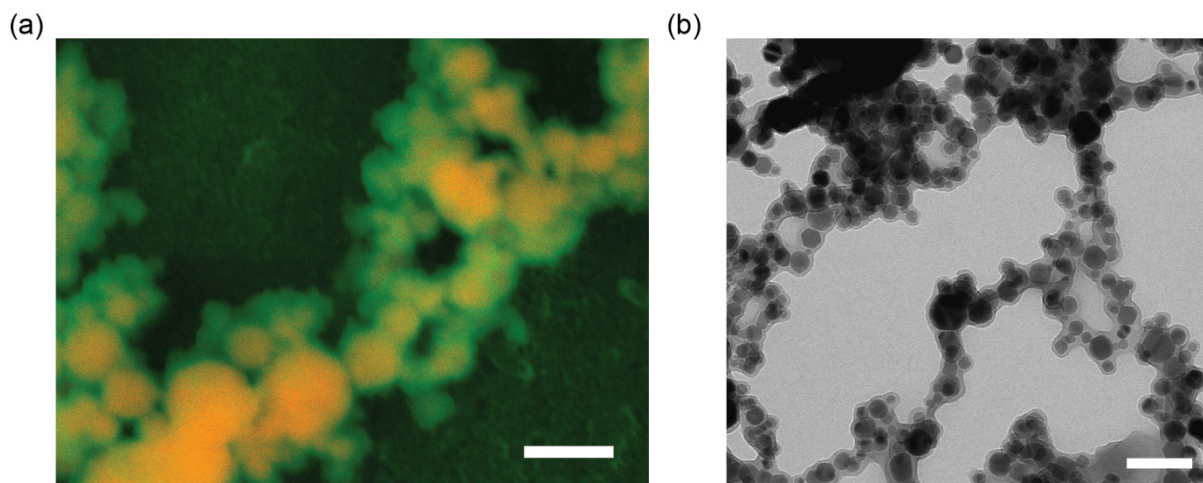
Figure 4-1: Characterization of the as-synthesized material by electron microscopy. (a) Overlay image of the back-scattered signal (orange) and the secondary electron signal (green). The iron in the iron oxide particles gives a strong back-scattered signal, while the carbon coating can be seen in green. (b) Transmission electron microscopy image of the material. The iron oxide particles can be clearly seen inside the carbon coating. Scale bars are 100 nm. This figure is part of a submitted manuscript.
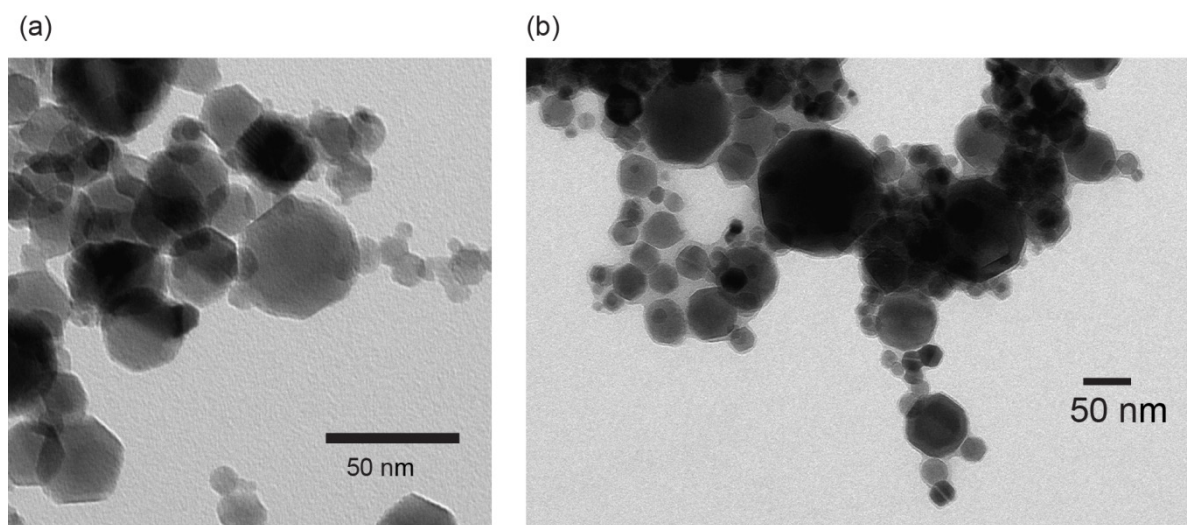
Figure 4-2: (a) Transmission electron microscopy image of untreated NanoArc iron(III) oxide nanoparticles. The particles were dried onto a copper grid after suspending them in deionized water. (b) Transmission electron microscopy image of NanoArc iron(III) oxide nanoparticles after HTC treatment as described in section 3.1. The carbon coating is visible, especially in comparison with the untreated nanoparticles in panel (a). Adapted from [116]. This is an unofficial adaptation of an article that appeared in an ACS publication. ACS has not endorsed the content of this adaptation or the context of its use.

4.1.2 Energy-dispersive X-ray Spectroscopy

The elemental composition of the synthesized nanostructures was investigated using energy-dispersive x-ray spectroscopy (EDX) (see section 3.3.2). The results are displayed in Figure 4-3. As expected, the synthesized nanostructures contain iron, oxygen and carbon. This is consistent with the synthesized nanostructures consisting of iron-oxide nanoparticles coated with hydrothermal carbon. The hydrothermal carbon probably contains also residual oxygen and hydrogen (which is not visible in EDX). The synthesized nanostructures thus do not seem to contain any unexpected contaminations.
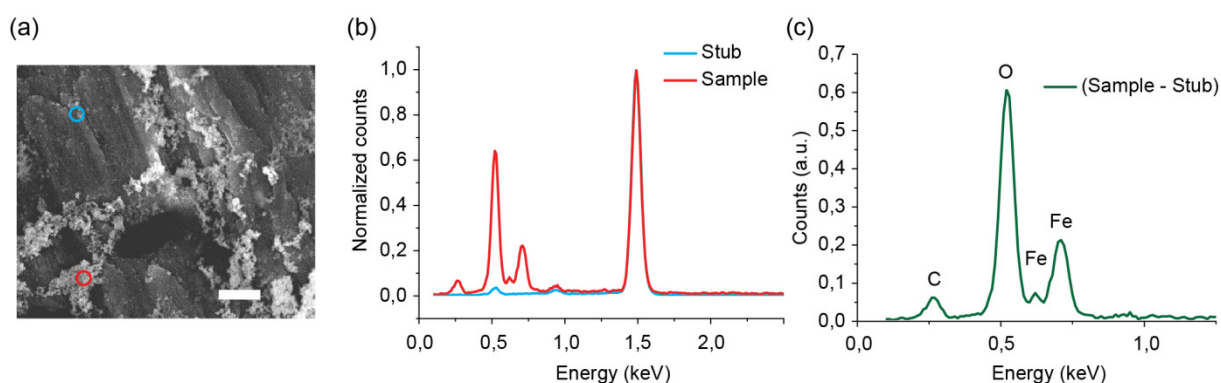
Figure 4-3: (a) Secondary electron image of as-synthesized nanostructures dried onto an aluminum stub in a 100 Hz, 1mT rotating magnetic field. The blue circle marks the spot where an EDX measurement was performed on the stub. The red circle marks the spot where an EDX measurement was performed on the synthesized nanostructures. The scale bar is 1 μm. (b) The two EDX spectra of the stub (blue) and the nanostructures (red) were normalized by their maximum value (peak due to aluminum). (c) The difference between the normalized stub spectrum and the normalized nanostructure spectrum is plotted. This figure is part of a submitted manuscript.

4.1.3 Carbon Coating can be Functionalized

Carboxyl groups on the HTC carbon can be used to functionalize the synthesized magnetic nanostructures. This was demonstrated by fluorescently labeling the nanostructures (see section 3.4.3). Fluorescence and bright-field images were compared for a fluorescently labeled structure and it was shown that the labeled structure was still able to propel parallel to the lower capillary surface as well as upwards against gravity (Figure 4-4).
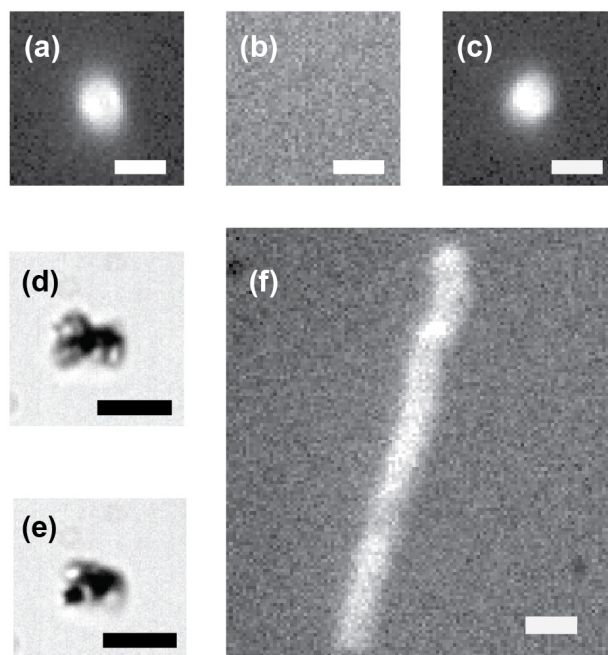
Figure 4-4: (a) Fluorescence image of a labeled propeller moving towards the upper inner surface of a glass capillary, actuated by a magnetic field of 1 mT rotating at 50 Hz. (b) When the magnetic field is switched off, the same propeller falls out of focus and the fluorescence disappears. (c) When the field is switched back on, this propeller returns to the upper inner surface of the capillary and is visible again. Panels (d) and (e) show brightfield images of the propeller in different orientations. Panel (f) shows the movement of this propeller along the lower surface of the capillary during 7 seconds exposure time. Scale bars are 4 μm. Adapted from [116]. This is an unofficial adaptation of an article that appeared in an ACS publication. ACS has not endorsed the content of this adaptation or the context of its use.

4.1.4 Discussion

The ability to functionalize the synthesized nanostructures as demonstrated by fluorescent labeling is important for potential applications.

Besides for magnetic actuation, carbon coated iron oxide nanostructures are promising for a broad range of applications (see also section 3.1). Similar magnetic nanomaterials have been used for water treatment [328, 329], for the triggered release of chemical species [330], for medical applications [331], as catalyst supports [80] and for lithium ion batteries [293, 296, 332, 333]. The ability to functionalize the synthesized nanostructures, as demonstrated by fluorescent labeling, is important for such applications. The fact that these structures can be actuated by external magnetic fields (see section 4.2) can allow the assembly of nanostructures into organized superstructures (see section 4.6). These superstructures might

then be tailored to the requirements of particular applications. This makes studying the magnetic actuation of this material particularly promising.

4.2 Versatile Maneuverability of Synthesized Structures

This section was partially adapted from a submitted manuscript. While it is often useful to categorize microscopic actuators as propellers, rollers or swimmers (see section 2.2), it is in fact possible to reproduce all three modes of actuation using the synthesized magnetic nanostructures described in section 4.1. The variability in this ensemble of shapes enables the versatile magnetic actuation, but also leads different structures to move with different speeds. Due to the possibility to actuate and steer the structures, those with desirable properties can be selected in a straight-forward manner from the pool of synthesized aggregates (see section 3.5.1).

4.2.1 All Types of Hydrodynamic Actuation can be Reproduced

It is possible to use the synthesized nanostructures as propellers, by actuating the aggregates with rotating magnetic fields. An example of a rotating magnetic field is shown in Figure 2-3 b. The random shape of the particles makes them sufficiently asymmetric, which leads to a hydrodynamic coupling between rotation and translation. The propellers move approximately parallel to the vector of rotation of the magnetic field (Figure 4-5 a,b). Deviations from a straight line are apparent and due to diffusion, which is superimposed on the linear movement of the propeller (see section 4.3.5). The average propulsion speed was measured as 3.8 μm × s^{-1} when actuating structures at 20 Hz. The structures had an average size of around 6.3 μm and were used as synthesized, without selection (see section 4.4.2).
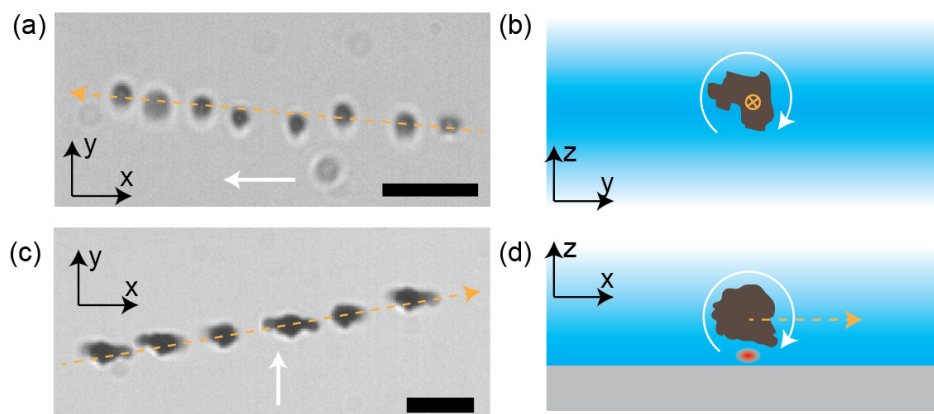
Figure 4-5: (a) Time-lapse image of propulsion. A particle is rotated in bulk liquid by a rotating magnetic field. The images are overlaid in 0.52 s intervals. The x, y, z directions form a right-handed orthogonal coordinate system. (b) Schematic illustrating the propulsion mechanism. The view is rotated with respect to panel (a). Propulsion is achieved due to the hydrodynamic coupling between rotation and translation. (c) Time-lapse image of rolling movement. Images are overlaid in 0.32 s intervals. (d) Schematic illustrating the rolling mechanism. The actuated magnetic structure is pulled towards a glass surface (grey area) by gravity. The red dot marks a region in the fluid that experiences higher shear, due to the vicinity of two no-slip boundaries. The imbalance between shear forces below and above the propeller leads to translation. Images are cut from videos recorded at 50 frames per second. The white arrows indicate the vectors of rotation of the rotating magnetic fields (right hand rule). The dashed orange arrows indicate the directions of motion. Scale bars are 5 µm. This figure is part of a submitted manuscript.

Rolling motion is achieved also by the application of rotating magnetic fields, like those used for propulsion. However, in this case, the structures need to be close to an interface, which is easily achieved by sedimentation. The movement due to the rolling effect (Figure 4-5 d) is perpendicular to the vector of rotation of the magnetic field (Figure 4-5 c). Depending on the strength of the hydrodynamic coupling between rotation and translation, the direction of movement will have a smaller or larger component parallel to the vector of rotation of the magnetic field. When actuated with a 20 Hz rotating field the average rolling speed is around 7.2 µm × s^{-1} (at a mean size of around 6.3 µm). Again the structures were used as synthesized without selection (see section 4.4.2).

Finally, swimming motion can be achieved by actuating a flexible structure with a magnetic field that would induce reciprocal motion in a rigid structure. An example of such a magnetic field is shown in Figure 2-3 a. The individual aggregates are sufficiently stiff not to be bent by magnetic actuation and hydrodynamic forces. Individual aggregates thus cannot be used as swimmers. Several aggregates can, however, be assembled into a chain-like structure by applying a constant magnetic field first (see section 3.5.5). Since the individual aggregates in

the chain-like assembly are not identical, symmetry breaking is immediately achieved. A high-speed camera was used to image the deformations induced in an exemplary chain-like assembly (Figure 4-6 a). The chain-like assembly goes through these deformations repeatedly, which leads to translatory movement along a linear trajectory (Figure 4-6 b).

4.2.2 Self-assembled Swimmers can Move in Arbitrary Directions

Typically such swimming movements have been described as a bending wave traveling along a filament [9, 182]. In this framework, it would be expected that the structure moves parallel to its long axis. Here it is observed, however, that different chain-like assemblies can move in seemingly arbitrary directions while being actuated by the same magnetic field (Figure 4-6 c-f). The self-assembled swimmers (Figure 4-6 b-e) move with 3.5 µm × s^{-1}, 2.1 µm × s^{-1}, 1.8 µm × s^{-1} and 1.6 µm × s^{-1} respectively. A particular chain-like assembly will move along a linear trajectory persistently, but the direction of movement can be different for different assemblies. This shows that the chain-like assemblies are not moving erratically, but are continuously repeating a particular set of deformations.
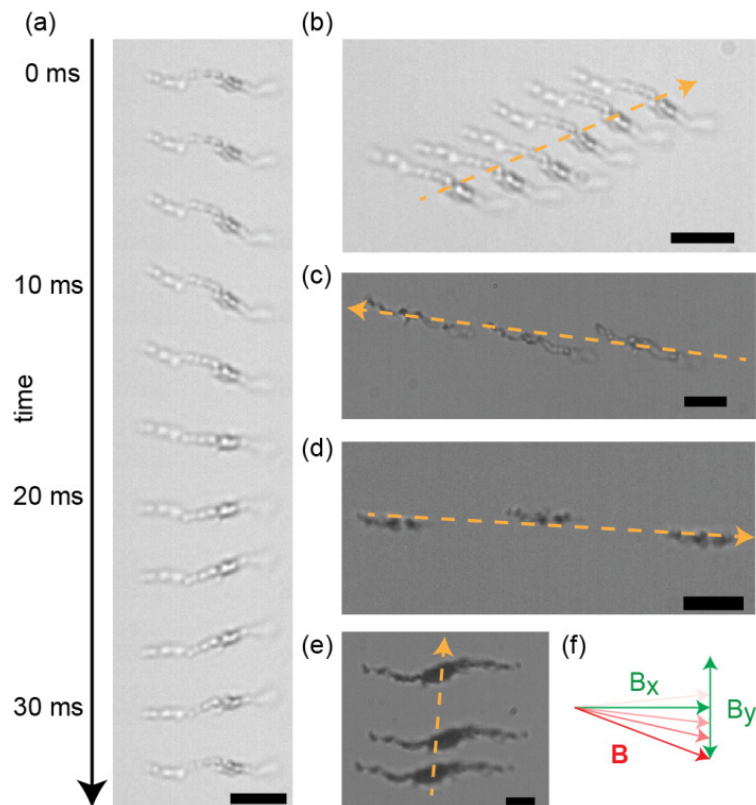
Figure 4-6: Self-assembled swimmers form and start moving under the influence of a time-reversible actuating field. The x-component (horizontal) of the field has constant field strength and the y-component (vertical) is sinusoidal with a frequency of 30 Hz. (a) Sequential shape and orientation changes of a self-assembled swimmer. Images are cut from a video recorded at 600 frames per second. (b) Time-lapse image of the movement of the self-assembled swimmer from (a). The field strengths are 2 mT and 1 mT along the x and y directions respectively. Images are overlaid in 1 s intervals. (c) A different self-assembled swimmer is moving in the same field as (b). Images are overlaid in 7 s intervals. (d) Another self-assembled swimmer is actuated by a different field. The field strengths are 1 mT and 2 mT along the x and y directions respectively. Images are overlaid in 6.4 s intervals. (e) Another self-assembled swimmer is moved by the same field as (e). Images are overlaid in 10 s intervals. (f) Schematic representation of the applied fields. The dashed orange arrows indicate the directions of the movements. The scale bars are 5 μm. This figure is part of a submitted manuscript.

4.2.3 Discussion

The obtained different chain-like assemblies demonstrated for the first time that chain-like assemblies do not necessarily move in the direction of their long-axis. It seems that all previously published microscopic flexible swimmers moved along their long axis, usually by means of a bending wave [9, 133-138]. From a theoretical standpoint, it has been known for a long time that the direction of movement of a swimmer is determined by the cyclic deformation it undergoes and that this movement does not need to be parallel to the long axis of a chain-like swimmer [139]. Such modes of swimming have been investigated theoretically, but so far not realized in experiments [334, 335]. Based on the deformation cycles visualized in the recorded high-speed videos, future work could compare the observed swimming to hydrodynamic simulations.

In general, the magnetic nanostructures used in this study have several properties, which seem to be essential for the reported reproduction of all three types of magnetic actuation. First the material has a sufficiently high volume magnetization to be actuated by weak external magnetic fields (1-2 mT), but the magnetization is not so high as to lead to irreversible aggregation due to inter-particle forces. Secondly, the carbon coating fixes the structures into aggregates of varied shapes, which can resist hydrodynamic shear and lead to the hydrodynamic coupling between rotation and translation. The carbon coating also passivates individual structures, so that the surfaces of different aggregates repel each other and aggregation due to van-der-Waals or electrostatic interactions is avoided. This is particularly important for the self-assembly of chain-like swimmers. The chain-like assemblies are indeed held together by magnetic interactions, but the short range repulsion that avoids aggregation keeps the assemblies flexible, so that cyclic deformations can lead to swimming.

The finding that all three types of magnetic actuation for microscopic devices in liquid can be realized using a single type of nanostructured magnetic material demonstrates that precise control over the shape of magnetic actuators is not a prerequisite for obtaining movement. In contrast, variety of shapes can lead to versatile possibilities for actuation. The shape of micro- and nanorobots could thus be tailored to other requirements (e.g. manipulation and sensing capabilities or ease of fabrication) without compromising the ability to power and steer such devices with external magnetic fields.

4.3   Self-assembled Nanopropellers

This section was partially adapted from [116].

4.3.1   Size Distribution Depends on Actuating Field

The as-synthesized propellers have a broad size distribution, ranging from about 0.3 µm to about 20 µm. The size distribution of selected propellers is different and depends on the actuating field. Which fields need to be applied to select particularly small propellers can be qualitatively understood using scaling arguments. In order to arrive at the top of the vial, a structure needs to overcome the gravitational force F_g. For steady state upwards movement the force balance is $F_H = F_D + F_g$, where F_H is the force arising from the rotation-translation coupling and F_D is the fluid drag. F_H can be estimated based on the fact that it must be equal to a drag force $F_H = 6\pi\eta R_{\text{eff}}v_0$, in the absence of gravity. Here η is the dynamic viscosity of water, R_{eff} is the effective radius of Stokes' law and v_0 is the propulsion velocity of the structure in the absence of gravity. The force balance can thus be rewritten as $6\pi\eta R_{\text{eff}}(v_0 - v) = g\,\rho\,V$, where v is the speed of the structure when swimming against gravity (positive for upwards movement), g is Earth's acceleration due to gravity, ρ is the density of the structure and V its volume. The quantity $(v_0 - v)$ will thus scale approximately with R^2, where R is a length scale of the structure. This means that the reduction in propulsion speed due to gravity will be less pronounced for small structures. Therefore the selection method is already biased for the selection of small structures and does not simply select for structures with a strong rotation-translation coupling.

Furthermore, the critical frequency of a structure is expected to decrease when the structure becomes larger. This can be seen by modeling the structure as a sphere or as a cylinder. In the

case of a sphere, the critical frequency will scale like $\omega_C = \frac{BM}{c_F} \propto M_V \frac{\frac{4}{3}\pi R^3}{8\pi\eta R^3}$, where R is the radius of the sphere, η is the viscosity of the solution and M_V is the magnetization per volume. M_V is expected to increase with reduced nanopropeller size, since the magnetic moments of the individual particles will tend to align in small aggregates, but will form structures like flux closure rings in larger aggregates in order to minimize magnetic stray fields (see section 2.1.1). In this situation the magnetic moments average out, with the residual magnetization growing slower than the volume. Therefore the critical frequency decreases with increased nanopropeller size. For a cylinder with radius R and length L the critical frequency will scale approximately like $\omega_C = \frac{BM}{c_F} \propto R^2\pi L \, M_V \frac{3\ln\left(\frac{L}{2R}\right)}{\pi\eta L^3}$ [336]. Thus, the critical frequency decreases with increasing structure size (since M_V is expected to decrease) and with increasing aspect ratio $\frac{L}{R}$. This is in accordance with observations of magnetic structures in the optical microscope. Therefore, the selection bias for small structures can be increased by applying weak rotating magnetic fields of high frequencies.

This prediction was tested experimentally by optically estimating (see section 3.5.2) the sizes of propellers that arrived at the upper capillary surface. The resulting size distributions and mean sizes are displayed in Figure 4-7 a. Optical size estimation was used instead of electron microscopy due to problems with aggregation. Even at very low concentrations, propellers tended to aggregate while drying onto the sample holder for electron microscopy. Since aggregates of propellers could not be reliably distinguished from single carbon coated aggregates, the size of propellers measured using electron microscopy could only yield an upper limit. Likewise optical size estimation can also only yield an upper limit for structure sizes close to the resolution limit of the microscope (< 1 μm). The smallest propeller sizes were therefore measured with electron microscopy (Figure 4-7 b).
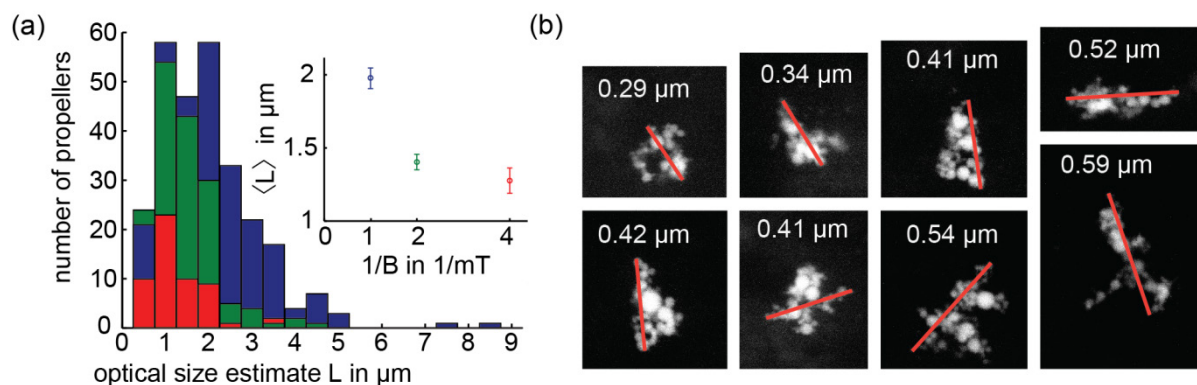
Figure 4-7: (a) Size distribution of propellers selected in different rotating magnetic fields (red 0.25 mT, green 0.5 mT, blue 1 mT, frequency always 100 Hz). Synthesized nanostructures of a fixed concentration were injected (without prior selection) into a glass capillary and subjected to a rotating magnetic field. A fixed area of the upper, inner surface of the capillary was imaged, while the rotating magnetic field was continuously applied. The histograms display the total number of structures of a particular size that were found to propel against gravity in the applied rotating magnetic field. As expected from scaling arguments, fewer larger structures can propel upwards in a weaker magnetic field. This is also apparent in the inset, where the mean size is plotted against the inverse magnetic field strength (error bars are standard error). The size estimation is based on optical images, therefore its accuracy is limited by diffraction, which is particularly apparent for nanopropellers smaller than 1 μm. (b) To study the smallest propellers, backscattered electron images were aquired of structures that were selected in a 0.5 mT, 100 Hz magnetic field. Based on the distance travelled and the duration of the selection experiment, the dimensionless speed value of a nanopropeller 1 μm in size can be estimated to be above 10, for propulsion against gravity. This minimal dimensionless speed is proportionally larger for smaller nanopropellers. Here the eight smallest observed structures are displayed. More images of nanopropellers are presented in Figure 4-8. Adapted from [116]. This is an unofficial adaptation of an article that appeared in an ACS publication. ACS has not endorsed the content of this adaptation or the context of its use.

4.3.2 Selection of Propellers Smaller than 1 μm in Every Dimension

Due to potential aggregation, measuring propeller sizes with electron microscopy yields only an upper limit. All propellers that were imaged in the electron microscope after selecting with a 0.5 mT 100 Hz actuating field are displayed in Figure 4-8. The larger structures might be aggregates, but the smallest structures are likely individual propellers. Nanopropellers down to about 0.3 μm could be selected after swimming against gravity. This was significantly smaller than any nanopropeller published at that time. Recently even smaller propellers were published [153]. These propellers could not propel in water at room temperature due to thermal noise, but were successfully actuated in a viscoelastic medium. Based on the distance traveled by the propellers in the selection experiment (~2.1 cm) and the duration of the

selection (~6 h) it can be estimated that the dimensionless speed of a 1 μm propeller is at least 10. This minimal dimensionless speed is proportionally larger for smaller nanopropellers.
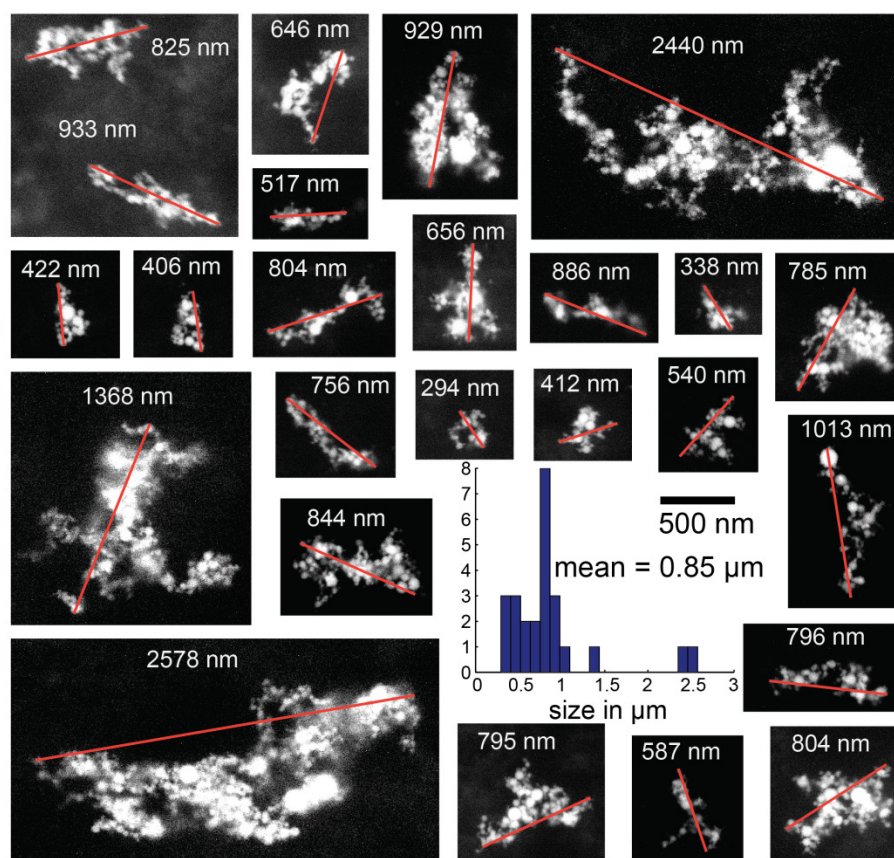
Figure 4-8: Backscattered electron images of propellers selected with a rotating magnetic field of 0.5 mT and 100 Hz. The scale is the same in all images. Aggregation of magnetic nanostructures during drying makes it hard to tell whether the larger structures are genuine propellers, or aggregates of smaller propellers that formed during drying (see two almost aggregated structures in the upper left corner). Because the aggregation during drying could not be prevented, even in extremely dilute samples and by drying the propellers in a rotating magnetic field, optical size estimation was used, as in Figure 4-7 a, in order to accurately measure size distributions and their dependence on the field strength of the actuating magnetic field. The images presented here and in Figure 4-7 were recorded using a stub, where the attached nanostructures were sparse and no very large aggregates (of propellers) were present. Adapted from [116]. This is an unofficial adaptation of an article that appeared in an ACS publication. ACS has not endorsed the content of this adaptation or the context of its use.

4.3.3 Electron Microscopy after Hydrodynamic Characterization

Due to the resolution limit of the optical microscope, it is not possible to determine the precise shape of a nanopropeller, when propulsion is visible in the optical microscope. To overcome this limitation nanopropellers were consecutively imaged in the optical microscope and the

electron microscope (see section 3.5.2). The propulsion properties of the propellers were first characterized, by tracking swimming trajectories and determining the swimming speeds at different frequencies. Electron microscopy was then used to image the nanostructure of the propellers (Figure 4-9). The nanostructures look similar to those imaged in electron microscopy after selection, but without prior observation in the optical microscope. This is further proof that the propellers that can be observed in the optical microscope are indeed the synthesized carbon coated nanostructures.
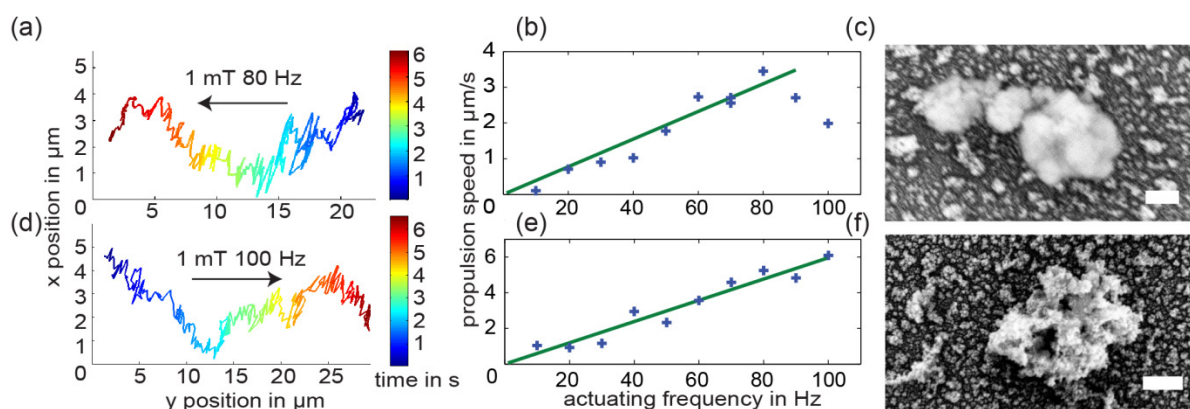
Figure 4-9: Two exemplary nanopropellers were first studied in the optical microscope. Two example traces of these measurements are displayed (a, d). The black arrows indicate the direction of the vector of rotation of the actuating magnetic field. Diffusive and translatory movements are superimposed. Speed versus frequency measurements show that the propulsion speed varies linearly with the frequency of the actuating magnetic field up to a critical frequency (around 80 Hz in (b) and above 100 Hz in (e)). Backscattered electron images of the two nanopropellers are displayed in panels (c) and (f). Scale bars are 200 nm. The dimensionless speeds are estimated from these measurements as $U = 32$ ($v = 2.7$ μm s^{-1}, $L = 1.22$ μm, $f = 70$ Hz) for the upper nanopropeller (c) and $U = 69$ ($v = 6.1$ μm s^{-1}, $L = 0.88$ μm, $f = 100$ Hz) for the lower nanopropeller (f). Adapted from [116]. This is an unofficial adaptation of an article that appeared in an ACS publication. ACS has not endorsed the content of this adaptation or the context of its use.

4.3.4 Verification of Simple Propulsion Model

A simple torque-balance model for the magnetic actuation of propellers (see section 2.2.2) predicts that the frequency speed relationship of propellers should take the form given in equation 26. The physical model used in the derivation of equation 26 is shown schematically in Figure 4-10. To verify this model experimentally, high precision speed measurements were conducted (see section 3.5.3). The propeller was actuated with fields of different field strength B and frequency ω. Then, the theoretical model was fit to the data, by adjusting the two model parameters B/ω_C and c_v (Figure 4-10).
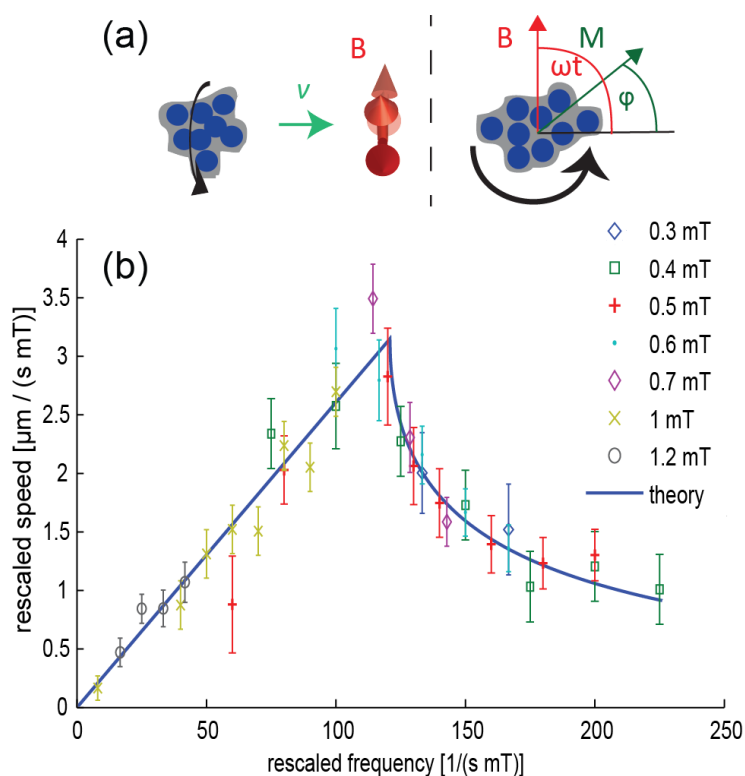
Figure 4-10: (a) Schematic illustrating the proposed theoretical model and the variables used. On the left the propulsion speed v is drawn parallel to the vector of rotation of the turning magnetic fields. The red arrows indicate a time series of magnetic field vectors. Turning this schematic out of the plane results in the schematic on the right. The magnetic field B and the magnetic moment M are indicated as well as the angle φ that is used to describe the orientation of the nanopropeller, relative to the magnetic field vector which is rotating at the frequency ω. (b) For one individual nanopropeller (imaged in Figure 3-3 i), the propulsion speed was measured at various magnetic field strengths and frequencies. The speed divided by the magnetic field strength is plotted against the frequency divided by the magnetic field strength. Error bars are based on the expected standard deviation of the end position measurement due to diffusion. The diffusion constant was measured to be $0.9~\mu\mathrm{m}^2\,\mathrm{s}^{-1}$ (see section 3.5.3). The theoretically expected curve is plotted in blue. Two parameters were determined by nonlinear regression (using the Matlab function *nlinfit*): $c_v = 26.1$ nm and $B/\omega_c = 8.27$ mT ms. This measurement is more precise than the one shown in Figure 4-9, as speed measurements could here be performed in bulk water, far away from a potentially disturbing surface. Adapted from [116]. This is an unofficial adaptation of an article that appeared in an ACS publication. ACS has not endorsed the content of this adaptation or the context of its use.

The obtained fit value $c_v = 26.1$ nm can be converted to a dimensionless speed value when making an assumption about the propeller size. Assuming the propeller size is equal to the value measured in Figure 3-3 i ($L = 0.55~\mu$m), the dimensionless speed is $U = \frac{c_v}{L} \times 1000 = 47.4$. This value is well within the range of dimensionless speeds expected for a randomly shaped propeller (see section 4.4.2). The other fit parameter $B/\omega_c = 8.27$ mT ms, can be

rewritten as $B/\omega_c = c_F/M$. Using assumptions about the shape and size of the nanopropeller, c_F can be estimated (see section 4.3.1). In the following this will be done first assuming the propeller is spherical and then again, assuming that the propeller has cylindrical shape (rotating around its short axis). After an estimate for c_F has been obtained, M can be calculated and divided by the magnetization a propeller of the same shape and size would have, if magnetized to saturation (leading to M/M_s).

Assuming the propeller is spherical this ratio is becomes: $\frac{M}{M_s} = \frac{12\,\pi\,\eta}{M_V\,(B/\omega_C)} = 1.2\,\%$. Assuming the propeller has cylindrical shape with length L and radius R (and $L/R = 5$) and rotates around an axis perpendicular to (and in the middle of) its long axis, the ratio becomes: $\frac{M}{M_s} = \frac{2\,\pi(L/R)^2\eta}{3\ln(L/2R)M_V(B/\omega_C)} = 1.8\,\%$. This means that if the proposed model for the propeller movement is correct, the propeller magnetization is probably only a small fraction of the saturation magnetization. This is not surprising, since the propellers consist of randomly assembled magnetic nanoparticles, the magnetization directions of which will tend to cancel out. In addition, the magnetization state of most individual nanoparticles is probably not SD. Also the propellers consist not only of magnetic iron-oxide but also of hydrothermal carbon. The obtained fit parameters are thus not unrealistic.

4.3.5   Diffusion is Superimposed on Propulsion Movement

Thermal noise influences the movement of nanopropellers significantly. Thermal noise is not incorporated in the simple model for propeller actuation, but was assumed to be simply superimposed in the form of Brownian motion. To investigate whether this is the case, the movement of a propeller was tracked and the corresponding trajectories split into a propulsion component, described by the simple model, and a noise component (Figure 4-11 a,b). The noise components were interpreted as Brownian motion and diffusion coefficients were extracted as described in section 3.5.3. The resulting diffusion coefficients were close to the diffusion coefficient that was extracted from a propeller trajectory recorded in the absence of external magnetic fields (freely diffusing). Further evidence that the noise components can be interpreted as Brownian motion was obtained, by fitting linear functions of the form $\log(|\mathcal{F}(y_B)|) = a - b\log(f)$ (a and b constants) to the power spectrum of the noise components. The resulting fit parameter b was always close to 1, as expected for Brownian motion.
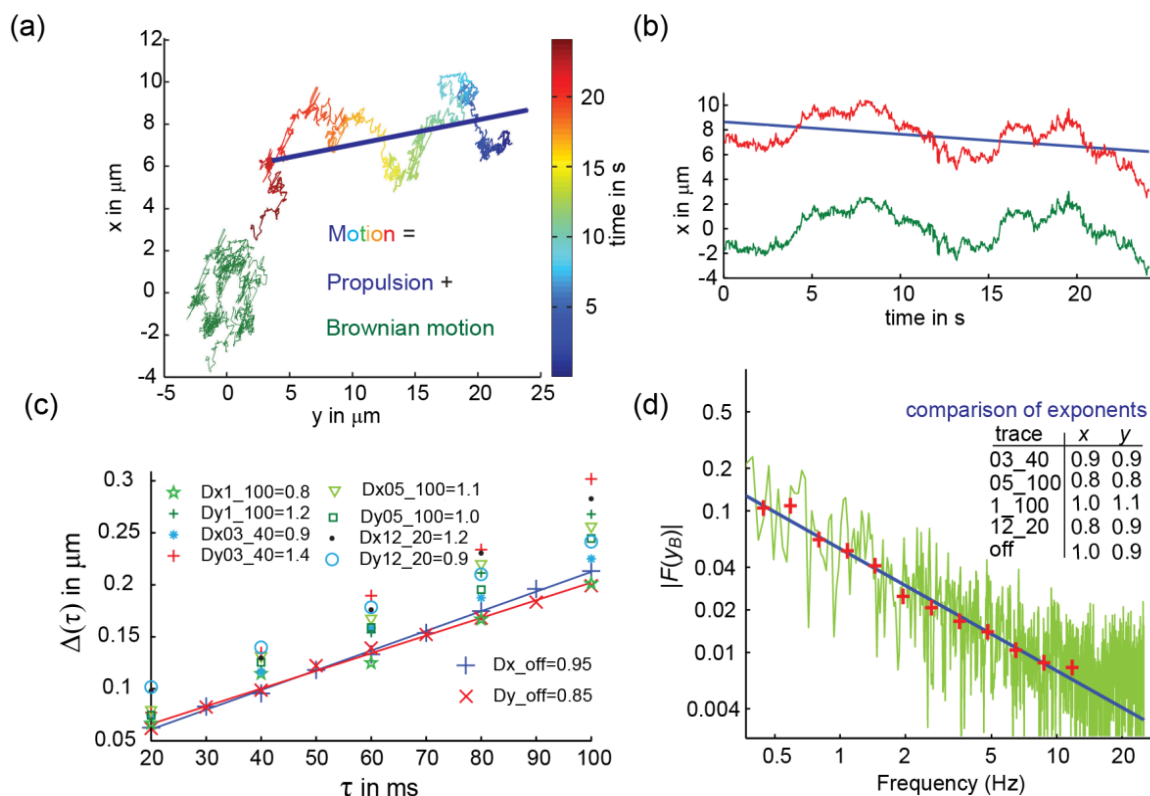
Figure 4-11: Decomposition of the motion of the nanopropeller into a propulsion component described by the proposed theoretical model and a noise component that can be described as Brownian motion. All data stem from measurements of the nanopropeller displayed in Figure 3-3 i. (a) Trace of the nanopropeller moving in a 0.3 mT field rotating at 40 Hz. The propulsion is slow as the propeller is actuated above its critical frequency. By fitting (least-squares) linear functions to the x and y components of the trajectory, the trace can be split into a propulsion component (in blue) and a noise component (in green). Adding these components reproduces the original trace. (b) The splitting procedure is exemplified for the x coordinate of the same trace (in red). The propulsion component is a linear fit (in blue). The difference between the two is the noise component (in green). Splitting of the y coordinate is done equivalently. (c) Determination of the diffusion coefficient based on the noise components of various traces. $\Delta(\tau)$ is the width of a Gaussian fit to the distribution of distances (using the Matlab function *nlinfit*), traversed during a time τ (see Figure 3-4). A linear fit yields an estimate for the diffusion coefficient [301]. The obtained diffusion coefficients are displayed with the data labels, whereby the first number denotes the field strength and the second number the frequency. The fact that the noise component data allow this analysis is a strong indication that the origin of the noise component is Brownian motion. The diffusion coefficients are very similar to the values obtained from a high speed measurement with the magnetic field turned off. The biggest discrepancy is observed in trace 03_40, which is the reason it is displayed in the next panel. (d) The absolute value of the Fourier transform of the y noise component of trace 03_40 is plotted against the frequency in a log-log plot. After binning the data (red crosses) a straight line (in blue) could be fit. The negative of the slope of this line is an exponent, which is expected to be 1 for Brownian motion. The inset shows that the fitted exponents for the noise components of all traces are close to 1. Adapted from [116]. This is an unofficial adaptation of an article that appeared in an ACS publication. ACS has not endorsed the content of this adaptation or the context of its use.

4.3.6 Discussion

The reported nanopropellers are smaller than any published previously. The smallest propellers in the literature were reported by Ghosh et al. to be about 0.5 µm in diameter and about 2 µm in length [5]. Interestingly it has been estimated that it should not be possible to produce propellers significantly smaller than the propellers by Ghosh et al., due to orientational noise caused by thermal fluctuations [115]. The nanopropellers reported here, might therefore be close to the smallest nanopropeller sizes that can be practically achieved. In principle, nanopropellers of any size could be controlled by magnetic fields of sufficient field strength and high field frequencies, but this quickly becomes impractical, since the required actuating frequency grows with the inverse cube of the nanopropeller size [115]. Indeed, Schamel et al. recently reported a particularly small propeller (about 0.1×0.4 µm) that could only be actuated in a viscoelastic medium, not in water [153].

The proposed model for the propulsion and the corresponding speed frequency relationship has been derived independently by another group as well [154]. The torque balance for magnetic particles actuated by an external magnetic field had also been published previously [174, 175, 337], although not used to explain the frequency speed relationship for magnetic propellers. An alternative model, based on the numerical simulation of a rotating magnetized ellipsoid has been published by Ghosh et al. [156]. This model takes into account that the vector of magnetization of the propeller is not necessarily parallel to the magnetic field vector (see section 2.1.1). The experimental data reported by Ghosh et al. can, however, be fit equally well by the simple model reported here, as by the more complex model they propose (Figure 4-12).
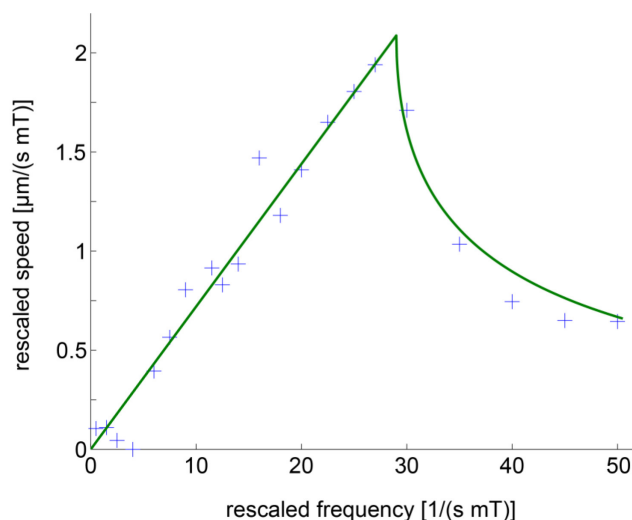
Figure 4-12: The speed versus frequency data presented here (blue crosses), is taken from the paper by Ghosh et al. investigating the motion of a helical nanopropeller [156]. Their measurements were performed with a magnetic field (B) of 2 mT. For the theoretically expected curve (green line, equation 26) two parameters needed to be found by nonlinear regression (using the Matlab function *nlinfit*): $c_v = 72$ nm and $B/\omega_C = 34.5$ mT ms. Adapted from [116]. This is an unofficial adaptation of an article that appeared in an ACS publication. ACS has not endorsed the content of this adaptation or the context of its use.

Both models have two free fit parameters. The assumption of the simple model, that the axis of rotation of the propeller is independent of the actuating frequency, is not to always valid [156]. In particular, for a helical propeller which has a magnetization component along its long axis, the long axis of the propeller aligns with the vector of rotation of the actuating field only for sufficiently high actuating frequencies [180].

The simple model seems to work for other magnetic actuators as well [8, 129]. This might be due to the fact that the ability of the magnetization to follow the magnetic field, an effect that is well described by the model presented here, is generally dominating the frequency-speed relationship.

The finding that diffusion is superimposed on the propulsive motion described by the simple model might not be universally valid for all nanopropellers. Orientational diffusion does apparently sometimes lead certain propellers to switch between a tumbling mode and a propulsion mode [156]. For the model proposed here, the effect of orientational diffusion might be hidden in the fit parameters of the model. It is conceivable that nanopropeller motion can be described as the sum of Brownian motion and propulsion as described by the simple model, but that the fit parameters of the simple model depend on the magnitude of orientational diffusion.

4.4   Geometric Determinants of Propulsion Properties

The dimensionless propulsion speed of a propeller depends only on the propeller geometry, as discussed in section 2.2.2. The relationship between propulsion speed and geometry has been investigated theoretically [180, 181] and experimentally [11] for helical propellers. A much larger variety of shapes can be studied based on the random shapes that result from the presented hydrothermal synthesis method (see section 3.1).

4.4.1   Synthesized Shapes are Random

The geometry of synthesized shapes was studied based on the 3D reconstruction method discussed in section 3.6.4. After their dimensionless speeds had been measured experimentally, 47 shapes could be reconstructed. It was a priori unclear whether the synthesis procedure favors particular shapes over others. Therefore it was necessary to show that the resulting structures are indeed random. A rigorous mathematical definition of a random shape was beyond the scope of this thesis, therefore the distributions of geometric parameters for the reconstructed shapes were compared to those of artificial shapes generated by a random process (see section 3.7.3). The resulting distributions are displayed in Figure 4-13 by plotting surface area, volume, handedness and chirality against the maximum voxel to voxel distance l_{max}. This visualization for the parameter distributions was chosen since l_{max} is the most intuitive geometric parameter.

Surface area and volume are similarly scattered for reconstructed as well as artificial shapes and lower than the expected values for single spheres with diameter l_{max}. Some artificial shapes have surface areas higher than a sphere of the same size, which might be due to surface roughness (cubic voxels) or the combined surface area of many spheres being particularly high. The handedness parameter has a higher standard deviation for reconstructed shapes than for artificial shapes, but the mean is close to zero in both cases, as expected for symmetry reasons. The mean chirality parameter is close to 0.56 in both cases. The distributions of geometric parameters for reconstructed and artificial shapes are in general similar. This confirms that the shapes resulting from the hydrothermal synthesis are random in the sense that they seem to be the product of a random process.
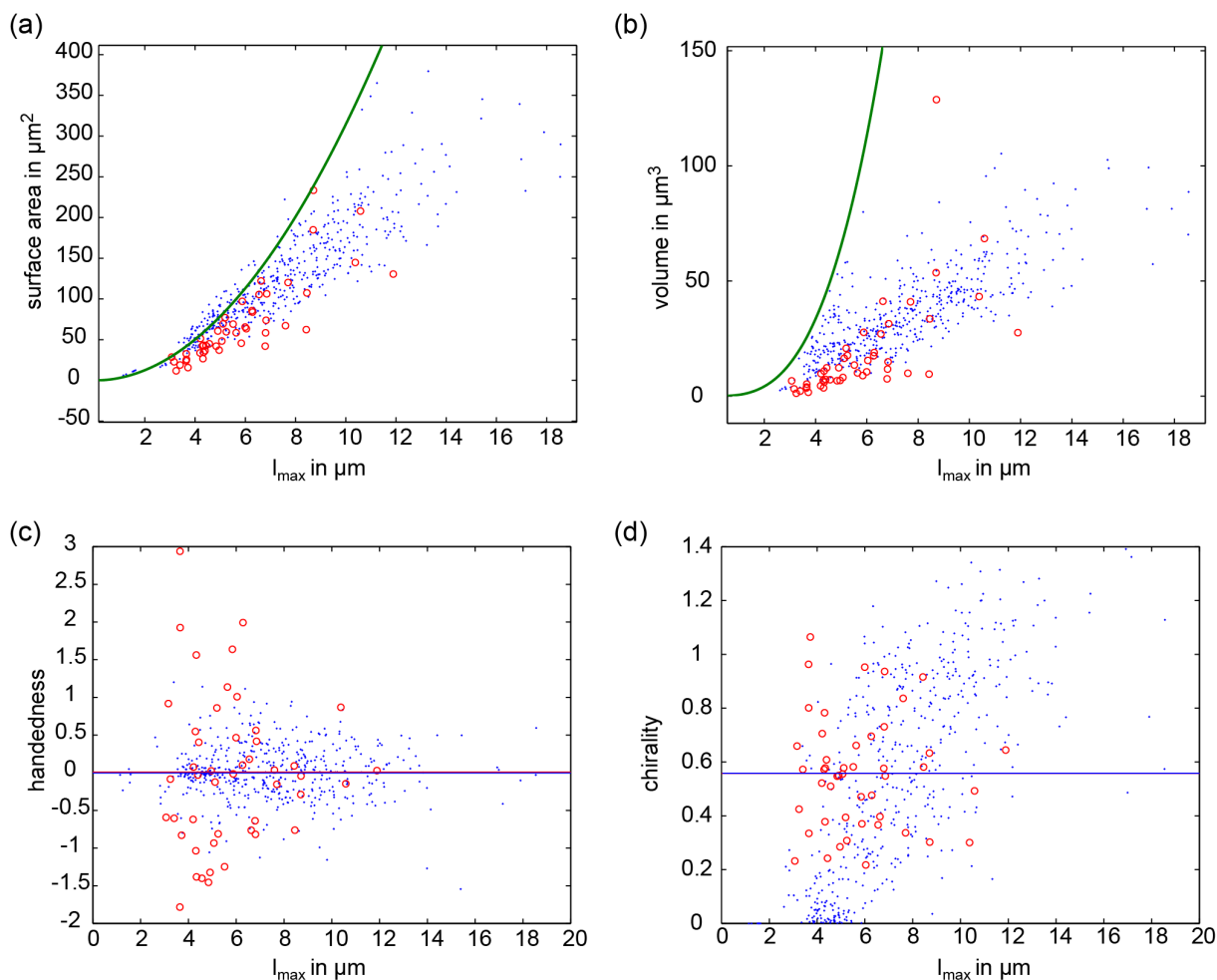
Figure 4-13: Comparison of reconstructed shapes (red circles) with randomly generated shapes (blue dots). Exemplary geometric parameters are plotted against the maximum voxel to voxel distance l_{max} in order to visualize their distributions. (a) The surface area is plotted against the maximum voxel to voxel distance. The green line would be expected for spherical particles with diameter l_{max}. (b) Same as (a), but for the volume instead of the surface area. (c) The handedness parameter H is plotted against the maximum voxel to voxel distance. The horizontal lines mark the mean handedness, which is close to zero in both cases. (d) Same as (c), but for the chirality parameter instead of handedness. The mean chirality is close to 0.56 in both cases.

4.4.2 High Dimensionless Speeds of Random Shapes

Dimensionless speeds were measured for 512 propellers (see section 3.5.4). A histogram of the dimensionless speed values together with exemplary reconstructed propeller shapes is shown in Figure 4-14. A Gaussian fit to the data (using the Matlab function *nlinfit*) yields a width of 46.5 which coincides with the standard deviation. The mean is close to zero as expected for symmetry reasons. The standard deviation of the dimensionless speeds of the subset of propellers for which a 3D shape could be reconstructed is 59.6. This is somewhat higher than the standard deviation calculated from all 512 measured propellers. The

discrepancy might be due to finite sampling, or some unidentified bias for propellers with high dimensionless speed to be successfully reconstructed.
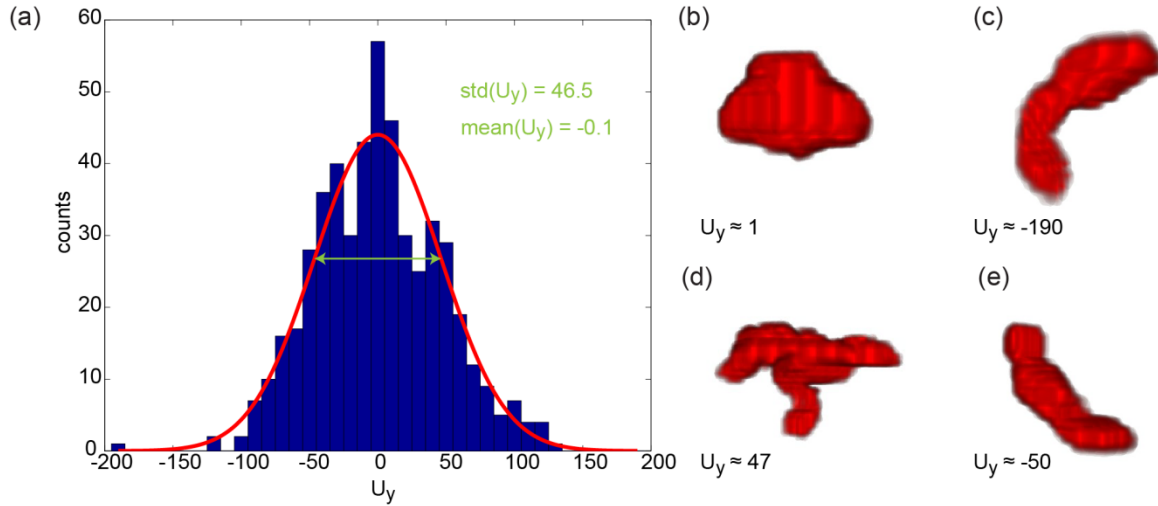
Figure 4-14: The distribution of dimensionless speed for random shapes has a surprisingly high standard deviation. (a) The measured values for the dimensionless propulsion speed U_y are displayed as a histogram. The red line is a Gaussian fit to the data (using the Matlab function *nlinfit*). The standard deviation of the data and the width of the Gaussian fit is 46.5. The mean of the distribution is -0.1 and thus close to zero as expected for symmetry reasons. (b-e) From all propellers for which the 3D shape was reconstructed, four examples were selected according to the following criteria: The absolute value of the dimensionless speed was closest to zero in (b) ($U_y \approx 1$), highest in (c) ($U_y \approx -190$), and closest to the standard deviation in (d) ($U_y \approx 47$) and (e) ($U_y \approx -50$). The propeller in panel (c) is also displayed in Figure 3-11.

4.4.3   Comparison with Previously Published Propellers

The observed standard deviation of 46.5 in the dimensionless speed of random shapes is surprisingly high when compared to the dimensionless speed of previously published propellers (see Figure 4-15). Most previously published propellers have dimensionless speeds below 3 standard deviations. Some nanofabricated propellers have dimensionless speeds which are smaller than the standard deviation of the dimensionless speeds of random shapes. Assuming a Gaussian distribution for the distribution of dimensionless speeds of random shapes, the chance of a random shape outperforming a nanofabricated propeller with dimensionless speed below 46.5, is about one in three. The highest dimensionless speed found in the set of reconstructed random shapes is 190 (absolute value, see Figure 4-14 c) and higher than most previously published nanofabricated propellers. The shape of this fastest propeller

is indeed approximately helical, with less than one helical turn, similar to optimized shapes reported by Keaveny et al. [181].
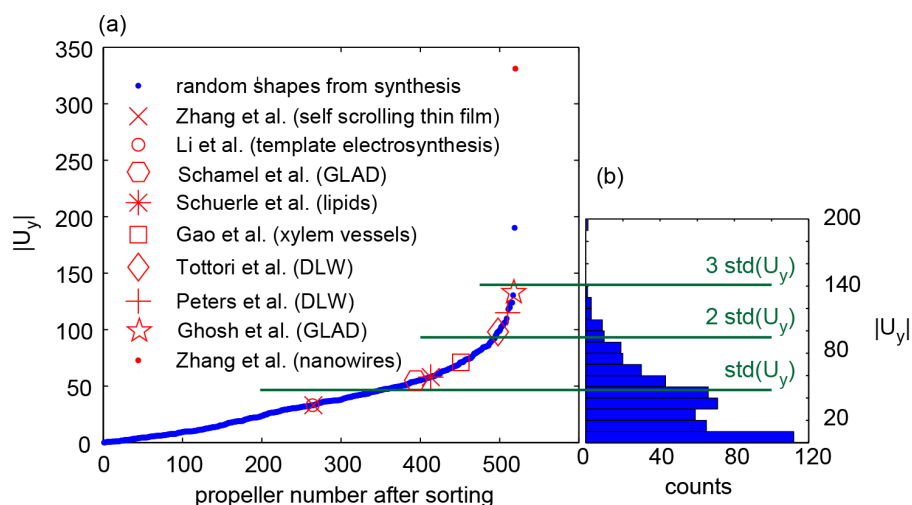
Figure 4-15: Comparison of randomly shaped propellers from solution synthesis with previously published nanofabricated propellers. The dimensionless speeds of nanofabricated propellers are shown in the same order as in Figure 2-4 (Zhang et al. [6], Li et al. [128], Schamel et al. [153], Schuerle et al. [167], Gao et al. [127], Tottori et al. [11], Peters et al. [166], Ghosh et al. [5], Zhang et al. [152]). (a) The absolute value of the dimensionless speed is plotted against the propeller number after sorting the dimensionless speeds in ascending order. (b) The distribution of absolute dimensionless speed values is displayed as a histogram. The scale of $|U_y|$ is the same as in (a). The multiples of the standard deviation of U_y are displayed as horizontal green lines. Assuming a Gaussian distribution, 68 % of random shapes have dimensionless speeds lower than the one standard deviation, 95 % lower than two, and 99.7 % lower than three standard deviations.

4.4.4 Geometric Parameters Correlate with Swimming Properties

Various geometric parameters can be extracted based on the reconstructed 3D shapes (see section 3.7.3). As an additional check for the reliability of the reconstruction and parameter extraction procedures, the optical size measurement was plotted against the maximum voxel to voxel distance in Figure 4-16 a. The two measures are generally in agreement, although the maximum voxel to voxel distance tends to be a little larger. This is not unexpected, due to the fact that only five different 2D projections were recorded and the 2D projection in which the propeller would appear largest might not have been one of them. Then again, the maximum voxel to voxel distance in the reconstruction might be larger than the true size of the propeller due to overshadowing. Various geometric parameters correlate with the dimensionless propulsion speed. While searching for the strongest correlation, all multiplicative parameter combinations (using every parameter once) with the right physical units (μms^{-1}) were tried.

The strongest correlation for the dimensionless propulsion speed was found with the product of the chirality parameter χ and the sphericity parameter Ψ (Figure 4-16 b). The rolling speed v_x of the propellers was also correlated with geometric parameters. The strongest correlation was observed to be $v_x \propto f \, S \, \gamma \frac{V}{O}$ (see Figure 4-16 c). The rolling speed thus grows also linearly with the actuating frequency f and with a length scale, namely the ratio of volume V to surface area O. This observed scaling behavior would allow the definition of a dimensionless rolling speed similar to the dimensionless propulsion speed. This dimensionless rolling speed grows with the spikyness parameter S and the average width to length ratio γ.
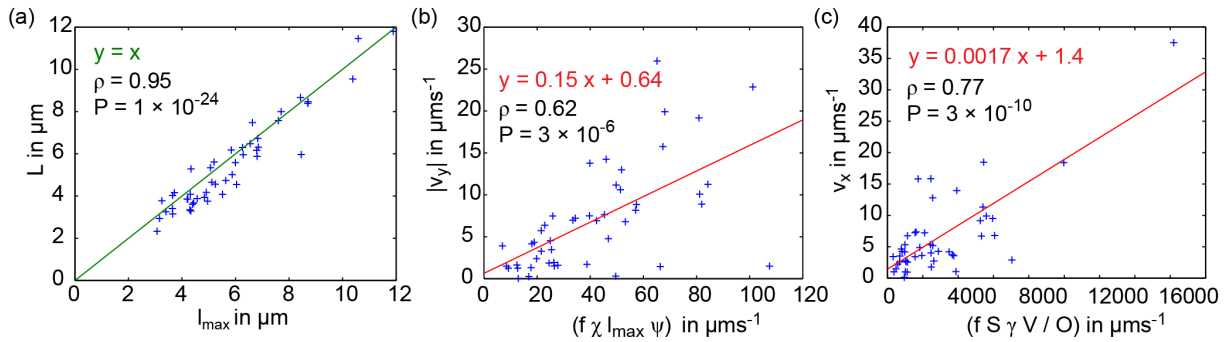
Figure 4-16: Correlations between geometric parameters and propeller properties. (a) The optical size estimate (based on the 2D projection in which the propeller appears largest) is strongly correlated with the maximum voxel to voxel distance l_{max}. The green line is not a fit to the data, but a reference line with slope one. The remaining scatter is probably due to measurement and reconstruction errors. ρ is the Pearson correlation coefficient. The low P values indicate that the null hypothesis of the data being uncorrelated can be rejected with high confidence. (b) The absolute value of the propulsion speed $|v_y|$ correlates with the product of the actuating frequency f, the chirality parameter χ, l_{max} and the sphericity Ψ. The red line is a linear (least-squares) fit to the data (equation in red). (c) The rolling speed v_x correlates with the product of f, the spikyness parameter S, the average width to length ratio γ and the volume V divided by the surface area O.

4.4.5 Discussion

The observed correlation of the dimensionless speed with the chirality measure χ was expected. As discussed in section 2.2.2, highly symmetric objects cannot propel, since the sign of the rotation translation coupling (C) needs to change for the mirror image of a structure, assuming a fixed axis of rotation. Thus, for example, objects with three orthogonal mirror planes of symmetry cannot propel [111]. Multiplying the chirality with the sphericity increases the correlation. This is rather unexpected since one would think intuitively that more

spherical propellers have lower dimensionless speeds. In fact, sphericity and chirality are anticorrelated ($\rho = -0.63, \mathrm{P} = 2 \times 10^{-6}$).

The rolling speed also increases with frequency and a length scale, which might be ultimately grounded in the linearity of the Stokes equations for Newtonian fluids. The rolling speed increases with spikyness and the average width to length ratio, suggesting that objects elongated perpendicular to the axis of rotation make good rollers. Previous experimental realizations of rollers also used rodlike structures rotating around their short axis [129, 131, 132, 143, 144], but a hydrodynamic explanation why this should be advantageous could not be found so far.

The observed discrepancy between reconstructed and artificial shapes for the handedness parameter, could hint at peculiarities of either the synthesis method or the reconstruction procedure. The latter option seems more likely, because the standard deviation of dimensionless speed is elevated for the reconstructed shapes with respect to all measured propellers (see section 4.4.2). In any case this should not matter much, since the handedness parameter does not correlate with the dimensionless speed (see section 4.4.4).

The speed measurements on which the reported dimensionless speed values are based, were done close to a glass interface (see section 3.5.4). Propulsion speeds measured in this way might be different from the propulsion speeds that would have been observed if the structure had been actuated in bulk liquid. However, the propulsion speed was measured in the same way for previously reported nanofabricated propellers. Therefore, this measurement scheme was used here as well, despite being potentially unsuited to accurately measure dimensionless propulsion speeds.

The measured distribution of dimensionless propulsion speeds seems to be Gaussian, but at 512 samples, fat tails cannot be excluded. The distribution is also lower than expected for a Gaussian at $|U_y| \approx 25$ and higher than expected at $U_y \approx 0$. Whether this is due to finite sampling or a real effect due to some unidentified mechanism remains to be investigated.

The only nanofabricated propeller that is significantly faster than all random shapes is the Nickel nanowire propeller reported by Zhang et al. [152]. These speed measurements were not performed in water at room temperature, but in a high density suspension of 0.5 µm microbeads. Equation 11 suggests that an increased viscosity should not matter for the dimensionless propulsion speed (which depends purely on the propeller geometry), but the

presence of microbeads could allow the propeller to behave more like a screw drilling through sand instead of a hydrodynamic propeller. For a screw with one helical turn moving through a solid, the dimensionless speed will be 1000, which seems unattainable for a hydrodynamic propeller. Therefore the reported dimensionless speed of 331 should be taken with a grain of salt.

As discussed in section 2.2.2 arbitrarily shaped propellers might have a tendency to rotate around an axis for which the rotation translation coupling is strong. This could potentially explain the high observed dimensionless speed values. However, the axis around which the structure rotates depends on the direction of magnetization of the structure as well. Also it could be that the motion of the propeller is more complex than the simple rotation around a single axis. Nonetheless it is conceivable that the dependence of the rotational friction constant (c_F) on the rotation translation (C) coupling increases the observed dimensionless speed values beyond the dimensionless speed distribution expected for random shapes, rotating around arbitrary axes of rotation. Further theoretical and experimental investigations are needed to determine whether this effect occurs and whether it has a significant influence on the distribution of dimensionless speeds.

Assessing propellers based on their dimensionless speed is useful when experimental limitations to the producible field strengths are of no concern. Since the dimensionless speed is related only to the propeller geometry it does not take into account the degree to which a propeller can be magnetized, or the magnetic torques needed to rotate it. The effect of magnetization and necessary magnetic torques have been discussed in theoretical studies [180, 181]. Bale et al. recently introduced the energy-consumption coefficient which can be used to compare the energy efficiency of swimming and flying animals (including bacteria) [338]. Whether a similar measure can also be applied to magnetic propellers remains to be seen, since the hydrodynamics of externally driven structures as discussed here are rather different from those of self-propelled swimmers. At first sight, energy efficiency does not seem to be of primary importance for magnetically actuated nano- and microstructures, but it would nevertheless be interesting to work out how energy dissipation differs between actuating strategies and swimmer or propeller shapes.

4.5 Swarm Control for Magnetic Nanopropellers

This section was adapted from a submitted manuscript. Controlling multiple magnetic nanopropellers independently by subjecting them to the same external magnetic field is a challenging task (see section 2.3.2). Such swarm control is possible, due to the nonlinear relationship between speed and actuating frequency, as described by the simple model for nanopropeller actuation (equation 26) [120, 164]. Before introducing a general mathematical model for swarm control, the simpler situation of controlling just two propellers will be discussed.

4.5.1 Controlling two Propellers Independently

For two propellers with different properties (Figure 4-17 a), a control task can be stated as follows: Given start and end positions for the propellers, a sequence of rotating magnetic fields (frequency ω^j, field strength B^j, applied for time t^j) needs to be found, which moves the propellers from the start to the end positions. As an example, two frequencies ω^1 and ω^2 are chosen and the magnetic field strength is fixed to some constant value. The start positions are set to zero and the end positions are a^1 and a^2 respectively. This first control task is in only one spatial dimension. Finding the correct times t^1 and t^2 for which the actuating frequencies need to be applied is equivalent to solving a linear set of equations (negative values for t^j mean rotating counter-clockwise instead of clockwise). The result is illustrated in Figure 4-17 b for two choices of control frequencies.
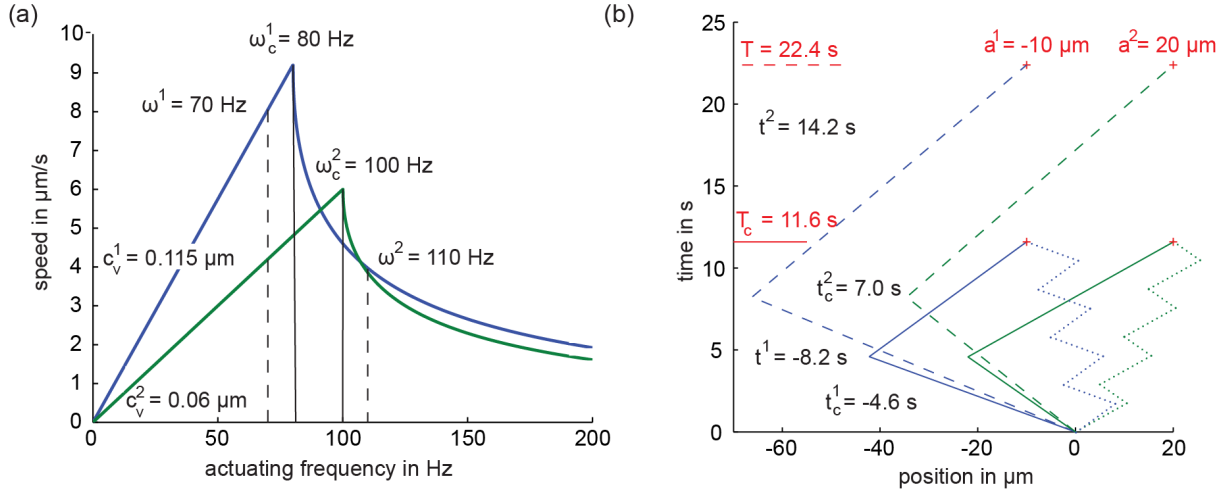
Figure 4-17: (a) Speed is plotted against frequency for two exemplary propellers. The dashed lines mark one choice of control frequencies. The solid lines mark control frequencies that are equal to the critical frequencies of the propellers. (b) The two propellers from panel (a) are now used for a 1D control task. The position of the propellers is plotted against time until the propellers have reached their designated end positions. The dashed lines correspond with the choice of control frequencies marked by dashed lines in panel (a). The solid lines correspond to control frequencies equal to the critical frequencies. A trajectory can obviously be split into parts to better approximate a linear trajectory from the start to the end positions. Splitting the two parts of the solid trajectory into four parts each, leads to the dotted line. The ratio of the total length of the trajectory to the length of a linear trajectory from the start to the end positions (the excursion ratio) is unchanged upon such splitting of a trajectory. The meaning of the variables provided as insets is explained in the main text. This figure is part of a submitted manuscript.

4.5.2 Mathematical Model of Swarm Control

In general the swarm control problem can be stated as follows: Given n propellers and n corresponding d-dimensional trajectories of the form $\vec{r}_i(t)$, what is a sequence of rotating magnetic fields (ω_j, B^j) that, if consecutively applied for times t^j, lead to propeller movements approximating $\vec{r}_i(t)$.

This problem can be simplified. Firstly, starting coordinates $\vec{r}_i(0) = 0$ can be chosen without loss of generality. Secondly, since the propellers only need to approximate the intended trajectory, the problem can be restricted to one spatial dimension. This is due to the fact that a multi-dimensional trajectory can always be split up into segments along orthogonal coordinates. For the same reason only a single step from $\vec{r}_i(t) = 0$ to $\vec{r}_i(\tau) = a_i$ must be considered. The swarm control problem then takes the following form:

$$\mathbf{G}\,\mathbf{t} = \mathbf{a}, \tag{40}$$

where $\mathbf{G}$ is a matrix with elements $g_i^j = v_i(\omega^j, B^j)$. j is an integer between 1 and m with $m \geq n$ (n being the number of propellers in the control task). In addition, the total duration of a control step is constrained as:

$$\sum_{j=1}^{m} |t^j| = T = \tau, \tag{41}$$

where T is the total time it takes to reach the final positions with all propellers and τ is a target time that defines an effective speed. The vector $\mathbf{t}$, contains the times t^j for which a magnetic field with frequency ω^j and field strength B^j is applied.

In the following, the combined equations 40 and 41 are referred to as the swarm control problem. A particular swarm control problem is defined by the propeller properties ω_C^i (B) and c_v^i as well as end positions a_i and control time τ. The solution is a sequence of magnetic field strengths, actuating frequencies and times (B^j, ω^j, t^j) for which equations 40 and 41 are satisfied. This solution can be found when $\mathbf{G}$ is invertible. Two rows of $\mathbf{G}$ are linearly dependent if two critical frequencies are equal. This is due to the fact that the propeller speed v_i is linear in the propulsion parameter c_v^i as can be seen in equation 26. Thus equation 40 does not have a solution if two or more critical frequencies ω_C^i are equal. In addition, at least n actuating frequencies ω^j must be chosen distinct and less than $m - n + 2$ frequencies ω^j must be smaller than the smallest critical frequency at all B^j. Assuming a solution (B^j, ω^j, t^j), which satisfies equation 40 has been found, it is immediately possible to find another solution $(\hat{B}^j, \hat{\omega}^j, \hat{t}^j)$, which satisfies equation 40 and equation 41 simultaneously, by rescaling the field strengths and frequencies with $\tau/T(B^j, \omega^j)$. This is due to the fact that the critical frequencies are linear in B and the propulsion velocities are linear in a factor that rescales ω and ω_C. Thus, the necessary and sufficient conditions for a solution to equations 40 and 41 to exist can be summarized as follows:

$$\left(\omega_C^i, \omega_C^j\right) \neq \left(\omega_C^j, \omega_C^i\right) \quad \text{for} \quad i \neq j \tag{42}$$

$$\left|\{(\omega^i, \omega^j) = (\omega^j, \omega^i)\}\right| < m - n + 1 \quad \text{for} \quad i \neq j \tag{43}$$

$$\left|\{\omega^i \quad \text{with} \quad \omega^j < \min\{\omega_C^i(B^j)\}\}\right| < m - n + 2 \tag{44}$$

4.5.3 Critical Control is Optimal

As the conditions 42, 43 and 44 are not very restrictive, the choice of actuating field strengths and frequencies can be optimized according to criteria based on practical considerations. Since it is difficult to produce strong magnetic fields, the largest B^j needs to be as small as possible. As the maximum propeller speeds are proportional to B, the largest B^j can be minimized by minimizing the control time for a given maximum magnetic field strength B_0. It will be indicated below that the control time is minimized when the control frequencies are equal to the critical frequencies. Secondly, propellers should not stray too far away from a linear path from $r_i(0) = 0$ to $r_i(\tau)$. This can be quantified by the excursion ratio, defined as the average length travelled by the propellers divided by the average linear distance from start to end positions,

$$E = \frac{\sum_{j=1}^{m} \sum_{i=1}^{n} v_i(\omega^j, B_0)|t^j|}{\sum_{i=1}^{n} |a_i|}. \tag{45}$$

It will be indicated below that E is minimized as well when the magnetic field strengths are chosen constant and the critical frequencies are chosen as control frequencies. The control strategy of using critical frequencies as control frequencies at constant field strength (so that $T = \tau$) will be called critical control.

How should the m field strengths and actuating frequencies be chosen, so as to minimize the control time T? This problem will be discussed in two steps. First, it is shown that for a particular choice of m actuating frequencies, the control time T is reduced when all field strengths are increased to the maximum possible field strength B_0 and the control frequencies are rescaled accordingly. Then, numerical optimization and random sampling will be used to indicate that, for $B^j = B_0$, the control time is minimized when the critical frequencies of the propellers are used as the actuating frequencies $w^j = w_c^i$.

Given a control strategy (B^j, ω^j, t^j) with corresponding control time $T(B^j, \omega^j)$, a new control strategy $(B_0, \omega^j \times B_0/B^j, t^j \times B^j/B_0)$ can be devised. This transformation scales the speeds of all propellers during control step j by a factor of B_0/B_j. The duration of control step j is reduced by a factor B^j/B_0, thus the propellers reach the same positions at the end of every control step and thus the correct final positions after a shorter total control time. Therefore, the control strategy with minimal control time will use field strengths $B^j = B_0$.

It remains to show that with $B^j = B_0$, the control time is minimized for $w^j = w_c^i$. First, the relatively simple case of $n = m = 2$ is investigated. This case is illustrated in Figure 4-18. It can be seen that T is minimal for $w^j = w_c^i$.

Second, the case $m = n + 1$ is treated using numerical optimization. Control tasks were randomly generated and solved using critical frequencies as control frequencies and a constant magnetic field strength. The resulting control time is T_c. Then the same randomly generated control task was solved with randomly selected control frequencies and numerical optimization (using the Matlab function *fminsearch*) was used to try to find new control frequencies for which the control time is minimized. The resulting control time is called T_o. The optimized control time T_o was found to be always larger than the critical control time T_c. The optimization usually leads to one time step t^j being set to zero. This means that it is not helpful to use more than n control frequencies. Since setting $m = n + 1$ cannot reduce the control time, the case $m > n + 1$ was not considered. It is of course possible to construct equivalent control strategies, by splitting and reordering control steps, but this ambiguity is of no interest here.

When the optimization was initialized with the critical frequencies, the optimization algorithm terminated immediately. In order to see if the optimization procedure tends to find control frequencies close to the critical frequencies, a distance measure Θ was constructed:

$$\Theta = |t_o^1|\omega_o^1 + \sum_{j=2}^{m} \left| |t_c^{j-1}|\omega_c^{j-1} - |t_o^j|\,\omega_o^j \right|, \tag{46}$$

where ω are the critical frequencies as control frequencies and ω_o are the optimized control frequencies. The control frequencies are indexed after sorting the values $|t^j|\omega^j$ in ascending order. t_o^1 is therefore the time step that was usually set to zero by the optimization algorithm. Θ is plotted against $T_o - T_c$ in Figure 4-19. As can be seen, the relationship between the two is approximately linear. This means that the optimized frequencies are close to the critical frequencies when the optimized control time is close to the critical control time, although the critical control time is always smaller. This strongly suggests that control frequencies at the critical frequencies lead to minimal control time. In Figure 4-19, propeller numbers from 2 to 6 were plotted.
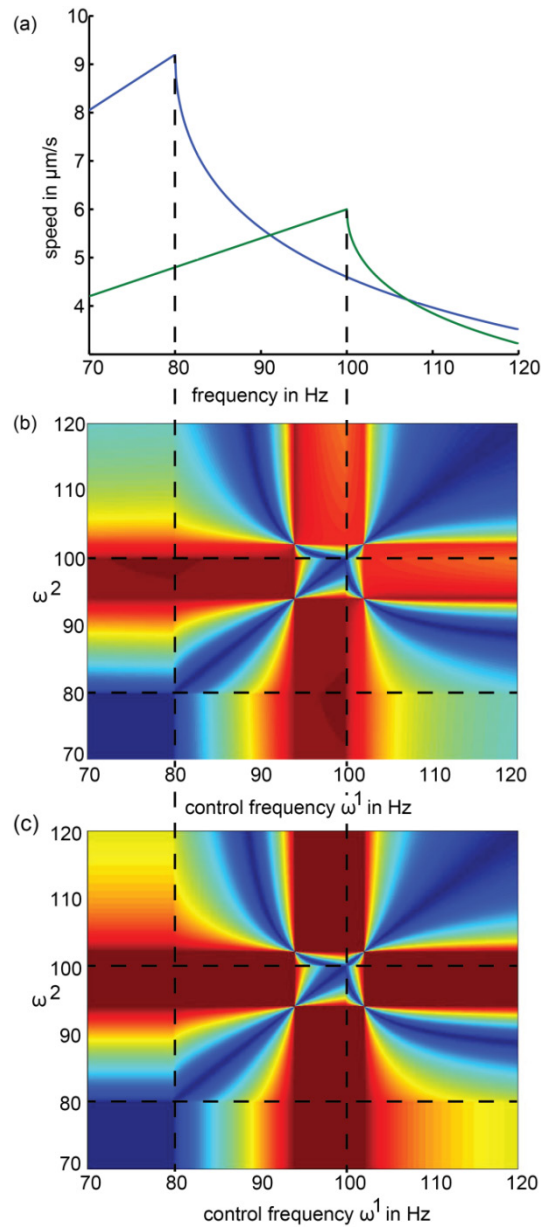
Figure 4-18: Dependence of control time and excursion ratio on the actuating frequency. (a) The speed vs. frequency relationship in the case of two propellers. The critical frequencies are $w_c^1 = 80$ Hz and $w_c^2 = 100$ Hz. (b) The control time T is color coded from small (red) to big (blue). T depends on the two control frequencies (ω^1 and ω^2). The global minimum is at the critical frequencies (intersection of the dashed lines). (c) The excursion ratio E is color coded from small (red) to big (blue). E has a degenerate minimum at the critical frequencies. The dark red areas all correspond to $E = 1$, meaning that the propellers can travel to the intended end positions on a linear trajectory. The plots are symmetric around the line $\omega^1 = \omega^2$, since the problem is symmetric to exchanging the order in which the control frequencies are applied. The control time and excursion ratio landscapes are not convex and can already be quite complicated for two propellers. This figure is part of a submitted manuscript.
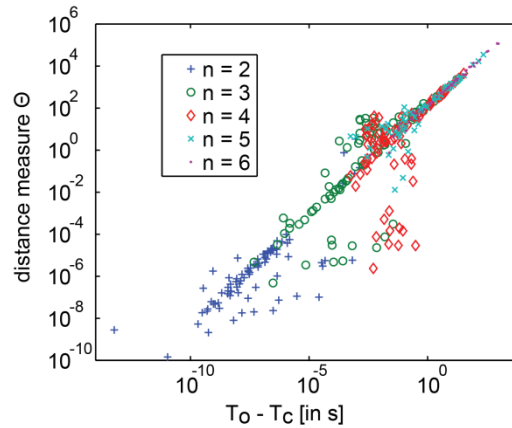
Figure 4-19: A distance measure Θ (see equation 46) for the difference between the optimized control frequencies and the critical frequencies is plotted against the difference between the corresponding control times (T_o and T_c). This was done for propeller numbers n from 2 to 6. The number of control frequencies that were optimized were always $n + 1$. The optimization algorithm (using the Matlab function *fminsearch*) usually set one control time to zero. The start frequencies for the optimization procedure were chosen at random. If the optimization was initialized at the critical frequencies it terminated immediately. This plot shows that the control time is close to the optimal control time, if the control strategy is close to the optimal control strategy. This figure is part of a submitted manuscript.

To further test the hypothesis that control frequencies equal to the critical frequencies lead to minimal control time, the difference between the control time resulting from randomly sampled control frequencies (T_r) to the control time obtained when using critical frequencies (T_c) was computed as well. Control tasks were randomly generated and ($T_r - T_c$) calculated 10 million times each, for propeller numbers between 2 and 16. The results of these calculations are displayed in Figure 4-20. Again, the control time is always smaller when the control frequencies are equal to the critical frequencies. Indeed, when the control frequencies are chosen at random the control times become many orders of magnitude longer than the control time for critical control. Figure 4-20 b shows that the random sampling finds a minimum which is close to the value for critical control, relative to the mean control time for critical control. This shows that the control frequency sampling is sufficiently exhaustive to come close to the critical frequencies, suggesting that control frequencies equal to the critical frequencies are indeed the global minimum for the control time.
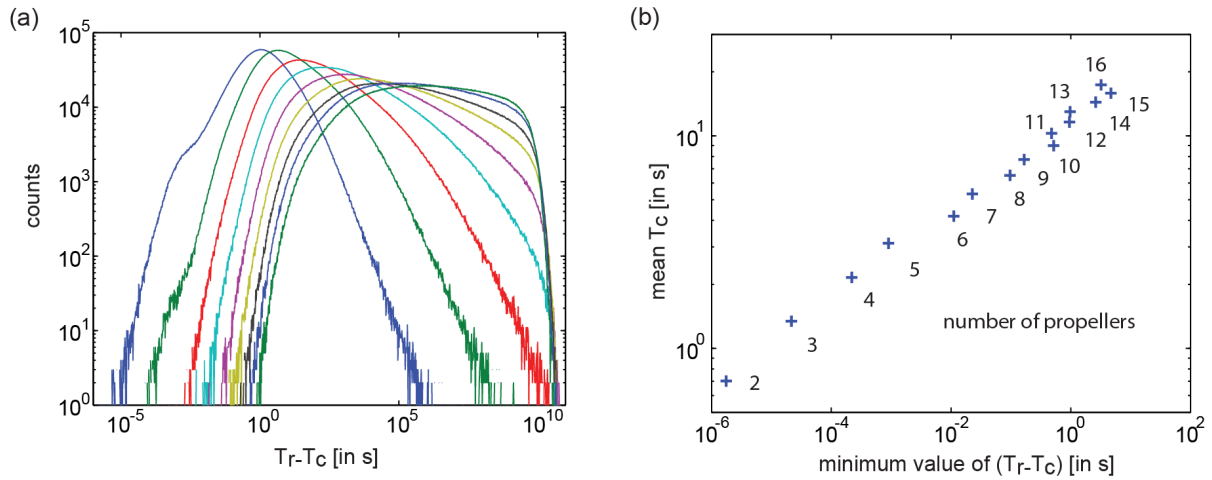
Figure 4-20: (a) Comparison of control times T_c and T_r. T_c is the control time of a randomly generated control task with n propellers, when using critical control. T_r is the control time when using randomly generated control frequencies and constant magnetic field strength. Both were calculated for 10^7 randomly generated control tasks. This was repeated for propeller numbers from 2 to 16. Here histograms of the generated data are displayed for control tasks with 2 to 10 propellers. The minimal time difference increases with increasing propeller number. The difference is always positive, meaning that the control time is always shorter when choosing critical frequencies as control frequencies. (b) The mean control time when using critical frequencies is plotted against the minimal difference between T_c and T_r (from all 10^7 samples each) for n from 2 to 16. It can be seen that the minimal time difference is significantly smaller than the mean control time, indicating that the used number of samples was sufficient to come close to the suspected global control time minimum at the critical frequencies. This figure is part of a submitted manuscript.

Having established that the control time is minimal for critical control, it will next be shown that critical control also minimizes the excursion ratio E. As can be seen in Figure 4-18 the dependence of E on the actuating frequencies ω^j is similar to that of the control time T. This can be intuitively understood, when considering that the average speed $\langle v \rangle$ with which the propellers travel at a certain control frequency is set by the propeller properties and is thus independent of the target positions a^j. The average excursion ratio can be estimated as $\langle E \rangle \approx \frac{\langle v \rangle T}{\langle |a| \rangle}$. $\langle E \rangle$ is then minimized when T is minimized. This argument, however, does not show that E is always minimal when $\omega^j = \omega_c^i$. To show that E is always minimal for critical control, numerical optimization (using the Matlab function *fminsearch*) was performed. In Figure 4-21 excursion ratios are plotted for critical control (E_c) and for control frequencies obtained from the optimization procedure (E_o). It can be seen that excursion ratio is always smaller for critical control.
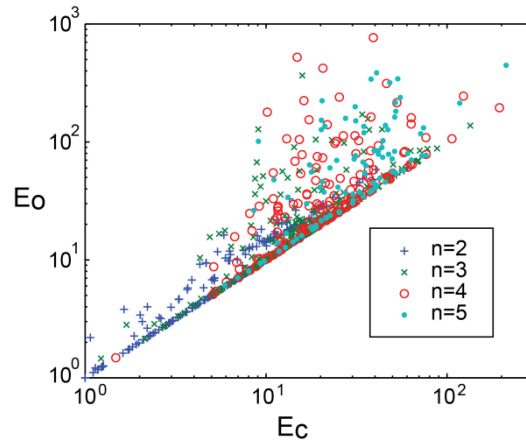
Figure 4-21: The optimized excursion ratio E_o was obtained for a number of randomly generated control problems using numerical optimization (using the Matlab function *fminsearch*). The start frequencies of the optimization were chosen at random. If the optimization was initialized with critical frequencies the optimization terminated immediately. It can be seen in the plot of E_o against E_c that critical control leads to minimal excursions. This figure is part of a submitted manuscript.

4.5.4 Optimal Propeller Design

After having determined an optimal control strategy, it was investigated how the control time T depends on the various physical parameters. For the propulsion parameters c_v, the critical frequencies ω_c, and the final positions a, this dependence can be readily deduced from equation 26. Concerning the influence of these parameters on T, these parameters were characterized by their averages $\langle |a| \rangle$, $\langle c_v \rangle$ and $\langle \omega_c \rangle$. From the form of equation 26, it can be deduced that $\langle T \rangle \propto \frac{\langle |a| \rangle}{\langle c_v \rangle \langle \omega_c \rangle}$. For the parameters n and Δ, the influence on the control time is not obvious. Fit parameters were used to determine this dependence, initially assuming a power law relationship. Δ is a parameter that characterizes the spacing of the critical frequencies, which was constrained as $\langle \omega_c \rangle / \Delta > n/2$, to keep the critical frequencies larger than zero. n is the number of propellers in the control task. In order to determine the dependence of T on the parameters n and Δ, the other parameters were sampled from random distributions. To be able to sample c_v, ω_c and a distributions were constructed in such a way that pathological cases, like two critical frequencies being equal or a propulsion parameter being zero, were avoided. Specifically, $3n$ random variables $\chi_{1,2,3}^i$ were drawn from the uniform distribution between 0 and 1 and the parameters chosen as follows:

$$a^i = \left(\lambda_1 + \lambda_2 \chi_1^i \right) \times 1 \, \mu m, \tag{47}$$

$$c_v^i = \left(\lambda_3 + \lambda_4\, \chi_2^i\right) \times 1 \text{ μm}, \tag{48}$$

$$\omega_c^i = \langle\, \omega_c\, \rangle - \frac{(n-1)\Delta}{2} + \Delta\left(i - \chi_3^i + 0.5\right)\lambda_5, \tag{49}$$

with λ_k real numbers, $\lambda_{3,4} > 0$ and $0 < \lambda_5 < 1$. In the numerical calculations, these parameters were further constrained as $\lambda_{3,4} > 0.01$ and $0 < \lambda_5 < 0.95$ to ensure numerical stability and to keep the needed number of samples manageable, since T can become very large when two critical frequencies are almost equal or one propulsion parameter is very close to zero. Initially, the function $T(n,\Delta)$ was modelled as $T(n,\Delta) \propto n^\beta (\Delta/\langle\, \omega_c\, \rangle)^\gamma$, with fit parameters β and γ. It turned out that the fit parameter γ was very close to $\gamma = -0.5$ and therefore the relationship $\langle\, T\, \rangle \propto \frac{1}{\sqrt{\Delta/\langle\, \omega_c\, \rangle}}$ was assumed in order to reduce the number of fit parameters. The final model function was determined by combining the a priori known dependence $\langle\, T\, \rangle \propto \frac{\langle\, |a|\, \rangle}{\langle\, c_v\, \rangle\langle\, \omega_c\, \rangle}$ with the assumed dependence $\langle\, T\, \rangle \propto \frac{n^\beta}{\sqrt{\Delta/\langle\, \omega_c\, \rangle}}$. After sampling $T(n,\Delta)$ for n between 2 and 10 and Δ between 1 and 18 Hz, this model was used for fitting:

$$\langle\, T\, \rangle = \alpha\, \frac{\langle\, |a|\, \rangle n^\beta}{\sqrt{\langle\, \omega_c\, \rangle \Delta}\, \langle\, c_v\, \rangle}, \tag{50}$$

where α and β are dimensionless fit parameters. The magnetic field strength B_0 is implicitly contained in $\langle\, \omega_c\, \rangle$.

The resulting fit is shown in Figure 4-22. The value of α depends on $\lambda_{3,4,5}$ ($0.9 < \alpha < 2$). α is smaller if the distributions of c_v and ω_c have narrower peaks. β was found to be approximately equal to 1.1, independently of the distributions for the propeller parameters. It can thus be concluded that the control time T grows only slowly (approximately linear) with the number of propellers in the swarm.
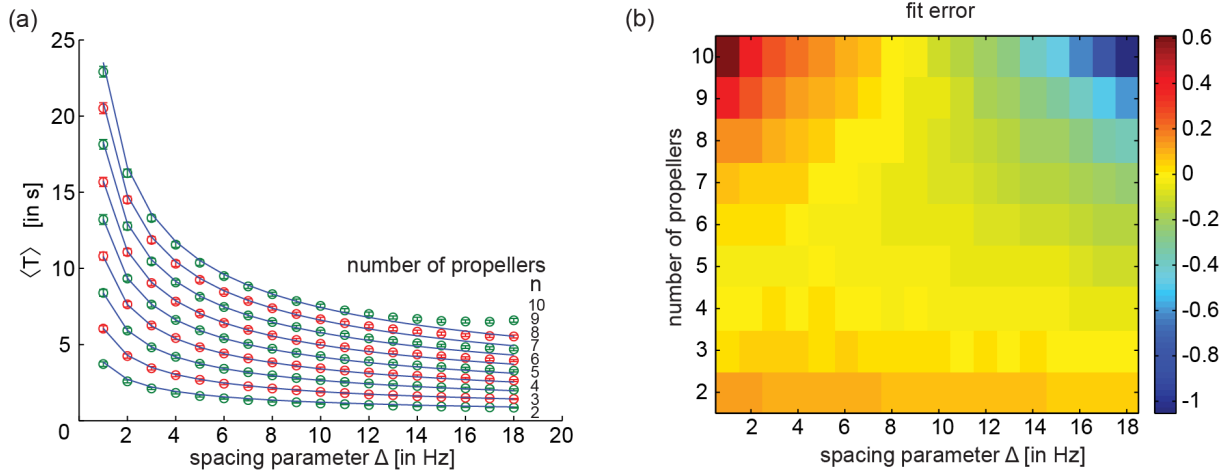
Figure 4-22: (a) The mean control time T is plotted against the spacing parameter Δ. The data points for different numbers of propellers are plotted on top of each other. 1000 control tasks were randomly generated for each data point and averaged ($\langle \omega_c \rangle = 100$ Hz, $\lambda_1 = 2$, $\lambda_2 = 4$, $\lambda_3 = 0.01$, $\lambda_4 = 0.18$, $\lambda_5 = 0.9$). This was repeated 100 times and the resulting standard deviation is displayed as the error bar. The blue lines are the best fit (using the Matlab function *nlinfit*) obtained based on equation 50 ($\alpha = 1.76$ and $\beta = 1.13$). (b) The error of the fit displayed above, is here color coded and displayed as a function of propeller number n and spacing parameter Δ. The overall fit is reasonably good. The sampling error appears to be quite low as is also apparent in the error bars in panel (a). This means that the remaining error is due to the limitations of the model. This figure is part of a submitted manuscript.

The precision with which propellers can be positioned is limited by the size of propellers and by diffusion. During the target control time (τ) the propellers will diffuse on average a distance $\tilde{x}$. At this point a size parameter R needed to be introduced, to allow the estimation of the diffusion coefficient of the propellers. Since R is implicitly contained in the propulsion parameter, it is substituted as: $c_v = \hat{c}_v R$. R was assumed equal for all propellers in the swarm, since the goal was to obtain the same precision for all propellers. Assuming that the size parameter R is identical to the hydrodynamic radius of the propeller, $\tilde{x}$ can be calculated as:

$$\tilde{x} = \sqrt{2dD\langle \tau \rangle} = \frac{d\, k_B T}{3\,\pi\,\eta\,R\,\langle \tau \rangle} \tag{51}$$

Using equation 50 this can be rewritten as:

$$\tilde{x} = \sqrt{\frac{d\, k_B T\, \alpha\, \langle |a| \rangle n^\beta}{3\,\pi\,\eta\,R^2\,\sqrt{\langle \omega_c \rangle}\,\Delta\,\langle \hat{c}_v \rangle}} \tag{52}$$

Diffusion decreases with increasing R. Thus, the less diffusion limits the control precision, the more the propeller size limits control precision itself. Maximizing control precision therefore means that both limitations have to be approximately equal:

$$\tilde{x} = h_1 R \tag{53}$$

The parameter h_1 was introduced since it is not obvious how the size parameter R should be compared to the diffusion length scale (e.g. radius or diameter). Using equation 52, this can be rewritten as:

$$R = \sqrt[4]{\frac{d k_B T \, \alpha \, \langle |a| \rangle n^\beta}{h_1^2 \, 3 \, \pi \, \eta \sqrt{\langle \omega_c \rangle \Delta} \, \langle \hat{c}_v \rangle}} \tag{54}$$

If the step length $\langle |a| \rangle$ is too small, the propellers diffuse more than they propel during one control step. During the next control step, the propellers would have to cancel the diffusion that occurred during the last control step and additionally reach the intended end positions of the second control step. Thus, the propellers end up unsuccessfully trying to cancel out diffusion and do not advance along the intended trajectory. Therefore, it is necessary to demand that the propellers outswim diffusion at least h_2 times:

$$\langle |a| \rangle > h_2 \, \hat{x} = h_2 \, h_1 \, R \tag{55}$$

Using equations 53 and 55, equation 54 can be rewritten as:

$$R > \sqrt[3]{\frac{h_2 \, d \, k_B \, T \, \alpha \, n^\beta}{h_1 \, 3 \, \pi \, \eta \, \sqrt{\langle \omega_c \rangle \Delta} \langle \hat{c}_v \rangle}} \tag{56}$$

The control precision is maximized when R and $\tilde{x}$ are minimized, i.e. when the inequalities 55 and 56 become equalities. From this an optimal size for the propeller R^{opt} can be obtained:

$$R^{\text{opt}} = \sqrt[3]{\frac{h_2 \, d \, k_B \, T \, \alpha \, n^\beta}{h_1 \, 3 \, \pi \, \eta \, \sqrt{\langle \omega_c \rangle \Delta} \langle \hat{c}_v \rangle}} \tag{57}$$

The corresponding optimal average control time is:

$$\langle \tau^{\text{opt}} \rangle = \frac{\alpha \, n^\beta h_1 \, h_2}{\sqrt{\langle \omega_c \rangle \Delta} \, \langle \hat{c}_v \rangle} \tag{58}$$

Based on experimental observations [116] and theoretical calculations [181], the achievable swarm control precision can be estimated. Using $h_1 = 1$, $h_2 = 2$, $d = 2$ (assuming the

propellers are gravitationally bound to a surface), $n = 5$, $\langle \omega_c \rangle = 100$ Hz, $\Delta = 10$, $\langle \hat{c}_v \rangle = 0.2$, $\alpha \approx 1.7$ and a medium of water at room temperature results in:

$$R^{\text{opt}} = 1.4 \, \mu\text{m}, \qquad \langle |a^{\text{opt}}| \rangle = 2.8 \, \mu\text{m} \quad \text{and} \quad \tau^{\text{opt}} = 3.3 \, \text{s} \qquad (59)$$

The average control time τ^{opt} corresponds in this case to an average of 154 rotations of the propeller with the smallest critical frequency during one control step. The additional constraint, that it is not possible to switch arbitrarily fast between orthogonal step directions, thus seems less restrictive than the need of the propeller to outswim diffusion. This justifies a posteriori the use of equation 55 in the derivation of R^{opt}. The parameter h_2 is not set by propeller properties or the control task, but must be chosen. Since R^{opt} grows with h_2, h_2 needs to be chosen as small as possible. The choice $h_2 = 2$, seems like a lower limit as it means $\langle |a| \rangle = R + \tilde{x}$. Reducing $\langle |a| \rangle$ by reducing the parameter h_2, will most likely not increase the control accuracy.

It might seem that the average speed with which the propellers move, $\langle v \rangle = \langle |a^{\text{opt}}| \rangle / \tau^{\text{opt}}$, cannot be chosen anymore. This is not the case since $\langle v \rangle$ depends on B and h_2:

$$\langle v \rangle = \sqrt[3]{\frac{h_2 \, d \, k_B \, T}{h_1 \, 3 \, \pi \, \eta} \left(\frac{\alpha \, n^\beta \sqrt{c_F}}{\sqrt{B} \, M \, \Delta \, \langle \hat{c}_v \rangle} \right)^{-\frac{2}{3}}} \propto \sqrt[3]{h_2 \, B} \qquad (60)$$

The speed with which the propellers move can be increased by increasing B. Increasing h_2 also increases $\langle v \rangle$, since $R^{\text{opt}} \propto \sqrt[3]{h_2}$ and since larger propellers are faster for constant $\langle \hat{c}_v \rangle$. Thus choosing propeller sizes and control times at optimal values still leaves the freedom of choosing the speed with which the propellers travel along their trajectories.

4.5.5 Comparison to Simulations

To check the analytical results described above, an exemplary 2D control task was simulated using realistic assumptions about propeller properties and control electronics and taking diffusion into account (see section 3.7.1). Parameters in the simulation were adjusted, so that the mean applied magnetic field strength is 1 mT and the parameter h_2 is equal to 2 on average. Since the chosen control task requires that the propellers move with different effective speeds along their trajectories, the condition $h_2 = 2$ is not fulfilled for individual propellers. The simulation is thus similar but not identical to the theoretical case considered in section 4.5.4, also because the sampled propeller properties do not correspond to the average values of their distributions.
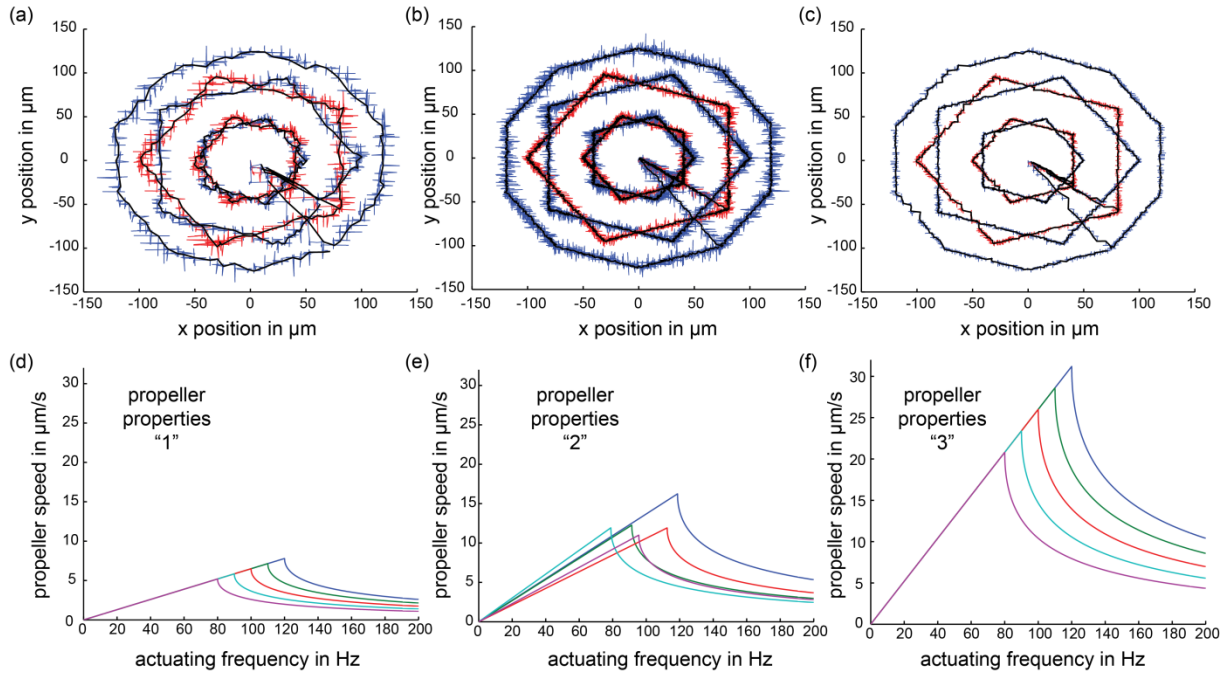
Figure 4-23: Visualization of simulations. Five propellers trace a pattern of intertwined pentagons surrounded by a decagon. The effective speed with which the outermost propeller travels along the trajectory is approximately constant, but different in the three cases, so that the mean magnetic field strength is equal to 1 mT. The minimum step length was adjusted so that the propellers outswim diffusion on average twice (h_2=2). The propeller size (R) was set to 1.3 µm. The propeller properties for the three explored cases are displayed in panels d, e and f. The resulting propeller trajectories are displayed in panels a, b and c respectively. The red and blue lines trace the complete movement of the propellers, including excursions. The black lines trace the positions of the propellers at the end of completed control steps. It is apparent that well-spaced critical frequencies and high propulsion parameters increase the accuracy of the trajectories. This figure is part of a submitted manuscript.

In order to show that swarm control can have interesting applications, a pattern of braided pentagons was chosen to demonstrate swarm control (Figure 4-23). Catalytic patterning [185] could be used to translate such trajectories into intertwined structures that would be very difficult to produce in other ways. A decagon was added, around which a propeller is moving at approximately constant speed, to show that it is possible to impose the speed of the propeller motion. Three sets of propeller properties ω_c and c_v were sampled from the distributions given in equations 49 and 48. The chosen parameters are given in Table 1.

Table 1:

propeller properties	"1"	"2"	"3"
$(\lambda_3 \times \mu m)/R$	0.05	0.08	0.2
$(\lambda_4 \times \mu m)/R$	0	0.06	0
λ_5	0	0.9	0

R^{min}	1.4 µm	1.1 µm	0.9 µm
corresponding R^{opt}	2.3 µm	1.7 µm	1.4 µm
$R^{\text{min}}/R^{\text{opt}}$	0.61	0.65	0.64

Three sets of properties were considered for five propellers of equal size. In set "2" the propellers have randomly sampled properties. In set "1" and "3" the critical frequencies are well spaced and the propulsion parameters are equal for all propellers and relatively low in set "1" and close to maximal in set "3". The spacing parameter Δ was always equal to 10 Hz and the mean critical frequency $\langle \omega_c \rangle$ was always equal to 100 Hz. The corresponding propeller properties are realistic based on experimental observations [116] and theoretical calculations [181]. The resulting propeller trajectories are displayed in Figure 4-23 for all three sets of propeller parameters. It can be seen that the intended trajectory can be most accurately traced, when the propellers have a high propulsion parameter and well-spaced critical frequencies. If the propeller properties are random, swarm control is still possible as can be seen in Figure 4-23 b.

The accuracy with which the intended trajectory is traced can be quantified by the average distance of the propeller from the trajectory. Figure 4-24 displays the achieved control accuracy for different propeller sizes and the three sets of propeller properties (Table 1). Two different accuracy measures are displayed. The first is the average distance from the intended trajectory taking excursions into account. The second is the average distance to the intended trajectory of propeller positions after completed control steps. This second measure thus does not take excursions into account and is thus different from zero only due to diffusion. The propeller size at which this second accuracy measure is equal to the propeller size is called R^{min} (see Table 1). It is similar to the theoretical concept of R^{opt} defined above. Indeed the ratio $R^{\text{min}}/R^{\text{opt}}$ is similar for all three sets of propeller properties, despite the fact that the simulations are in many ways not equivalent to the situation that was assumed in deriving R^{opt} (e.g. $\tilde{x}$ is not equal to the average distance to the intended trajectory). This ratio would also have been approximately constant if the accuracy measure with excursions had been used to define R^{min}.
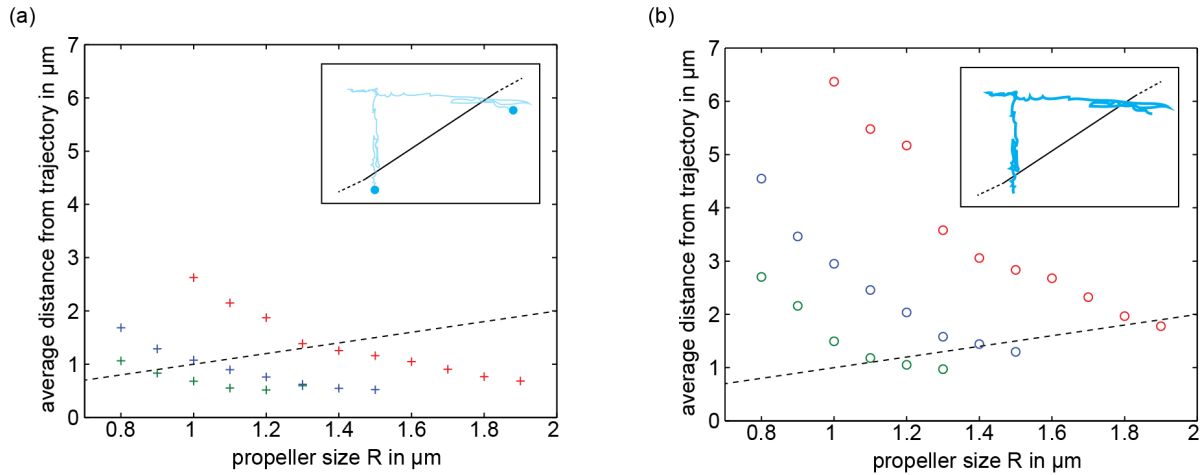
Figure 4-24: The achieved control accuracies depend on the propeller size. This relationship is shown here for three sets of propeller properties (set "1" in green, set "2" in blue, set "3" in red). Data points were generated by running simulations of an exemplary control task as described in the main text. The parameter h_2 was adjusted to 2, by changing the minimum step length. The mean magnetic field strength was set equal to 1 mT by adjusting the target speed with which the propellers moved. (a) Crosses indicate the average distance from the intended trajectory for propeller positions after completed control steps. This measure of accuracy is visualized in the inset. The distance to the intended trajectory (black line) is measured only at the beginning and the end of the control step (blue dots). The dashed line indicates where the control accuracy is equal to the propeller size. The intersections of the crosses with this line define R^{min}. (b) Circles indicate the overall average distance from the intended trajectory, a measure of accuracy that takes excursions into account. The average distance to the intended trajectory would be averaged over the complete blue line in the explanatory inset. The intersections of the circles with the dashed line could be used to define another optimal propeller size. This figure is part of a submitted manuscript.

4.5.6   Discussion

Critical control is a very promising control strategy that might enable the practical realization of swarm control for magnetic propellers. When critical control is not used and control frequencies are chosen at random, the control times grow many orders of magnitude longer, making swarm control impossible in practice.

In demonstrating the optimality of critical control, equation 26 has been used explicitly for the relationship between the propeller speed and the actuating frequency. While this expression is in good agreement with experimental data (see section 4.3.4), its derivation depends on assumptions, which in practice are only approximately valid. For example, the axis of rotation can depend on the frequency [156], although this does not seem to change the relationship between propeller speed and actuating frequency significantly (see section 4.3.4). Small changes to equation 26 probably do not make critical control suboptimal. In fact, it might be

possible to generalize the notion of critical control. It might be always optimal to operate propellers at points of greatest nonlinearity or maximum speed in the relationship between propeller speed and actuating frequency.

An important next step would be to perform a sensitivity analysis, since in practice the propeller parameters can only be measured with finite precision. How errors in the propeller parameters, the applied field frequencies and actuation durations translate into errors in the final propeller positions should be investigated. The necessary precision should be considered when designing propellers, as well as when designing an experimental setup for the practical realization of swarm control.

The derivation of the optimal propeller size (R^{opt}) assumes that the propeller size should be approximately equal to the diffusion that occurs during one control step. This measure for control accuracy is certainly not the only possible one. When control accuracy is measured by the mean distance from the intended trajectory in the context of the simulations, a different "optimal" propeller size (R^{min}) is indeed obtained. The fact that the ratio between these two is constant seems to show that the choice of control accuracy measure results in a multiplicative factor. The dependence of R^{opt} on the number of propellers, the propeller parameters, temperature and viscosity and the dimensionality of the control problem as described in equation 57, is thus probably independent of the choice of control accuracy measure.

In addition, the simulations are based on one particular sampling of propeller properties whereas the theoretical treatment is based on averages for these properties. That the discrepancy between theory and simulation is nonetheless only a multiplicative factor suggests that the predictions of equation 57 are quite robust and could be used to guide the design of magnetic propellers for swarm control tasks.

In the simulations, the effect of diffusion on the position of propellers was explicitly included. Effects that diffusion could have on the propulsion of the propeller itself were, however, not included [115]. If the propeller is so small that rotational diffusion is significant in comparison with the rotation of the propeller due to the actuating magnetic field, the possibility of swarm control might indeed be compromised. Whether this is the case or not will depend on the propeller geometry, its magnetization and the applied magnetic fields. For the smallest propeller sizes discussed here ($\approx$ 1 μm), it is possible to construct propellers that still behave as described by equation 26 (see section 4.3.4). Therefore, performing control

tasks in practice with similar accuracies as those demonstrated in the presented simulations seems feasible.

In the theoretical considerations and the simulations, the effects of interactions between propellers or between propellers and other objects and surfaces were not considered. Propellers can obviously not move through each other, but the flow fields they produce might influence each other also when propellers are close together without actually touching. If the movement of propellers has to be controlled not in isotropic liquid, but in constrained geometries, friction might alter the movement of the propellers. Propellers gravitating towards a surface would for example tend to roll along the surface (see section 4.2). In microfluidic devices or for in vivo applications the movement of the liquid itself would be superimposed on the movement of the propellers. Although these effects do not seem to make swarm control impossible, nor to impose fundamental limitations on it, realizing swarm control for magnetic propellers in practice will probably be easiest if the propellers move in homogenous fluid and are sufficiently separated. This situation was studied here.

4.6   Collective Behavior of Magnetic Propellers

4.6.1   Dynamic Self-assembly of Magnetic Propellers at an Interface

When propellers were swimming upwards against gravity, towards the upper capillary surface, the formation of clusters was observed (see section 3.5.7). Clusters formed when using homogenous nanofabricated propellers (see section 3.2) as well as when using heterogeneous self-assembled propellers of random shape (see section 3.1). Individual propellers start to assemble into small clusters, which over time merge into larger clusters. When the actuating rotating field was switched off the propellers aggregated into chain-like arrangements which slowly sediment towards the bottom of the capillary. Switching the field back on restarted the cluster formation process.

The dynamic equilibrium shape of clusters is circular and relaxation times grow with the cluster size, from seconds to many minutes, for the observed range of cluster sizes from about 10 μm to about 300 μm. Clusters can be quasi 2D monolayers of propellers, but they can also extend downward, perpendicular to the upper capillary surface. Especially larger clusters tend to have a 3D structure with propellers rotating below the first layer of propellers in a way that is reminiscent of a tornado. In clusters based on identical nanofabricated propellers, a crystal

like arrangement of propellers can be observed. Clusters slowly rotate in the direction of the actuating field and smaller clusters rotate faster than larger clusters. Sufficiently large clusters are surrounded by a boundary layer in which the angular velocity with which propellers move around the cluster center is much higher than in the rest of the cluster. Examples of clusters are presented in Figure 4-25.
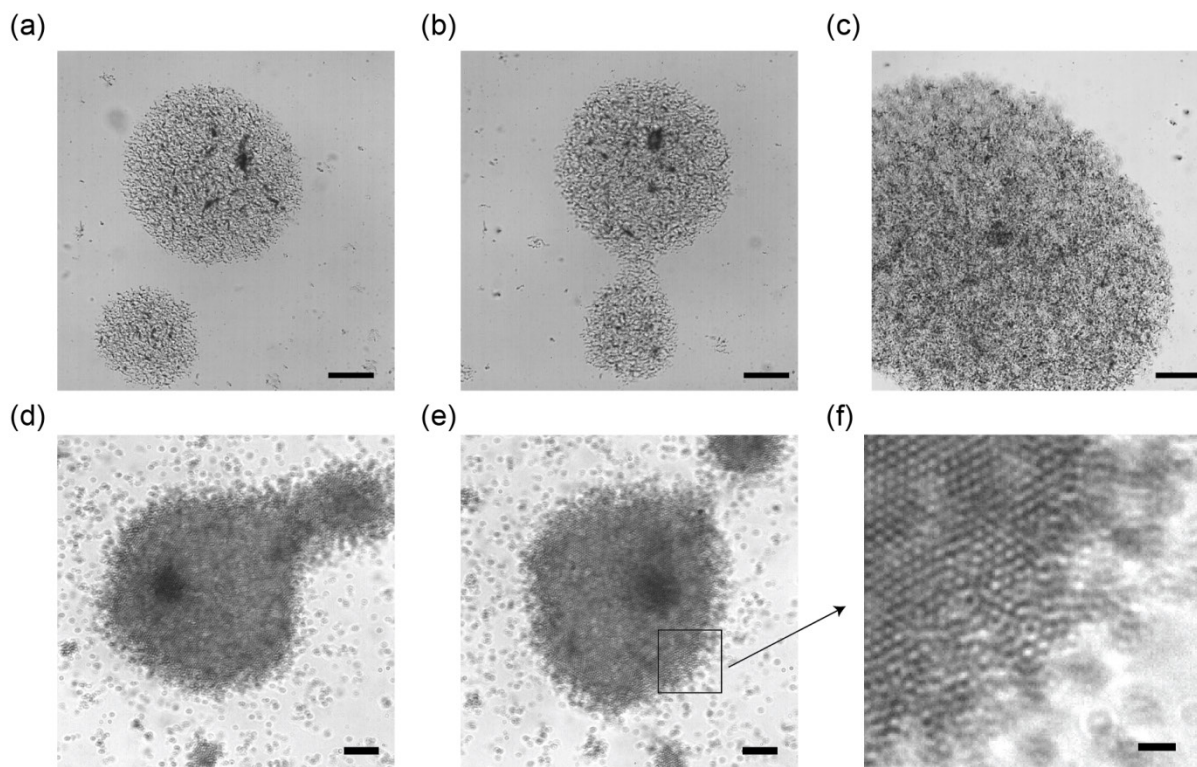
Figure 4-25: Examples of clusters formed by dynamic self-assembly. (a)-(c) Propellers from solution synthesis (see section 3.1). (d)-(f) Nanofabricated propellers (see section 3.2) (a) Clusters obtain a circular shape in dynamic equilibrium. Scale bar is 20 μm. (b) After initial formation or after the merging of circular clusters, more complex cluster shapes can be observed. These complex shapes can persist from seconds to many minutes, depending on their size. Scale bar is 20 μm. (c) If the propeller concentration at the upper capillary surface is sufficiently high, very big clusters can be observed. Scale bar is 20 μm. (d) Complex cluster shapes can also be observed for nanofabricated propellers. Scale bar is 10 μm. (e) The dynamic equilibrium shape is circular for nanofabricated propellers as well. The square indicates the position of image (f). Scale bar is 10 μm. (f) Close view of a cluster consisting of nanofabricated propellers. Individual propellers are visible as bright dots. Single or small groups of propellers can be seen outside of the cluster. After a transition zone at the edge of the cluster, a crystalline pattern can be seen inside the cluster. Scale bar is 2 μm.

4.6.2   Conditions for Self-assembly

It was observed in experiments that several conditions need to be fulfilled for cluster formation to occur. Firstly, the propeller concentration needs to be sufficiently high. In

general, higher concentrations of propellers allow the formation of larger clusters. The propeller concentration at the upper capillary surface depends on the propeller concentration of the starting solution. For propellers from solution synthesis the concentration depends also on the actuating field (see section 4.3.1). For nanofabricated propellers, nearly all propellers in solution reach the upper capillary surface if the actuating field allows any propeller to reach the upper capillary surface. Secondly, the frequency of the actuating field needs to be set to suitable values for clusters to form. If the frequency is too high, the propellers do not rotate with the field frequency, lose synchrony and only aggregate into irregular chain-like arrangements. If the frequency is too low, multiple propellers rotate around a common center, instead of around their body axes. Clusters can form in an intermediate frequency region (see Figure 4-26). The frequency range which allows cluster formation depends on the viscosity of the fluid, the field strength of the actuating magnetic field and the magnetic and hydrodynamic properties of the propellers.
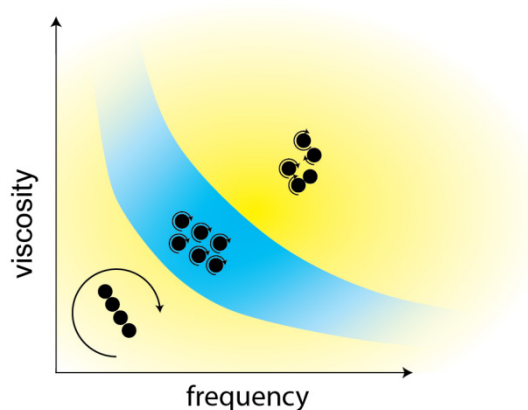
Figure 4-26: Schematic of conditions for cluster formation. If the frequency is too high, the propellers do not rotate with the field frequency and lose synchrony. If the frequency is too low, multiple propellers rotate around a common center, instead of their individual center. Clusters can form in an intermediate region (blue area). The field strength of the magnetic field influences the position and potentially also the shape of the blue region. In addition, a sufficiently high propeller concentration is a requirement for cluster formation. The concentration of propellers at the upper glass surface is (at least for the self-assembled propellers) influenced by the field strength and field frequency.

4.6.3 All Observed Clusters have Similar Properties

Studying the assembly of propellers in a cluster is challenging, since the size of the propellers is comparable to the resolution limit of the used optical microscope. For clusters consisting of

propellers from solution synthesis with different sizes and shapes, the reliable identification of individual propellers was not possible. Individual identical nanofabricated propellers can be identified despite their small size (see sections 3.2 and 3.6.2). Based on a 2D Fourier transform of the propeller positions, the arrangement of nanofabricated propellers seems to be hexagonal (Figure 4-27). The Fourier patterns of clusters of different sizes as well as clusters actuated at different frequencies are very similar (Figure 4-27 a, b, c and f). For low actuating frequencies, the hexagonal arrangement is not visible anymore, although some cluster formation still occurs (Figure 4-27 d and e). The arrangement of propellers in a cluster thus seems to be independent of the cluster size, as well as the actuating frequency.
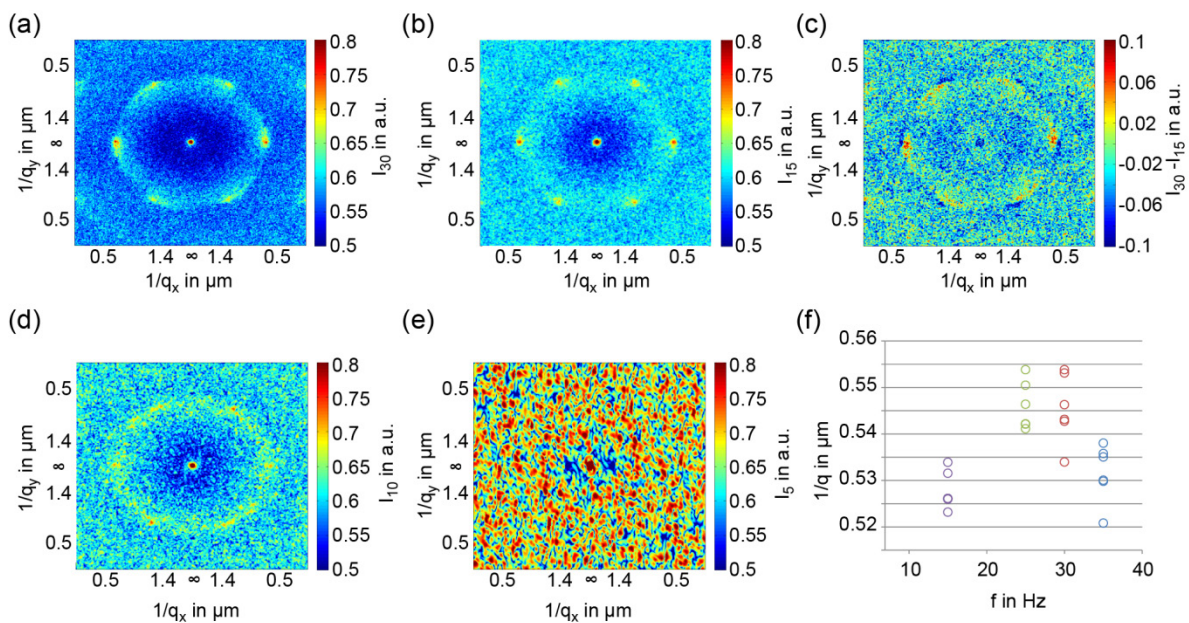
Figure 4-27: Weighted sum of normalized 2D Fourier transforms of propeller positions in clusters for different actuating frequencies (see section 3.6.2). The x and y axes denote distances in real space (q being a point in reciprocal space). The field strength of the actuating field was 2 mT in all cases. The frequency is 30 Hz in (a), 15 Hz in (b), 10 Hz in (d) and 5 Hz in (e). Panel (c) displays the difference between (a) and (b). (f) The distances ($q = \sqrt{q_x^2 + q_y^2}$) to the six peaks (hexagonal lattice) are measured for different frequencies f. The measurements for f = 15 Hz and f = 30 Hz are based on panel (b) and (a) respectively.

4.6.4 No Cluster Formation for Ferromagnetic Spheres

Complementary experiments were performed using ferromagnetic spheres of diameter 8.5 μm (see section 3.5.7). Under the influence of a rotating magnetic field (vector of rotation perpendicular to the lower capillary surface) these spheres stayed at the lower capillary surface and started to rotate. The applied magnetic fields were not sufficiently strong to keep

the magnetic moment of the ferromagnetic spheres confined to the plane parallel to the lower capillary surface. Non-planar sphere rotation was observed in videos of actuated spheres.

In the absence of an external magnetic field, the ferromagnetic spheres assembled into irregular chain-like aggregates (Figure 4-28 a). When an external magnetic field was switched on, the spheres started their non-planar rotation, breaking up most chain-like aggregates and started to move around each other. No cluster formation was observed in this system (Figure 4-28 b).

A simple calculation shows how non-planar rotation can result in repulsive magnetic interactions between ferromagnetic particles. Assuming two spheres precess around an axis perpendicular to the lower capillary surface with precession angle ϑ, the cycle averaged magnetic interaction between the spheres is given by $F_{\text{mag}} = \frac{3\mu_0 m^2}{4\pi r^5}\left(\frac{2}{3} - \sin^2\vartheta\right)$ (see Figure 4-28 c). Here, μ_0 is the vacuum permeability, m the magnetization of the spheres and r the distance between the spheres. The interaction becomes repulsive for $\vartheta < 57{,}74°$. This angle is known as the magic angle [262]. The actual motion of the ferromagnetic spheres as observed in video recordings appears to be more complex than simple precession. The presented calculation is only meant to show that out of plane rotation can in principle lead to repulsive magnetic interactions.
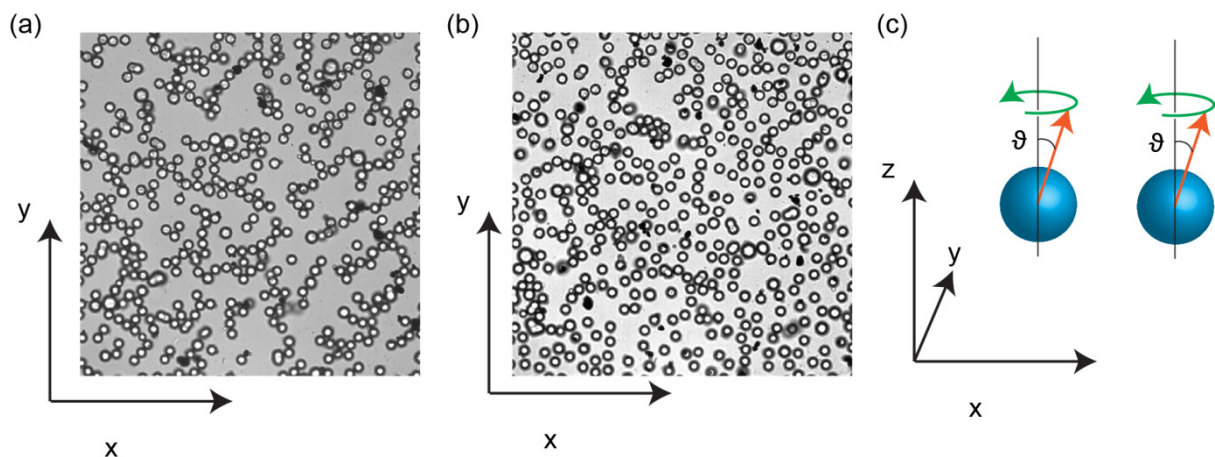
Figure 4-28: Ferromagnetic spheres under the influence of a rotating external magnetic field. (a) Ferromagnetic spheres at the bottom surface of the capillary in the absence of a rotating magnetic field. (b) After the application of an external magnetic field, rotating in the x-y plane with 2 Hz and 2 mT, partial disaggregation is observed, but no cluster formation. Partial disaggregation is more easily observed in a video of the disaggregation process than in the image presented here. (c) Schematic illustration of the possibility that the magnetic moments of the ferromagnetic spheres rotate out of the x-y plane. The actual motion of the spheres is most likely more complex than the situation depicted in this schematic.

4.6.5 Hydrodynamic Interactions Studied by Flow Visualization

Polystyrene particles are non-magnetic probes which move only due to hydrodynamic forces (see section 3.5.6). Their movement can thus be used to estimate the relative importance of hydrodynamic interactions between propellers.

Single propellers interact with single beads in that they move the bead on a circular trajectory around the propeller whereas the distance between bead and propeller stays approximately constant (Figure 4-29). This is consistent with the assumption that the propeller behaves hydrodynamically similar to a sphere.
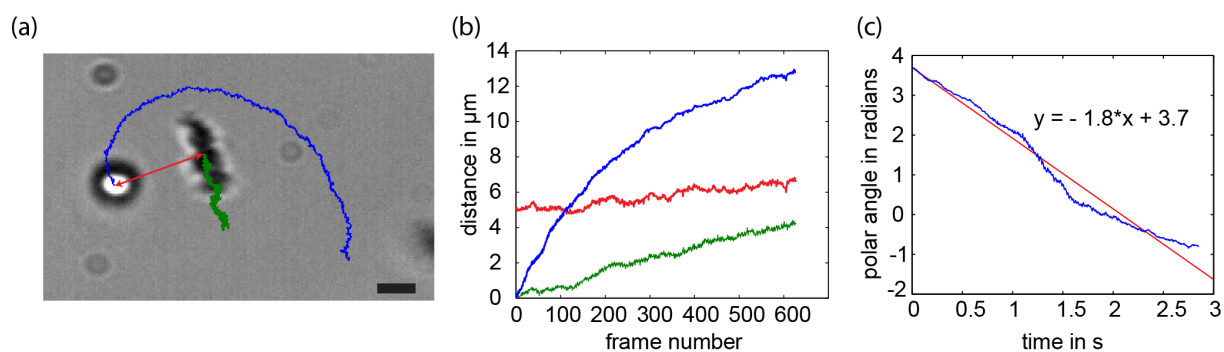
Figure 4-29: Visualization of the flow produced by a propeller as observed using a polystyrene tracer particle. (a) Image taken from a video of a propeller interacting with a polystyrene particle recorded at 220 frames per second. The propeller rotates with the frequency of the actuating field (1.3 mT, 40 Hz). The blue trace indicates the movement of the bead during the 2.8 s of recorded video. The green trace indicates the movement of the propeller. The red arrow indicates the distance between the propeller and the bead. Scale bar is 2 μm. (b) The distance of the propeller (green) and the bead (blue line) from their respective starting positions is plotted against the frame number. The red line is the distance between the propeller and the bead. (c) The motion of the propeller can be subtracted from the motion of the bead, resulting in a roughly circular trajectory. The bead positions relative to the propeller can be converted to polar coordinates. The polar angle is plotted against time, showing that the bead rotates around the propeller with approximately constant angular velocity. The red line is a linear fit and the slope of the fit can be converted to the rotation frequency of the bead around the propeller of about 0.3 Hz.

110

Figure 4-30 displays images taken from a video showing two interacting propellers, one of which is also interacting with a polystyrene bead. This video was used to compare the relative magnitude of hydrodynamic and magnetic interactions. Assuming that the propellers behave hydrodynamically similar to spheres, the force that brings the propellers closer to each other must be purely magnetic. The left propeller in Figure 4-30 a moves with about 0.9 µm × s^{-1} perpendicular to the line connecting the propellers, thus moving only about 23 nm during one propeller rotation. Assuming the propeller does not move at all during one rotation, the magnetic interaction can be shown to be purely radial. This suggests that the non-radial movement is due to hydrodynamic interactions between the propellers. The radial distance between the propellers decreases from 9.3 µm to 6.3 µm in a period of 4 seconds corresponding to an average speed of 0.38 µm × s^{-1}. Thus the effect of the hydrodynamic interactions is here of comparable magnitude to the effect of the magnetic interactions.
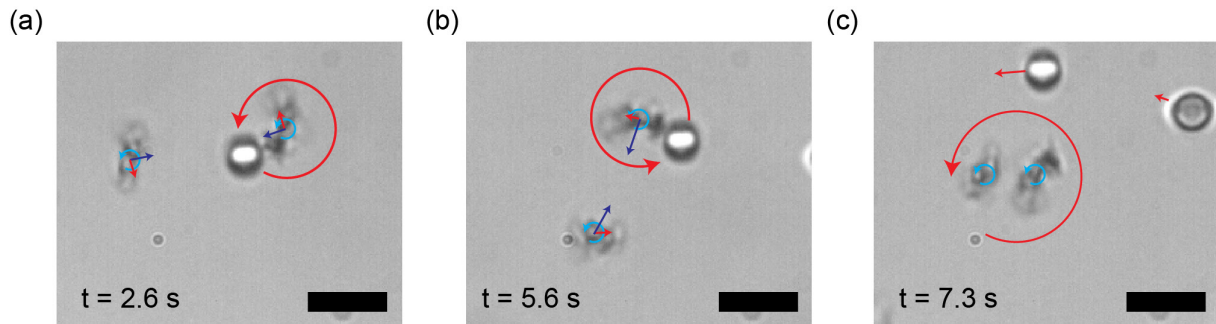
Figure 4-30: Visualization of hydrodynamic interactions using polystyrene tracer particles. Images are taken from a movie recorded at 220 frames per second. The time points from which the frames are taken are indicated in the lower left corner of each panel. Red arrows indicate movement caused by hydrodynamic interactions. Dark blue arrows indicate movement caused by magnetic interactions and light blue arrows indicate the propeller rotation caused by the external rotating magnetic field. Scale bars are 5 µm. (a) A polystyrene tracer particle is moving around the right propeller at constant separation. (b) The propellers have moved closer to each other and around each other due to magnetic and hydrodynamic interactions respectively. The polystyrene bead is still rotating around the propeller. (c) The magnetic propellers have moved into close contact and move around each other quickly. The two polystyrene beads are subject to the flow fields created by the propeller pair.

4.6.6 Simulations Qualitatively Reproduce Observations

Simulations were performed to gain a better understanding of the cluster formation process. The interactions between propellers were modelled as described in section 3.7.2. Three types of simulations were performed. In all simulations, propellers were modelled as magnetic

dipoles, rotating in and confined to a 2D plane, with the magnetic dipole rigidly linked to the propeller orientation.

In **Simulation 1**, hydrodynamic interactions were excluded except for the linear coupling of forces and torques to translational and angular velocities. Propellers were kept apart by an artificially introduced short-range repulsion. This simulation could already qualitatively reproduce the conditions needed for cluster formation described in section 4.6.2 (Figure 4-31). Clusters formed in an intermediate frequency range where the direction of the magnetization of all propellers followed the external magnetic field with a small phase lag.

Therefore, the time dependent dipole orientation was imposed in **Simulation 2**, reducing the degrees of freedom per propeller to two. Magnetic dipole-dipole interactions were considered explicitly (no cycle averaging) in **Simulation 2**. Additionally introducing an interaction cut-off and a neighbor list increased the number of propellers that could be handled from about 50 to about 1600. In this case, however, only the parameter regime suitable for cluster formation could be investigated. Simulated clusters also rotate with the direction of the actuating field, albeit much slower. Larger clusters rotate more slowly than smaller clusters in the simulations. This is in agreement with experimental observations. Some propellers at the edge of the cluster seem to move faster around the cluster than would be expected based on the angular velocity of the cluster rotation also in **Simulation 2**. However, the experimental observation of a boundary layer with increased angular velocity could not be reproduced using **Simulation 2**.
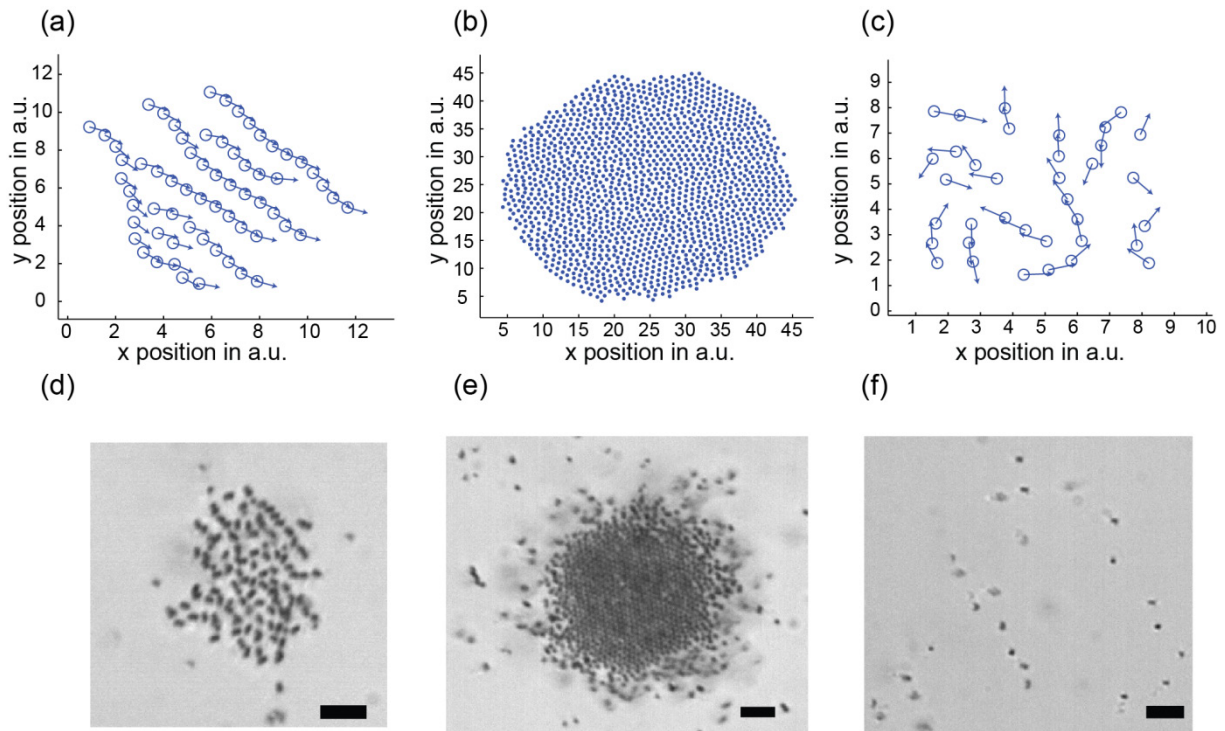
Figure 4-31: Comparison of simulations with experiments. The actuating fields are always rotating in the image plane. (a) Simulations with explicit magnetic moment orientations (**Simulation 1**). The simulated actuating field has amplitude $B_0 = 2$ and rotates with a frequency of 2 Hz. Starting with 64 particles arranged on a square grid. Chain-like structures are able to turn with the slow actuating field and break and reform constantly. (b) Simulated actuating field rotates with frequency 40 Hz and sufficiently strong to align all propellers with the field at all times. Simulations with magnetic moment orientations fixed to the external field (**Simulation 2**). Starting with 1600 particles arranged on a square grid. After a while a circular cluster forms, which rotates in the same direction as the magnetic field (though much more slowly). (c) Simulations with explicit magnetic moment orientations (**Simulation 1**). Simulated actuating field has amplitude $B_0 = 2$ and rotates with frequency 200 Hz. Starting with 36 particles arranged on a square grid. Individual magnetic moments cannot follow the fast rotation of the external magnetic field. The particles slowly aggregate into chain-like structures, while the magnetic moments twitch while trying to follow the external magnetic field. (d) The qualitative behavior observed in simulations has also been observed in experiments. The actuating field is 2 mT, 5 Hz. Chain-like structures tend to form, which continuously break and reform. Some propellers are not fully parallel to the vector of rotation of the actuating field. (e) The actuating field is 2 mT, 15 Hz. Propellers are mostly oriented perpendicular to the field of view and form a cluster. The cluster turns slowly in the direction of rotation of the external magnetic field. Propellers at the edge of the cluster move around the cluster at higher speed than the angular velocity of the cluster rotation. (f) The actuating field is 2 mT, 100 Hz. Propellers are mostly parallel to the field of view. They interact weakly and move around due to diffusion. Scale bars are 4 μm.

As discussed in section 4.6.5, hydrodynamic interactions between propellers do not seem to be entirely negligible. In **Simulation 3**, an effective hydrodynamic interaction between propellers was introduced. This effective interaction was chosen such that it reproduces the

analytical solution of a situation in which two spheres (rotating around their centers) rotate around each other (see section 3.7.2). Since this effective hydrodynamic interaction only exists when propellers rotate fast compared to their translational movement, the magnetic interaction was replaced by its cycle averaged equivalent. The magnetic interaction is thus purely radial, whereas the effective hydrodynamic interaction is purely azimuthal. Figure 4-32 shows that **Simulation 3** reproduces the cluster edge layer with fast moving propellers much better than **Simulation 2**. **Simulation 3** also reproduces the observation that small clusters do not possess an edge layer containing fast propellers, whereas sufficiently large clusters do. All simulations can reproduce the hexagonal arrangement of propellers. Large clusters can have many differently oriented crystallites leading to approximate rotational symmetry.
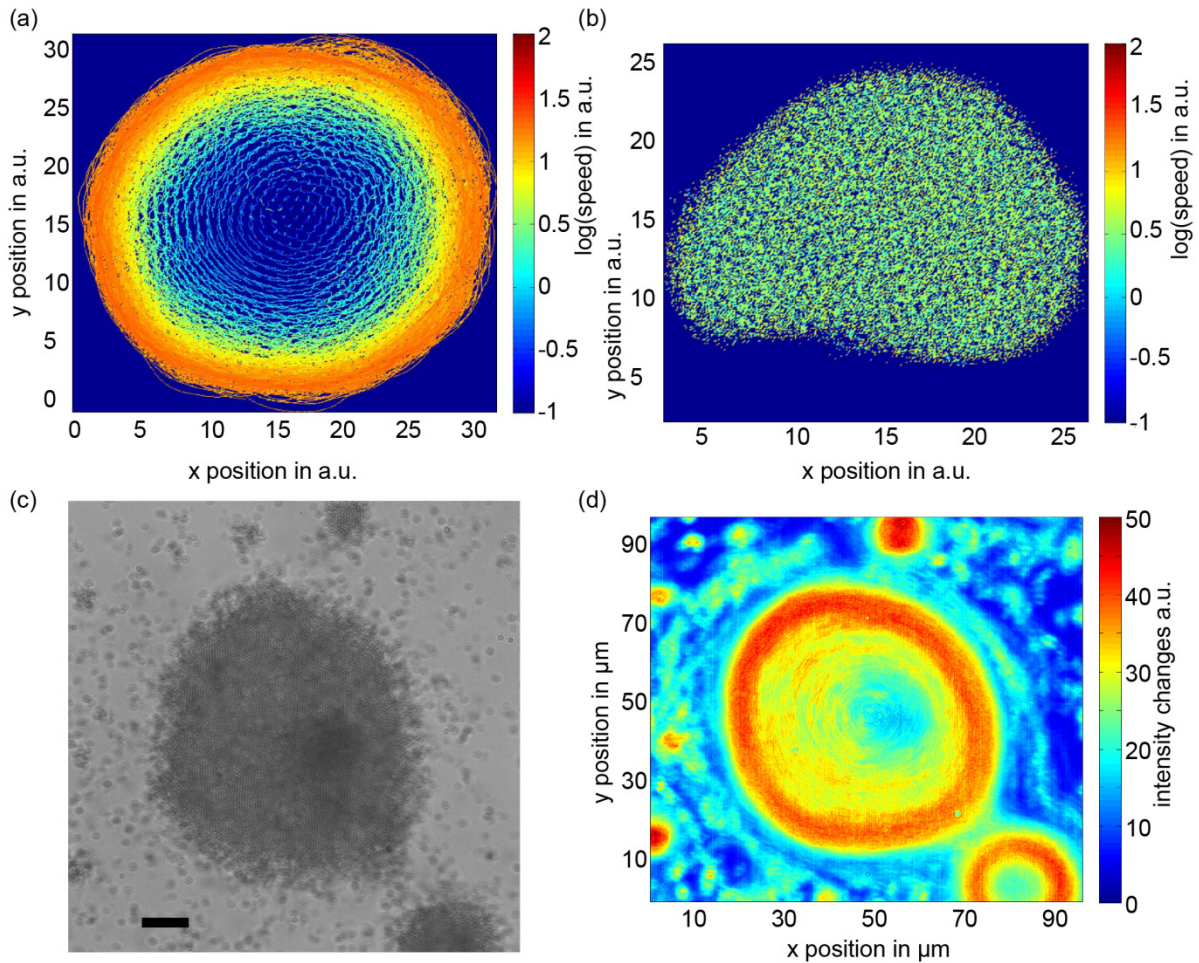
Figure 4-32: Comparison of experimentally observed boundary layer with simulations. (a) Visualization of spatial speed distribution based on **Simulation 3** (cycle averaged magnetic interactions with effective hydrodynamic interactions). The simulation was run for 10 seconds, starting with 900 particles arranged on a square grid. Speeds were visualized for the last 4.4 seconds when a steady state had been reached. The actuating frequency was 40 Hz. For the visualization, instantaneous speeds were averaged in a 500 by 500 pixel grid. (b) Visualization of the spatial speed distribution for **Simulation 2** (no effective hydrodynamic interactions). The simulation was run for 20 seconds, starting with 400 particles arranged on a square grid. Speeds were visualized for the last 5 seconds when a steady state had been reached. The actuating frequency was 40 Hz. For the visualization, speeds were averaged in a 300 by 300 pixel grid. (c) Optical microscopy image of an experimentally observed cluster (actuating field: 25 Hz, 2 mT). Scale bar is 10 μm. (d) Visualization of spatial speed distribution for the cluster in (c) (see section 3.6.3). Intensity differences between frames are summed over a period of 4.5 seconds for every pixel in a video recorded at 200 frames per second (see section 3.6.3).

4.6.7   Discussion

At first sight, the observed cluster formation appears similar to the dynamic self-assembly of magnetic spinners described by Grzybowski et al. [4] (see also section 2.4.2). However, the experiments described above show that the hydrodynamics and the mechanism behind cluster

formation is very different here. In the studies by Grzybowski et al., a force pulling all propellers to a central position due to an external gradient field (produced by a bar magnet spinning below the sample) was balanced by radial hydrodynamic repulsion. In these experiments, magnetic inter-particle forces were considered to be negligible. In the system described in this thesis, the external field is homogenous and magnetic as well as hydrodynamic inter-particle forces are not negligible. Conversely, a potential radial component of the effective hydrodynamic forces seems to be negligible here, whereas Grzybowski et al. observed hydrodynamic repulsion.

The 2D arrangement of propellers in a steady state cluster is hexagonal. No clear influence of the actuating field on the propeller-propeller distance could be observed, although the propeller-propeller distance might be slightly elevated at intermediate actuation frequencies (Figure 4-27 f). Improved position measurement techniques for the propellers would be necessary to resolve such a small change. Since no radially repulsive forces are expected at small Reynolds numbers (except steric repulsion), an influence of the actuating frequency on the propeller-propeller distance would also not be expected. The observed propeller-propeller distances are compatible with a close packing of the propellers. The measurement accuracy is, however, not sufficient to exclude the possibility that there is a narrow liquid layer separating the propellers at all times. The long-range order (presence of crystallites, order parameters, etc.) in clusters could be investigated as well, if the detection precision of propeller positions could be improved.

The phase diagram presented in Figure 4-26 is only qualitative. Efforts to make this phase diagram quantitative and map it experimentally are ongoing. Additional experiments could investigate phase transitions or other dynamic phenomena, beyond the steady-state cluster behavior. Theoretical studies have shown that cluster formation is only possible in a certain regime [276, 277]. When hydrodynamic interactions are neglected, the phase transition is first order and the cluster formation proceeds through spinodal decomposition [277]. The presented experimental system seems promising for the study of non-equilibrium effects like dynamic clustering [339, 340] or dynamic self-assembly [4, 85, 256, 341]. It could also be used as a model for crystal nucleation [342-344] or for the study of non-equilibrium pattern formation [345, 346]. The external actuating field provides several control parameters that could be dynamically varied in such experiments.

The simulations qualitatively reproduce the principal features which were experimentally observed during cluster formation, suggesting that the most important interactions between

propellers were captured by the used model. The initial hypothesis that magnetic interactions alone can explain cluster formation had to be rejected, since the edge region with increased angular velocity could only be reproduced when the effective hydrodynamic interactions were included. The parameter c_3 was set to equal to 0.27 in the simulations presented here (see section 3.7.2). Changing this parameter to 0.4 results in qualitatively similar results, indicating that the qualitative behavior is independent of the details of the effective hydrodynamic interaction.

The fact that three different simulations needed to be used is due to numerical constraints. Explicit magnetic interactions (not cycle averaged) and the effective hydrodynamic interaction could in principle be merged into a single simulation and one would expect that this single simulation could qualitatively reproduce cluster formation as well, were it not for impractically long integration times. However, when magnetic interactions are considered explicitly (not cycle averaged) it would be preferable to simulate the hydrodynamics explicitly as well. In addition it would be interesting to see if new effects would be expected at small but non-zero Reynolds number. Such more challenging simulations could be addressed in future work.

Diffusion was not incorporated in the simulations and the simulations were also not quantitative, since the magnetic moment of the propellers, the details of the short-range repulsion and of the hydrodynamic interactions were not known. Future work could improve the simulations in this respect. Especially the tornado-like 3D structure that was observed for some of the larger clusters remains poorly understood.

The simulations suggest that the upwards propulsion of the actuated propellers is not necessary for cluster formation. Cluster formation could not be reproduced using ferromagnetic spheres, but this was probably due to the fact that the actuating fields were not strong enough to enforce in-plane rotation. Since the propellers were hydrodynamically modeled in the simulations as spheres, cluster formation should be reproducible with ferromagnetic spheres when using sufficiently strong magnetic fields. Nevertheless the differences in material properties between ferromagnetic spheres and propellers might also play a role (electrostatic interactions, van der Waals forces, etc.) and it remains to be seen in which systems cluster formation can be reproduced.

The effective hydrodynamic interaction used in the simulations can qualitatively reproduce the formation of a boundary layer which seems very similar to that observed in experiments. The resulting simulated propeller movements are, however, not a solution to the Stokes

equations (equations 2 and 3) that describe the motion of liquids at low Reynold's number. Jäger et al. have applied more advanced simulation techniques on a very similar system [276] (see section 2.4.2). They obtain results which are generally similar to those presented above. Contrary to the observations presented here, cluster rotation was only observed in the presence of hydrodynamic interactions. This might be due to differences in the parameter regimes. The magnetic interaction is indeed purely radial if the translatory propeller movement during one field rotation is negligible. When hydrodynamic interactions were included by Jäger et al., the clusters rotated and the angular velocity increased slightly with the distance to the cluster center. This increase in angular velocity is much more pronounced in the simulations presented here and, in addition, largely confined to a boundary layer. However, further investigations are needed to decide which simulation agrees better with experimental observations. In particular, it would be necessary to reliably identify individual propellers, and to accurately measure angular velocities. If the effective hydrodynamic interaction used in this thesis does indeed capture some important behavior, it should be investigated how this (or a similar) effective hydrodynamic interaction can be derived rigorously from the underlying Stokes equations.

A detailed understanding of the mechanisms behind cluster formation and related non-equilibrium processes could be used to develop new methods for the magnetically guided self-assembly of technologically promising micro- and nanostructures.

5.   Conclusion

5.1   Summary and Outlook

The aim of the presented work was the development of new, simpler and cheaper techniques for the manipulation and assembly of matter on the micro- and nanoscale. Initial synthetic efforts to produce propellers with a specific geometric shape were not successful. However, it was observed that magnetic nanostructures of arbitrary shape, produced in solution by hydrothermal carbonization, can be effectively actuated by external magnetic fields. In fact, all three types of magnetic actuation (rolling, swimming, and propulsion) could be reproduced using the synthesized structures. The developed synthesis is a simple method for the cheap production of large quantities of magnetic nanostructured propellers. Particularly small propellers could be specifically selected, leading to nanopropellers smaller than any previously produced (below 1 µm in every dimension). The propulsion properties are comparable to those of nanofabricated propellers. The geometric properties of propellers (based on 3D reconstructions) could be correlated with their propulsion properties. However, it has so far not been possible to build a model which can predict propulsion properties based on propeller geometry. Interestingly, one of the observed propellers was able to move faster than most previously published nanofabricated propellers.

A simple relationship between actuation frequency and propulsion speed could be theoretically predicted and experimentally verified. This advanced theoretical understanding opened the door for additional theoretical work on swarm control, i.e. the independent control of several propellers, all subject to the same time-dependent magnetic field. Based on analytical results and simulations, it could be demonstrated that such swarm control is in principle feasible, when a particular control strategy (critical control) is used. In addition, conclusions could be drawn about the optimal propeller design for swarm control. Finally, the collective behavior of large numbers of propellers, propelling upwards against gravity and towards a glass interface, was investigated experimentally and using simulations. The observed formation of clusters seems to be mainly due to the magnetic attraction between the propellers. Hydrodynamic interactions are not negligible, but a simple model for effective hydrodynamic interactions is sufficient to capture the most important effects and reach qualitative agreement between simulations and observations. The most important results presented in this thesis are summarized in Figure 5-1.
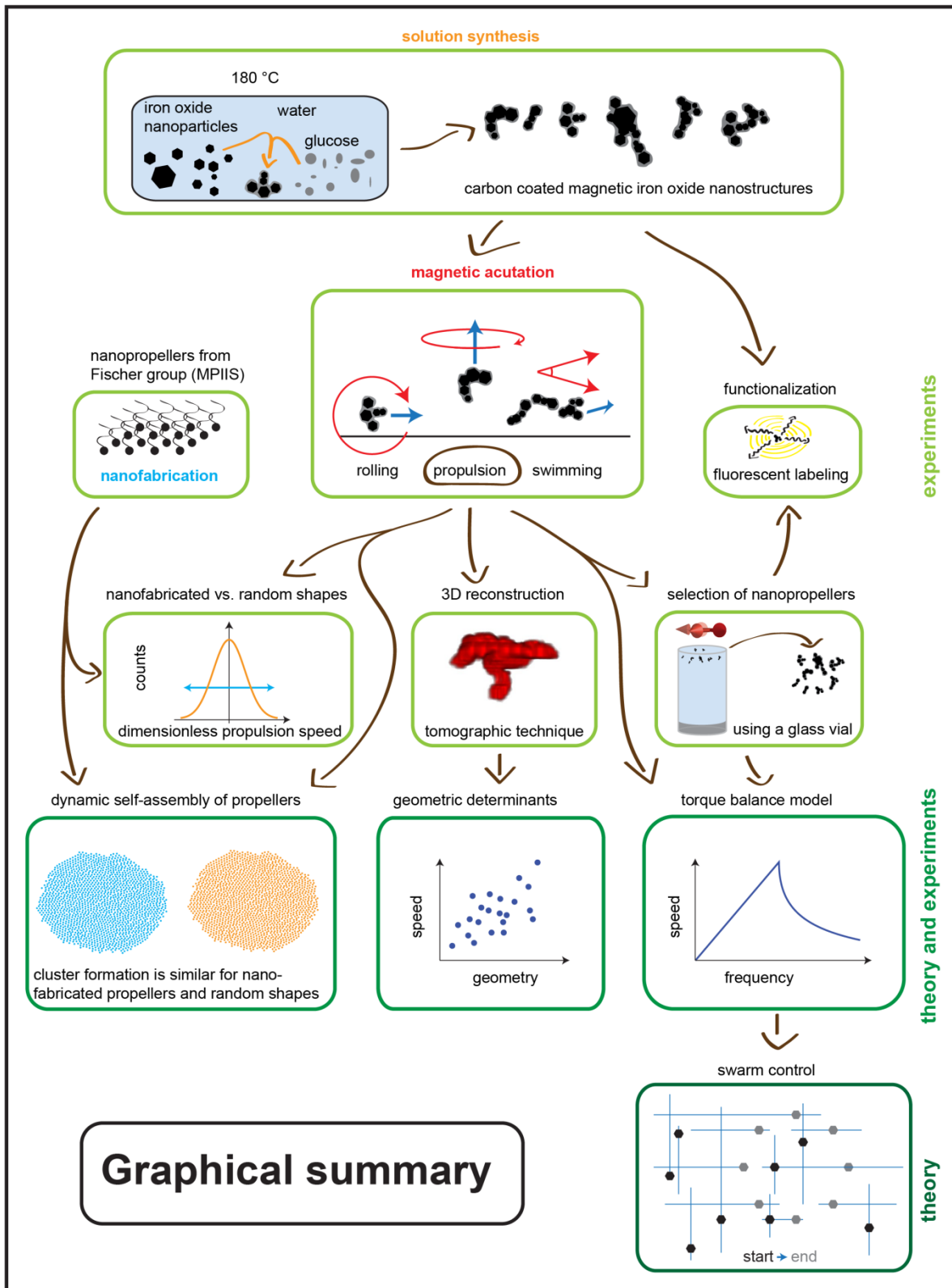
Figure 5-1: Graphical summary of the most important results described in this thesis.

Several open questions and challenges remain. It is interesting to ask whether the smallest nanopropellers reported here have reached a practical lower size limit. Theoretical arguments show that such a lower limit exists, but it remains unclear, which specific size corresponds to this lower limit [115]. It was previously thought that propellers as small as those reported here would not be feasible [115]. The fact that particularly small propellers could be specifically selected suggests that sorting propellers by other criteria (e.g. propulsion speed, rolling speed or magnetic properties) should be possible as well. For a particular application, magnetic nanostructures with suitable properties could be selected from a large pool of cheaply producible randomly shaped nanostructures. Exploring the relationship between propeller geometry and propulsion properties of the propellers with hydrodynamic simulations is ongoing work. An experimental demonstration of swarm control for magnetic propellers could so far not be realized, although several groups seem to be working towards it [164]. A detailed understanding of the collective behavior of propellers is also still missing at present, since the simulations only qualitatively reproduce the observations. A refined understanding of cluster formation could make this experimental system useful for the investigation of non-equilibrium statistical mechanics and dynamic self-assembly.

5.2 Potential Applications

The reported synthesis procedure can cheaply produce large amounts of nano- and micropropellers that can be actuated by rotating magnetic fields. The synthesis method will thus be particularly interesting for applications that require large amounts of propellers and do not require a homogenous propulsion response. The most expensive ingredients in the synthesis are the magnetic nanoparticles. The used NanoArc iron (III) oxide particles are sold for about 1800 € per kg, but suitable magnetic iron oxide nanoparticles could be produced even more cheaply (e.g. by milling iron oxides [347]), since the synthesis of magnetic propellers does not require a particular (e.g. spherical) shape nor a narrow size distribution. According to their website, Sky Spring Nanomaterials Inc. sells suitable nanoparticles for 380 $ per kg.

One potential application that requires large numbers of propellers could be micromixing. As discussed in section 2.1.2 (equation 5), mixing fluids at small scales (low Reynolds numbers) is a difficult task. Theoretical work has shown that it could be achieved by making propellers

move along curved trajectories [348]. The propeller motion can increase the speed of chemical reactions, if for example a catalyst is attached to the propellers [349].

This approach has the additional advantage that the catalyst can be recovered. Catalyst recovery has previously been realized using magnetic nanoparticles that can be actuated by magnetic gradient fields [79-81]. Yet, as discussed in section 2.2, using magnetic torques to actuate propellers instead of gradient fields can be advantageous if the source of the magnetic field cannot be physically close to the actuated structure. If desired, the propellers can also move upwards against gravity and can be thus prevented from sedimentation and separated from sedimenting materials. Similarly, magnetic propellers can be used to adsorb and remove substances from solution [188] (e.g. for water treatment).

The finding that structures of diverse shapes can be used effectively as propellers, suggests that magnetic propulsion could be applied to a wide range of magnetic nanostructures. For example a recently reported diagnostic method for Malaria exploited the magnetic properties of hemozoine molecules [350]. The propeller effect [154], which, as discussed in section 4.4, is not limited to helical shapes, might potentially be useful for the separation and identification of weakly magnetic structures that cannot be conveniently manipulated by magnetic gradient fields.

The discovery of critical control as a promising control strategy for swarm control of several magnetic propellers could enable complex microassembly tasks. One possibility would be to use swarms of propellers to pick up objects and place them at specific locations [11]. The simpler task of positioning propellers (possibly carrying pre-attached objects) at specific locations might be even more interesting. As demonstrated in section 4.5.5, propellers could use catalytic patterning to produce complex, inter-twined structures that would be difficult to produce with conventional microfabrication techniques. One could also arrange a swarm of propellers in a specific pattern and then use microwaves for localized heating [351]. The parallel actuation of large numbers of magnetic propellers or surface rollers without swarm control (e.g. using a single rotating magnetic field for actuation) could also be used for micropatterning and alignment applications.

The observed collective behavior of propellers (cluster formation) seems promising for applications as well. For example, Heurlin et al. reported the gas-phase synthesis of nanorods which could enable highly efficient solar cells, batteries or light-emitting diodes [352]. However, the post-synthesis alignment of these nanorods remains challenging. Applying rotating magnetic fields could offer a simple method to align rod-like nanostructures and

arrange them into dense patterns. Figure 5-2 shows schematically how this could be done. The potential of such strategies has been demonstrated for alumina platelets, which could be organized to produce structures with interesting material properties [15, 274]. Furthermore, the collective behavior of magnetic propellers might present an interesting model system for crystal nucleation, the study of non-equilibrium effects and dynamic self-assembly phenomena.
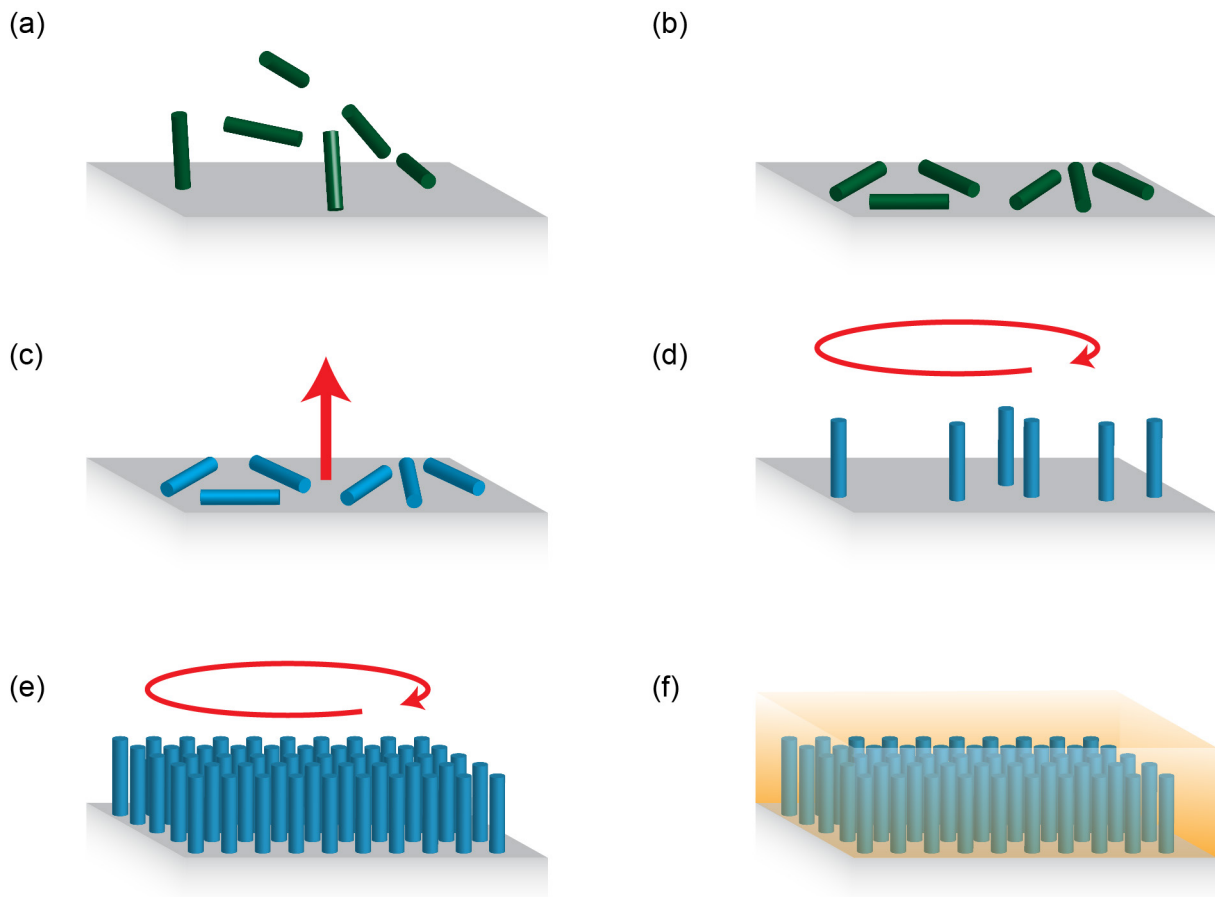
Figure 5-2: Schematic depiction of the proposed nanorod alignment procedure. (a) Magnetic nanorods are dispersed in solution above a surface. (b) Steric alignment of nanorods with the surface can be achieved by sedimentation or by pulling the nanorods towards the surface using a magnetic gradient field. (c) Application of a strong magnetic field perpendicular to the surface magnetizes the nanorods perpendicular to their long axis. (d) Applying a rotating magnetic field makes the nanorods rotate and align perpendicular to the surface. (e) Cluster formation occurs over time and nanorods are organized in a dense hexagonal arrangement (see section 4.6). (f) The nanorod assembly could be permanently fixated using a photocurable resin or other means of solidification.

Bibliography

1. Feynman, R.P., *There's plenty of room at the bottom.* Engineering and Science, 1960. **23**(5): p. 22-36.

2. Erb, R.M., H.S. Son, B. Samanta, V.M. Rotello, and B.B. Yellen, *Magnetic assembly of colloidal superstructures with multipole symmetry.* Nature, 2009. **457**(7232): p. 999-1002.

3. Yellen, B.B., O. Hovorka, and G. Friedman, *Arranging matter by magnetic nanoparticle assemblers.* Proceedings of the National Academy of Sciences of the United States of America, 2005. **102**(25): p. 8860-8864.

4. Grzybowski, B.A., H.A. Stone, and G.M. Whitesides, *Dynamic self-assembly of magnetized, millimetre-sized objects rotating at a liquid–air interface.* Nature, 2000. **405**(6790): p. 1033-1036.

5. Ghosh, A. and P. Fischer, *Controlled Propulsion of Artificial Magnetic Nanostructured Propellers.* Nano Letters, 2009. **9**(6): p. 2243-2245.

6. Zhang, L., J.J. Abbott, L. Dong, K.E. Peyer, B.E. Kratochvil, H. Zhang, C. Bergeles, and B.J. Nelson, *Characterizing the Swimming Properties of Artificial Bacterial Flagella.* Nano Letters, 2009. **9**(10): p. 3663-3667.

7. Kumar, T.A., A. Bardea, Y. Shai, A. Yoffe, and R. Naaman, *Patterning Gradient Properties from Sub-Micrometers to Millimeters by Magnetolithography.* Nano Letters, 2010. **10**(6): p. 2262-2267.

8. Tierno, P., R. Golestanian, I. Pagonabarraga, and F. Sagués, *Controlled swimming in confined fluids of magnetically actuated colloidal rotors.* Physical Review Letters, 2008. **101**(21): p. 218304.

9. Dreyfus, R., J. Baudry, M.L. Roper, M. Fermigier, H.A. Stone, and J. Bibette, *Microscopic artificial swimmers.* Nature, 2005. **437**(7060): p. 862-865.

10. Demirörs, A.F., P.P. Pillai, B. Kowalczyk, and B.A. Grzybowski, *Colloidal assembly directed by virtual magnetic moulds.* Nature, 2013. **503**(7474): p. 99-103.

11. Tottori, S., L. Zhang, F. Qiu, K.K. Krawczyk, A. Franco-Obregón, and B.J. Nelson, *Magnetic Helical Micromachines: Fabrication, Controlled Swimming, and Cargo Transport.* Advanced Materials, 2012. **24**(6): p. 811-816.

12. Tasoglu, S., E. Diller, S. Guven, M. Sitti, and U. Demirci, *Untethered micro-robotic coding of three-dimensional material composition.* Nature Communications, 2014. **5**(Article number: 3124).

13. Khalil, K.S., A. Sagastegui, Y. Li, M.A. Tahir, J.E. Socolar, B.J. Wiley, and B.B. Yellen, *Binary colloidal structures assembled through Ising interactions.* Nature Communications, 2012. **3**(Article number 794).

14. Yan, J., M. Bloom, S.C. Bae, E. Luijten, and S. Granick, *Linking synchronization to self-assembly using magnetic Janus colloids.* Nature, 2012. **491**(7425): p. 578-581.

15. Erb, R.M., R. Libanori, N. Rothfuchs, and A.R. Studart, *Composites reinforced in three dimensions by using low magnetic fields.* Science, 2012. **335**(6065): p. 199-204.

16. Whitesides, G.M. and J. Deutch, *Let's get practical.* Nature, 2011. **469**(7328): p. 21-22.

17. Grantham, J., *Be persuasive. Be brave. Be arrested (if necessary).* Nature, 2012. **491**: p. 303.

18. Rees, M., *Denial of catastrophic risks.* Science, 2013. **339**(6124): p. 1123-1123.

19.   Steinacher, M., F. Joos, and T.F. Stocker, *Allowable carbon emissions lowered by multiple climate targets.* Nature, 2013. **499**(7457): p. 197-201.

20.   Mora, C., A.G. Frazier, R.J. Longman, R.S. Dacks, M.M. Walton, E.J. Tong, J.J. Sanchez, L.R. Kaiser, Y.O. Stender, and J.M. Anderson, *The projected timing of climate departure from recent variability.* Nature, 2013. **502**(7470): p. 183-187.

21.   Hansen, J., P. Kharecha, M. Sato, V. Masson-Delmotte, F. Ackerman, D.J. Beerling, P.J. Hearty, O. Hoegh-Guldberg, S.-L. Hsu, and C. Parmesan, *Assessing "Dangerous Climate Change": required reduction of carbon emissions to protect young people, future generations and nature.* Plos One, 2013. **8**(12): p. e81648.

22.   Lenton, T.M., H. Held, E. Kriegler, J.W. Hall, W. Lucht, S. Rahmstorf, and H.J. Schellnhuber, *Tipping elements in the Earth's climate system.* Proceedings of the National Academy of Sciences, 2008. **105**(6): p. 1786-1793.

23.   Sanford, T., P.C. Frumhoff, A. Luers, and J. Gulledge, *The climate policy narrative for a dangerously warming world.* Nature Climate Change, 2014. **4**(3): p. 164-166.

24.   Singer, P., *Famine, affluence, and morality.* Philosophy & Public Affairs, 1972: p. 229-243.

25.   Diffenbaugh, N.S. and C.B. Field, *Changes in ecologically critical terrestrial climate conditions.* Science, 2013. **341**(6145): p. 486-492.

26.   Laurance, W.F., D.C. Useche, J. Rendeiro, M. Kalka, C.J. Bradshaw, S.P. Sloan, S.G. Laurance, M. Campbell, K. Abernethy, and P. Alvarez, *Averting biodiversity collapse in tropical forest protected areas.* Nature, 2012. **489**(7415): p. 290-294.

27.   Cardinale, B.J., J.E. Duffy, A. Gonzalez, D.U. Hooper, C. Perrings, P. Venail, A. Narwani, G.M. Mace, D. Tilman, and D.A. Wardle, *Biodiversity loss and its impact on humanity.* Nature, 2012. **486**(7401): p. 59-67.

28.   McCarthy, D.P., P.F. Donald, J.P. Scharlemann, G.M. Buchanan, A. Balmford, J.M. Green, L.A. Bennun, N.D. Burgess, L.D. Fishpool, and S.T. Garnett, *Financial costs of meeting global biodiversity conservation targets: current spending and unmet needs.* Science, 2012. **338**(6109): p. 946-949.

29.   Naeem, S., J.E. Duffy, and E. Zavaleta, *The functions of biological diversity in an age of extinction.* Science, 2012. **336**(6087): p. 1401-1406.

30.   Pimm, S., C. Jenkins, R. Abell, T. Brooks, J. Gittleman, L. Joppa, P. Raven, C. Roberts, and J. Sexton, *The biodiversity of species and their rates of extinction, distribution, and protection.* Science, 2014. **344**(6187): p. 1246752.

31.   Garcia, R.A., M. Cabeza, C. Rahbek, and M.B. Araújo, *Multiple Dimensions of Climate Change and Their Implications for Biodiversity.* Science, 2014. **344**(6183): p. 1247579.

32.   Seddon, P.J., C.J. Griffiths, P.S. Soorae, and D.P. Armstrong, *Reversing defaunation: Restoring species in a changing world.* Science, 2014. **345**(6195): p. 406-412.

33.   Dirzo, R., H.S. Young, M. Galetti, G. Ceballos, N.J. Isaac, and B. Collen, *Defaunation in the Anthropocene.* Science, 2014. **345**(6195): p. 401-406.

34.   Foley, J.A., N. Ramankutty, K.A. Brauman, E.S. Cassidy, J.S. Gerber, M. Johnston, N.D. Mueller, C. O'Connell, D.K. Ray, and P.C. West, *Solutions for a cultivated planet.* Nature, 2011. **478**(7369): p. 337-342.

35.   Heffernan, O., *The dry facts.* Nature, 2013. **501**(7468): p. S2-S3.

II

36. Scholes, M.C. and R.J. Scholes, *Dust Unto Dust.* Science, 2013. **342**(6158): p. 565-566.

37. Lewis, N.S. and D.G. Nocera, *Powering the planet: Chemical challenges in solar energy utilization.* Proceedings of the National Academy of Sciences, 2006. **103**(43): p. 15729-15735.

38. Armaroli, N. and V. Balzani, *The future of energy supply: challenges and opportunities.* Angewandte Chemie International Edition, 2007. **46**(1-2): p. 52-66.

39. Armaroli, N. and V. Balzani, *Energy for a sustainable world.* 2011: Wiley-VCH, Weinheim.

40. Rockström, J., W. Steffen, K. Noone, Å. Persson, F.S. Chapin, E.F. Lambin, T.M. Lenton, M. Scheffer, C. Folke, and H.J. Schellnhuber, *A safe operating space for humanity.* Nature, 2009. **461**(7263): p. 472-475.

41. Brillet, J., J.-H. Yum, M. Cornuz, T. Hisatomi, R. Solarska, J. Augustynski, M. Graetzel, and K. Sivula, *Highly efficient water splitting by a dual-absorber tandem cell.* Nature Photonics, 2012. **6**(12): p. 824-828.

42. Atwater, J.H., P. Spinelli, E. Kosten, J. Parsons, C. Van Lare, J. Van de Groep, J.G. de Abajo, A. Polman, and H.A. Atwater, *Microphotonic parabolic light directors fabricated by two-photon lithography.* Applied Physics Letters, 2011. **99**(15): p. 151113.

43. Wallentin, J., N. Anttu, D. Asoli, M. Huffman, I. Åberg, M.H. Magnusson, G. Siefer, P. Fuss-Kailuweit, F. Dimroth, and B. Witzigmann, *InP Nanowire Array Solar Cells Achieving 13.8% Efficiency by Exceeding the Ray Optics Limit.* Science, 2013. **339**(6123): p. 1057-1060.

44. Kosten, E.D., J.H. Atwater, J. Parsons, A. Polman, and H.A. Atwater, *Highly efficient GaAs solar cells by limiting light emission angle.* Light: Science & Applications, 2013. **2**(1): p. e45.

45. Lee, M.M., J. Teuscher, T. Miyasaka, T.N. Murakami, and H.J. Snaith, *Efficient hybrid solar cells based on meso-superstructured organometal halide perovskites.* Science, 2012. **338**(6107): p. 643-647.

46. Dang, X., H. Yi, M.-H. Ham, J. Qi, D.S. Yun, R. Ladewski, M.S. Strano, P.T. Hammond, and A.M. Belcher, *Virus-templated self-assembled single-walled carbon nanotubes for highly efficient electron collection in photovoltaic devices.* Nature Nanotechnology, 2011. **6**(6): p. 377-384.

47. Polman, A. and H.A. Atwater, *Photonic design principles for ultrahigh-efficiency photovoltaics.* Nature Materials, 2012. **11**(3): p. 174-177.

48. Ferry, V.E., L.A. Sweatlock, D. Pacifici, and H.A. Atwater, *Plasmonic nanostructure design for efficient light coupling into solar cells.* Nano Letters, 2008. **8**(12): p. 4391-4397.

49. Mubeen, S., J. Lee, N. Singh, S. Krämer, G.D. Stucky, and M. Moskovits, *An autonomous photosynthetic device in which all charge carriers derive from surface plasmons.* Nature Nanotechnology, 2013. **8**(4): p. 247-251.

50. Atwater, H.A. and A. Polman, *Plasmonics for improved photovoltaic devices.* Nature Materials, 2010. **9**(3): p. 205-213.

51. Warren, S.C., K. Voïtchovsky, H. Dotan, C.M. Leroy, M. Cornuz, F. Stellacci, C. Hébert, A. Rothschild, and M. Grätzel, *Identifying champion nanostructures for solar water-splitting.* Nature Materials, 2013. **12**(9): p. 842-849.

52. Nam, K.T., D.-W. Kim, P.J. Yoo, C.-Y. Chiang, N. Meethong, P.T. Hammond, Y.-M. Chiang, and A.M. Belcher, *Virus-enabled synthesis and assembly of nanowires for lithium ion battery electrodes.* Science, 2006. **312**(5775): p. 885-888.

53.   Law, M., L.E. Greene, J.C. Johnson, R. Saykally, and P. Yang, *Nanowire dye-sensitized solar cells.* Nature Materials, 2005. **4**(6): p. 455-459.

54.   Cohen-Tanugi, D. and J.C. Grossman, *Water desalination across nanoporous graphene.* Nano Letters, 2012. **12**(7): p. 3602-3608.

55.   Chan, C.K., H. Peng, G. Liu, K. McIlwrath, X.F. Zhang, R.A. Huggins, and Y. Cui, *High-performance lithium battery anodes using silicon nanowires.* Nature Nanotechnology, 2008. **3**(1): p. 31-35.

56.   Khalil, I.S.M., H.C. Dijkslag, L. Abelmann, and S. Misra, *MagnetoSperm: A microrobot that navigates using weak magnetic fields.* Applied Physics Letters, 2014. **104**(22).

57.   Riedel, I.H., K. Kruse, and J. Howard, *A self-organized vortex array of hydrodynamically entrained sperm cells.* Science, 2005. **309**(5732): p. 300-303.

58.   Drescher, K., K.C. Leptos, I. Tuval, T. Ishikawa, T.J. Pedley, and R.E. Goldstein, *Dancing Volvox: Hydrodynamic bound states of swimming algae.* Physical Review Letters, 2009. **102**(16): p. 168101.

59.   Yuan, J., D.M. Raizen, and H.H. Bau, *Gait synchronization in Caenorhabditis elegans.* Proceedings of the National Academy of Sciences, 2014. **111**(19): p. 6865-6870.

60.   Sakaue, T., R. Kapral, and A.S. Mikhailov, *Nanoscale swimmers: hydrodynamic interactions and propulsion of molecular machines.* The European Physical Journal B-Condensed Matter and Complex Systems, 2010. **75**(3): p. 381-387.

61.   Bennet, M., A. McCarthy, D. Fix, M.R. Edwards, F. Repp, P. Vach, J.W.C. Dunlop, M. Sitti, G.S. Buller, S. Klumpp, and D. Faivre, *Influence of Magnetic Fields on Magneto-Aerotaxis.* Plos One, 2014. **9**(7): p. e101150.

62.   Lefèvre, Christopher T., M. Bennet, L. Landau, P. Vach, D. Pignol, Dennis A. Bazylinski, Richard B. Frankel, S. Klumpp, and D. Faivre, *Diversity of Magneto-Aerotactic Behaviors and Oxygen Sensing Mechanisms in Cultured Magnetotactic Bacteria.* Biophysical Journal, 2014. **107**(2): p. 527-538.

63.   Dong, B., T. Zhou, H. Zhang, and C.Y. Li, *Directed self-assembly of nanoparticles for nanomotors.* Acs Nano, 2013. **7**(6): p. 5192-5198.

64.   Wang, W., S. Li, L. Mair, S. Ahmed, T.J. Huang, and T.E. Mallouk, *Acoustic Propulsion of Nanorod Motors Inside Living Cells.* Angewandte Chemie International Edition, 2014. **53**(12): p. 3201-3204.

65.   Garcia-Gradilla, V., J. Orozco, S. Sattayasamitsathit, F. Soto, F. Kuralay, A. Pourazary, A. Katzenberg, W. Gao, Y. Shen, and J. Wang, *Functionalized Ultrasound-Propelled Magnetically Guided Nanomotors: Toward Practical Biomedical Applications.* Acs Nano, 2013. **7**(10): p. 9232-9240.

66.   Lee, T.-C., M. Alarcón-Correa, C. Miksch, K. Hahn, J.G. Gibbs, and P. Fischer, *Self-propelling nanomotors in the presence of strong Brownian forces.* Nano Letters, 2014.

67.   Nakata, S., M. Hata, Y.S. Ikura, E. Heisler, A. Awazu, H. Kitahata, and H. Nishimori, *Motion with Memory of a Self-propelled Object.* The Journal of Physical Chemistry C, 2013. **117**(46): p. 24490-24495.

68.   Liu, M., T. Zentgraf, Y. Liu, G. Bartal, and X. Zhang, *Light-driven nanoscale plasmonic motors.* Nature Nanotechnology, 2010. **5**(8): p. 570-573.

69.   Kim, K., X. Xu, J. Guo, and D. Fan, *Ultrahigh-speed rotating nanoelectromechanical system devices assembled from nanoscale building blocks.* Nature Communications, 2014. **5**.

IV

70.   Solovev, A.A., S. Sanchez, M. Pumera, Y.F. Mei, and O.G. Schmidt, *Magnetic Control of Tubular Catalytic Microbots for the Transport, Assembly, and Delivery of Micro-objects.* Advanced Functional Materials, 2010. **20**(15): p. 2430-2435.

71.   Lee, T.-C., M. Alarcón-Correa, C. Miksch, K. Hahn, J.G. Gibbs, and P. Fischer, *Self-propelling nanomotors in the presence of strong Brownian forces.* Nano Letters, 2014. **14**(5): p. 2407-2412.

72.   Boncheva, M., S.A. Andreev, L. Mahadevan, A. Winkleman, D.R. Reichman, M.G. Prentiss, S. Whitesides, and G.M. Whitesides, *Magnetic self-assembly of three-dimensional surfaces from planar sheets.* Proceedings of the National Academy of Sciences, 2005. **102**(11): p. 3924-3929.

73.   Chen, C.L., P.J. Zhang, and N.L. Rosi, *A new peptide-based method for the design and synthesis of nanoparticle superstructures: Construction of highly ordered gold nanoparticle double helices.* Journal of the American Chemical Society, 2008. **130**(41): p. 13555-13557.

74.   Dujardin, E., C. Peet, G. Stubbs, J.N. Culver, and S. Mann, *Organization of Metallic Nanoparticles Using Tobacco Mosaic Virus Templates.* Nano Letters, 2003. **3**(3): p. 413-417.

75.   Mao, C.B., D.J. Solis, B.D. Reiss, S.T. Kottmann, R.Y. Sweeney, A. Hayhurst, G. Georgiou, B. Iverson, and A.M. Belcher, *Virus-based toolkit for the directed synthesis of magnetic and semiconducting nanowires.* Science, 2004. **303**: p. 213-217.

76.   Kuzyk, A., R. Schreiber, Z. Fan, G. Pardatscher, E.-M. Roller, A. Högele, F.C. Simmel, A.O. Govorov, and T. Liedl, *DNA-based self-assembly of chiral plasmonic nanostructures with tailored optical response.* Nature, 2012. **483**(7389): p. 311-314.

77.   Zerrouki, D., J. Baudry, D. Pine, P. Chaikin, and J. Bibette, *Chiral colloidal clusters.* Nature, 2008. **455**(7211): p. 380-382.

78.   Liu, J., S.Z. Qiao, and Q.H. Hu, *Magnetic nanocomposites with mesoporous structures: synthesis and applications.* Small, 2011. **7**(4): p. 425-443.

79.   Dussan, K., C. Cardona, O. Giraldo, L. Gutiérrez, and V. Pérez, *Analysis of a reactive extraction process for biodiesel production using a lipase immobilized on magnetic nanostructures.* Bioresource technology, 2010. **101**(24): p. 9542-9549.

80.   Lu, A.-H., E.L. Salabas, and F. Schüth, *Magnetic Nanoparticles: Synthesis, Protection, Functionalization, and Application.* Angewandte Chemie International Edition, 2007. **46**(8): p. 1222-1244.

81.   Yiu, H.H. and M.A. Keane, *Enzyme–magnetic nanoparticle hybrids: new effective catalysts for the production of high value chemicals.* Journal of Chemical Technology and Biotechnology, 2012. **87**(5): p. 583-594.

82.   Colombo, M., S. Carregal-Romero, M.F. Casula, L. Gutiérrez, M.P. Morales, I.B. Böhm, J.T. Heverhagen, D. Prosperi, and W.J. Parak, *Biological applications of magnetic nanoparticles.* Chemical Society Reviews, 2012. **41**(11): p. 4306-4334.

83.   Chen, M., J. Kim, J. Liu, H. Fan, and S. Sun, *Synthesis of FePt nanocubes and their oriented self-assembly.* Journal of the American Chemical Society, 2006. **128**(22): p. 7132-7133.

84.   Zöttl, A. and H. Stark, *Hydrodynamics Determines Collective Motion and Phase Behavior of Active Colloids in Quasi-Two-Dimensional Confinement.* Physical Review Letters, 2014. **112**(11): p. 118101-118101.

85.   Bricard, A., J.-B. Caussin, N. Desreumaux, O. Dauchot, and D. Bartolo, *Emergence of macroscopic directed motion in populations of motile colloids.* Nature, 2013. **503**(7474): p. 95-98.

86.   Schaller, V., C. Weber, C. Semmrich, E. Frey, and A.R. Bausch, *Polar patterns of driven filaments.* Nature, 2010. **467**(7311): p. 73-77.

87.   Werfel, J., K. Petersen, and R. Nagpal, *Designing Collective Behavior in a Termite-Inspired Robot Construction Team.* Science, 2014. **343**(6172): p. 754-758.

88.   Amir, Y., E. Ben-Ishay, D. Levner, S. Ittah, A. Abu-Horowitz, and I. Bachelet, *Universal computing by DNA origami robots in a living animal.* Nature Nanotechnology, 2014. **9**: p. 353-357.

89.   Kim, S., C. Laschi, and B. Trimmer, *Soft robotics: a bioinspired evolution in robotics.* Trends in Biotechnology, 2013. **31**(5): p. 287-294.

90.   Kim, Y., A.A. Shah, and M.J. Solomon, *Spatially and temporally reconfigurable assembly of colloidal crystals.* Nature Communications, 2014. **5**(Articel number: 3676).

91.   Yan, Z., S.K. Gray, and N.F. Scherer, *Potential energy surfaces and reaction pathways for light-mediated self-organization of metal nanoparticle clusters.* Nature Communications, 2014. **5**(Articel number: 3751).

92.   Diao, Y., B.C. Tee, G. Giri, J. Xu, D.H. Kim, H.A. Becerril, R.M. Stoltenberg, T.H. Lee, G. Xue, and S.C. Mannsfeld, *Solution coating of large-area organic semiconductor thin films with aligned single-crystalline domains.* Nature Materials, 2013. **12**(7): p. 665-671.

93.   De Volder, M. and A.J. Hart, *Engineering Hierarchical Nanostructures by Elastocapillary Self-Assembly.* Angewandte Chemie International Edition, 2013. **52**(9): p. 2412-2425.

94.   Galloway, J.M., J.P. Bramble, A.E. Rawlings, G. Burnell, S.D. Evans, and S.S. Staniland, *Biotemplated Magnetic Nanoparticle Arrays.* Small, 2012. **8**(2): p. 204-208.

95.   Mann, S., *Self-assembly and transformation of hybrid nano-objects and nanostructures under equilibrium and non-equilibrium conditions.* Nature Materials, 2009. **8**: p. 781-792.

96.   Sanchez, T., D.T. Chen, S.J. DeCamp, M. Heymann, and Z. Dogic, *Spontaneous motion in hierarchically assembled active matter.* Nature, 2012. **491**(7424): p. 431-434.

97.   Cui, M., T. Emrick, and T.P. Russell, *Stabilizing Liquid Drops in Nonequilibrium Shapes by the Interfacial Jamming of Nanoparticles.* Science, 2013. **342**(6157): p. 460-463.

98.   Cullity, B.D. and C.D. Graham, *Introduction to magnetic materials.* 2011: John Wiley & Sons.

99.   Aharoni, A., *Introduction to the Theory of Ferromagnetism.* 1996: Oxford University Press.

100.   Dunlop, D.J. and Ö. Özdemir, *Rock magnetism: fundamentals and frontiers.* 1997: Cambridge University Press.

101.   Brechet, Y., T. Speck, I. Burgert, F. Brüemmer, G. Duda, E. Arzt, A. Parker, O. Paris, D. Faivre, and P. Fratzl, *Materials Design Inspired by Nature: Function Through Inner Architecture.* 2013: Royal Society of Chemistry.

102.   Serna, C. and M. Morales, *Maghemite (γ-Fe2O3): A versatile magnetic colloidal material*, in *Surface and Colloid Science.* 2004, Springer. p. 27-81.

103.   Kittel, C., *Introduction to Solid State Physics.* 1986: John Wiley & Sons.

104.   Schüler, D., *Magnetoreception and magnetosomes in bacteria.* Microbiology Monographs, ed. A. Steinbüchel. Vol. 3. 2007, Heidelberg: Springer.

105.   Winklhofer, M., K. Fabian, and F. Heider, *Magnetic blocking temperatures of magnetite calculated with a three-dimensional micromagnetic model.* Journal of Geophysical Research: Solid Earth (1978–2012), 1997. **102**(B10): p. 22695-22709.

106.   Muxworthy, A.R. and W. Williams, *Critical single-domain/multidomain grain sizes in noninteracting and interacting elongated magnetite particles: Implications for magnetosomes.* Journal of Geophysical Research: Solid Earth (1978–2012), 2006. **111**(B12): p. S12.

107.   Muxworthy, A.R. and W. Williams, *Critical superparamagnetic/single-domain grain sizes in interacting magnetite particles: implications for magnetosome crystals.* Journal of the Royal Society Interface, 2009. **6**(41): p. 1207-1212.

108.   Muxworthy, A.R., D.J. Dunlop, and W. Williams, *High-temperature magnetic stability of small magnetite particles.* Journal of Geophysical Research: Solid Earth (1978–2012), 2003. **108**(B5): p. 2281.

109.   Witt, A., K. Fabian, and U. Bleil, *Three-dimensional micromagnetic calculations for naturally shaped magnetite: Octahedra and magnetosomes.* Earth and Planetary Science Letters, 2005. **233**: p. 311-324.

110.   Peters, R.D. and L. Sumner, *Intuitive derivation of Reynolds number.* arXiv preprint physics/0306193, 2003.

111.   Happel, J. and H. Brenner, *Low Reynolds number hydrodynamics: with special applications to particulate media.* Vol. 1. 1983: Springer.

112.   Liu, C. and Z. Li, *On the validity of the Navier-Stokes equations for nanoscale liquid flows: The role of channel size.* AIP Advances, 2011. **1**(3): p. 032108.

113.   Kim, S. and S.J. Karrila, *Microhydrodynamics: Principles and selected applications*, 1991, Butterworth-Heinemann (Boston).

114.   Fily, Y., A. Baskaran, and M.C. Marchetti, *Cooperative self-propulsion of active and passive rotors.* Soft Matter, 2012. **8**(10): p. 3002-3009.

115.   Ghosh, A., D. Paria, G. Rangarajan, and A. Ghosh, *Velocity Fluctuations in Helical Propulsion: How Small Can a Propeller Be.* The Journal of Physical Chemistry Letters, 2013. **5**(1): p. 62-68.

116.   Vach, P.J., N. Brun, M. Bennet, L. Bertinetti, M. Widdrat, J. Baumgartner, S. Klumpp, P. Fratzl, and D. Faivre, *Selecting for function: Solution synthesis of magnetic nanopropellers.* Nano Letters, 2013. **13**(11): p. 5373-5378.

117.   Lauga, E., *Life around the scallop theorem.* Soft Matter, 2011. **7**(7): p. 3060-3065.

118.   Abbott, J.J., K.E. Peyer, M.C. Lagomarsino, L. Zhang, L. Dong, I.K. Kaliakatsos, and B.J. Nelson, *How should microrobots swim?* The International Journal of Robotics Research, 2009. **28**(11-12): p. 1434-1447.

119.   Fischer, P. and A. Ghosh, *Magnetically actuated propulsion at low Reynolds numbers: towards nanoscale control.* Nanoscale, 2011. **3**(2): p. 557-563.

120.   Peyer, K.E., L. Zhang, and B.J. Nelson, *Bio-inspired magnetic swimming microrobots for biomedical applications.* Nanoscale, 2013. **5**(4): p. 1259-1272.

121.   Zeeshan, M.A., S. Pané, S.K. Youn, E. Pellicer, S. Schuerle, J. Sort, S. Fusco, A.M. Lindo, H.G. Park, and B.J. Nelson, *Graphite Coating of Iron Nanowires for Nanorobotic Applications: Synthesis, Characterization and Magnetic Wireless Manipulation.* Advanced Functional Materials, 2013. **23**(7): p. 823-831.

122. Kim, S., F. Qiu, S. Kim, A. Ghanbari, C. Moon, L. Zhang, B.J. Nelson, and H. Choi, *Fabrication and Characterization of Magnetic Microrobots for Three-Dimensional Cell Culture and Targeted Transportation.* Advanced Materials, 2013. **25**(41): p. 5863-5868.

123. Steager, E.B., M.S. Sakar, C. Magee, M. Kennedy, A. Cowley, and V. Kumar. *Automated biomanipulation of single cells.* in *2012 IEEE International Conference on Robotics and Automation (ICRA).* 2012. IEEE.

124. Schurle, S., K.E. Peyer, B. Kratochvil, and B.J. Nelson. *Holonomic 5-DOF magnetic control of 1D nanostructures.* in *2012 IEEE International Conference on Robotics and Automation (ICRA)* 2012. IEEE.

125. Kummer, M.P., J.J. Abbott, B.E. Kratochvil, R. Borer, A. Sengul, and B.J. Nelson, *OctoMag: An electromagnetic system for 5-DOF wireless micromanipulation.* IEEE Transactions on Robotics, 2010. **26**(6): p. 1006-1017.

126. Bergeles, C., B.E. Kratochvil, and B.J. Nelson, *Visually servoing magnetic intraocular microdevices.* IEEE Transactions on Robotics, 2012. **28**(4): p. 798-809.

127. Gao, W., X. Feng, A. Pei, C.R. Kane, R. Tam, C. Hennessy, and J. Wang, *Bioinspired Helical Microswimmers Based on Vascular Plants.* Nano Letters, 2013. **14**(1): p. 305-310.

128. Li, J., S. Sattayasamitsathit, R. Dong, W. Gao, R. Tam, X. Feng, S. Ai, and J. Wang, *Template electrosynthesis of tailored-made helical nanoswimmers.* Nanoscale, 2014.

129. Sing, C.E., L. Schmid, M.F. Schneider, T. Franke, and A. Alexander-Katz, *Controlled surface-induced flows from the motion of self-assembled colloidal walkers.* Proceedings of the National Academy of Sciences, 2010. **107**(2): p. 535-540.

130. Tierno, P. and F. Sagués, *Steering trajectories in magnetically actuated colloidal propellers.* The European Physical Journal E, 2012. **35**(8): p. 1-5.

131. Mair, L.O., B. Evans, A.R. Hall, J. Carpenter, A. Shields, K. Ford, M. Millard, and R. Superfine, *Highly controllable near-surface swimming of magnetic Janus nanorods: application to payload capture and manipulation.* Journal of Physics D: Applied Physics, 2011. **44**(12): p. 125001.

132. Zhang, L., T. Petit, Y. Lu, B.E. Kratochvil, K.E. Peyer, R. Pei, J. Lou, and B.J. Nelson, *Controlled propulsion and cargo transport of rotating nickel nanowires near a patterned solid surface.* Acs Nano, 2010. **4**(10): p. 6228-6234.

133. Benkoski, J.J., J.L. Breidenich, O.M. Uy, A.T. Hayes, R.M. Deacon, H.B. Land, J.M. Spicer, P.Y. Keng, and J. Pyun, *Dipolar organization and magnetic actuation of flagella-like nanoparticle assemblies.* Journal of Materials Chemistry, 2011. **21**(20): p. 7314-7325.

134. Roper, M., R. Dreyfus, J. Baudry, M. Fermigier, J. Bibette, and H.A. Stone, *Do magnetic micro-swimmers move like eukaryotic cells?* Proceedings of the Royal Society A: Mathematical, Physical and Engineering Science, 2008. **464**(2092): p. 877-904.

135. Cheang, U.K., D. Roy, J.H. Lee, and M.J. Kim, *Fabrication and magnetic control of bacteria-inspired robotic microswimmers.* Applied Physics Letters, 2010. **97**(21): p. 213704.

136. Gao, W., K.M. Manesh, J. Hua, S. Sattayasamitsathit, and J. Wang, *Hybrid Nanomotor: A Catalytically/Magnetically Powered Adaptive Nanowire Swimmer.* Small, 2011. **7**(14): p. 2047-2051.

137. Gao, W., S. Sattayasamitsathit, K.M. Manesh, D. Weihs, and J. Wang, *Magnetically Powered Flexible Metal Nanowire Motors.* Journal of the American Chemical Society, 2010. **132**(41): p. 14403-14405.

138. Pak, O.S., W. Gao, J. Wang, and E. Lauga, *High-speed propulsion of flexible nanowire motors: Theory and experiments.* Soft Matter, 2011. **7**(18): p. 8169-8181.

139. Purcell, E.M., *Life at low Reynolds number.* American Journal of Physics, 1977. **45**(1): p. 3-11.

140. Trouilloud, R., S.Y. Tony, A. Hosoi, and E. Lauga, *Soft swimming: Exploiting deformable interfaces for low Reynolds number locomotion.* Physical Review Letters, 2008. **101**(4): p. 048102.

141. Tierno, P., R. Golestanian, I. Pagonabarraga, and F. Sagués, *Magnetically actuated colloidal microswimmers.* The Journal of Physical Chemistry B, 2008. **112**(51): p. 16525-16528.

142. Tierno, P., *Synchronization and Beating in Dipolarly Coupled Colloidal Rotators.* The Journal of Physical Chemistry B, 2010. **115**(1): p. 23-26.

143. Zhang, L., T. Petit, K.E. Peyer, B.E. Kratochvil, J. Zhang, J. Lou, and B.J. Nelson. *Noncontact and contact micromanipulation using a rotating nickel nanowire.* in *2010 IEEE 4th International Conference on Nano/Molecular Medicine and Engineering (NANOMED).* 2010. IEEE.

144. Zhang, L., T. Petit, K.E. Peyer, and B.J. Nelson, *Targeted cargo delivery using a rotating nickel nanowire.* Nanomedicine: Nanotechnology, Biology and Medicine, 2012. **8**(7): p. 1074-1080.

145. Ye, Z. and M. Sitti, *Dynamic trapping and two-dimensional transport of swimming microorganisms using a rotating magnetic microrobot.* Lab on a Chip, 2014.

146. Zhang, L., J.J. Abbott, L. Dong, B.E. Kratochvil, D. Bell, and B.J. Nelson, *Artificial bacterial flagella: Fabrication and magnetic control.* Applied Physics Letters, 2009. **94**(6): p. 064107-3.

147. Sitti, M., *Miniature devices: Voyage of the microrobots.* Nature, 2009. **458**(7242): p. 1121-1122.

148. Zhang, L., K.E. Peyer, and B.J. Nelson, *Artificial bacterial flagella for micromanipulation.* Lab Chip, 2010. **10**(17): p. 2203-2215.

149. Zhang, L., J.J. Abbott, L. Dong, B.E. Kratochvil, H. Zhang, K.E. Peyer, and B.J. Nelson. *Micromanipulation using artificial bacterial flagella.* in *2009 IEEE/RSJ International Conference on Intelligent Robots and Systems (IROS).* 2009. IEEE.

150. Peyer, K.E., L. Zhang, B.E. Kratochvil, and B.J. Nelson. *Non-ideal swimming of artificial bacterial flagella near a surface.* in *2010 IEEE International Conference on Robotics and Automation (ICRA).* 2010. IEEE.

151. Peyer, K.E., L. Zhang, and B.J. Nelson, *Localized non-contact manipulation using artificial bacterial flagella.* Applied Physics Letters, 2011. **99**(17): p. 174101.

152. Zhang, L., K.E. Peyer, T. Petit, B.E. Kratochvil, and B.J. Nelson. *Motion control of artificial bacterial flagella.* in *2010 10th IEEE Conference on Nanotechnology (IEEE-NANO).* 2010. IEEE.

153. Schamel, D., A.G. Mark, J.G. Gibbs, C. Miksch, K.I. Morozov, A.M. Leshansky, and P. Fischer, *Nanopropellers and Their Actuation in Complex Viscoelastic Media.* Acs Nano, 2014.

154. Schamel, D., M. Pfeifer, J.G. Gibbs, B.r. Miksch, A.G. Mark, and P. Fischer, *Chiral Colloidal Molecules And Observation of The Propeller Effect.* Journal of the American Chemical Society, 2013. **135**(33): p. 12353-12359.

155. Pooyath, L.V., R. Sai, Y. Chandorkar, B. Basu, S. Shivashankar, and A. Ghosh, *Conformal Cytocompatible Ferrite Coatings Facilitate the Realization of a Nano-voyager in Human Blood.* Nano Letters, 2014.

156.   Ghosh, A., D. Paria, H.J. Singh, P.L. Venugopalan, and A. Ghosh, *Dynamical configurations and bistability of helical nanostructures under external torque.* Physical Review E, 2012. **86**(3): p. 031401.

157.   Mandal, P. and A. Ghosh, *Observation of Enhanced Diffusivity in Magnetically Powered Reciprocal Swimmers.* Physical Review Letters, 2013. **111**(24): p. 248101.

158.   Qiu, F., R. Mhanna, L. Zhang, Y. Ding, S. Fujita, and B.J. Nelson, *Artificial bacterial flagella functionalized with temperature-sensitive liposomes for controlled release.* Sensors and Actuators B: Chemical, 2014. **196**: p. 676-681.

159.   Tottori, S., N. Sugita, R. Kometani, S. Ishihara, and M. Mitsuishi, *Selective control method for multiple magnetic helical microrobots.* Journal of Micro-Nano Mechatronics, 2011. **6**(3-4): p. 89-95.

160.   Qiu, F., L. Zhang, K.E. Peyer, M. Casarosa, A. Franco-Obregón, H. Choi, and B.J. Nelson, *Noncytotoxic artificial bacterial flagella fabricated from biocompatible ORMOCOMP and iron coating.* Journal of Materials Chemistry B, 2014. **2**(4): p. 357-362.

161.   Peyer, K.E., F. Qiu, L. Zhang, and B.J. Nelson. *Movement of artificial bacterial flagella in heterogeneous viscous environments at the microscale.* in *2012 IEEE/RSJ International Conference on Intelligent Robots and Systems (IROS).* 2012.

162.   Mhanna, R., F. Qiu, L. Zhang, Y. Ding, K. Sugihara, M. Zenobi-Wong, and B.J. Nelson, *Artificial Bacterial Flagella for Remote-Controlled Targeted Single-Cell Drug Delivery.* Small, 2014. **10**(10): p. 1953-1957.

163.   Tottori, S. and B.J. Nelson, *Artificial helical microswimmers with mastigoneme-inspired appendages.* Biomicrofluidics, 2013. **7**(6): p. 061101.

164.   Mahoney, A.W., N.D. Nelson, K.E. Peyer, B.J. Nelson, and J.J. Abbott, *Behavior of rotating magnetic microrobots above the step-out frequency with application to control of multi-microrobot systems.* Applied Physics Letters, 2014. **104**(14): p. 144101.

165.   Zeeshan, M.A., R. Grisch, E. Pellicer, K.M. Sivaraman, K.E. Peyer, J. Sort, B. Özkale, M.S. Sakar, B.J. Nelson, and S. Pané, *Hybrid Helical Magnetic Microrobots Obtained by 3D Template-Assisted Electrodeposition.* Small, 2013. **10**(7): p. 1284-1288.

166.   Peters, C., O. Ergeneman, P.D.W. García, M. Müller, S. Pané, B.J. Nelson, and C. Hierold, *Superparamagnetic Twist-type Actuators with Shape-Independent Magnetic Properties and Surface Functionalization for Advanced Biomedical Applications.* Advanced Functional Materials, 2014.

167.   Schuerle, S., S. Pané, E. Pellicer, J. Sort, M.D. Baró, and B.J. Nelson, *Helical and Tubular Lipid Microstructures that are Electroless-Coated with CoNiReP for Wireless Magnetic Manipulation.* Small, 2012. **8**(10): p. 1498-1502.

168.   Purcell, E.M., *The efficiency of propulsion by a rotating flagellum.* Proceedings of the National Academy of Sciences, 1997. **94**(21): p. 11307-11311.

169.   Peyer, K.E., E.C. Siringil, L. Zhang, M. Suter, and B.J. Nelson, *Bacteria-inspired magnetic polymer composite microrobots*, in *Biomimetic and Biohybrid Systems.* 2013, Springer. p. 216-227.

170.   Peyer, K.E., S. Tottori, F. Qiu, L. Zhang, and B.J. Nelson, *Magnetic helical micromachines.* Chemistry-A European Journal, 2013. **19**(1): p. 28-38.

171.   Nelson, B.J., I.K. Kaliakatsos, and J.J. Abbott, *Microrobots for minimally invasive medicine.* Annual review of biomedical engineering, 2010. **12**: p. 55-85.

172. Fomin, V.M., E.J. Smith, D. Makarov, S. Sanchez, and O.G. Schmidt, *Dynamics of radial-magnetized microhelix coils.* Physical Review B, 2011. **84**(17): p. 174303.

173. Korneva, G., H. Ye, Y. Gogotsi, D. Halverson, G. Friedman, J.-C. Bradley, and K.G. Kornev, *Carbon Nanotubes Loaded with Magnetic Particles.* Nano Letters, 2005. **5**(5): p. 879-884.

174. Tierno, P., J. Claret, F. Sagués, and A. Cēbers, *Overdamped dynamics of paramagnetic ellipsoids in a precessing magnetic field.* Physical Review E, 2009. **79**(2): p. 021501.

175. McNaughton, B.H., K.A. Kehbein, J.N. Anker, and R. Kopelman, *Sudden breakdown in linear response of a rotationally driven magnetic microparticle and application to physical and chemical microsensing.* The Journal of Physical Chemistry B, 2006. **110**(38): p. 18958-18964.

176. McNaughton, B.H., R.R. Agayan, J.X. Wang, and R. Kopelman, *Physiochemical microparticle sensors based on nonlinear magnetic oscillations.* Sensors and Actuators B: Chemical, 2007. **121**(1): p. 330-340.

177. Helgesen, G., P. Pieranski, and A.T. Skjeltorp, *Dynamic behavior of simple magnetic hole systems.* Physical Review A, 1990. **42**(12): p. 7271-7280.

178. Chevry, L., N.K. Sampathkumar, A. Cebers, and J.F. Berret, *Magnetic wire-based sensors for the microrheology of complex fluids.* Physical Review E, 2013. **88**(6): p. 062306.

179. Frka-Petesic, B., K. Erglis, J.F. Berret, A. Cebers, V. Dupuis, J. Fresnais, O. Sandre, and R. Perzynski, *Dynamics of paramagnetic nanostructured rods under rotating field.* Journal of Magnetism and Magnetic Materials, 2011. **323**(10): p. 1309-1313.

180. Morozov, K.I. and A.M. Leshansky, *The chiral magnetic nanomotors.* Nanoscale, 2014. **6**(3): p. 1580-1588.

181. Keaveny, E.E., S.W. Walker, and M.J. Shelley, *Optimization of Chiral Structures for Microscale Propulsion.* Nano Letters, 2013. **13**(2): p. 531-537.

182. Becker, L.E., S.A. Koehler, and H.A. Stone, *On self-propulsion of micro-machines at low Reynolds number: Purcell's three-link swimmer.* Journal of Fluid Mechanics, 2003. **490**: p. 15-35.

183. Najafi, A. and R. Golestanian, *Simple swimmer at low Reynolds number: Three linked spheres.* Physical Review E, 2004. **69**(6): p. 062901.

184. Avron, J., O. Gat, and O. Kenneth, *Optimal Swimming at Low Reynolds Numbers.* Physical Review Letters, 2004. **93**(18): p. 186001.

185. Manesh, K.M., S. Campuzano, W. Gao, M.J. Lobo-Castañón, I. Shitanda, K. Kiantaj, and J. Wang, *Nanomotor-based biocatalytic patterning of helical metal microstructures.* Nanoscale, 2013. **5**(4): p. 1310-1314.

186. Casic, N., N. Quintero, R. Alvarez-Nodarse, F.G. Mertens, L. Jibuti, W. Zimmermann, and T.M. Fischer, *Propulsion efficiency of a dynamic self-assembled helical ribbon.* Physical Review Letters, 2013. **110**(16): p. 168302.

187. Hudak, N.S. and G.G. Amatucci, *Small-scale energy harvesting through thermoelectric, vibration, and radiofrequency power conversion.* Journal of Applied Physics, 2008. **103**(10): p. 101301.

188. Gao, W. and J. Wang, *The Environmental Impact of Micro/Nanomachines: A Review.* Acs Nano, 2014.

189. Douglas, S.M., I. Bachelet, and G.M. Church, *A logic-gated nanorobot for targeted transport of molecular payloads.* Science, 2012. **335**(6070): p. 831-834.

190. Pawashe, C., S. Floyd, and M. Sitti, *Modeling and experimental characterization of an untethered magnetic micro-robot.* The International Journal of Robotics Research, 2009. **28**(8): p. 1077-1094.

191. Floyd, S., C. Pawashe, and M. Sitti, *Two-dimensional contact and noncontact micromanipulation in liquid using an untethered mobile magnetic microrobot.* IEEE Transactions on Robotics, 2009. **25**(6): p. 1332-1342.

192. Frutiger, D.R., K. Vollmers, B.E. Kratochvil, and B.J. Nelson, *Small, fast, and under control: wireless resonant magnetic micro-agents.* The International Journal of Robotics Research, 2010. **29**(5): p. 613-636.

193. Diller, E. and M. Sitti, *Three-Dimensional Programmable Assembly by Untethered Magnetic Robotic Micro-Grippers.* Advanced Functional Materials, 2014. **24**(28): p. 4397-4404.

194. Donald, B.R., C.G. Levey, and I. Paprotny, *Planar microassembly by parallel actuation of MEMS microrobots.* Microelectromechanical Systems, Journal of, 2008. **17**(4): p. 789-808.

195. Diller, E., S. Floyd, C. Pawashe, and M. Sitti, *Control of multiple heterogeneous magnetic microrobots in two dimensions on nonspecialized surfaces.* IEEE Transactions on Robotics, 2012. **28**(1): p. 172-182.

196. Diller, E., J. Giltinan, and M. Sitti, *Independent control of multiple magnetic microrobots in three dimensions.* The International Journal of Robotics Research, 2013. **32**(5): p. 614-631.

197. Biswal, S.L. and A.P. Gast, *Rotational dynamics of semiflexible paramagnetic particle chains.* Physical Review E, 2004. **69**(4): p. 041406.

198. Biswal, S.L. and A.P. Gast, *Mechanics of semiflexible chains formed by poly (ethylene glycol)-linked paramagnetic particles.* Physical Review E, 2003. **68**(2): p. 021402.

199. Vuppu, A.K., A.A. Garcia, and M.A. Hayes, *Video microscopy of dynamically aggregated paramagnetic particle chains in an applied rotating magnetic field.* Langmuir, 2003. **19**(21): p. 8646-8653.

200. Biswal, S.L. and A.P. Gast, *Micromixing with linked chains of paramagnetic particles.* Analytical Chemistry, 2004. **76**(21): p. 6448-6455.

201. Nakata, K., Y. Hu, O. Uzun, O. Bakr, and F. Stellacci, *Chains of Superparamagnetic Nanoparticles.* Advanced Materials, 2008. **20**(22): p. 4294-4299.

202. Goubault, C., F. Leal-Calderon, J.-L. Viovy, and J. Bibette, *Self-assembled magnetic nanowires made irreversible by polymer bridging.* Langmuir, 2005. **21**(9): p. 3725-3729.

203. Cebers, A., *Dynamics of a chain of magnetic particles connected with elastic linkers.* Journal of Physics: Condensed Matter, 2003. **15**(15): p. S1335.

204. Ahniyaz, A., Y. Sakamoto, and L. Bergström, *Magnetic field-induced assembly of oriented superlattices from maghemite nanocubes.* Proceedings of the National Academy of Sciences, 2007. **104**(45): p. 17570-17574.

205. Tierno, P., T.H. Johansen, and T.M. Fischer, *Fast and rewritable colloidal assembly via field synchronized particle swapping.* Applied Physics Letters, 2014. **104**(17): p. 174102.

206. Chitu, L., Y. Chushkin, S. Luby, E. Majkova, G. Leo, A. Satka, M. Giersig, and M. Hilgendorff, *Effect of magnetic field on self-assembling of colloidal Co magnetic nanoparticles.* Applied surface science, 2006. **252**(15): p. 5559-5562.

207. Ku, J., D.M. Aruguete, A.P. Alivisatos, and P.L. Geissler, *Self-assembly of magnetic nanoparticles in evaporating solution.* Journal of the American Chemical Society, 2010. **133**(4): p. 838-848.

XII

208. Goubault, C., P. Jop, M. Fermigier, J. Baudry, E. Bertrand, and J. Bibette, *Flexible magnetic filaments as micromechanical sensors.* Physical Review Letters, 2003. **91**(26): p. 260802.

209. Sahoo, Y., M. Cheon, S. Wang, H. Luo, E. Furlani, and P. Prasad, *Field-directed self-assembly of magnetic nanoparticles.* The Journal of Physical Chemistry B, 2004. **108**(11): p. 3380-3383.

210. Wiedenmann, A., U. Keiderling, K. Habicht, M. Russina, and R. Gähler, *Dynamics of field-induced ordering in magnetic colloids studied by new time-resolved small-angle neutron-scattering techniques.* Physical Review Letters, 2006. **97**(5): p. 057202.

211. He, L., M. Wang, J. Ge, and Y. Yin, *Magnetic assembly route to colloidal responsive photonic nanostructures.* Accounts of chemical research, 2012. **45**(9): p. 1431-1440.

212. Cheng, G., D. Romero, G.T. Fraser, and A. Hight Walker, *Magnetic-field-induced assemblies of cobalt nanoparticles.* Langmuir, 2005. **21**(26): p. 12055-12059.

213. Neto, C., M. Bonini, and P. Baglioni, *Self-assembly of magnetic nanoparticles into complex superstructures: spokes and spirals.* Colloids and Surfaces A: Physicochemical and Engineering Aspects, 2005. **269**(1): p. 96-100.

214. Ge, J., H. Lee, L. He, J. Kim, Z. Lu, H. Kim, J. Goebl, S. Kwon, and Y. Yin, *Magnetochromatic microspheres: rotating photonic crystals.* Journal of the American Chemical Society, 2009. **131**(43): p. 15687-15694.

215. Zorba, S., R.T. Maxwell, C. Farah, L. He, M. Ye, and Y. Yin, *Superparamagnetic magnetite nanoparticle superstructures for optical modulation/chopping.* The Journal of Physical Chemistry C, 2010. **114**(41): p. 17868-17873.

216. Ge, J., Y. Hu, and Y. Yin, *Highly tunable superparamagnetic colloidal photonic crystals.* Angewandte Chemie, 2007. **119**(39): p. 7572-7575.

217. Sheparovych, R., Y. Sahoo, M. Motornov, S. Wang, H. Luo, P.N. Prasad, I. Sokolov, and S. Minko, *Polyelectrolyte stabilized nanowires from Fe3O4 nanoparticles via magnetic field induced self-assembly.* Chemistry of Materials, 2006. **18**(3): p. 591-593.

218. Li, D., C.N. Lam, and S.L. Biswal, *Measuring short-range repulsive forces by imaging directed magnetic-particle assembly title.* Soft Matter, 2010. **6**(2): p. 239-242.

219. Bodnarchuk, M.I., M.V. Kovalenko, S. Pichler, G. Fritz-Popovski, G.n. Hesser, and W. Heiss, *Large-area ordered superlattices from magnetic wustite/cobalt ferrite core/shell nanocrystals by doctor blade casting.* Acs Nano, 2009. **4**(1): p. 423-431.

220. Li, D., J. Rogers, and S.L. Biswal, *Probing the Stability of Magnetically Assembled DNA-Linked Colloidal Chains.* Langmuir, 2009. **25**(16): p. 8944-8950.

221. Kim, H., J. Ge, J. Kim, S.-e. Choi, H. Lee, H. Lee, W. Park, Y. Yin, and S. Kwon, *Structural colour printing using a magnetically tunable and lithographically fixable photonic crystal.* Nature Photonics, 2009. **3**(9): p. 534-540.

222. Lisiecki, I. and M.-P. Pileni, *Ordering at Various Scales: Magnetic Nanocrystals.* The Journal of Physical Chemistry C, 2011. **116**(1): p. 3-14.

223. Klokkenburg, M., B.E. Erné, J.D. Meeldijk, A. Wiedenmann, A.V. Petukhov, R.P.A. Dullens, and A.P. Philipse, *In Situ Imaging of Field-Induced Hexagonal Columns in Magnetite Ferrofluids.* Physical Review Letters, 2006. **97**: p. 185702.

224.   Gajula, G.P., M.T. Neves-Petersen, and S.B. Petersen, *Visualization and quantification of four steps in magnetic field induced two-dimensional ordering of superparamagnetic submicron particles.* Applied Physics Letters, 2010. **97**(10): p. 103103.

225.   Martínez-Pedrero, F., J. Benet, J. Rubio, E. Sanz, R. Rubio, and F. Ortega, *Field-induced sublimation in perfect two-dimensional colloidal crystals.* Physical Review E, 2014. **89**(1): p. 012306.

226.   Li, D., S. Banon, and S.L. Biswal, *Bending dynamics of DNA-linked colloidal particle chains.* Soft Matter, 2010. **6**(17): p. 4197-4204.

227.   Heinrich, D., A. Goni, A. Smessaert, S. Klapp, L. Cerioni, T. Osan, D. Pusiol, and C. Thomsen, *Dynamics of the field-induced formation of hexagonal zipped-chain superstructures in magnetic colloids.* Physical Review Letters, 2011. **106**(20): p. 208301.

228.   Lyubchanskii, I., N. Dadoenkova, M. Lyubchanskii, E. Shapovalov, and T. Rasing, *Magnetic photonic crystals.* Journal of Physics D: Applied Physics, 2003. **36**(18): p. R277.

229.   Ge, J., L. He, Y. Hu, and Y. Yin, *Magnetically induced colloidal assembly into field-responsive photonic structures.* Nanoscale, 2011. **3**(1): p. 177-183.

230.   Panda, P., K.W. Bong, T.A. Hatton, and P.S. Doyle, *Branched networks by directed assembly of shape anisotropic magnetic particles.* Langmuir, 2011. **27**(22): p. 13428-13435.

231.   Euliss, L.E., S.G. Grancharov, S. O'Brien, T.J. Deming, G.D. Stucky, C.B. Murray, and G.A. Held, *Cooperative assembly of magnetic nanoparticles and block copolypeptides in aqueous media.* Nano Letters, 2003. **3**(11): p. 1489-1493.

232.   Byun, M., J. Wang, and Z. Lin, *Massively ordered microstructures composed of magnetic nanoparticles.* Journal of Physics: Condensed Matter, 2009. **21**(26): p. 264014.

233.   Li, K.H. and B.B. Yellen, *Magnetically tunable self-assembly of colloidal rings.* Applied Physics Letters, 2010. **97**(8): p. 083105.

234.   He, L., Y. Hu, H. Kim, J. Ge, S. Kwon, and Y. Yin, *Magnetic assembly of nonmagnetic particles into photonic crystal structures.* Nano Letters, 2010. **10**(11): p. 4708-4714.

235.   Zhang, G., T. Zhang, X. Lu, W. Wang, J. Qu, and X. Li, *Controlled synthesis of 3D and 1D nickel nanostructures using an external magnetic field assisted solution-phase approach.* The Journal of Physical Chemistry C, 2007. **111**(34): p. 12663-12668.

236.   Zhang, Z., H. Duan, S. Li, and Y. Lin, *Assembly of magnetic nanospheres into one-dimensional nanostructured carbon hybrid materials.* Langmuir, 2010. **26**(9): p. 6676-6680.

237.   Wu, M., Y. Xiong, Y. Jia, H. Niu, H. Qi, J. Ye, and Q. Chen, *Magnetic field-assisted hydrothermal growth of chain-like nanostructure of magnetite.* Chemical Physics Letters, 2005. **401**: p. 374-379.

238.   Sajanlal, P. and T. Pradeep, *Magnetic Mesoflowers: Synthesis, Assembly, and Magnetic Properties†.* The Journal of Physical Chemistry C, 2010. **114**(38): p. 16051-16059.

239.   Ruder, W.C., C.-P.D. Hsu, B.D. Edelman Jr, R. Schwartz, and P.R. LeDuc, *Biological colloid engineering: Self-assembly of dipolar ferromagnetic chains in a functionalized biogenic ferrofluid.* Applied Physics Letters, 2012. **101**(6): p. 063701.

240.   Zhang, F., G.-H. Hou, and C.-C. Wang, *Preparation of wormlike PNIPAM microcontainers with magnetic nanoparticle inclusions.* Materials Letters, 2012. **89**: p. 97-100.

241. Benkoski, J.J., S.E. Bowles, B.D. Korth, R.L. Jones, J.F. Douglas, A. Karim, and J. Pyun, *Field induced formation of mesoscopic polymer chains from functional ferromagnetic colloids.* Journal of the American Chemical Society, 2007. **129**(19): p. 6291-6297.

242. Keng, P.Y., I. Shim, B.D. Korth, J.F. Douglas, and J. Pyun, *Synthesis and self-assembly of polymer-coated ferromagnetic nanoparticles.* Acs Nano, 2007. **1**(4): p. 279-292.

243. Ma, M., Q. Zhang, J. Dou, H. Zhang, D. Yin, W. Geng, and Y. Zhou, *Fabrication of one-dimensional Fe3O4P (GMA–DVB) nanochains by magnetic-field-induced precipitation polymerization.* Journal of Colloid and Interface Science, 2012. **374**(1): p. 339-344.

244. Wang, M., L. He, S. Zorba, and Y. Yin, *Magnetically Actuated Liquid Crystals.* Nano Letters, 2014. **14**(7): p. 3966-3971.

245. Thévenot, J., H. Oliveira, O. Sandre, and S. Lecommandoux, *Magnetic responsive polymer composite materials.* Chemical Society Reviews, 2013. **42**(17): p. 7099-7116.

246. Tracy, J.B. and T.M. Crawford, *Magnetic field-directed self-assembly of magnetic nanoparticles.* Mrs Bulletin, 2013. **38**(11): p. 915-920.

247. Dai, Q. and A. Nelson, *Magnetically-responsive self assembled composites.* Chemical Society Reviews, 2010. **39**(11): p. 4057-4066.

248. Hill, L.J. and J. Pyun, *Colloidal Polymers via Dipolar Assembly of Magnetic Nanoparticle Monomers.* ACS applied materials & interfaces, 2014. **6**(9): p. 6022-6032.

249. Godoy, M., A. Moreno, G. Jorge, H. Ferrari, P. Antonel, J. Mietta, M. Ruiz, R. Negri, M. Pettinari, and V. Bekeris, *Micrometric periodic assembly of magnetotactic bacteria and magnetic nanoparticles using audio tapes.* Journal of Applied Physics, 2012. **111**(4): p. 044905.

250. Bardea, A. and R. Naaman, *Magnetolithography: From Bottom‐Up Route to High Throughput.* Small, 2009. **5**(3): p. 316-319.

251. Bardea, A., A. Baram, A.K. Tatikonda, and R. Naaman, *Magnetolithographic Patterning of Inner Walls of a Tube: A New Dimension in Microfluidics and Sequential Microreactors.* Journal of the American Chemical Society, 2009. **131**(51): p. 18260-18262.

252. Yu, C., J. Zhang, and S. Granick, *Directed colloidal assembly: Printing with magnets.* Nature Materials, 2014. **13**(1): p. 8-9.

253. Grzybowski, B.A. and G.M. Whitesides, *Directed dynamic self-assembly of objects rotating on two parallel fluid interfaces.* The Journal of Chemical Physics, 2002. **116**(19): p. 8571-8577.

254. Grzybowski, B.A., H.A. Stone, and G.M. Whitesides, *Dynamics of self assembly of magnetized disks rotating at the liquid–air interface.* Proceedings of the National Academy of Sciences, 2002. **99**(7): p. 4147-4151.

255. Grzybowski, B.A., X. Jiang, H.A. Stone, and G.M. Whitesides, *Dynamic, self-assembled aggregates of magnetized, millimeter-sized objects rotating at the liquid-air interface: Macroscopic, two-dimensional classical artificial atoms and molecules.* Physical Review E, 2001. **64**(1): p. 011603.

256. Grzybowski, B.A. and G.M. Whitesides, *Dynamic aggregation of chiral spinners.* Science, 2002. **296**(5568): p. 718-721.

257. Tierno, P., R. Muruganathan, and T.M. Fischer, *Viscoelasticity of dynamically self-assembled paramagnetic colloidal clusters.* Physical Review Letters, 2007. **98**(2): p. 028301.

258. Müller, K., N. Osterman, D. Babic, C.N. Likos, J. Dobnikar, and A. Nikoubashman, *Pattern formation and coarse-graining in 2D colloids driven by multiaxial magnetic fields.* Langmuir, 2014.

259. Wittbracht, F., B. Eickenberg, A. Weddemann, and A. Hütten. *Rotating magnetic field assisted formation of highly ordered two-dimensional magnetic bead arrays.* in *ICQNM 2011, The Fifth International Conference on Quantum, Nano and Micro Technologies.* 2011.

260. Weddemann, A., F. Wittbracht, B. Eickenberg, and A. Hütten, *Magnetic field induced assembly of highly ordered two-dimensional particle arrays.* Langmuir, 2010. **26**(24): p. 19225-19229.

261. Koser, A.E., N.C. Keim, and P.E. Arratia, *Structure and dynamics of self-assembling colloidal monolayers in oscillating magnetic fields.* Physical Review E, 2013. **88**(6): p. 062304.

262. Tierno, P., S. Schreiber, W. Zimmermann, and T.M. Fischer, *Shape Discrimination with Hexapole−Dipole Interactions in Magic Angle Spinning Colloidal Magnetic Resonance.* Journal of the American Chemical Society, 2009. **131**(15): p. 5366-5367.

263. Tierno, P., T.H. Johansen, and J. Sancho, *Unconventional dynamic hysteresis in a periodic assembly of paramagnetic colloids.* Physical Review E, 2013. **87**(6): p. 062301.

264. Tierno, P., *Depinning and Collective Dynamics of Magnetically Driven Colloidal Monolayers.* Physical Review Letters, 2012. **109**(19): p. 198304.

265. Tierno, P., *Magnetically reconfigurable colloidal patterns arranged from arrays of self-assembled microscopic dimers.* Soft Matter, 2012. **8**(45): p. 11443-11446.

266. Tierno, P., T.M. Fischer, T.H. Johansen, and F. Sagués, *Colloidal assembly on magnetically vibrated stripes.* Physical Review Letters, 2008. **100**(14): p. 148304.

267. Straube, A.V. and P. Tierno, *Tunable interactions between paramagnetic colloidal particles driven in a modulated ratchet potential.* Soft Matter, 2014. **10**(22): p. 3915-3925.

268. Tierno, P., *Magnetic assembly and annealing of colloidal lattices and superlattices.* Langmuir, 2014.

269. Sarella, A., A. Torti, M. Donolato, M. Pancaldi, and P. Vavassori, *Two‑Dimensional Programmable Manipulation of Magnetic Nanoparticles on‑Chip.* Advanced Materials, 2014.

270. Llera, M., J. Codnia, and G.A. Jorge, *Formation and Kinetics of Self-Assembled Structures of Magnetic Microparticles in Rotating Fields.* IEEE Transactions on Magnetics, 2013. **49**(8): p. 4725-4728.

271. Snezhko, A. and I.S. Aranson, *Magnetic manipulation of self-assembled colloidal asters.* Nature Materials, 2011. **10**(9): p. 698-703.

272. Alexey, S., *Non-equilibrium magnetic colloidal dispersions at liquid–air interfaces: dynamic patterns, magnetic order and self-assembled swimmers.* Journal of Physics: Condensed Matter, 2011. **23**(15): p. 153101.

273. Snezhko, A., M. Belkin, I. Aranson, and W.-K. Kwok, *Self-assembled magnetic surface swimmers.* Physical Review Letters, 2009. **102**(11): p. 118103.

274. Erb, R.M., J. Segmehl, M. Charilaou, J.F. Löffler, and A.R. Studart, *Non-linear alignment dynamics in suspensions of platelets under rotating magnetic fields.* Soft Matter, 2012. **8**(29): p. 7604-7609.

275. Erb, R.M., J. Segmehl, M. Schaffner, and A.R. Studart, *Temporal response of magnetically labeled platelets under dynamic magnetic fields.* Soft Matter, 2013. **9**(2): p. 498-505.

276.   Jäger, S., H. Stark, and S.H. Klapp, *Dynamics of cluster formation in driven magnetic colloids dispersed on a monolayer.* Journal of Physics: Condensed Matter, 2013. **25**(19): p. 195104.

277.   Jäger, S., H. Schmidle, and S.H. Klapp, *Nonequilibrium condensation and coarsening of field-driven dipolar colloids.* Physical Review E, 2012. **86**(1): p. 011402.

278.   Jäger, S. and S.H. Klapp, *Pattern formation of dipolar colloids in rotating fields: layering and synchronization.* Soft Matter, 2011. **7**(14): p. 6606-6616.

279.   Nguyen, N.H.P., D. Klotsa, M. Engel, and S.C. Glotzer, *Emergent Collective Phenomena in a Mixture of Hard Shapes through Active Rotation.* Physical Review Letters, 2014. **112**(7): p. 075701.

280.   Titirici, M.-M., R.J. White, C. Falco, and M. Sevilla, *Black perspectives for a green future: hydrothermal carbons for environment protection and energy storage.* Energy & Environmental Science, 2012. **5**(5): p. 6796-6822.

281.   Titirici, M.-M. and M. Antonietti, *Chemistry and materials options of sustainable carbon materials made by hydrothermal carbonization.* Chemical Society Reviews, 2010. **39**(1): p. 103-116.

282.   Hu, B., K. Wang, L. Wu, S.H. Yu, M. Antonietti, and M.M. Titirici, *Engineering carbon materials from the hydrothermal carbonization process of biomass.* Advanced Materials, 2010. **22**(7): p. 813-828.

283.   Wohlgemuth, S.-A., R.J. White, M.-G. Willinger, M.-M. Titirici, and M. Antonietti, *A one-pot hydrothermal synthesis of sulfur and nitrogen doped carbon aerogels with enhanced electrocatalytic activity in the oxygen reduction reaction.* Green Chemistry, 2012. **14**(5): p. 1515-1523.

284.   Hu, Y.S., R. Demir-Cakan, M.M. Titirici, J.O. Müller, R. Schlögl, M. Antonietti, and J. Maier, *Superior Storage Performance of a Si@ SiOx/C Nanocomposite as Anode Material for Lithium-Ion Batteries.* Angewandte Chemie International Edition, 2008. **47**(9): p. 1645-1649.

285.   Wang, Q., H. Li, L. Chen, and X. Huang, *Monodispersed hard carbon spherules with uniform nanopores.* Carbon, 2001. **39**(14): p. 2211-2214.

286.   Tang, K., L. Fu, R.J. White, L. Yu, M.M. Titirici, M. Antonietti, and J. Maier, *Hollow Carbon Nanospheres with Superior Rate Capability for Sodium-Based Batteries.* Advanced Energy Materials, 2012. **2**(7): p. 873-877.

287.   Zhu, H., X. Wang, F. Yang, and X. Yang, *Promising carbons for supercapacitors derived from fungi.* Advanced Materials, 2011. **23**(24): p. 2745-2748.

288.   Falco, C., J.M. Sieben, N. Brun, M. Sevilla, T. van der Mauelen, E. Morallón, D. Cazorla-Amorós, and M.M. Titirici, *Hydrothermal Carbons from Hemicellulose-Derived Aqueous Hydrolysis Products as Electrode Materials for Supercapacitors.* ChemSusChem, 2013. **6**(2): p. 374-382.

289.   Steinbeiss, S., G. Gleixner, and M. Antonietti, *Effect of biochar amendment on soil carbon balance and soil microbial activity.* Soil Biology and Biochemistry, 2009. **41**(6): p. 1301-1310.

290.   Titirici, M.-M., A. Thomas, and M. Antonietti, *Back in the black: hydrothermal carbonization of plant material as an efficient chemical process to treat the CO2 problem?* New Journal of Chemistry, 2007. **31**(6): p. 787-789.

291.   Zheng, J., Z. Liu, X.S. Zhao, M. Liu, X. Liu, and W. Chu, *One-step solvothermal synthesis of Fe3O4@ C core–shell nanoparticles with tunable sizes.* Nanotechnology, 2012. **23**(16): p. 165601.

292.   Wang, H., Y.-B. Sun, Q.-W. Chen, Y.-F. Yu, and K. Cheng, *Synthesis of carbon-encapsulated superparamagnetic colloidal nanoparticles with magnetic-responsive photonic crystal property.* Dalton Transactions, 2010. **39**(40): p. 9565-9569.

293. Lee, J.E., S.-H. Yu, D.J. Lee, D.-C. Lee, S.I. Han, Y.-E. Sung, and T. Hyeon, *Facile and economical synthesis of hierarchical carbon-coated magnetite nanocomposite particles and their applications in lithium ion battery anodes.* Energy & Environmental Science, 2012. **5**(11): p. 9528-9533.

294. Hao, W., E. Björkman, Y. Yun, M. Lliestråle, and N. Hedin, *Iron oxide nanoparticles embedded in activated carbons prepared from hydrothermally treated waste biomass.* ChemSusChem, 2014. **7**(3): p. 875-882.

295. Kong, L., X. Lu, X. Bian, W. Zhang, and C. Wang, *Constructing carbon-coated Fe3O4 microspheres as antiacid and magnetic support for palladium nanoparticles for catalytic applications.* ACS applied materials & interfaces, 2010. **3**(1): p. 35-42.

296. Zhang, W.-M., X.-L. Wu, J.-S. Hu, Y.-G. Guo, and L.-J. Wan, *Carbon Coated Fe3O4 Nanospindles as a Superior Anode Material for Lithium-Ion Batteries.* Advanced Functional Materials, 2008. **18**(24): p. 3941-3946.

297. Chen, Y.-J., G. Xiao, T.-S. Wang, Q.-Y. Ouyang, L.-H. Qi, Y. Ma, P. Gao, C.-L. Zhu, M.-S. Cao, and H.-B. Jin, *Porous Fe3O4/carbon core/shell nanorods: synthesis and electromagnetic properties.* The Journal of Physical Chemistry C, 2011. **115**(28): p. 13603-13608.

298. Cui, X., M. Antonietti, and S.H. Yu, *Structural effects of iron oxide nanoparticles and iron ions on the hydrothermal carbonization of starch and rice carbohydrates.* Small, 2006. **2**(6): p. 756-759.

299. Baumgartner, J., A. Dey, P.H. Bomans, C. Le Coadou, P. Fratzl, N.A. Sommerdijk, and D. Faivre, *Nucleation and growth of magnetite from solution.* Nature Materials, 2013. **12**(4): p. 310-314.

300. Bennet, M.A., P.R. Richardson, J. Arlt, A. McCarthy, G.S. Buller, and A.C. Jones, *Optically trapped microsensors for microfluidic temperature measurement by fluorescence lifetime imaging microscopy.* Lab on a Chip, 2011. **11**(22): p. 3821-3828.

301. Crocker, J.C. and D.G. Grier, *Methods of digital video microscopy for colloidal studies.* Journal of Colloid and Interface Science, 1996. **179**(1): p. 298-310.

302. Vestergaard, C.L., P.C. Blainey, and H. Flyvbjerg, *Optimal estimation of diffusion coefficients from single-particle trajectories.* Physical Review E, 2014. **89**(2): p. 022726.

303. Squires, T.M., *Effective pseudo-potentials of hydrodynamic origin.* Journal of Fluid Mechanics, 2001. **443**: p. 403-412.

304. Gehrig, E. and O. Hess, *Nonlinear dynamics and self-organization of rotary molecular motor ensembles.* Physical Review E, 2006. **73**(5): p. 051916.

305. Lenz, P., J.-F. Joanny, F. Jülicher, and J. Prost, *Membranes with rotating motors.* Physical Review Letters, 2003. **91**(10): p. 108104.

306. Chen, Y., T. Kolokolnikov, and D. Zhirov, *Collective behaviour of large number of vortices in the plane.* Proceedings of the Royal Society A: Mathematical, Physical and Engineering Science, 2013. **469**(2156).

307. Aref, H., P.K. Newton, M.A. Stremler, T. Tokieda, and D.L. Vainchtein, *Vortex crystals.* Advances in applied Mechanics, 2003. **39**: p. 1-79.

308. Aref, H. and D.L. Vainchtein, *Point vortices exhibit asymmetric equilibria.* Nature, 1998. **392**(6678): p. 769-770.

309. Schreiber, S., T. Fischer, and W. Zimmermann, *Hydrodynamic attraction and repulsion between asymmetric rotors.* New Journal of Physics, 2010. **12**(7): p. 073017.

XVIII

310.   Allen, M.P. and D.J. Tildesley, *Computer simulation of liquids.* 1989: Oxford university press.

311.   Petitjean, M., *Chirality and symmetry measures: A transdisciplinary review.* Entropy, 2003. **5**(3): p. 271-312.

312.   Faivre, D. and D. Schüler, *Magnetotactic Bacteria and Magnetosomes.* Chemical Reviews, 2008. **108**(11): p. 4875-4898.

313.   Lang, C., D. Schüler, and D. Faivre, *Synthesis of Magnetite Nanoparticles for Bio- and Nanotechnology: Genetic Engineering and Biomimetics of Bacterial Magnetosomes.* Macromolecular Bioscience, 2007. **7**(2): p. 144-151.

314.   Alphandéry, E., A.T. Ngo, C. Lefevre, I. Lisiecki, L.F. Wu, and M.P. Pileni, *Difference between the magnetic properties of the magnetotactic bacteria and those of the extracted magnetosomes: Influence of the distance between the chains of magnetosomes.* Journal of Physical Chemistry C, 2008. **112**(32): p. 12304-12309.

315.   Maeda, Y., T. Yoshino, M. Takahashi, H. Ginya, J. Asahina, H. Tajima, and T. Matsunaga, *Noncovalent immobilization of streptavidin on in vitro- and in vivo-biotinylated bacterial magnetic particles.* Applied and Environmental Microbiology, 2008. **74**(16): p. 5139-5145.

316.   Ceyhan, B., P. Alhorn, C. Lang, D. Schüler, and C.M. Niemeyer, *Semisynthetic Biogenic Magnetosome Nanoparticles for the Detection of Proteins and Nucleic Acids.* Small, 2006. **2**(11): p. 1251-1255.

317.   Reinhard, B.M., J.M. Yassif, P. Vach, and J. Liphardt, *Chapter Eight-Plasmon Rulers as Dynamic Molecular Rulers in Enzymology.* Methods in enzymology, 2010. **475**: p. 175-198.

318.   Fischer, A., M. Schmitz, B. Aichmayer, P. Fratzl, and D. Faivre, *Structural purity of magnetite nanoparticles in magnetotactic bacteria.* Journal of the Royal Society Interface, 2011. **8**: p. 1011-1018.

319.   Yang, D., J. Hu, and S. Fu, *Controlled Synthesis of Magnetite− Silica Nanocomposites via a Seeded Sol− gel Approach.* The Journal of Physical Chemistry C, 2009. **113**(18): p. 7646-7651.

320.   Lu, Y., Y. Yin, B.T. Mayers, and Y. Xia, *Modifying the surface properties of superparamagnetic iron oxide nanoparticles through a sol-gel approach.* Nano Letters, 2002. **2**(3): p. 183-186.

321.   Hu, Y., L. He, and Y. Yin, *Magnetically responsive photonic nanochains.* Angewandte Chemie International Edition, 2011. **50**(16): p. 3747-3750.

322.   Baumgartner, J., P. Lesevic, M. Kumari, K. Halbmair, M. Bennet, A. Körnig, M. Widdrat, J. Andert, M. Wollgarten, and L. Bertinetti, *From magnetotactic bacteria to hollow spirilla-shaped silica containing a magnetic chain.* RSC Advances, 2012.

323.   Iglesias-Silva, E., J. Rivas, L. León Isidro, and M. López-Quintela, *Synthesis of silver-coated magnetite nanoparticles.* Journal of Non-Crystalline Solids, 2007. **353**(8): p. 829-831.

324.   Mandal, M., S. Kundu, S.K. Ghosh, S. Panigrahi, T.K. Sau, S. Yusuf, and T. Pal, *Magnetite nanoparticles with tunable gold or silver shell.* Journal of Colloid and Interface Science, 2005. **286**(1): p. 187-194.

325.   Marková, Z., K. Šišková, J. Filip, K. Šafářová, R. Prucek, A. Panáček, M. Kolář, and R. Zbořil, *Chitosan-based synthesis of magnetically-driven nanocomposites with biogenic magnetite core, controlled silver size, and high antimicrobial activity.* Green Chemistry, 2012. **14**(9): p. 2550-2558.

326.   Prucek, R., J. Tuček, M. Kilianová, A. Panáček, L. Kvítek, J. Filip, M. Kolář, K. Tománková, and R. Zbořil, *The targeted antibacterial and antifungal properties of magnetic nanocomposite of iron oxide and silver nanoparticles.* Biomaterials, 2011. **32**(21): p. 4704-4713.

327. Liu, Z., B. Zhao, Y. Shi, C. Guo, H. Yang, and Z. Li, *Novel nonenzymatic hydrogen peroxide sensor based on iron oxide–silver hybrid submicrospheres.* Talanta, 2010. **81**(4): p. 1650-1654.

328. Gao, M.-R., S.-R. Zhang, J. Jiang, Y.-R. Zheng, D.-Q. Tao, and S.-H. Yu, *One-pot synthesis of hierarchical magnetite nanochain assemblies with complex building units and their application for water treatment.* Journal of Materials Chemistry, 2011. **21**(42): p. 16888-16892.

329. Liu, J.-f., Z.-s. Zhao, and G.-b. Jiang, *Coating Fe3O4 magnetic nanoparticles with humic acid for high efficient removal of heavy metals in water.* Environmental science & technology, 2008. **42**(18): p. 6949-6954.

330. Giri, S., B.G. Trewyn, M.P. Stellmaker, and V.S.Y. Lin, *Stimuli-Responsive Controlled-Release Delivery System Based on Mesoporous Silica Nanorods Capped with Magnetic Nanoparticles.* Angewandte Chemie International Edition, 2005. **44**(32): p. 5038-5044.

331. Ito, A., M. Shinkai, H. Honda, and T. Kobayashi, *Medical application of functionalized magnetic nanoparticles.* Journal of Bioscience and Bioengineering, 2005. **100**(1): p. 1-11.

332. Lv, P., H. Zhao, Z. Zeng, J. Wang, T. Zhang, and X. Li, *Facile preparation and electrochemical properties of carbon coated Fe3O4 as anode material for lithium-ion batteries.* Journal of Power Sources, 2014. **259**: p. 92-97.

333. Kang, E., Y.S. Jung, A.S. Cavanagh, G.H. Kim, S.M. George, A.C. Dillon, J.K. Kim, and J. Lee, *Fe3O4 Nanoparticles Confined in Mesocellular Carbon Foam for High Performance Anode Materials for Lithium-Ion Batteries.* Advanced Functional Materials, 2011. **21**(13): p. 2430-2438.

334. Ghanbari, A., M. Bahrami, and M. Nobari, *Methodology for artificial microswimming using magnetic actuation.* Physical Review E, 2011. **83**(4): p. 046301.

335. Ērglis, K., R. Livanovičs, and A. Cēbers, *Three dimensional dynamics of ferromagnetic swimmer.* Journal of Magnetism and Magnetic Materials, 2011. **323**(10): p. 1278-1282.

336. Dhont, J.K., *An introduction to dynamics of colloids*. Vol. 2. 1996: Elsevier Science.

337. Ghosh, A., P. Mandal, S. Karmakar, and A. Ghosh, *Analytical theory and stability analysis of an elongated nanoscale object under external torque.* Physical Chemistry Chemical Physics, 2013. **15**(26): p. 10817-10823.

338. Bale, R., M. Hao, A.P.S. Bhalla, and N.A. Patankar, *Energy efficiency and allometry of movement of swimming and flying animals.* Proceedings of the National Academy of Sciences, 2014. **111**(21): p. 7517-7521.

339. Theurkauff, I., C. Cottin-Bizonne, J. Palacci, C. Ybert, and L. Bocquet, *Dynamic clustering in active colloidal suspensions with chemical signaling.* Physical Review Letters, 2012. **108**(26): p. 268303.

340. Palacci, J., S. Sacanna, A.P. Steinberg, D.J. Pine, and P.M. Chaikin, *Living crystals of light-activated colloidal surfers.* Science, 2013. **339**(6122): p. 936-940.

341. Timonen, J.V., M. Latikka, L. Leibler, R.H. Ras, and O. Ikkala, *Switchable static and dynamic self-assembly of magnetic droplets on superhydrophobic surfaces.* Science, 2013. **341**(6143): p. 253-257.

342. Zhang, K.-Q. and X.Y. Liu, *In situ observation of colloidal monolayer nucleation driven by an alternating electric field.* Nature, 2004. **429**(6993): p. 739-743.

343. Zhang, T.H. and X.Y. Liu, *How does a transient amorphous precursor template crystallization.* Journal of the American Chemical Society, 2007. **129**(44): p. 13520-13526.

XX

344.   Zhang, T.H. and X.Y. Liu, *Experimental modelling of single-particle dynamic processes in crystallization by controlled colloidal assembly.* Chemical Society Reviews, 2014.

345.   Tretiakov, K.V., K.J. Bishop, and B.A. Grzybowski, *The dependence between forces and dissipation rates mediating dynamic self-assembly.* Soft Matter, 2009. **5**(6): p. 1279-1284.

346.   Fialkowski, M., K.J.M. Bishop, R. Klajn, S.K. Smoukov, C.J. Campbell, and B.A. Grzybowski, *Principles and Implementations of Dissipative (Dynamic) Self-Assembly.* The Journal of Physical Chemistry B, 2006. **110**(6): p. 2482-2496.

347.   Arbain, R., M. Othman, and S. Palaniandy, *Preparation of iron oxide nanoparticles by mechanical milling.* Minerals Engineering, 2011. **24**(1): p. 1-9.

348.   Pushkin, D.O. and J.M. Yeomans, *Fluid mixing by curved trajectories of microswimmers.* Physical Review Letters, 2013. **111**(18): p. 188101.

349.   Soler, L., V. Magdanz, V.M. Fomin, S. Sanchez, and O.G. Schmidt, *Self-Propelled Micromotors for Cleaning Polluted Water.* Acs Nano, 2013. **7**(11): p. 9611-9620.

350.   Butykai, A., A. Orbán, V. Kocsis, D. Szaller, S. Bordács, E. Tátrai-Szekeres, L.F. Kiss, A. Bóta, B.G. Vértessy, T. Zelles, and I. Kézsmárki, *Malaria pigment crystals as magnetic micro-rotors: key for high-sensitivity diagnosis.* Scientific Reports, 2013. **3**(Article number: 1431).

351.   Babincová, M., V. Altanerova, Č. Altaner, P. Čičmanec, and P. Babinec, *In vivo heating of magnetic nanoparticles in alternating magnetic field.* Medical physics, 2004. **31**(8): p. 2219-2221.

352.   Heurlin, M., M.H. Magnusson, D. Lindgren, M. Ek, L.R. Wallenberg, K. Deppert, and L. Samuelson, *Continuous gas-phase synthesis of nanowires with tunable properties.* Nature, 2012. **492**(7427): p. 90-94.

Acknowledgments

Selbstständigkeitserklärung

Hiermit versichere ich, dass ich meine Dissertation mit dem Titel „Solution synthesis and actuation of magnetic nanostructures" selbstständig angefertigt und keine anderen, als die von mir angegebenen Hilfsmittel und Quellen verwendet habe. Ich versichere, dass ich bisher an keiner Universität, weder im In- noch im Ausland, einen Promotionsversuch unternommen habe.

Ich erkläre hiermit außerdem, dass ich die Promotionsordnung der Mathematisch-Naturwissenschaftlichen Fakultät der Humboldt-Universität zu Berlin in der Fassung vom 06. Juli 2009 anerkenne.

Peter Vach

Potsdam, August 2014